Title
The submesoscale in upper-ocean fronts: pathways of vertical transport and coupling with turbulence

Author
Verma, Vicky

Publication Date
2021

UNIVERSITY OF CALIFORNIA SAN DIEGO

The submesoscale in upper-ocean fronts: pathways of vertical transport and coupling with turbulence

A dissertation submitted in partial satisfaction of the
requirements for the degree
Doctor of Philosophy

in

Engineering Sciences (Mechanical Engineering)

by

Vicky Kumar Verma

Committee in charge:

Professor Sutanu Sarkar, Chair
Professor Juan C. Del Alamo
Professor Stefan G. Llewellyn Smith
Professor Daniel L. Rudnick
Professor William R. Young

2021

The dissertation of Vicky Kumar Verma is approved, and it is acceptable in quality and form for publication on microfilm and electronically.

University of California San Diego

2021

DEDICATION

To my wife and my family,

without whom,

I wouldn’t be where I am today.

EPIGRAPH

Life is not easy for any of us. But what of that? We must have perseverance and above all confidence in ourselves. We must believe that we are gifted for something, and that this thing, at whatever cost, must be attained.

—Marie Curie

TABLE OF CONTENTS

LIST OF FIGURES

LIST OF TABLES

ACKNOWLEDGEMENTS

I would like to acknowledge my advisor, Professor Sutanu Sarkar, for his continued support and guidance through my Ph.D. research. I have benefited immensely from our discussions, as I have from his patience and attention to detail that enabled me to pursue research my own way. I would also like to thank other committee members: Professor Juan Carlos Del Alamo, Professor Stefan G. Llewellyn Smith, Professor Daniel L. Rudnick, and Professor William R. Young; their helpful comments and suggestions were invaluable.

I would like to thank all my friends and lab mates here at UCSD for their help and their company within and outside the lab. Doing research and life, in general, would not have been as enjoyable without them. I want to give my thank to Dr. Hieu Pham for his guidance and for patiently clarifying many of my doubts. I am also grateful to other lab members: Anikesh Pal, Narsimha Reddy Rapaka, Vamsi Chalamalla, Masoud Jalali, Iman Gohar, Alexandra Vandine, Karu Chongsiripinyo, Jose Luis Ortiz Tarin, Pranav Suresh, Sungwon Lee, Sheel Nidhan, and Divyanshu Gola. Thank you guys for everything that you did for me! A thank you to my old friend Priyesh Srivastava; his practical wisdom always helped me navigate the rough waters.

I express my deep and sincere gratitude to my family. Their unconditional love and support had kept me going through tough and uncertain times. I am also indebted to my wife Priyanka for her love, support, and encouragement. The sacrifices she has made for me all this time are much appreciated.

I acknowledge funding from the Office of Naval Research for supporting this work. I have performed a significant part of the thesis research under the CALYPSO DRI, and I am thankful to the group members for providing observation data and helpful discussions.

I would also like to thank my coauthors for allowing me to include the following papers as a part of this thesis.

Chapter 2 is a reprint of material published as follows: V. Verma, H. T. Pham and S. Sarkar, “The submesoscale, the finescale and their interaction at a mixed layer front,” *Ocean*

Model., 140, 101400 (2019). The dissertation author is the primary investigator and author of this work.

Chapter 3 is a reprint of material under review for publication as follows: V. Verma and S. Sarkar, “Lagrangian three-dimensional transport and dispersion by submesoscale currents at an upper-ocean front,” *Ocean Model.*, 2021. The dissertation author is the primary investigator and author of this work.

Chapter 4 is a reprint of material in preparation for publication as follows: V. Verma, H. T. Pham, and S. Sarkar, “Interaction between submesoscale currents and convection at upper-ocean fronts,” 2021. The dissertation author is the primary investigator and author of this work.

VITA

2010	B.Tech. in Aerospace Engineering, IIT Kharapur, Kharagpur, India
2014	M.S. in Engineering Mechanics, JNCASR, Bangalore, India
2021	Ph. D. in Engineering Sciences (Mechanical Engineering), University of California San Diego, USA

PUBLICATIONS

- **V. Verma**, H. T. Pham and S. Sarkar , “Interaction between submesoscale currents and convection at upper-ocean fronts,” *in preparation*
- **V. Verma** and S. Sarkar, “Lagrangian three-dimensional transport and dispersion by submesoscale currents at an upper-ocean front,” *submitted to Ocean Model.*
- **V. Verma**, H. T. Pham and S. Sarkar, “The submesoscale, the finescale and their interaction at a mixed layer front,” *Ocean Model.*, 140, 101400 (2019)

ABSTRACT OF THE DISSERTATION

The submesoscale in upper-ocean fronts: pathways of vertical transport and coupling with turbulence

by

Vicky Kumar Verma

Doctor of Philosophy in Engineering Sciences (Mechanical Engineering)

University of California San Diego, 2021

Professor Sutanu Sarkar, Chair

Large Eddy Simulation (LES) approach is utilized to investigate submesoscale $(0.1 - 10\,\mathrm{km})$ dynamics at isolated upper-ocean fronts, with a focus on vertical transport and its interaction with the turbulent finescale (0.1 - 100 m). The study considers an unforced front and also a more realistic scenario with surface cooling.

In unforced simulations, the evolution of baroclinic mixed layer instability spawns coherent vortex filaments and eddies, which are similar to the coherent features observed during the Lagrangian Submesoscale Experiment (LASER) in the Gulf of Mexico. Turbulence is generated locally in the vortex filaments. Because of localized turbulence, a 2D low-pass filter in the horizontal with cutoff wavelength at O(100 m) is used to decompose the flow into submesoscale (quasi-2D) and finescale (3D) components to study their energy interaction explicitly. The decomposition also helps understand the organization of persistent upwelling and downwelling regions at the front. Material transport is further examined by releasing Lagrangian tracer particles. Analyzing particle trajectories, we identify an eddy/lobe/filament framework that describes the coherent transport of particles at the front and elucidates the restratification process. The sub-inertial time scale observed for the vertical motion of particle clouds suggests that submesoscale dynamics control vertical transport and restratification. Dispersion characteristics of the turbulent submesoscale currents using single-, pair- and multi-particle statistics are investigated.

Simulations with surface cooling show that coherent structures are preserved in the face of mixing by boundary-layer convective turbulence. We find a strong two-way coupling between submesoscale currents and convection. Convective plumes are able to develop through vortex filaments, but are suppressed in other parts of the front. The submesoscales are also affected. The organization of vertical velocity changes, the front develops greater imbalance, and the release of potential energy by the submesoscale buoyancy production increases. Cooling assists the downscale energy cascade by significantly enhancing the conversion from submesoscale to finescale velocity.

Chapter 1

Introduction

Ocean circulation is forced by the surface fluxes of momentum, heat, and freshwater, which mostly input energy at the planetary scale. The system has to dissipate the input energy to equilibrate. The energy dissipation occurs at the Kolmogorov length scale, typically in centimeters. Thus, kinetic energy must traverse through nine orders of magnitude in length to get dissipated. The instabilities of the large-scale currents transfer energy directly to mesoscale eddies of $O(100\,\mathrm{km})$ horizontal scales and the evolutionary time scale of weeks. The dynamics at these scales are largely geostrophic, with a dominant balance between Coriolis force and the horizontal pressure gradient. However, geostrophic turbulence is characterized by an inverse energy cascade, where the kinetic energy is transferred to larger scales rather than to smaller scales (Charney, 1971, Kraichnan, 1967). The pathway for the transfer of energy from mesoscale currents to 3D, small-scale turbulence is not apparent. The bottom friction and the excitation of inertia gravity waves from bottom topographies can be significant sinks of mesoscale kinetic energy. However, most mesoscale currents are well separated from the boundary, and the transfer of mesoscale kinetic energy to small scales is not straightforward. This raises the possibility of a kinetic energy sink in the interior, a distinct submesoscale dynamical regime, typically in the range of 0.1 - 10 km, that bridges the gap between the balanced mesoscale dynamics and small-scale turbulence and provides a route for the dissipation of mesoscale kinetic energy (McWilliams, 2016, Thomas et al., 2008).

The submesoscale can be more formally defined in terms of Rossby number $Ro = U/fL$ and Froude number $Fr = U/NH$, where U is a characteristic scale of horizontal velocity, L a characteristic horizontal length scale, H a characteristic height, f is the Coriolis parameter and $N = \sqrt{-(g/\rho)\partial\rho/\partial z}$ is the buoyancy frequency. Rossby number measures the rotational control over the dynamics, while Froude number measures the control of density stratification. In the submesoscale regime, these numbers are $O(1)$ as opposed to being asymptotically small in the mesoscale regime and large in the small-scale regime. The local Richardson number $Ri = N^2/(\partial U/\partial z)^2 \sim Fr^{-2}$ is also $O(1)$. Thus, simplifications of geostrophy and its generalizations – quasigeostrophy and semigeostrophy – become questionable; the *ansatz* of three-dimensional motions free of buoyancy and rotational control is inapplicable as well. However, operating at the margins of balanced dynamics, the submesoscale currents can easily transition towards three-dimensional turbulence with a direct route to dissipation.

The role of submesoscale dynamics in forward energy cascade has been investigated using numerical models. Capet et al. (2008c) studied submesoscale dynamics in the California Current System employing Regional Ocean Modeling System (ROMS) with a range of horizontal grid resolutions. At the finest level, the horizontal grid resolution was 750 m. The simulations also included atmospheric forcing such as surface fluxes of momentum, heat, and freshwater. In these simulations, they observed a forward cascade of ageostrophic kinetic energy through submesoscale range. However, in an unforced simulation of a 50 km wide density front using the Massachusetts Institute of Technology general circulation model (MITgcm) in a channel configuration of $100\,\text{km} \times 100\,\text{km} \times 300\,\text{m}$, Boccaletti et al. (2007) observed significant energization of large scales, especially when the barolinic mixed layer instabilities became nonlinear. This is indicative of considerable inverse energy cascade through the submesoscale range. It is therefore unclear how effective the submesoscale dynamics are in forward energy cascade, and how the interaction with background flows, especially the finescale turbulence, modifies this process. Understanding the role of submesoscale dynamics in the forward energy cascade is a primary focus of this thesis.

A major drawback of the hydrostatic, large-scale simulations is that the turbulent scales where a direct forward energy cascade occurs are not resolved. An alternative approach, which is also preferred in this thesis, is to use turbulence resolving simulations of upper-ocean fronts and appropriately resolve the energetic small-scale features while compromising on the influence of large-scale currents on submesoscale dynamics. Skyllingstad and Samelson (2012) simulated an LES model of a warm-filament with $1.2\,\mathrm{km}$ wide fronts at the edges using a grid with 3 m resolution along the three coordinate directions. They observed that 3D turbulence is generated locally in thin ($O(100\,\mathrm{m})$) filament structures that developed during the evolution of baroclinic instability at the front. This study revealed that 3D isotropization and the development of a direct forward energy cascade occurs at relatively small scales. The role of boundary forced turbulence in extracting energy from the submesoscale can also be important and requires further investigation. Since 3D turbulence in these simulations develop at $O(100\,\mathrm{m})$, a suitable framework is needed for decomposing the flow appropriately to capture the interaction between the small-scale and the large-scale dynamics. In this thesis, a 2D low-pass filter in the horizontal is employed to accomplish the flow decomposition.

The lack of rotational and stratification control over submesoscale dynamics, i.e., $O(1)$ Rossby and Froude numbers, allows large vertical velocities to develop, which remain suppressed in the balanced mesoscale regime. Model studies, e.g., Mahadevan and Tandon (2006), show that negative vertical velocity magnitudes as large as $1\,\mathrm{mm\,s^{-1}}$ occur in submesoscale structures with high lateral strain rate, large vertical vorticity, and the loss of geostrophic balance. The submesoscale vertical velocity is therefore an order of magnitude larger than the typical mesoscale vertical velocity observed in the ocean (Rudnick, 1996). The ability of submesoscale dynamics to generate strong downwelling has significant impact on a wide range of physical and biological processes in the ocean.

The submesoscale currents can transport heat, salt, carbon, and chemical tracers such as oxygen and nitrogen from the surface ocean to the interior. Omand et al. (2015) observed subduction of non-sinking particulate organic matter through submesoscale filamentous features, often located at the perimeter of eddies. Large vertical velocity associated with submesoscale dynamics establishes a vertical buoyancy flux that restratifies the mixed layer (Boccaletti et al., 2007). This, in turn, affects the interaction between the interior ocean and the atmosphere. Su et al. (2018) in a study of the global ocean find that resolving the submesoscale warms the sea surface up to $0.3\,^{\circ}C$ at mid-latitudes, in comparison to a coarse simulation. This leads to an annual-mean air-sea heat flux anomaly of 4-10 $\mathrm{W\,m^{-2}}$, which is significant for climate modeling. They conclude that submesoscales are an important component for the heat exchange between the ocean and the atmosphere. Since submesoscales are not resolved in large-scale ocean models, Fox-Kemper et al. (2008) have developed a parameterization to model upper-ocean restratification by submesoscale dynamics. The parameterization can be expressed in the from of an overturning stream function that flattens the out-cropped isopycnals.

The upper-ocean submesoscale dynamics also impact the primary production by phytoplankton, which is crucial for sustaining the life in the ocean (Mahadevan, 2016). The availability of light and nutrients strongly impact the phytoplankton growth. Both of these factors are influenced by submesoscale dynamics of the upper ocean. In nutrient-limited condition, submesoscale currents support phytoplankton growth by injecting nutrient-rich upper pycnocline water to the mixed layer. On the other hand, in light-limited conditions, they support phytoplankton growth by slumping the out-cropped isopycnals and restratifying the upper ocean. The restratification by the submesoscale motions suppresses the deepening of the mixed layer by the finescale turbulence, which helps phytoplanktons remain near the surface with most radiation. Mahadevan et al. (2012) observed that in an oligotrophic (nutrient-limited) region, submesoscale restratification of the mixed layer caused phytoplanktons to bloom earlier during the spring time, before the stratification due to warming became important. Numerical models of Mahadevan and Archer (2000) and

Lévy et al. (2001) support the significant role of submesoscale dynamics in supplying nutrients to the upper ocean. A considerable increase in nutrient fluxes to the mixed layer was observed as the horizontal grid resolution is decreased from 40 km to 10 km in the simulations of Mahadevan and Archer (2000) and from 6 km to 2 km in the simulations of Lévy et al. (2001). However, it is unclear at what scales the vertical transport becomes optimal. The filament-like features that develop large vertical velocity in submesoscale dynamics can be appropriately captured in turbulence resolving simulations, providing a suitable framework for the detailed investigation of material exchange between the upper pycnocline and the mixed layer.

It is evident from the above discussions that submesoscale dynamics have profound implications for various physical and biological processes. However, for a detailed understanding of these processes, it is imperative to understand the dynamics itself, e.g., how it develops and what specific flow features it carries. In the open ocean, fronts are the most important source of submesoscale dynamics, which develop through instabilities. The regions with lateral density gradients are commonly known as fronts. They are ubiquitous in the upper ocean and are often found largely in thermal wind balance. Multiple processes can lead to the formation of fronts, such as the interaction between mesoscale eddies, out-cropping of isopycnals by the curl of surface wind stress, and differential cooling/heating at the surface. Haine and Marshall (1998) investigated the scenario of differential cooling and found that the front that formed attained thermal wind balance through geostrophic adjustment (Ou, 1984, Tandon and Garrett, 1994). However, such configurations are unstable and are susceptible to further instabilities. This can be illustrated using a simple analysis following parcel theory (e.g. Haine and Marshall, 1998). The analysis reveals that the balanced fronts are not in the state of minimum potential energy; if the fluid elements at the front are exchanged such that the heavier elements are organized at the bottom and the lighter ones at the top, the potential energy of the system decreases. The instabilities that grow drive the system to more stable configurations through restratification and give rise to submesoscale motions. Thus upper-ocean fronts provide a convenient means of modeling and studying submesoscale dynamics. We note that submesoscale features, such as coherent eddies, can also develop in the wake when the boundary layer separates off of a topography (Gula et al., 2015).

Baroclinic instability, which grows by extracting potential energy from the front, is the commonly occurring instability at upper-ocean fronts. Stone (1966, 1970) performed a linear stability analysis of the 'Eady' problem (Eady, 1949) by including ageostrophic perturbations and reported that barolinic instability is the fastest growing mode when $Ri > 0.95$. This condition can be attained easily at a mixed layer front. The analysis of Stone (1966) also provided a length scale, L_b, and a time scale, τ_b, for the growth of the dominant baroclinic mode, given by

$$L_b = 2\pi H \frac{M^2}{f^2} \sqrt{\frac{1+Ri}{5/2}}, \tag{1.1}$$

$$\tau_b = \sqrt{\frac{54}{5}} \frac{\sqrt{1+Ri}}{f}. \tag{1.2}$$

Here, $M = \sqrt{-g\partial_y \ln(\rho)}$ is the lateral buoyancy gradient and H is the depth of the front. In Eq. 1.1, the nondimensional parameter M^2/f^2, associated with the frontal strength, and the front depth H control the length scale of the baroclinic mode. Both M^2/f^2 and H are associated with the available potential energy of the front, which increases as the parameters increase in magnitude. The thermal-wind kinetic energy related to the lateral buoyancy gradient also increases, since $U/f = M^2H/f^2$. Consistent with these results, Callies et al. (2015) observed energetic submesoscale motions during the winter when the mixed layer was deep, but they were absent during the summer. Callies et al. (2015) argued that the shallow mixed layer during the summer perhaps leads to weak submesoscales, which are easily suppressed by boundary layer turbulence. In recent literature, barolinic instabilities developing at upper-ocean fronts have been referred to as mixed layer instabilities (MLIs) to distinguish them from barolinic instabilities that grow at pycnocline fronts.

Turbulence resolving simulations show that nonlinear evolution of MLIs generate coherent

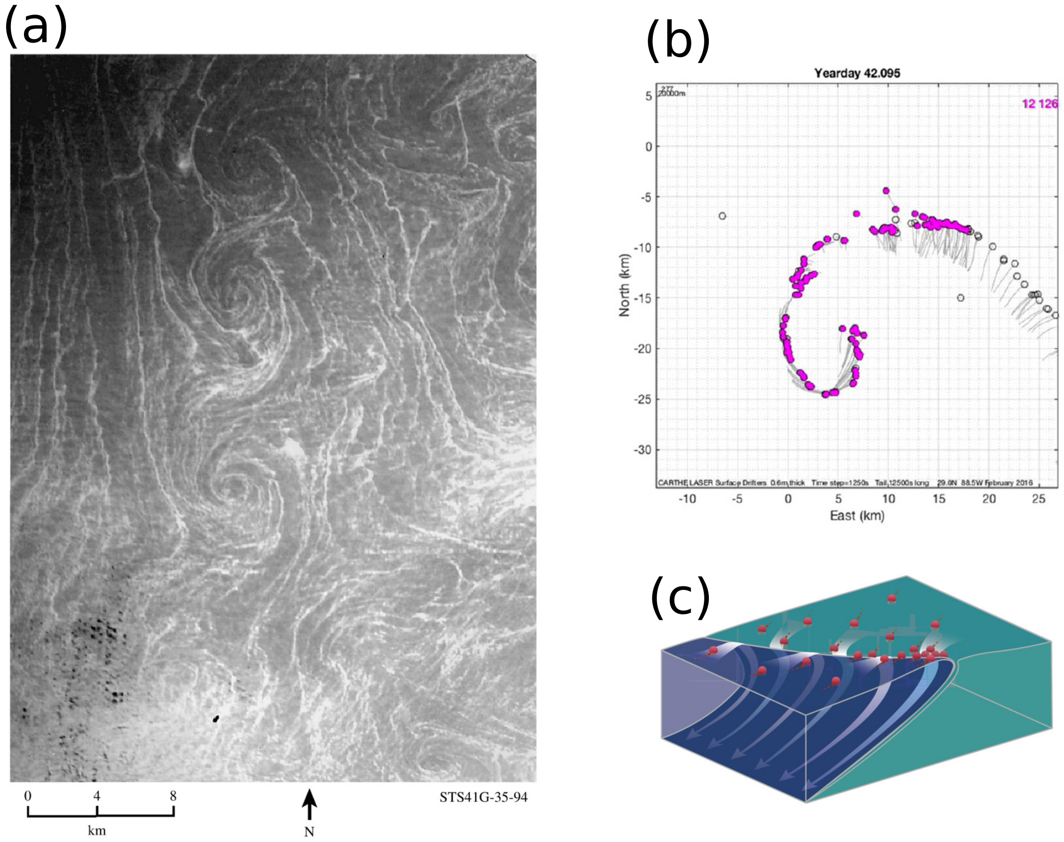

Figure 1.1: (a) A photograph taken from the sun-glint in the Mediterranean Sea off Egypt coast. The photograph shows submesoscale filaments and the formation of spirals, i.e. eddies, with radii about 5 km in the sea. This figure is adapted from Munk et al. (2000). (b) LASER drifters are shown in circles and their trajectory tails of 12500 s are also shown in gray. Positions are given in kilometers from 29°N, 88.25°W. This figure is adapted from the supplementary material of D'Asaro et al. (2018). (c) A schematic showing surface convergence and downwelling through a convergent filament in the upper ocean. This figure is adapted from D'Asaro et al. (2018).

submesoscale filaments and eddies, and these coherent structures exert strong influence on submesoscale dynamics at the front (Hamlington et al., 2014, Skyllingstad and Samelson, 2012, Stamper and Taylor, 2017, Verma et al., 2019). The submesoscale filaments and eddies have been identified in the satellite images taken in different parts of the ocean and point to the ubiquity of submesoscale dynamics in the upper ocean. Some of the satellite images are discussed in Munk et al. (2000). Figure 1.1a shows one such photograph taken from the sun-glint in the Mediterranean Sea. The photograph clearly shows the submesoscale coherent structures, i.e., the coherent filaments and eddies. These coherent features have recently been observed during the Lagrangian Submesoscale Experiment (LASER) conducted in the Gulf of Mexico by deploying a large number of surface drifters (D'Asaro et al., 2018). It was found that some of the surface drifters were attracted to convergent filaments, less than 1 km in width, which then wrapped around a cyclonic eddy (Fig. 1.1b). There was a large density contrast across the filaments, and measurements taken within these structures revealed large vertical vorticity ($\xi/f = 3.5 \pm 2.1$) and horizontal convergence of velocity ($\delta/f = -2.1 \pm 1.6$). Furthermore, the downwelling vertical velocity was as large as $1-2\,\mathrm{cm\,s^{-1}}$. However, a detailed understanding of vertical transport by these convergent features is still lacking. A visualization of vertical transport depicted by D'Asaro et al. (2018) showed sliding of the surface water and tracers through the convergent filaments into the interior(Fig. 1.1c). In this picture there was no consideration of upwelling of interior water masses to the surface. It is unclear how the small volumes of water sliding through the filaments displace the large quantities of water surrounding these structures. Since turbulence resolving simulations can capture these filamentary structures, they provide an ideal setup for investigating the vertical transport mediated by submesoscale coherent structures.

In simulations of upper-ocean fronts, submesoscale coherent filaments form due to frontogenesis mediated by the nonlinearly evolving MLIs (Samelson and Skyllingstad, 2016). Frontogenesis is a process by which an initially weak density front in thermal wind balance becomes increasingly sharp; as a result, the horizontal density gradients and the associated velocity gradients increase. The process has been commonly associated with the strain field of a large-scale flow, with shear much weaker than Coriolis frequency, as studied by Hoskins and Bretherton (1972). There are other mechanism which have been identified as frontogenetic. McWilliams et al. (2015) showed that interaction of a cold filament with boundary layer turbulence drives secondary circulations at the edges. These secondary circulations acting together lead to frontogenesis that sharpens the cold filament and restratifies the structure. The evolution of the secondary circulation can be understood in the framework of turbulent thermal wind (TTW) balance, which takes into account the additional effect of vertical mixing in the system. Sullivan and McWilliams (2018) obtained similar results in 3D simulations of a cold filament with boundary layer turbulence. The cold filament undergoes frontogenesis after interacting with the boundary layer turbulence, and the system quickly restratifies, even before the growing baroclinic instabilities could become important. In these simulations, the short along-front domain practically prohibited the MLI from growing. In contrast, Skyllingstad and Samelson (2020) using a large, MLI permitting domain, found that the instability grows even with boundary layer turbulence. The downfront wind at a front can also result in its intensification because of the nonlinear Ekman transport (Thomas and Lee, 2005). The finescale turbulence generated locally in the vortex filaments are critical for arresting frontogenesis near the surface (Sullivan and McWilliams, 2018, Verma et al., 2019). It is therefore crucial to capture the finescale interaction within the vortex filaments for modeling the dynamics of submesoscale coherent structures appropriately.

An important feature of frontogenesis is that the cyclonic vorticity becomes intensified in the region of density intensification. In accordance with this tendency, Shcherbina et al. (2013) observed asymmetry (skewness 2.5) in the distribution of vertical vorticity in the North Atlantic Mode Water region during the winter, which corresponded to a picture of strands of strong cyclonic vorticity being embedded in the background of weak anticyclonic vorticity. This asymmetric distribution of vertical vorticity has been observed in numerical studies (e.g. Capet et al., 2008a). Frontogenesis in the submesoscale dominant regions of upper ocean is suitably characterized by the asymptotic model of Barkan et al. (2019). In this asymptotic model, the near-surface horizontal convergence is comparable in magnitude to near-surface vertical vorticity, which is consistent with the observations of Shcherbina et al. (2013) and D'Asaro et al. (2018). In contrast, the deformation-driven frontogenesis studied by Hoskins and Bretherton (1972) predict much weaker horizontal convergence than vorticity as the cross-front velocity is assumed to be much weaker than the along-front velocity at all times.

The submesoscale coherent structures in turbulence resolving models have been found to be persistent against mixing by finescale turbulence. Whitt and Taylor (2017) simulated the passing of a storm over a front with active submesoscales and found that the mixed layer remains stratified during the passage. This suggests that the submesoscale dynamics is not fully suppressed. Using the Eady model and applying cooling/heating fluxes at the top/bottom boundary, Callies and Ferrari (2018) studied the evolution of submesoscale dynamics among different cases, where the boundary fluxes were varied to cover a wide range of scenarios ranging from very weak cooling to very strong cooling. In all cases, submesoscale coherent structures developed and they organized the convective plumes. Submesoscale coherent structures are also observed in the simulations of Hamlington et al. (2014) with wind and Langmuir turbulence. However, the influence of the submesoscale-finescale interaction on their individual dynamics is not fully understood. We need to quantify this interaction to improve the parameterizations of both the submesoscale and the finescale in mixed layer fronts, not resolved in the global ocean models. The forced LES models provide the necessary framework to study the interaction between the submesoscale and the finescale dynamics in detail.

Recent research in submesoscale dynamics has greatly improved our understanding of oceanic flows in the intermediate scales between mesoscale and finescale flows. It is also becoming increasingly clear that the intervening scales between the submesoscale and the finescale where the two regimes interact are crucial for understanding the process of forward energy cascade and vertical transport. A full understanding of the dynamics in this intervening regime is still lacking and is the principal focus of this thesis. In particular, we would like to answer the following scientific questions.

- What are the roles of submesoscale and finescale turbulence in the vertical transport at upper-ocean fronts? What scales are involved in this transport?
- What processes are involved in frontogenesis, responsible for generating vortex filaments at the front? What processes lead to its arrest near the surface and the length scale at which the arrest happens?

- Are there coherent transport pathways that fluid parcels follow as they circulate under the influence of coherent structures? How do the moving parcels interact to restratify the front. A related question is what controls the time scale of the vertical transport – the fast-developing finescales or the slow-evolving submesoscales controlled by MLI? Also, what are the dispersion characteristics of turbulent submesoscale flows at upper-ocean fronts?

- How do submesoscale dynamics dominated by coherent structures interact with the boundary layer turbulence? What is the effect of this interaction on the energy balance of the submesoscale and the finescale? More specifically, how do the submesoscale buoyancy production and the finescale dissipation change in response to this interaction?

To answer these questions, we perform large eddy simulations of upper-ocean fronts with and without surface forcing. In such studies, it is critical to resolve the submesoscales at $O(1\,\mathrm{km})$, the thin filaments of $O(100\,\mathrm{m})$ width, and also the finescale features at $O(10\,\mathrm{m})$ for capturing the important interactions in the dynamics. A large scale separation, spanning three orders of magnitude, makes this problem challenging to simulate. In our LES models, a grid resolution of $O(1\,\mathrm{m})$ is sufficiently high to resolve the energetic finescale motions of 3D turbulence, but not enough to resolve the dissipative scale.

The thesis is organized as follows. Chapter 2 presents the simulation of an unforced front. Coherent structures such as vortex filaments and eddies develop during the nonlinear evolution of MLI, which are similar to the observed filaments and cyclonic eddies of the LASER experiment. In this chapter, the methodology for decomposing the flow into submesoscale and finescale components using a 2D low-pass filter in the horizontal is elaborated. The decomposed fields are then utilized to elucidate the submesoscale and finescale dynamics at the front and their interaction. Chapter 3 uses the coherent structures dominated frontal dynamics of Chapter 2 and examines its transport and dispersion characteristics by releasing a large number of tracer particles. These particles move with the local fluid velocity and behave as material points. In Chapter 4, the setup of a warm filament with edge-fronts in thermal wind balance is used to investigate the influence of boundary layer turbulence on submesoscale dynamics, evolving with nonlinear MLI. In this setup, turbulence is generated by applying surface cooling, and a parametric study is performed by varying the cooling magnitude among different cases. The method of scale separation developed in Chapter 2 is employed to elucidate the interaction between submesoscale currents and the finescale convection. The energy pathways between the kinetic and potential energy reservoirs at the two scales are mapped.

Chapter 2

The submesoscale, the finescale and their interaction at a mixed layer front

2.1 Introduction

The mixed layer in the upper ocean contains fronts (regions that have sharp density gradient) that exhibit lateral density variability at sub-10 km scale, e.g. Hosegood et al. (2006), Sengupta et al. (2016), Timmermans et al. (2012). Submesoscale (0.1-10 km) instabilities (e.g. McWilliams (2016), Thomas et al. (2008)) at frontal regions have the following important consequences for the state of the upper ocean. There is restratification that changes the local properties of the mixed layer and influences the upper-ocean fluxes that are transmitted through the base of the mixed layer. The vertical velocity is enhanced, thereby promoting the exchange of heat, nutrients and material across the surface layer. There are unbalanced motions with O(1) values of Rossby number ($Ro_l = u/fl$ where u is a characteristic horizontal velocity, l is a characteristic horizontal length scale, and f the Coriolis parameter) that link the rotationally controlled mesoscale to three-dimensional turbulent motions.

The stratified, rotating flow at a front is susceptible to various spontaneous, unforced instabilities whose nonlinear evolution leads to multiscale dynamics which will be studied here. The canonical Eady model (Eady, 1949) of an inviscid geostrophically balanced flow with uniform values for lateral buoyancy gradient ($M^2 = |\partial b/\partial y|$), buoyancy frequency ($N$), and Coriolis parameter (f) is governed by two nondimensional parameters, Richardson number ($Ri = N^2/S^2$ with N the buoyancy frequency and $S = M^2/f$ the vertical shear) and the lateral buoyancy parameter (M^2/f^2). The linear evolution is dominated by symmetric instability (SI) when Richardson number lies between 0.25 and 0.95, and by baroclinic instability (BI) when $Ri > 0.95$ as shown by Stone (1966). The SI mode has no along-front variability (wavenumber $k = 0$) and the BI mode has no cross-front variability (wavenumber $l = 0$). The slantwise currents that develop during SI have vertical shear which becomes unstable to the Kelvin-Helmholtz (KH) mode as demonstrated in the 2-D simulations of Taylor and Ferrari (2009) while 3-D simulations (Arobone and Sarkar, 2015) exhibit additional mixed modes ($k \neq 0$, $l \neq 0$) before the KH instability develops. BI has received much attention owing to its relation to the growth of deep mesoscale eddies in the strongly stratified interior of the ocean. The weaker stratification of the mixed layer allows smaller-scale, shallower submesoscale eddies to develop through a version of the BI, sometimes called the mixed layer instability (MLI), that leads to a potent restratifying buoyancy flux (e.g. Boccaletti et al. (2007), Fox-Kemper et al. (2008)). In cases with initial Ri between 0.25 and 0.95, SI develops preferentially during the initial evolution, but eventually Ri increases to exceed 0.95 so that BI dominates (e.g. Fox-Kemper et al., 2008, Haine and Marshall, 1998)).

An important aspect of frontal evolution is frontogenesis (Hoskins, 1982, Hoskins and Bretherton, 1972), a process by which the width of a front decreases and there is an increase in horizontal buoyancy gradient, vertical velocity and vertical vorticity. Frontogenesis is particularly strong near the surface (Lapeyre et al., 2006), and Spall (1995) suggests that large vertical velocity needed to subduct a fluid parcel to the bottom of the mixed layer can occur through frontogenesis. Simulations of model fronts (e.g. Boccaletti et al. (2007), Fox-Kemper et al. (2008), Mahadevan and Tandon (2006)) show that submesoscale processes in the surface layer are indeed effective in restratifying the front as is also found in regional-scale models (e.g. Capet et al. (2008a,b)) that resolve the mesoscale-submesoscale transition. Nonhydrostatic, high-resolution numerical models such as that in the present work are able to access the progression of frontal thinning to the scale of turbulent eddies where frontogenesis is arrested. At these scales, the dynamics is better described by turbulent thermal wind (TTW) balance rather than geostrophic balance (Gula et al., 2014, McWilliams, 2016, 2017, McWilliams et al., 2015, Sullivan and McWilliams, 2018, Wenegrat and McPhaden, 2016).

Our understanding of dynamics at the submesoscale, that had progressed primarily by theoretical models and numerical experiments, has recently benefited from Lagrangian-based observations. D'Asaro et al. (2018) in a surface-drifter study in the northern Gulf of Mexico (DeSoto canyon region) found that some of the drifters cluster in a long, thin sharpened front which then rolls up into a cyclonic eddy which is only few kilometers in diameter. The drifters also reveal zipper structures where two sharpened fronts merge into one that wraps around the eddy. The front and eddy are convergent and have large positive vertical vorticity with values that are particularly strong in the convergent zipper region. Measurement of vertical velocity by floats reveals downwelling in the convergent region with magnitude as large as 1-2 $\mathrm{cm\,s^{-1}}$. Previously, in another observational study performed in the northern Gulf of Mexico using a large number of surface drifters, Poje et al. (2014) found energetic submesoscale turbulence that had considerable effect on the local dispersion in the submesoscale range. In a novel two-point, synchronized measurement of velocity on two parallel tracks, Shcherbina et al. (2013) found that the overall structure of the vertical vorticity on a horizontal plane is that of strands of strong cyclonic vorticity merged in the background of weak anticyclonic vorticity. Moreover, large positive vertical vorticity was found to be correlated with large strain rate.

In the present work, we explore submesoscale/finescale dynamics during the evolution of SI and BI in an unforced front. Our tool is high-resolution, nonhydrostatic modeling. Forcing by wind, buoyancy and waves in frontal regions lead to additional processes that, although of interest, are not studied here. Baroclinic instabilities in the mixed layer are able to develop in the presence of wind, surface waves and convection (e.g. Callies and Ferrari, 2018, Hamlington et al., 2014, Mahadevan et al., 2010) but their overall importance to vertical exchange, lateral stirring and mixing depends on the strength of the forcing.

The increasing resolution and accuracy of recent 3-D non-hydrostatic numerical models has enabled access to dynamics at the smallest submesoscales as well as the finescale turbulence as summarized below for unforced frontal problems. Skyllingstad and Samelson (2012) simulated the evolution of BI in a warm filament (double-front configuration with lateral and along-front periodicity) that has $\Delta T = 0.08$ K across a front width $L = 1.2$ km in a $H = 80$ m deep mixed layer with an LES model that was initially run at 6 m resolution with 8 hrs of surface cooling, and then continued without forcing after interpolation on to a 3 m grid. In fronts with finite width, L, in addition to M_0^2/f^2 ($M_0^2 = |\Delta b/L|$, where Δb is the buoyancy change across the front width L) and Ri that govern the Eady problem [1], there is another independent parameter, the Rossby number ($Ro = U_o/fL = M_0^2 H/f^2 L$) that is introduced by the initial horizontal shear. The dimensional parameters given in Skyllingstad and Samelson (2012) lead to $M_0^2/f^2 \approx 6.67$, $Ro \approx 0.44$. The initially unstratified surface layer develops stratification with $Ri \approx 2$ after the surface cooling. A major result of Skyllingstad and Samelson (2012) is that turbulence develops at isolated small-scale features on the sharpening baroclinic wave instead of the classical picture of a continuous energy cascade through intermediate wavenumbers. Further analysis (Samelson and Skyllingstad, 2016) of the model results showed that frontogenesis leads to features with unstable vertical shear ($Ri < 0.25$) where turbulence is found. Ozgokmen et al. (2011) conducted LES of BI in a front that is 3 km wide and has a 80 m deep mixed layer with a focus on drifter-based sampling strategies. They considered a $Ro = 0.066$ front with strong rotational control and dynamics different from our present interest. Arobone and Sarkar (2015) simulated the nonlinear

---

[1] The background lateral buoyancy gradient, M, is held constant in the Eady problem while it evolves from it initial value, M_0, in a finite-width front

evolution of SI into turbulence with $Ri = 0.5$ and $M^2/f^2 = 16$ on a grid with $1024 \times 1024 \times 256$ points and, in addition to the 2-D (in lateral-vertical plane) KH instability found by Taylor and Ferrari (2009), found a tertiary instability (in the downfront-vertical plane) that preceded 3-D turbulence. The integration time and domain size were not sufficiently large to allow BI to form. Stamper and Taylor (2017) performed simulations of the Eady problem with various Ri between 0.25 and 1, and fixed $M^2/f^2 = 10$ on a grid with 2.4 m horizontal resolution and 0.8 m vertical resolution. They found that mixed modes ($k \neq 0$ and $l \neq 0$) contain the maximum turbulent kinetic energy (TKE) in the transition period between SI and BI (dominates later when Ri exceeds 0.95), and the time-integrated buoyancy term dominates the shear production term in all cases. The Reynolds number, $Re = U_0 H/\nu = M_0^2 H^2/f\nu$ is another independent parameter in the simulations and takes the value of $Re = 1.6 \times 10^4$ in Ozgokmen et al. (2011), $Re = 8 \times 10^4$ in the 3-D turbulence case of Arobone and Sarkar (2015), $Re = 4.1 \times 10^4$ in Stamper and Taylor (2017), and is unspecified in Skyllingstad and Samelson (2012).

In the present work, we conduct high-resolution LES of a front at moderate values of $Ri = 0.26$ and $Ro = 0.32$, a relatively high $Re = 2.67 \times 10^6$, and a 2 m isotropic grid in a $4098\,\mathrm{m} \times 6146\,\mathrm{m} \times 130\,\mathrm{m}$ domain. The preceding paragraph shows that our knowledge of submesoscale and turbulence dynamics in unforced fronts has progressed owing to the deployment of non-hydrostatic, 3-D numerical models. However, the relative contributions of the submesoscale and the finescale turbulence to vertical velocity, vorticity, dissipation and mixing requires further quantification and the interactions between the submesoscale and the turbulence require improved understanding. In particular, since turbulence is spatially localized by the coherent submesoscale structures, a simple decomposition of the flow between a mean (e.g., along-front averaging) and a fluctuation is inadequate to understand the interaction between the coherent structures that emerge and the finescale turbulence. Instead of frontal averaging, we apply an explicit spatial filter to the simulation data that, as will be demonstrated, effectively separates the small-scale, resolved turbulence (the finescale) from the coherent submesoscale structures, and helps characterize their different roles in vertical transport, frontogenesis/frontolysis, dissipation and mixing. The submesoscale-finescale decomposition also enables separation of the balance equations between the individual KE components, and a quantification (local in physical space and nonlocal in wavenumber space) of the submesoscale-turbulence energy transfer that is better suited to the type of turbulence that develops in this problem.

The paper is structured as follows. The setup of a model front and the numerical model is presented in Section 2.2. Section 2.3 describes the spatial filtering scheme used for separating the submesoscale from the finescale motions. The frontal evolution under symmetric and baroclinic instabilities is summarized in Section 2.4. The choice of the length scale for the submesoscale-finescale decomposition is also explained. Section 2.5 describes the properties of the submesoscale and finescale fields with a focus on the vertical velocity and restratifying fluxes. The kinetic energy in the individual submesoscale and finescale components, and their transport equations are quantified in Section 2.6 to better understand the energy pathways. Submesoscale frontogenesis by the finite-amplitude baroclinic instability is investigated in Section 2.7 by diagnosing the balance equation for the horizontal buoyancy gradient. Finally, we conclude in Section 2.8 with a summary of the results and discussion in the context of previous work.

2.2 Model setup

The model consists of a density front that is geostrophically balanced by a surface jet. In Cartesian coordinates, the front and the jet align with the x-direction (along-front) and the lateral (cross-front) density variation is in the y-direction. The z-direction (vertical) coincides with the axis of rotation. A linear equation of state, $\rho/\rho_0 = -\alpha T$, is used to relate the temperature deviation, T, from a reference temperature T_0 to that of density deviation, ρ, from a reference density $\rho_0 = 1028\,\mathrm{kg\,m^{-3}}$, where $\alpha = 2\times10^{-4}\,\mathrm{K^{-1}}$ is the coefficient of thermal expansion.

The front is centered at $y = 0$, has a width of $L = 1.2\,\mathrm{km}$ and is confined in a mixed layer

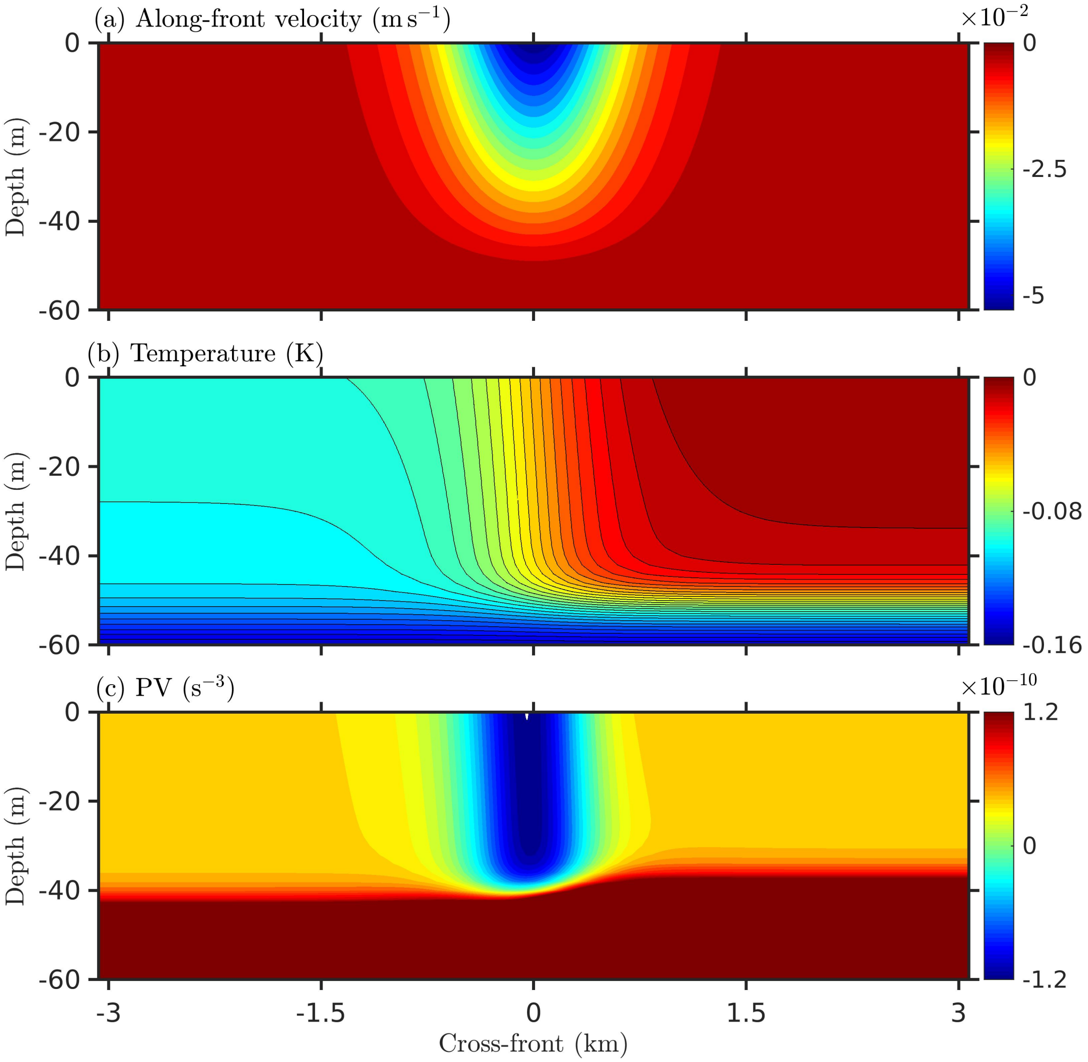

Figure 2.1: Initial profiles in the model front: (a) along-front velocity, (b) temperature and (c) potential vorticity. The profiles are uniform in the along-front direction and the initial cross-front velocity is zero. The plot of potential vorticity (panel c) shows that the front is unstable to symmetric perturbations.

with depth $H = 50\,\mathrm{m}$, situated over a thermocline. The initial velocity, temperature and potential vorticity vary in the cross-front (y) and vertical (z) directions as shown in Fig. 2.1. The potential vorticity is defined as $\mathrm{PV} = (\boldsymbol{\omega} + f\mathbf{k}) \cdot \nabla b$, where $\boldsymbol{\omega}$ is the relative vorticity, $\mathbf{k}$ is a unit vector in the vertical direction and $b = \alpha T g$ is the buoyancy. The temperature variation is given by:

$$T(y,z) = -\frac{M_0^2 L}{\alpha g}\left\{1 - 0.25\left[1 + \tanh\left(\frac{y}{0.5L}\right)\right]\left[1 + \tanh\left(\frac{z+H}{\delta_H}\right)\right]\right\} + \frac{0.5}{\alpha g}\left\{\left(N_M^2 + N_T^2\right) z + \delta_H\left(N_M^2 - N_T^2\right)\log\left[\frac{\cosh((z+H)/\delta_H)}{\cosh(H/\delta_H)}\right]\right\}. \tag{2.1}$$

Here M_0^2 is the value of $M^2 = -(g/\rho_0)\partial\rho/\partial y$ evaluated at the center $y = 0$, and M^2 is defined analogous to the square of buoyancy frequency associated with the vertical density gradient, $N^2 = -(g/\rho_0)\partial\rho/\partial z$; the parameters N_M^2 and N_T^2 are the square of buoyancy frequencies in the mixed layer and the thermocline, respectively; $\delta_H = 5\,\mathrm{m}$ is a thin region between the mixed layer and the thermocline where the temperature profile joins smoothly from its value in the mixed layer to that in the thermocline; $\mathrm{g} = 9.81\,\mathrm{m\,s^{-2}}$ is the gravitational acceleration. In the present simulation, $M_0^2 = 1.5 \times 10^{-7}\,\mathrm{s^{-2}}$, $N_M^2 = 3.0 \times 10^{-7}\,\mathrm{s^{-2}}$ and $N_T^2 = 10^{-5}\,\mathrm{s^{-2}}$. Thus, the squared buoyancy frequency in the thermocline is two-orders of magnitude larger than that in the mixed layer.

The geostrophic jet, $U(y,z)$, is constructed by integrating the density field to satisfy the thermal wind balance, i.e. $\partial U/\partial z = -M^2/f$, where $f = 1.4 \times 10^{-4}\,\mathrm{s^{-1}}$ is the Coriolis parameter. Additionally, broadband velocity fluctuations with amplitude of $10^{-4}\,\mathrm{m\,s^{-1}}$ are added to the frontal jet in order to initiate the instabilities.

The large eddy simulation (LES) approach is used to simulate the model front using non-hydrostatic Navier-Stokes equations under Boussinesq approximation. Along-front velocity u_1, cross-front velocity u_2, vertical velocity u_3, temperature T and dynamic pressure p are advanced in time t as follows:

$$\begin{aligned}
\frac{\partial u_j}{\partial x_j} &= 0,\\
\frac{\partial u_i}{\partial t}+\frac{\partial u_i u_j}{\partial x_j}+\varepsilon_{ijk} f_j u_k &= -\frac{1}{\rho_0}\frac{\partial p}{\partial x_i}+\alpha T g\delta_{i3}+\nu\frac{\partial^2 u_i}{\partial x_j^2}-\frac{\partial \tau_{ij}^{sgs}}{\partial x_j},\\
\frac{\partial T}{\partial t}+\frac{\partial u_j T}{\partial x_j} &= \kappa\frac{\partial^2 T}{\partial x_j^2}-\frac{\partial q_j^{sgs}}{\partial x_j},
\end{aligned} \tag{2.2}$$

where i, j, k = 1, 2, 3, and a repeated index implies summation. Here ν is the molecular viscosity and κ is the molecular diffusivity; $\tau_{ij}^{sgs} = -\nu^{sgs}(\partial u_i/\partial x_j + \partial u_j/\partial x_i)$ is the modeled LES subgrid stress tensor and $q_j^{sgs} = -\kappa^{sgs}(\partial T/\partial x_j)$ is the modeled LES subgrid heat flux; and, ν^{sgs} and κ^{sgs} denote the subgrid viscosity and diffusivity, respectively. Parameters ν and κ are related by the Prandtl number, $Pr = \nu/\kappa$; the value of molecular viscosity used is $\nu = 10^{-6}\,\mathrm{m^2 s^{-1}}$, and the Prandtl number $Pr = 7$. An alternate notation for the velocity components is also used wherein the along-front, cross-front and vertical velocity components are expressed as u, v and w, respectively.

When Eq. 2.2 is scaled by the velocity scale $U_0 = M_0^2 H/f$, the maximum geostrophic jet velocity at the ocean surface, and the buoyancy scale $N_M^2 H$, the non-dimensional parameters are as follows: the Ekman number, $Ek = \nu/fH^2$, the non-dimensional lateral buoyancy gradient, M_0^2/f^2, and the Richardson number, $Ri = N_M^2 f^2/M_0^4$. In the present study, $Ri = 0.26$ and $Ek = 2.86\times10^{-6}$. The ratio $M_0^2/f^2 = 7.65$ is comparable to the values used in the studies of Skyllingstad and Samelson (2012) and Hamlington et al. (2014). Also, note that the Rossby number, $Ro = U_0/fL$, based on the initial horizontal shear is 0.32 and the Reynolds number, $Re = U_0 H/\nu$, is 2.67×10^6.

The subgrid fluxes need parameterization in LES. Following Ducros et al. (1996), the subgrid viscosity, ν^{sgs}, is computed dynamically at every grid point (i, j, k) using a local velocity structure function F:

$$\nu^{sgs} = 0.0014 C_K^{-3/2}\Delta\left[F(x_i,\Delta x_i,t)\right]^{1/2}, \tag{2.3}$$

where $C_K = 0.5$ is the Kolmogorov constant, $\Delta = ||\Delta x_i||$ is the magnitude of the filter grid spacing, and

$$
\begin{aligned}
F(x,\Delta x_i,t) =& \frac{1}{4}(||\tilde{\mathbf{u}}_{i+1,j,k}-\tilde{\mathbf{u}}_{i,j,k}||^2+||\tilde{\mathbf{u}}_{i-1,j,k}-\tilde{\mathbf{u}}_{i,j,k}||^2 \\
&+||\tilde{\mathbf{u}}_{i,j+1,k}-\tilde{\mathbf{u}}_{i,j,k}||^2+||\tilde{\mathbf{u}}_{i,j-1,k}-\tilde{\mathbf{u}}_{i,j,k}||^2).
\end{aligned}
\tag{2.4}
$$

Here, $\tilde{\mathbf{u}}_{i,j,k}$ is the three-component velocity field that is obtained after passing the LES velocity through a discrete Laplacian high-pass filter. The model leads to substantial subgrid viscosity only at grid points with large velocity fluctuations and has been used previously in several problems including the oceanic examples of turbulent baroclinic eddies (Skyllingstad and Samelson, 2012) and the formation of gravity currents from strong fronts (Pham and Sarkar, 2018). The subgrid diffusivity for temperature is taken to be equal to the subgrid viscosity, i.e., the subgrid Prandtl number $Pr_{sgs}=1$.

The computational domain is a rectangular box bounded by $0 \le x \le 4098\,\mathrm{m}$, $-3073\,\mathrm{m} \le \mathrm{y} \le 3073\,\mathrm{m}$ and $-130\,\mathrm{m} \le \mathrm{z} \le 0$. A uniform grid with $2050 \times 3074 \times 66$ points provides a grid resolution of 2 m in each direction. The use of a fine grid resolution is needed in order to resolve the 3-D overturning motions associated with the vortex filaments that develop during the nonlinear evolution of BI. The domain size is chosen to accommodate the growth of the most unstable baroclinic mode (Stone, 1966) whose wavelength, L_b, and the time scale, τ_b, are:

$$
L_b = 2\pi H\frac{M_0^2}{f^2}\sqrt{\frac{1+Ri}{5/2}}, \quad \tau_b = \sqrt{\frac{54}{5}}\frac{\sqrt{1+Ri}}{f}. \tag{2.5}
$$

With the parameters used in the present study, the chosen domain is large enough to accommodate at least two wavelengths of the most unstable baroclinic mode. The simulations are run for about 100 h and are terminated when the coherent submesoscale eddies become comparable to the width of the front.

The boundary condition in the along-front (x) direction is periodic. Free-slip on the velocity and no-flux on the temperature are used as the boundary conditions at the surface (z=0) and side boundaries. At the bottom boundary, free-slip is used for the velocity and a constant heat flux corresponding to the temperature gradient in the pycnocline is imposed. Sponge layers are employed at the lateral and bottom boundaries to prevent reflection of spurious waves. The sponge layers at the lateral boundaries have a thickness of 64 m; the sponge layer at the bottom boundary is 20 m thick. The governing equations (Eq. 2.2) are advanced in time using a mixed third-order Runge-Kutta (for advective fluxes) and Crank-Nicolson (for diffusive fluxes). Second-order finite difference discretization is used to compute spatial derivatives. The dynamic pressure is obtained by solving the Poisson equation with a multi-grid iterative method.

2.3 Separation into the submesoscale and the finescale

The nonlinearly evolving frontal instabilities lead to three-dimensional turbulence that is highly local and concentrated at the coherent structures (Skyllingstad and Samelson, 2012, Stamper and Taylor, 2017). In order to understand how the three-dimensional finescale interacts with the large-scale flow, a spatial filter is used to decompose the flow between finescale and submesoscale components in the physical space. The submesoscale is obtained by applying a low-pass spatial filter to the LES field [2]. Here, we discuss the filtering method and the transport equations for the submesoscale and the finescale. The choice of the spatial filter length scale and the dynamics of the submesoscale are discussed later in section 2.5.

The LES field variable (ϕ) is decomposed into the submesoscale ($\overline{\phi}$) and the finescale (ϕ'') as follows:

$$\phi = \overline{\phi} + \phi''. \tag{2.6}$$

---

[2] This low-pass filter is an additional explicit spatial filter that has a length scale that is much larger than the grid length scale which is the filter implicit in the LES field.

The submesoscale is obtained by the spatial filtering defined as a convolution:

$$\overline{\phi}(\mathbf{x},t) \equiv G * \phi = \int G(\mathbf{r})\phi(\mathbf{x}-\mathbf{r},t)d\mathbf{r}, \tag{2.7}$$

where $\phi = (u, v, w, p, T)$ is a LES field variable, $G(\mathbf{r})$ is the filter kernel, and $\mathbf{r}$ is a position vector measured relative to $\mathbf{x}$. The finescale component is obtained by subtracting the submesoscale component from the LES field, $\phi'' = \phi - \overline{\phi}$. Notice that $(.)''$ is used to denote the finescale component and $(.)'$ is reserved to denote the fluctuation, $\phi' = \phi - \langle\phi\rangle_x$, with respect to the Reynolds average where the average is taken to be the along-front average, $\langle\phi\rangle_x = (1/L_x)\int_0^{L_x} \phi(\mathbf{x},t)dx$.

In this study, a two dimensional Lanczos filter has been used in the horizontal plane. The filter kernel in one dimension is given by

$$G_{1D}(\zeta) = \mathrm{sinc}(k_c\zeta)\,\mathrm{sinc}\left(\frac{k_c\zeta}{a}\right); \quad \mathrm{sinc}(k_c\zeta) = \frac{\sin(k_c\zeta)}{k_c\zeta}. \tag{2.8}$$

Here, a is a non-zero positive integer, k_c is a cutoff wavenumber, and ζ is the distance from the position where the filter is applied. The extension of the filter kernel to two dimensions is straight forward and is given by

$$G_{2D}(\zeta,\eta) = G_{1D}(\zeta)G_{1D}(\eta), \tag{2.9}$$

where ζ and η are distances in the x- and y-directions, respectively. The Lanczos filter provides the advantage of a sharp cut-off in the wavenumber space. This filter has been used in previous studies to separate the very-large scale flow (mesoscale) from the submesoscale (Haza et al., 2016, Mensa et al., 2013).

To understand the dynamical consequences of the separation into the submesoscale and finescale, it is useful to derive the equations that govern these individual components from the original Eq. 2.2. Since the filter function is homogeneous, continuity is satisfied at both scales, i.e.,

$$\frac{\partial \bar{u}_j}{\partial x_j} = 0, \quad \frac{\partial u''_j}{\partial x_j} = 0. \tag{2.10}$$

The momentum and temperature transport equations at the submesoscale become

$$\begin{gathered}
\frac{\partial \overline{u}_i}{\partial t} + \frac{\partial \overline{u}_i \overline{u}_j}{\partial x_j} + \varepsilon_{ijk} f_j \overline{u}_k = -\frac{1}{\rho_0}\frac{\partial \overline{p}}{\partial x_i} + \alpha \overline{T} g \delta_{i3} + \nu \frac{\partial^2 \overline{u}_i}{\partial x_j^2} - \frac{\partial \overline{\tau}_{ij}^{sgs}}{\partial x_j} - \frac{\partial \tau_{ij}^R}{\partial x_j}, \\
\frac{\partial \overline{T}}{\partial t} + \frac{\partial \overline{u}_j \overline{T}}{\partial x_j} = \kappa \frac{\partial^2 \overline{T}}{\partial x_j^2} - \frac{\partial \overline{q}_j^{sgs}}{\partial x_j} - \frac{\partial q_j^R}{\partial x_j},
\end{gathered} \tag{2.11}$$

where $\tau_{ij}^R = \overline{u_i u_j} - \overline{u}_i \overline{u}_j$ is the residual stress and $q_j^R = \overline{u_j T} - \overline{u}_j \overline{T}$ is the residual heat flux; $\overline{\tau_{ij}}^{sgs}$ and $\overline{q_j}^{sgs}$ are the model subgrid stress and heat flux, respectively, at the submesoscale after applying the additional Lanczos filter.

At the finescale, the momentum and temperature transport equations become

$$\begin{gathered}
\frac{\partial u''_i}{\partial t} + \overline{u}_j \frac{\partial u''_i}{\partial x_j} + u''_j \frac{\partial \overline{u}_i}{\partial x_j} + \frac{\partial u''_i u''_j}{\partial x_j} + \varepsilon_{ijk} f_j u''_k = -\frac{1}{\rho_0}\frac{\partial p''}{\partial x_i} + \alpha T'' g \delta_{i3} + \nu \frac{\partial^2 u''_i}{\partial x_j^2} - \frac{\partial \tau''^{sgs}_{ij}}{\partial x_j} + \frac{\partial \tau_{ij}^R}{\partial x_j}, \\
\frac{\partial T''}{\partial t} + \overline{u}_j \frac{\partial T''}{\partial x_j} + u''_j \frac{\partial \overline{T}}{\partial x_j} + \frac{\partial u''_j T''}{\partial x_j} = \kappa \frac{\partial^2 T''}{\partial x_j^2} - \frac{\partial q''^{sgs}_j}{\partial x_j} + \frac{\partial q_j^R}{\partial x_j}.
\end{gathered} \tag{2.12}$$

The 1st and 4th terms on the left hand side (LHS) of the finescale momentum and temperature equations are the temporal change and advection by the finescale, respectively. There are two additional terms on the LHS that represent interaction with the submesoscale velocity: advection by the submesoscale (2nd term) and distortion by the submesoscale gradient (3rd term). On the right hand side (RHS), τ_{ij}^R is the residual stress and q_j^R is the residual heat flux, same as those obtained at the submesoscale; τ''^{sgs}_{ij} and q''^{sgs}_j are the finescale contributions of the model subgrid stress and heat flux, respectively.

2.4 Evolution of frontal instabilities

The temporal evolution of the front under growing instabilities is summarized below before moving to the detailed analysis of the submesoscale and the finescale in the subsequent sections.

2.4.1 Symmetric instability

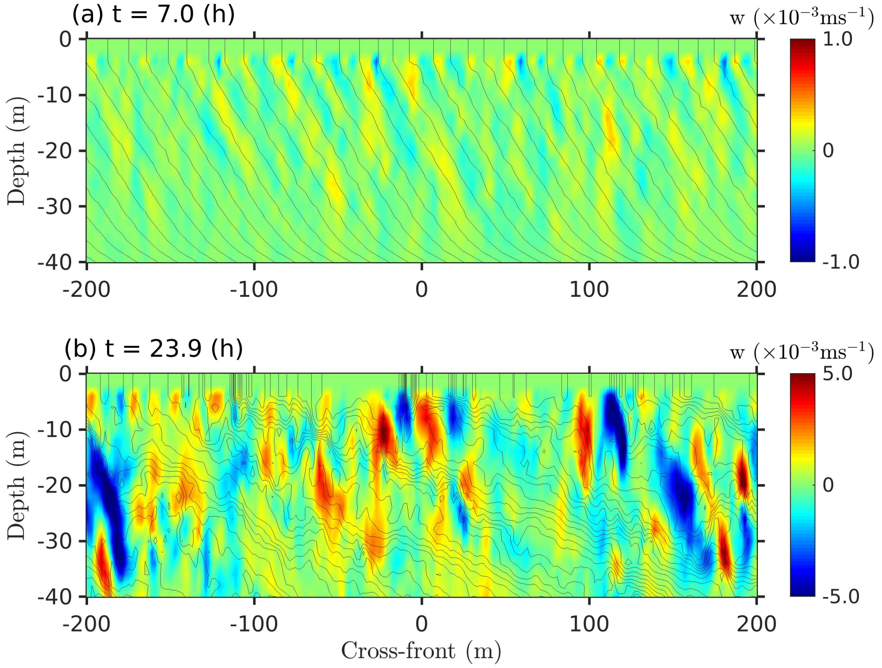

Figure 2.2: Evolution of SI: vertical velocity (*w*) at early (a) and late (b) stages of SI. The black solid lines represent isotherms.

The initial potential vorticity is negative at the simulated front (Fig. 2.1c), making the front unstable to symmetric instability (SI) (Hoskins, 1974). The evolution of SI is characterized by the formation of convection cells in the perturbation velocity which are nearly aligned with the isopycnals (Taylor and Ferrari, 2009). Figure 2.2 shows different stages of the SI evolution. Convection cells are illustrated in Fig. 2.2(a) by the bands of vertical velocity (*w*) with alternating positive and negative signs that are nearly aligned with the isotherms (coincident with isopycnals here). When the amplitude of SI becomes sufficiently large, it undergoes secondary Kelvin-Helmholtz (KH) instability due to large vertical shear ($\partial v/\partial z$) in the cells and KH billows form along the slanted isotherms (Taylor and Ferrari, 2009). Subsequently, the convection cells undergo an additional tertiary instability which appears as a lateral meandering in the $x-y$ plane with wavelength O(100) m relative to the direction in which the cells are aligned (not shown here). The tertiary instability enhances fluctuations in the cross-front vorticity component, ω_y', and subsequently leads to the breakdown of the flow into 3-D turbulence in a process, similar to that noted by Arobone and Sarkar (2015), that commences at $ft \approx 11$ ($t = 21.8\,\mathrm{h}$ in the present simulation). The turbulent stage is illustrated by the broadband, multiscale fluctuations of w in Fig. 2.2b. There are patches of positive and negative w that are O(10) m in both horizontal and vertical directions. The subsequent nonlinear evolution of SI continues with the strengthening of overturns, and w increasing up to $8\,\mathrm{mm\,s^{-1}}$ in magnitude.

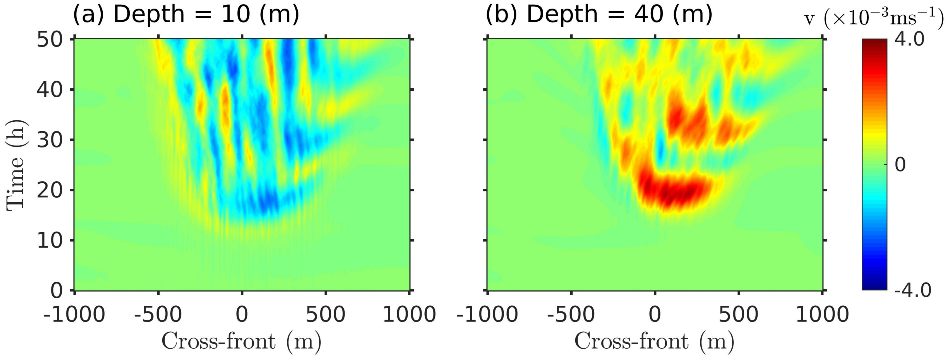

Figure 2.3: Ageostrophic secondary circulation develops during the evolution of SI. The time evolution of cross-front profiles of mean cross-front velocity, $\langle v\rangle_x$: (a) at 10 m depth and (b) at 40 m depth. The negative near-surface v in (a) transports water from the warmer side of the front (positive y) toward the colder side (negative y) while water at depth flows in the opposite direction in (b).

The growth of SI, especially the non-linear growth, leads to restratification of the front. The restratification is accompanied by the development of a secondary circulation in the y-z plane that is associated with an overall negative (light to heavy side) cross-front velocity (v) at the surface, oppositely-directed positive v below, and associated upwelling and downwelling limbs. Figure 2.3 shows the temporal evolution of v, averaged in the homogeneous along-front (x) direction, near the surface (10 m depth in Fig. 2.3a) and near the bottom (40 m depth in Fig. 2.3b) of the mixed layer. Although there is spatio-temporal variability in v, the behavior of v with increasing time indicates that the secondary circulation has overall $v < 0$ at 10 m depth that transports warm water to the colder side of the front in contrast to the oppositely-directed flow at 40 m depth with overall $v > 0$. Thus, the secondary circulation setup by SI restratifies the front, and the flow becomes stable to SI when PV becomes positive.

2.4.2 Baroclinic instability

As the SI subsides, baroclinic instability (BI) emerges to modulate the remnant of SI and eventually dominates the frontal instabilities. The growth of the BI mode results in the onset of large-scale meandering of the isotherms (Fig. 2.4a) with wavelength comparable to that predicted by the linear theory. Frontogenesis occurs as can be identified by the tightening of the isotherms in Fig. 2.4a. Vertical vorticity plots (Figs. 2.4c-d) show intensification of ω_z in the frontogenetic regions owing to locally enhanced horizontal shear. The vertical shear increases as well, following the increase in the lateral buoyancy gradient. The frontogenetic regions eventually break down into turbulence through processes which will be quantified in later sections. The development of finescale flow component in regions undergoing frontogenesis is evident from numerous small-scale structures in Figs. 2.4(b, d) and from the enhanced subgrid viscosity in Fig. 2.4f, which grows to become three orders of magnitude larger than the molecular viscosity.

The thin regions with concentrated ω_z at the front become elongated as BI grows and transform into vortex filaments (Fig. 2.4d) with lengths comparable to the wavelength of the dominant BI mode. The vortex filaments often appear in pairs – one coming from the heavier side of the front and another from the lighter side to join near the center line, $y = 0$. As the vortex-filament pairs advect downstream, they roll up and organize into vorticity patches, i.e. the coherent submesoscale eddies. In Figs. 2.4(b, d), two developing submesoscale eddies can be noted. The

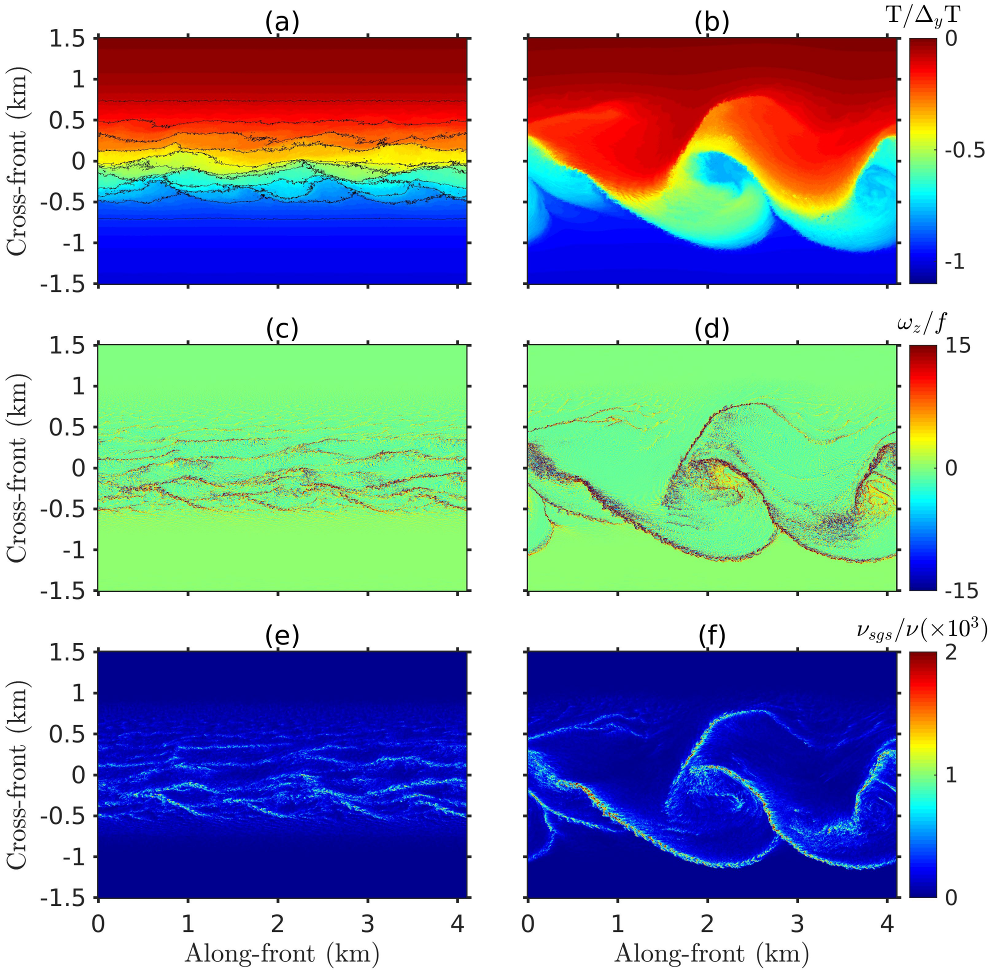

Figure 2.4: Frontogenesis occurs during the evolution of baroclinic instability. Non-dimensional temperature $T/\Delta_y T$, where $\Delta_y T = M_0^2 L/(\alpha g)$, is plotted in panels (a) and (b); non-dimensional vertical vorticity, ω_z/f, is plotted in (c) and (d); and non-dimensional subgrid viscosity, ν_{sgs}/ν, is plotted in (e) and (f). All the plots are on a horizontal $(x-y)$ plane 2 m below the surface. The figures in the left column are plotted at $t = 45$ h and those in the right column at $t = 86$ h.

overall sense of rotation in the eddies is cyclonic. Note that the cores of the submesoscale eddies are relatively colder (i.e., heavier) than the surrounding fluid due to entrainment of the cold water from the heavier side of the front. After forming, the submesoscale eddies continue to grow by the supply of vorticity from the filament structures. By the end of the simulation, the submesoscale eddies had grown to become 1 km in diameter, comparable in size to the initial width of the front.

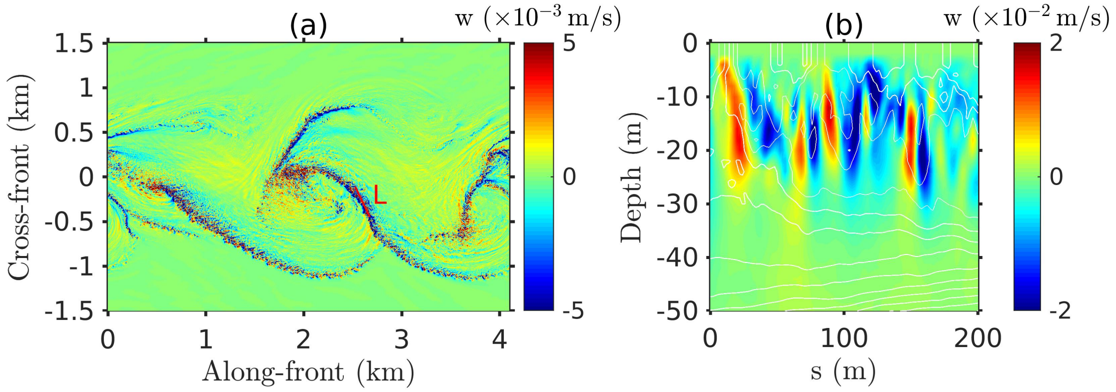

Figure 2.5: (a) Vertical velocity on a horizontal plane at 10 m depth at $t = 86$ h. (b) Vertical velocity on a vertical cross-section along the red solid line shown in the panel (a); s is the distance measured along the line, moving in the positive y-direction. The solid white lines in panel (b) represent isotherms.

Vertical vorticity is concentrated in the coherent structures, i.e. the vortex filaments and the coherent submesoscale eddies. The value of local Rossby number ($\hat{Ro} = |\omega_z|/f$) in the coherent structures is as large as 50 (Fig. 2.4d shows $\omega_z/f \in [-15, 15]$ for better visualization) and suggests significant ageostrophy and loss of balance in these structures. Moreover, the concentration of large subgrid viscosity (Fig. 2.4f) indicates strong turbulence in the coherent structures. The ageostrophic regions develop large vertical velocity. In Fig. 2.5a, w is plotted on a horizontal plane at 10 m depth; its similarity with the ω_z-field (Fig. 2.4d) is apparent with large-w regions concentrated within the coherent structures. The magnitude of w becomes as large as $0.02\,\mathrm{m\,s^{-1}}$ or about $0.35U_0$. Figure 2.5b shows w on a cross-section whose vertical coordinate is the depth and horizontal coordinate is length (s) along a vortex filament (the line L in Fig. 2.5a). The w-field (Fig. 2.5b) within the vortex filament reveals bands of positive and negative w with 20 m characteristic length scale.

The BI is effective in restratifying the front and the process is facilitated by an ASC (Hoskins, 1982). Although large patches with coherent w (especially upwelling) can be identified in Fig. 2.5a, the finescale of the eddies obscures the ASC. The probability density function (PDF) of w shows asymmetry for magnitudes greater than $2\,\mathrm{mm\,s^{-1}}$ in favor of downwelling motion (not shown here). However, the corresponding probability of these large-w regions is quite small and the presence of net downwelling motion in the coherent structures is not obvious. Indeed, separation of the finescale from the submesoscale is necessary to clarify vertical transport as is done in section 2.5.

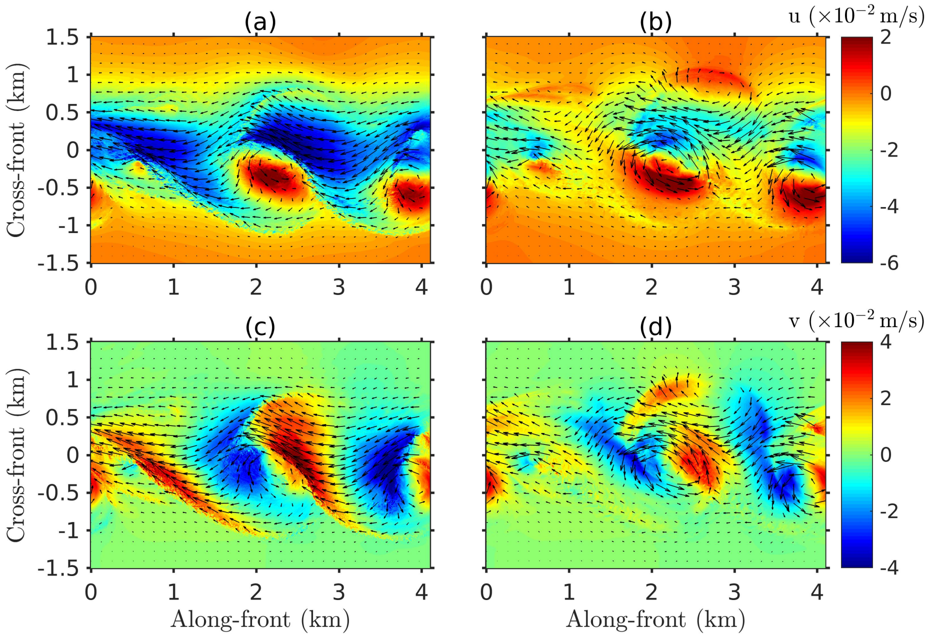

Figure 2.6: Deformation of the frontal jet due to the coherent filaments and eddies depicted at $t = 86$h. Along-front velocity component, u, at 10 m and 30 m depths are plotted in panels (a) and (b), respectively; similarly, cross-front velocity component, v, at 10 m and 30 m depths are plotted in panels (c) and (d). The arrows show the horizontal velocity vectors.

The growth of BI modifies the frontal jet as can be seen from the velocity contours and vectors of Fig. 2.6. The width of the jet near the surface increases, and it becomes more energized. The initial range of u from -5×10^{-2} to 0 $\mathrm{m\,s^{-1}}$ expands with increasing time and notably includes positive u up to $2 \times 10^{-2}\,\mathrm{m\,s^{-1}}$. The cross-front velocity (v), initially zero, becomes as large as u. Clearly, a considerable amount of kinetic energy is transferred to the swirling motion of the submesoscale eddies. These eddies speed up the jet on the lighter side of the front and slow it down on the heavier side. The eddies span the entire mixed layer depth and the modification of the jet below mid-depth is relatively strong since the initial u is small relative to the surface.

In this paper, we use the term ‘front’ to denote the region where there is significant horizontal velocity. The largest density gradients are located mainly in the coherent structures and found to be confined within the front.

2.4.3 A characteristic lateral dimension for the spatially coherent finescale

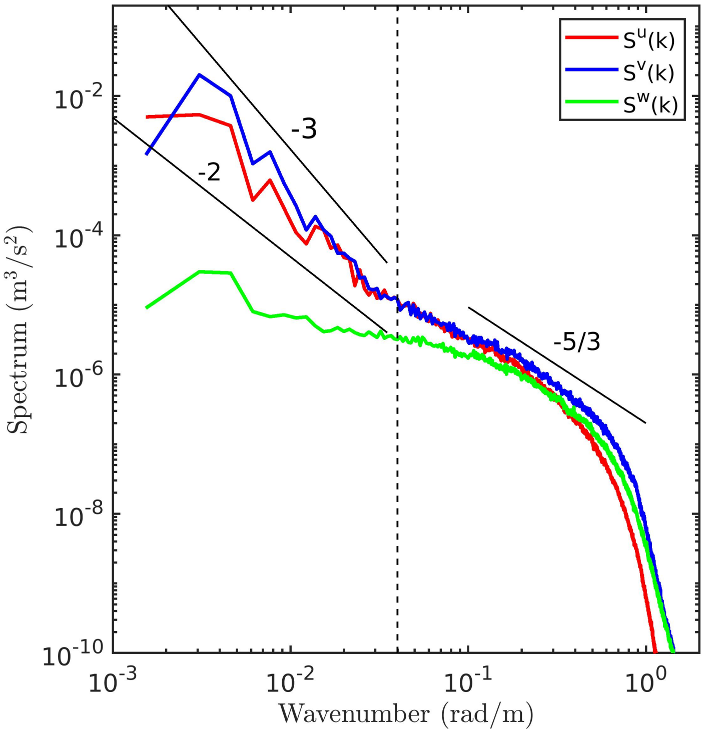

Figure 2.7: Power spectra of along-front velocity ($S^u(k)$), cross-front velocity ($S^v(k)$), and vertical velocity ($S^w(k)$) at 20 m depth and $t = 86$ h. The dashed vertical line is plotted at $k = 0.04\,\mathrm{rad\,m^{-1}}$.

Flow visualization shows formation of thin filament structures due to frontogenesis as BI evolves. Interrogation of the velocity and temperature fields in physical space reveals a characteristic lateral dimension of $O(100)$ m for the spatially-coherent finescale that is associated with the vortex filaments. The $O(100)$ m scale of frontal arrest also has an imprint on the spectra. The power spectra of the along-front velocity u, cross-front velocity v and vertical velocity w at

20 m depth are shown in Fig. 2.7. The spectra are computed as follows:

$$\begin{aligned} S^u(k) &= \frac{1}{2}\left\langle |\hat{u}(k)|^2 \right\rangle_y, \quad S^v(k) = \frac{1}{2}\left\langle |\hat{v}(k)|^2 \right\rangle_y, \\ S^w(k) &= \frac{1}{2}\left\langle |\hat{w}(k)|^2 \right\rangle_y, \end{aligned} \tag{2.13}$$

where k is the wavenumber in the along-front direction; the caret denotes the Fourier transform and $\langle\cdot\rangle_y$ denotes averaging in the lateral (y) direction over all computational grid lines between $-1.2 < y < 1.2\,\text{km}$.

The spectra (Fig. 2.7) show qualitative changes with increasing k. At low k, the kinetic energy in the vertical motion is much smaller than the energy in the horizontal motions, indicating a predominantly two-dimensional flow at these scales whereas, at higher k, the energy in the vertical motion becomes comparable to those in the horizontal motions, indicating three-dimensional turbulence. The spectra (S_u and S_v) of the horizontal velocity components also change from a steeper slope to a slope closer to $k^{-5/3}$ at k corresponding to $O(100)$ m.

A choice needs to be made for k_c, the cutoff wavenumber of the filter that determines the split between submesoscale and finescale. From the preceding discussion, k_c corresponds to $O(100)$ m. Table 2.1 shows the kinetic energy content $E^>$ in wavenumber $k > k_c$ and the distribution of $E^>$ among the three velocity components for different choices of k_c. The table shows an increase in the relative contribution of the vertical motion ($E_w^>$) with increasing k_c. At the value $k_c = 0.04\,\text{rad}\,\text{m}^{-1}$ chosen for the decomposition, $E_w^>$ becomes more than 20% and further increase of k_c leads to relatively gradual change in $E_w^>$. A posteriori, we find that our choice of k_c leads to a good separation of the submesoscale dynamics from the turbulent finescale.

A computational restriction is worth noting. It is clear that the coherent structures also introduce an important length scale to the problem – the width of the filament – which is much smaller, $O(100)$ m, compared to the wavelength of the baroclinic instability mode. This length scale restricts the horizontal grid size of submesoscale eddy-resolving simulations to be at least

Table 2.1: Influence of the cutoff wavenumber, k_c, on the kinetic energy ($E^>$) in large wavenumbers with $k > k_c$ (i.e., length scales less than or equal to $2\pi/k_c$). Here, $E^> = \int_{k_c}^{k_{max}} E(k)dk$ where $E(k)$ is the power spectrum of the kinetic energy. $E_u^>$, $E_v^>$ and $E_w^>$ are the contributions to $E^>$ from the velocity components u, v and w, respectively.

$k_c\,(\mathrm{rad\,m^{-1}})$	$E^>\,(\times 10^{-6}\,\mathrm{m^2s^{-2}})$	$E_u^>\,(\%)$	$E_v^>\,(\%)$	$E_w^>\,(\%)$
0.01	5.18	38	51	11
0.02	2.79	37	45	18
0.04	1.95	35	43	22
0.06	1.56	33	43	24
0.08	1.30	32	43	25
0.1	1.11	30	44	26

$O(100)$ m and of turbulence-resolving simulations to $O(10)$ m or less.

2.5 Submesoscale

The classical decomposition of the flow between an along-front mean and a fluctuation is not adequate to understand the role of the coherent submesoscale and its interaction with 3-D turbulence. The mean flow computed by averaging the flow in the along-front direction would overlook the spatio-temporal coherence of the submesoscale, as well as its imprint on the finescale. Here, the finescale is separated from the large-scale flow by using a low-pass filter: a two-dimensional Lanczos filter (Eq. 2.9) with $a = 2$ and $k_c = 0.04\,\mathrm{rad\,m^{-1}}$. The Lanczos filter successfully extracts the coherent structures (as will be shown) while providing a sharp cutoff in the wavenumber space; structures with $k > k_c$ are removed while the energy content of the larger structures remains largely unaffected. The value of the cutoff wavenumber, k_c, is motivated by the change in flow anisotropy (quasi-2D to 3D motions) and spectral slopes observed at $O(100)$ m that was discussed in section 2.4.3. The overall performance of the filter in separating the scales is assessed by the visualization of Fig. 2.8 where submesoscale fields, denoted by $\overline{(\cdot)}$, and finescale components, denoted by $(\cdot)''$, are shown on a horizontal plane. Qualitatively, the filter provides a good representation of the finescale in the flow while preserving the large-scale flow

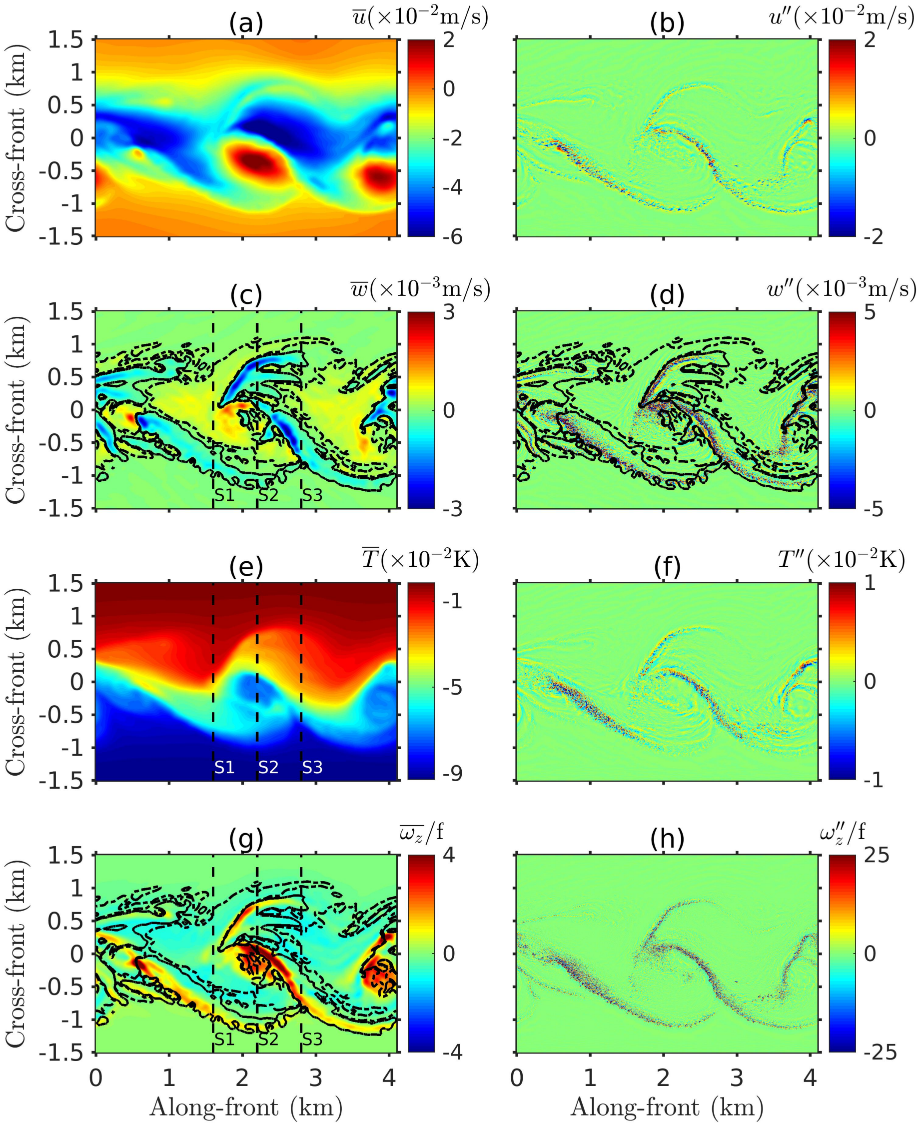

Figure 2.8: Submesoscale (left column) and finescale (right column) fields plotted at 10 m depth at $t = 86$ h: (a, b) along-front velocity, (c, d) vertical velocity, (e, f) temperature, and (g, h) non-dimensional vertical vorticity. The solid black lines and the dash-dot black lines in panels (c, d, g) correspond to $\overline{w} = -0.1\,\text{mm}\,\text{s}^{-1}$ and $\overline{w} = 0.1\,\text{mm}\,\text{s}^{-1}$, respectively, and approximately enclose the regions with downwelling and upwelling motions. Three vertical cross-sections S1, S2 and S3 at $x = 1.6, 2.2$ and 2.8 km, respectively, are also shown in panels (c, e, g).

features. It is clear that there is considerable energy corresponding to the swirling flow that is spread across the submesoscale while the finescale is localized.

2.5.1 Vertical transport

The front develops large vertical velocities as was shown by Fig. 2.5 and accompanying discussion. However, the w-field does not show distinct regions where upwelling and downwelling motions occur. The underlying structure of the vertical transport can be better understood using the submesoscale component of w.

In Fig. 2.8c, the submesoscale vertical velocity, $\overline{w}$, is plotted at 10 m depth. The $\overline{w}$-field reveals large patches with predominantly positive and negative values, separating regions with upwelling and downwelling motions. The downwelling motion, as will be shown subsequently, transports high density fluid to the interior. The organization of the patches with $\overline{w} < 0$ and $\overline{w} > 0$ is connected to the coherent structures. Negative vertical velocity is concentrated along the filaments and the magnitude is relatively stronger in regions where filaments curve into the coherent eddies. The solid black contours of $\overline{w} = -0.1\,\mathrm{mm\,s^{-1}}$ estimate the edges of the $\overline{w} < 0$ regions. On the other hand, the upwelling regions, $\overline{w} > 0$, are spatially extensive and occupy a much larger frontal area relative to $\overline{w} < 0$ regions. In Fig 2.8c, $\overline{w} > 0$ regions are identified by the black dash-dot lines corresponding to $\overline{w} = 0.1\,\mathrm{mm\,s^{-1}}$. Thus, at the submesoscale, the regions with positive and negative vertical velocities become separated, exposing the underlying structure of the upwelling and downwelling motions.

Similarly, at the submesoscale, regions of positive and negative vertical vorticity are well separated (Fig. 2.8g). The figure shows that $\overline{\omega}_z$ is positive (cyclonic) in the filament structures and in the coherent eddies, and has magnitude of 5-$7f$; negative $\overline{\omega}_z$ reaches only $1.2f$ in magnitude. The finescale vorticity (ω_z'') has large magnitude up to $50f$ which, unlike the submesoscale, is comparable for both negative and positive components. The intertwined positive and negative ω_z'' values cancel out in the finescale, and it is the submesoscale vorticity that dictates the rotation of the turbulent filament structure as it rolls-up anticlockwise to form a cyclonic eddy.

We now take a deeper look into downwelling and upwelling motions through the following decomposition of w:

$$w = w^{+} + w^{-};\begin{cases} w^{+} = 0, w^{-} \neq 0, w < 0 \\ w^{+} \neq 0, w^{-} = 0, w \geq 0. \end{cases}$$

Thus, w^{-} represents the negative part of w, while w^{+} represents the positive part including $w = 0$.

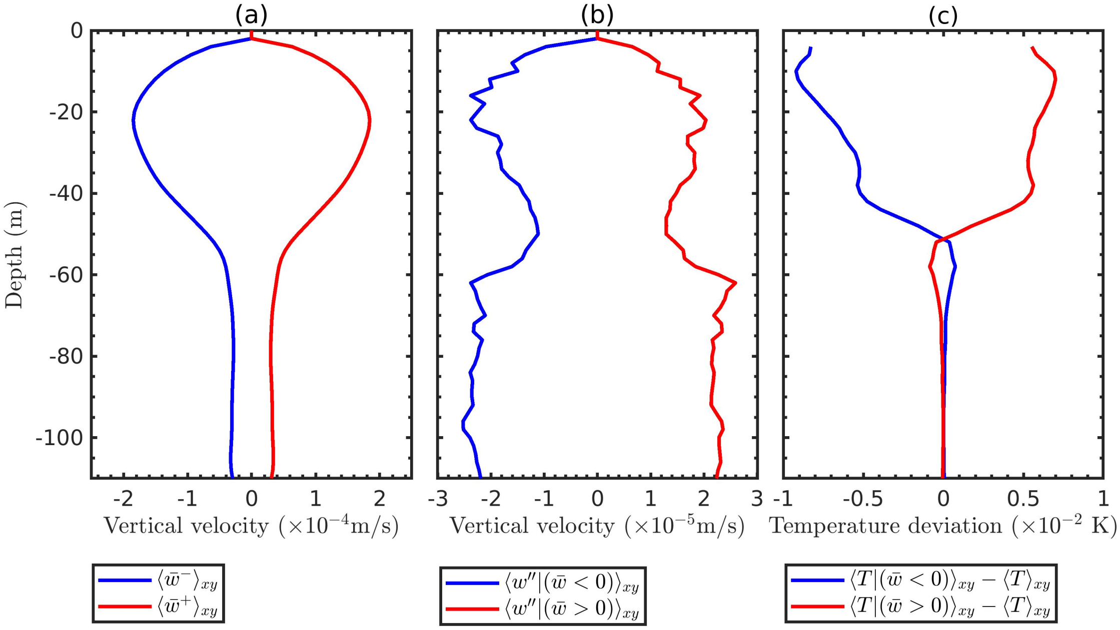

Figure 2.9: Vertical transport at the front at $t = 86$ h: (a) frontal averages of positive and negative parts of the vertical velocity, $\langle \overline{w}^{+} \rangle_{xy}$ and $\langle \overline{w}^{-} \rangle_{xy}$; (b) frontal averages of the finescale vertical velocity sampled in regions with $\overline{w} > 0$ and $\overline{w} < 0$; (c) frontal averages of T-deviation sampled in regions with $\overline{w} > 0$ and $\overline{w} < 0$, where the deviation is measured with respect to the overall horizontal average, $\langle T \rangle_{xy}$.

The frontal averages of the vertical velocity and the temperature are plotted in Fig. 2.9. The average has been calculated over the region most influenced by BI: the entire along-front length (L_x) and $-1.2 \leq y \leq 1.2$ km across the front. The vertical profiles of Fig. 2.9(a) show that $\langle \overline{w}^{+} \rangle_{xy}$ and $\langle \overline{w}^{-} \rangle_{xy}$ are nearly equal in magnitude, but opposite in sign (the difference in magnitudes is at least one-two orders smaller than either) in conformity with the continuity requirement at the submesoscale. Both $\langle \overline{w}^{+} \rangle_{xy}$ and $\langle \overline{w}^{-} \rangle_{xy}$, which are zero near the surface due to the no-penetration boundary condition, increase to their maximum values at the depth of ≈ 20 m and then decrease with increasing depth. However, they do not become zero at the mixed layer depth $H = 50\,\mathrm{m}$. The non-zero w in the thermocline is due to internal waves and found to have a different spatial structure than that in the mixed layer.

The overall upwelling and downwelling transport in the mixed layer is dominated by the submesoscale component, $\overline{w}$. Figure 2.9b shows averages of the finescale, conditioned on the sign of the submesoscale w. In the region with $\overline{w} < 0$, the net effect of the finescale is downwelling (average of w'' in that region is negative) and, in the region with $\overline{w} > 0$, the net effect is upwelling. The vertical upwelling and downwelling due to w'' of the finescale (Fig. 2.9b) is found to be much smaller, at least 7-8 times smaller than those by the submesoscale velocity. Therefore, measurement of the submesoscale vertical velocity is sufficient to obtain the net upwelling/downwelling.

The instability correlates temperature (density) with the vertical velocity. Figure 2.9c shows profiles of averaged T, conditioned on the sign of $\overline{w}$. In the regions with positive (negative) $\overline{w}$, the conditional mean of temperature is higher (lower) than the total average. Thus, the submesoscale motions transport high-density (low-T) fluid near the surface to the interior of the mixed layer and, consequently, the front restratifies. The correlation (not plotted) between the density and the vertical velocity is negative indicating the conversion of potential energy to kinetic energy.

Comparison of the $\overline{\omega}_z$ and $\overline{w}$ fields in Fig. 2.8 shows a correspondence between the regions with strong positive $\overline{\omega}_z$ and negative $\overline{w}$. It is tempting to use $\overline{\omega}_z > 0$ as a predictor of downwelling. However, the computed correlation between $\overline{\omega}_z$ and $\overline{w}$ is small. Also, the vertical downwelling (w^-) computed by conditioning on positive $\overline{\omega}_z$ is found to be substantially smaller than the net w^- at the front. The reason is that the eddy core with positive $\overline{\omega}_z$ has a substantial area of upwelling, not downwelling.

The downwelling and upwelling motions at the front can be considered as parts of an ageostrophic secondary circulation (ASC). In simplified models of fronts where the along-front variation is averaged or neglected, the ASC is a restratifying 2-D ($y-z$) circulation that is anticlockwise looking in the direction of the jet. The ASC transports near-surface water from the light ($y > 0$) to the heavy ($y < 0$) side while dense water subducts from the heavy side and moves toward the light side at depth.

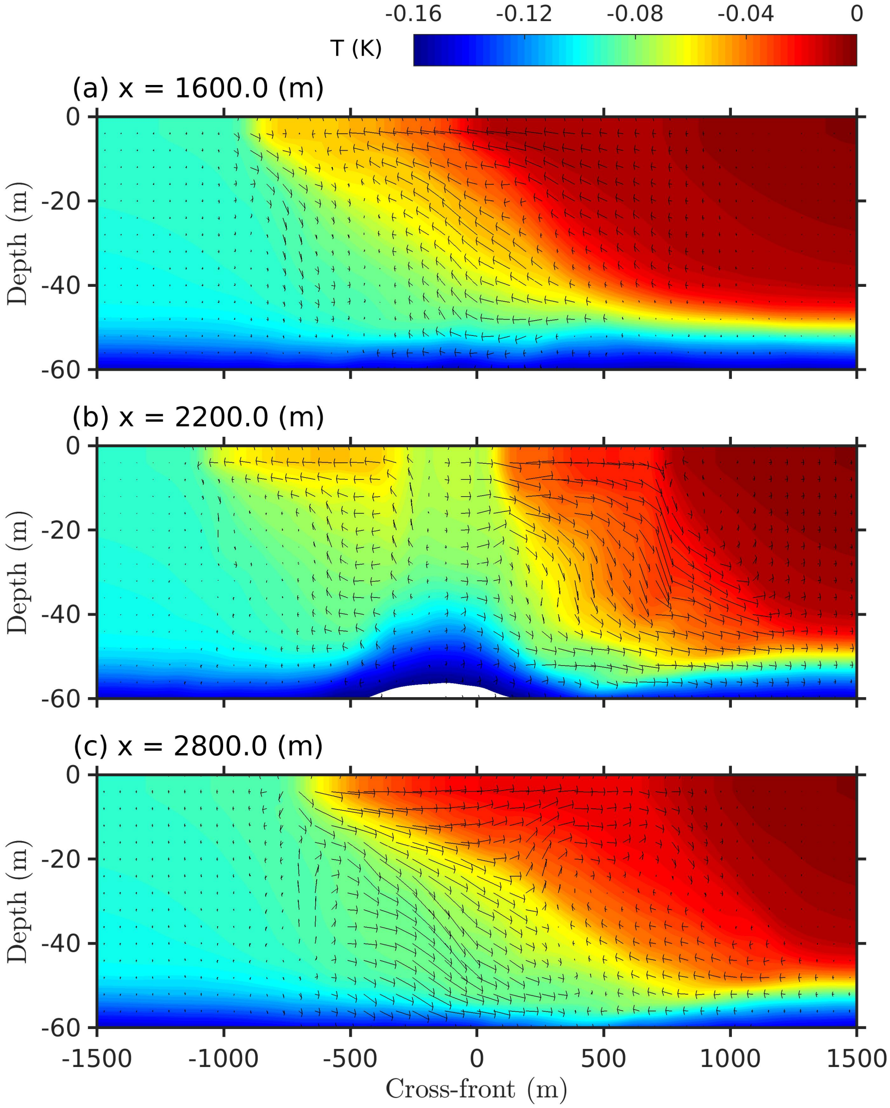

Figure 2.10: Ageostrophic secondary circulation at three different along-front locations (S1, S2 and S3) that were marked in Fig. 2.8(e). The secondary circulation is shown by vertical $y-z$ cuts: (a) at S1 ($x = 1.6\,\text{km}$), (b) at S2 ($x = 2.2\,\text{km}$), and (c) at S3 ($x = 2.8\,\text{km}$). The color contours show the temperature, and the arrows show the velocity vectors in the vertical planes.

The ASC which develops during the evolution of BI is in fact 3-D owing to the along-front variability associated with the coherent submesoscale. The along-front variability of the $y-z$ circulation is depicted in Fig. 2.10 by contrasting the circulation among three $y-z$ cuts (whose intersections with $z=10$ are marked as S1, S2 and S3 in Fig. 2.8) of a submesoscale eddy. If we define back-to-front of the eddy to be in the direction (negative x) of the average jet velocity, S3 is at the back, S2 is near the center, and S1 is at the front of the eddy. Note that, consistent with the anticlockwise $x-y$ circulation of the submesoscale eddy, surface water is transported in the negative y-direction at S1 (Fig. 2.10a) and the positive y-direction at S3 (Fig. 2.10c). The $y-z$ circulation at S1 (Fig. 2.10a) shows that there is downwelling in the filament ($-700 < y < -600$ m) and predominantly upwelling in the eddying region ($-300 < y < 500$ m). On the other hand, the circulation at S3 (Fig. 2.10c) shows substantial downward motion. S2 (Fig. 2.10b) is a $y-z$ section through the eddy core. Within the eddy, the temperature contours at the bottom of the mixed layer and in the vicinity of $y=0$ indicate isopycnal doming under the influence of low pressure, and the fluid has radially-outward horizontal velocity. At S2, there is both upwelling and downwelling with the former in the eddy core and the latter at the back of of the eddy. To summarize, the organization of the secondary circulation in the $y-z$ plane is associated with the coherent structures at the front, with upwelling dominant in the forward and central regions of the submesoscale eddy and downwelling in the aft-regions and the filaments.

2.5.2 3D structure of the coherent submesoscale

The downwelling of high-density water and the upwelling of low-density water are three-dimensional processes, each dominating in different parts of the front and mediated by the coherent structures. The three-dimensionality of the coherent structure helps shed light on the vertical exchange.

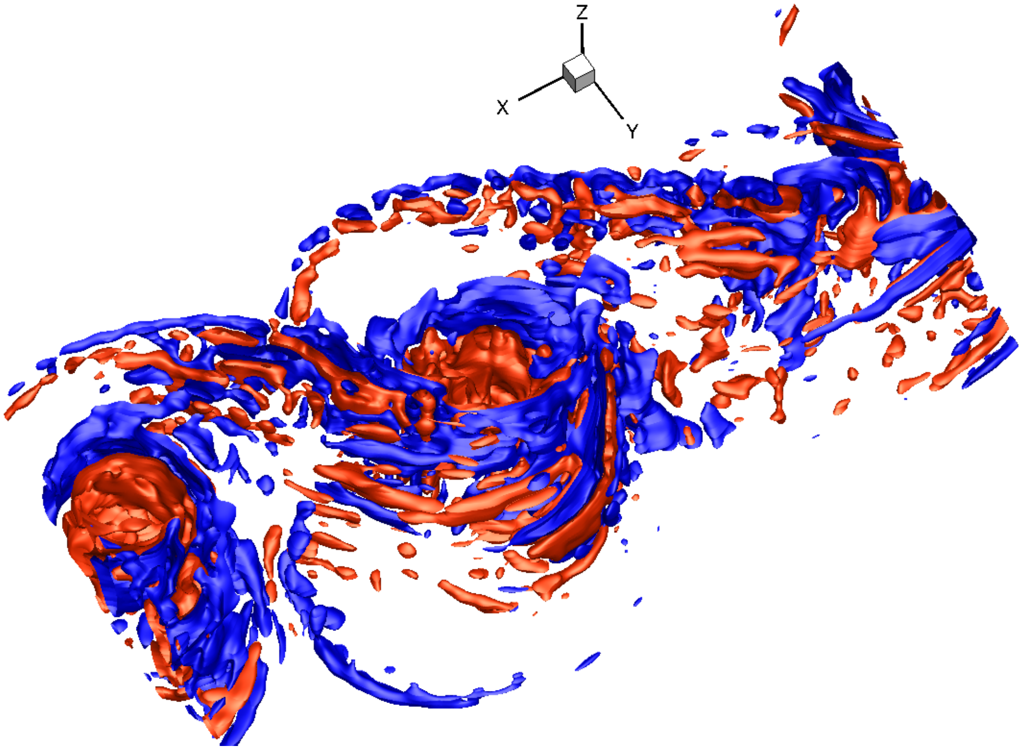

Figure 2.11: Three-dimensional visualization of the coherent structures using the Q-criterion at $t = 86\,\text{h}$. The iso-surfaces are plotted at $Q/f^2 = 0.4$ (red) and -0.4 (blue).

Here, the coherent structure is extracted using the Q criterion defined as

$$Q = \frac{1}{2}\left(\overline{\Omega}_{ij}^2 - \overline{S}_{ij}^2\right); \quad \overline{\Omega}_{ij} = \frac{1}{2}\left(\frac{\partial \overline{u}_i}{\partial x_j} - \frac{\partial \overline{u}_j}{\partial x_i}\right), \overline{S}_{ij} = \frac{1}{2}\left(\frac{\partial \overline{u}_i}{\partial x_j} + \frac{\partial \overline{u}_j}{\partial x_i}\right), \tag{2.14}$$

where $\overline{\Omega}_{ij}$ and $\overline{S}_{ij}$ are the rotation and strain tensors of the submesoscale, respectively. $Q > 0$ signifies rotation-dominated flow while $Q < 0$ signifies the domination of strain. Iso-surfaces of Q (Fig. 2.11) show that the coherent structures consist of both rotation- and strain-dominated regions which are organized in layers around the coherent submesoscale eddies. It can also be noted that the filament structure at the heavier side ($y < 0$) of the front is shallow at its origin, and its depth of influence increases as one moves along this structure towards the eddy; very close to the eddy and in the region surrounding the eddy, the filaments influence the whole of the mixed layer. The filamentary structures at the lighter side ($y > 0$) of the front seem to affect the entire mixed layer depth.

Thus, the separation of scales of motion into the submesoscale and the finescale provides a better understanding of the vertical velocity organization and the vertical transport at the baroclinic frontal instability. The submesoscale vertical velocity field shows well-separated regions where either negative or positive w dominates. Moreover, the vertical velocity field is connected to the coherent structures. Strong downwelling motions develop at vortex filaments and in some portions of the submesoscale eddies that adjoin the filaments.

2.6 Kinetic energy of the submesoscale and the finescale

In this section, we assess the relative contributions of the submesoscale and the finescale to the kinetic energy, quantify the dominant balances in the transport equations, Eq. 2.11 and Eq. 2.12 for the submesoscale and finescale, respectively, and make explicit the interaction between turbulence – the finescale – and the submesoscale.

The submesoscale velocity, as defined here, includes the along-front (x) average which at $t = 0$ is the velocity of the initially-balanced geostrophic jet. In order to focus on the fluctuations, we subtract the along-front average before computing the KE and contrast the evolution of the overall (volume-averaged) fluctuation energy in the submesoscale and the finescale components in Fig. 2.12. Initially, the mean KE dominates and the KE of the small-amplitude broadband fluctuations introduced at $t = 0$ resides mainly in the finescale. Figure 2.12 shows that both submesoscale and finescale KE increase during the growth of SI. When the instability becomes nonlinear at $t \approx 15$ h, the finescale KE saturates, but the submesoscale KE keeps increasing. At $t \approx 40$ h, the submesoscale KE overtakes the finescale KE. The subsequent evolution is dominated by BI which increases the submesoscale KE until it finally saturates at a value comparable to the mean KE. Although the volume-averaged KE of the finescale in the frontal region does not change significantly during the evolution of BI, there is substantial spatio-temporal variability

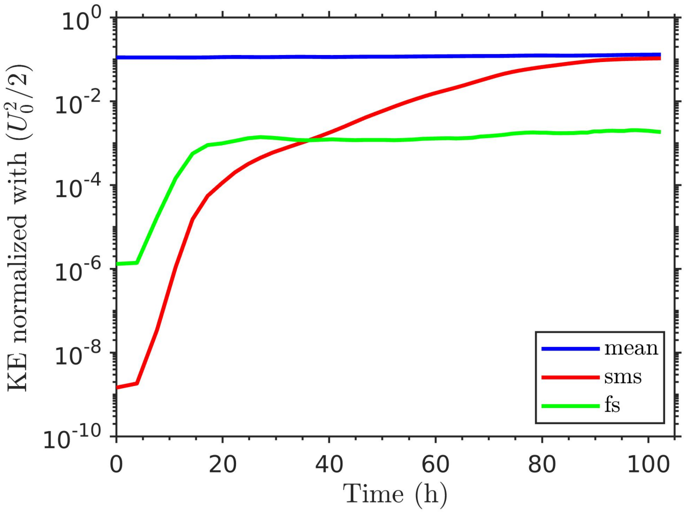

Figure 2.12: Plot of the bulk values of mean kinetic energy, $\langle u_i \rangle_x^2/2$, submesoscale fluctuation kinetic energy, $\left(\overline{u}_i - \langle \overline{u}_i \rangle_x\right)^2/2$, and finescale fluctuation kinetic energy, $\left(u_i'' - \langle u_i'' \rangle_x\right)^2/2$. The bulk values are obtained by volume averaging over the horizontal extent of the front and the entire mixed layer depth.

as the finescale, concentrated in the coherent filament structures and eddies, interacts with the submesoscale. How the submesoscale and finescale flows evolve and interact is investigated here by studying the KE budgets at the two scales. An outstanding question is what is the source of the finescale KE that counteracts its dissipation?

The submesoscale-KE equation, derived by multiplying Eq. 2.11 with $\overline{u}_i$, is given by

$$\frac{\partial}{\partial t}\frac{\overline{u}_i\overline{u}_i}{2} = -\frac{\partial \overline{T_j}}{\partial x_j} + \overline{B} - \overline{\mathcal{E}} - \overline{\mathcal{E}}^{sgs} - \overline{\mathcal{E}}^{R}, \tag{2.15}$$

where $\overline{T_j}$ is the transport term,

$$\overline{T_j} = \frac{\overline{u}_j\overline{u}_i\overline{u}_i}{2} + \frac{\overline{u}_j\overline{p}}{\rho_0} - \nu\frac{\partial}{\partial x_j}\frac{\overline{u}_i\overline{u}_i}{2} + \overline{u}_i(\overline{\tau}_{ij}^{sgs} + \tau_{ij}^{R}), \tag{2.16}$$

$\overline{B} = \alpha\overline{T}\,\overline{w}g$ is the submesoscale buoyancy production term, $\overline{\mathcal{E}} = \nu(\partial\overline{u}_i/\partial x_j)^2$ is the molecular dissipation, and $\overline{\mathcal{E}}^{sgs} = -\overline{\tau}_{ij}^{sgs}(\partial\overline{u}_i/\partial x_j)$ is the dissipation corresponding to the subgrid stresses.

The term $\overline{\mathcal{E}}^R = -\tau_{ij}^R(\partial\bar{u}_i/\partial x_j)$ that arises from the effect of the submesoscale velocity gradient on the residual stresses will be shown later to act as a loss of submesoscale KE. Note that the residual stress, $\tau_{ij}^R = \overline{u_i u_j} - \bar{u}_i\bar{u}_j$, which arises from the submesoscale-finescale decomposition is explicitly computed after applying the Lanczos filter and is different from the subgrid stress, τ_{ij}^{sgs}, which is modeled in the LES approach.

Similar to the KE budget at the submesoscale, the KE budget at the resolved finescale can be derived by multiplying Eq. 2.12 with u_i''. The KE transport equation at the finescale is given by

$$\frac{\partial}{\partial t}\frac{u_i''u_i''}{2} = -\frac{\partial T_j''}{\partial x_j} + Tr + B'' - \mathcal{E}'' - \mathcal{E}''^{sgs} - \mathcal{E}''^{R}, \tag{2.17}$$

where T_j'' is the transport term,

$$T_j'' = \frac{\bar{u}_j u_i''u_i''}{2} + \frac{u_j''u_i''u_i''}{2} + \frac{p''u_j''}{\rho_0} - \nu\frac{\partial}{\partial x_j}\frac{u_i''u_i''}{2} + u_i''(\tau_{ij}''^{sgs} - \tau_{ij}^R), \tag{2.18}$$

$Tr = -u_i''u_j''(\partial\bar{u}_i/\partial x_j)$ is the <u>transfer term</u> that represents the action of submesoscale velocity gradients (including shear) on the finescale, $B'' = \alpha T''w''g$ is the finescale buoyancy production, and $\mathcal{E}'' = \nu(\partial u_i''/\partial x_j)^2$ and $\mathcal{E}''^{sgs} = -\tau_{ij}''^{sgs}(\partial u_i''/\partial x_j)$ are the dissipation of finescale KE due to molecular viscosity and subgrid stresses, respectively. $\mathcal{E}''^R = \tau_{ij}^R(\partial u_i''/\partial x_j)$ term arises from the interaction of the residual stresses with the finescale velocity gradient; it will be shown later to act as a production term for the finescale KE.

The dominant terms of submesoscale and finescale KE budgets are frontally-averaged, i.e. over the entire along-front direction and $-1.5 < y < 1.5$ km in the cross-front direction, and the vertical profiles of the frontal averages are plotted in Fig. 2.13. In the following, we first discuss terms in the submesoscale KE balance and then the finescale KE budget.

The submesoscale KE can change due to the buoyancy term, $\overline{B}$, and the dissipation terms, namely, $\overline{\mathcal{E}}, \overline{\mathcal{E}}^{sgs}$, and $\overline{\mathcal{E}}^R$. The transport term, $\overline{T}$, represents the transfer of KE between different spatial regions by various processes such as advection, pressure work and the work by various

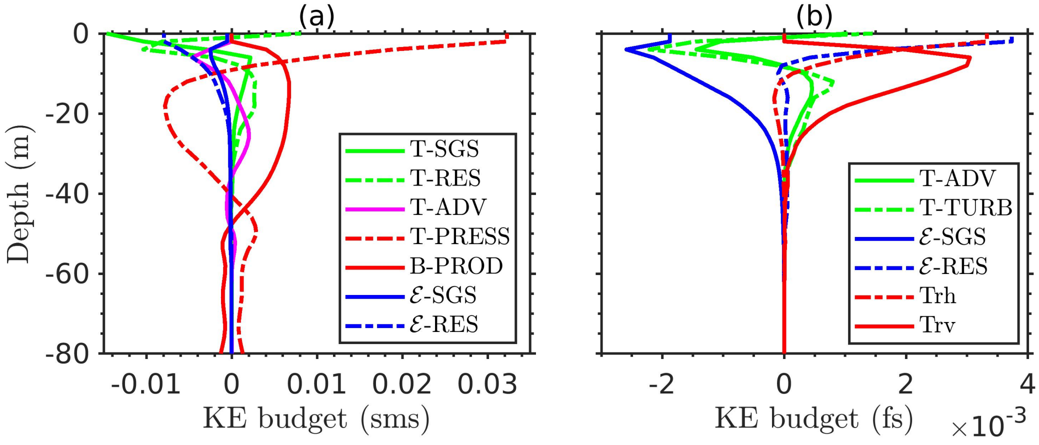

Figure 2.13: Submesoscale (a) and finescale (b) kinetic energy (KE) budgets at $t = 79.7\,\mathrm{h}$. Each term is a horizontal frontal average and is normalized by $U_0^2 f$. At submesoscale, the plotted terms are advective transport, T-ADV = $-(1/2)\partial(\overline{u}_j\overline{u}_i\overline{u}_i)/\partial x_j$, pressure transport, T-PRESS = $-(1/\rho_0)\partial(\overline{u}_j\overline{p})/\partial x_j$, subgrid-stress transport, T-SGS = $-\partial(\overline{u}_i\overline{\tau}_{ij}^{sgs})/\partial x_j$, residual-stress transport, T-RES = $-\partial(\overline{u}_i\overline{\tau}_{ij}^{R})/\partial x_j$, buoyancy production, B-PROD = $\overline{B}$ = $\alpha\overline{T}\overline{w}g$, subgrid dissipation, $\mathcal{E}$-SGS = $-\overline{\mathcal{E}}^{sgs}$ = $\overline{\tau}_{ij}^{sgs}(\partial\overline{u}_i/\partial x_j)$, and residual dissipation, $\mathcal{E}$-RES = $-\overline{\mathcal{E}}^{R}$ = $\tau_{ij}^{R}(\partial\overline{u}_i/\partial x_j)$. At finescale, the plotted terms are advective transport, T-ADV = $-(1/2)\partial(\overline{u}_j u_i'' u_i'')/\partial x_j$, finescale transport, T-TURB = $-(1/2)\partial(u_j'' u_i'' u_i'')/\partial x_j$, subgrid dissipation, $\mathcal{E}$-SGS = $-\mathcal{E}''^{sgs}$ = $\tau_{ij}''^{sgs}(\partial u_i''/\partial x_j)$, residual dissipation, $\mathcal{E}$-RES = $-\mathcal{E}''^{R}$ = $-\tau_{ij}^{R}(\partial u_i''/\partial x_j)$, and the transfer term, $Tr = -u_i'' u_j''(\partial\overline{u}_i/\partial x_j)$, split into contributions from horizontal gradients, Tr_h, and vertical gradients, Tr_v, of the submesoscale velocity.

stresses – molecular, subgrid and residual. The dominant terms of the submesoscale KE budget, Eq. 2.15, are plotted in Fig. 2.13a as a function of depth at $t = 79.7\,\mathrm{h}$.

Figure 2.13a shows that the buoyancy production ($\overline{B}$) is the main source of submesoscale KE in the mixed layer that extends to 50 m depth. $\overline{B}$ represents conversion into KE of the available potential energy associated with the horizontal buoyancy jump across the front. Below the mixed layer, the buoyancy term is negative. In the bulk of the mixed layer, except for the near-surface region from $z = 0$ to approximately $10\,\mathrm{m}$ depth, the buoyancy production is balanced mainly by the pressure transport, computed as $-(\bar{u}_j/\rho_0)(\partial\bar{p}/\partial x_j)$. The pressure transport redistributes energy from the 10-40 m depth to both the near-surface region and to the region below 40 m depth. We find that $\overline{B}$ is approximately balanced by $-(\bar{w}/\rho_0)(\partial\bar{p}/\partial z)$ over the domain. This suggests that the overall (horizontally-averaged over the front) submesoscale is in approximate hydrostatic balance for this moderate-strength front.

The dissipation terms are also plotted in Fig. 2.13a. The dissipation due to molecular viscosity is relatively small, and only the contributions from $\overline{\mathcal{E}}^{sgs}$ and $\overline{\mathcal{E}}^{R}$ are shown. The figure shows that both terms are significant in the near surface region, above 10 m, and have negative values which indicates removal of submesoscale KE. Note that $\overline{\mathcal{E}}^{sgs}$ is negative everywhere and represents dissipation of submesoscale KE by the LES subgrid model. On the other hand, $\overline{\mathcal{E}}^{R}$ can be either positive or negative and represents exchange of KE between the submesoscale and finescale. The role of $\overline{\mathcal{E}}^{R}$ in this exchange can be readily noticed by expressing τ^R_{ij} in the Galilean invariant components as suggested by Germano (1986): $\tau^R_{ij} = \mathcal{L}^o_{ij} + \mathcal{C}^o_{ij} + \mathcal{R}^o_{ij}$, where $\mathcal{L}^o_{ij} = \overline{\overline{u}_i\overline{u}_j} - \overline{\overline{u}}_i\overline{\overline{u}}_j$ are the Leonard stresses, $\mathcal{C}^o_{ij} = \overline{\overline{u}_i u''_j} + \overline{u''_i\overline{u}_j} - \overline{\overline{u}}_i\overline{u''}_j - \overline{u''}_i\overline{\overline{u}}_j$ are the cross stresses, and $\mathcal{R}^o_{ij} = \overline{u''_i u''_j} - \overline{u''}_i\overline{u''}_j$ are the stress tensor terms similar to the subgrid Reynolds stresses. Consequently, corresponding to stresses $\mathcal{R}^o_{ij} \approx \overline{u''_i u''_j}$, the term $\overline{Tr} = \overline{u''_i u''_j}(\partial\overline{u}_i/\partial x_j)$ appears which is similar to the transfer term, Tr, in the finescale kinetic energy budget. The frontal average of $\overline{\mathcal{E}}^{R}$, however, is negative and indicates a net transfer of energy to the finescale. In the near surface region, transport by the subgrid stresses, $\overline{\tau}^{sgs}_{ij}$, and residual stresses, τ^R_{ij}, are also important. The frontal averages of the transports by subgrid and residual stresses are negative and tend to remove the excess energy generated by the significantly large pressure transport in the region.

The dominant terms of the finescale KE budget are plotted in Fig. 2.13b. The transfer term, Tr, acts as the main source of finescale KE. Tr is split into two parts following Sullivan and McWilliams (2018): Tr_h with all the terms containing horizontal gradients of the submesoscale velocity and Tr_v with all the terms containing the vertical gradients of the submesoscale velocity.

Thus,

$$
\begin{aligned}
Tr_h &= -\left(u_1''u_1''\frac{\partial \overline{u}_1}{\partial x_1} + u_1''u_2''\frac{\partial \overline{u}_1}{\partial x_2} + u_2''u_1''\frac{\partial \overline{u}_2}{\partial x_1} + u_2''u_2''\frac{\partial \overline{u}_2}{\partial x_2} + u_3''u_1''\frac{\partial \overline{u}_3}{\partial x_1} + u_3''u_2''\frac{\partial \overline{u}_3}{\partial x_2}\right), \qquad (2.19) \\
Tr_v &= -\left(u_1''u_3''\frac{\partial \overline{u}_1}{\partial x_3} + u_2''u_3''\frac{\partial \overline{u}_2}{\partial x_3} + u_3''u_3''\frac{\partial \overline{u}_3}{\partial x_3}\right).
\end{aligned}
$$

Figure 2.13b shows that, in the near-surface region (approximately top 10 m of the mixed layer), Tr_h is large in magnitude relative to Tr_v. However, further below the free surface, Tr_v is the dominant source term. Below the mixed layer, the transfer terms Tr_h and Tr_v are small. It can also be observed that below the near-surface region, Tr_v and the subgrid dissipation, $\mathcal{E}''^{sgs}$ are the dominant terms, and approximately balance each other.

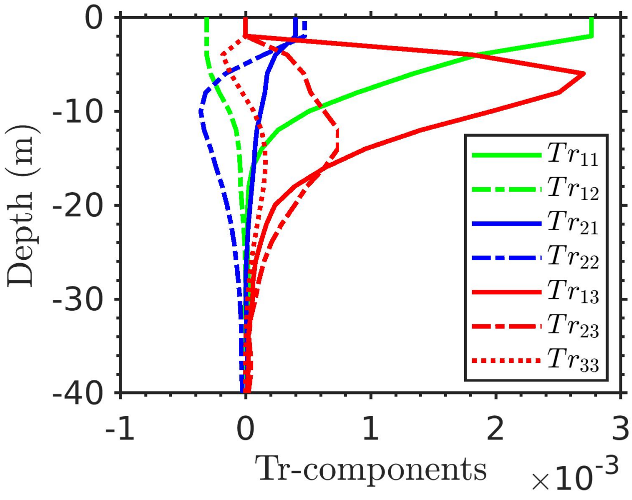

Figure 2.14: Dominant components in the transfer term, Tr, at $t = 79.7$ h. Each term has been normalized with $U_0^2 f$. Note that the component $Tr_{\alpha\beta}$ denotes $-u_\alpha''u_\beta''(\partial\overline{u}_\alpha/\partial x_\beta)$ with no summation over the Greek subscripts, α and β. Tr_{31} and Tr_{32} are negligible compared to the other terms and not plotted.

The velocity gradient tensor $(\partial\overline{u}_i/\partial x_j)$ in the transfer (Tr) between the submesoscale and the finescale has components that can be related to either shear (off-diagonal terms) or strain (diagonal terms) in the flow. The relative importance of the shear and strain components to Tr is further explored in Fig. 2.14 where front-averaged profiles of each component are plotted as a function of depth. Clearly, Tr is strongly influenced by $Tr_{11} = -u_1''u_1''(\partial\overline{u}_1/\partial x_1)$ (part of Tr_h) and $Tr_{13} = -u_1''u_3''(\partial\overline{u}_1/\partial x_3)$ (part of Tr_v) with the former related to horizontal strain and the latter to vertical shear. In the top 6 m, Tr_{11} dominates, pointing to the importance of the horizontal compressive strain associated with frontogenesis to the enhancement of turbulence. Below 10 m, vertical shear ($\partial\overline{u}_1/\partial x_3$ and additionally $\partial\overline{u}_2/\partial x_3$) is important. Interestingly, the frontal mean of $Tr_{12} = -u_1''u_2''(\partial\overline{u}_1/\partial x_2)$ is negative. This reverse energy transfer to horizontal eddying motions in physical space is consistent with the notion that, in this flow, finescale turbulence is organized into the coherent submesoscale in addition to the usual downscale energy transfer to turbulence. The sum of all the components of Tr is positive, i.e., overall, the submesoscale gradients act as a source of the finescale KE. Among gradients of the vertical velocity, only $Tr_{33} = -u_3''u_3''(\partial\overline{u}_3/\partial x_3)$ involving vertical strain is significant; however it is smaller than the dominant term Tr_{13}.

In addition to Tr, $\mathcal{E}''^R$ is another dominant source of the finescale kinetic energy, mainly near the surface. $\mathcal{E}''^R$ represents the interaction of the residual stress with the finescale shear. There is only a partial balance between the production of the kinetic energy and dissipation by the subgrid stresses, $\mathcal{E}''^{sgs}$. In this region, transport by both the submesoscale and finescale velocity fields is significant and removes energy from the layer.

The horizontal organization of selected terms that appear in the kinetic energy balance are shown in Fig. 2.15 at 10 m depth. The local value of submesoscale buoyancy production, $\overline{B}$ (Fig. 2.15b) has both positive regions (primarily in the filaments) and negative regions (primarily in the eddy cores). However, the horizontal average of $\overline{B}$ is positive (Fig. 2.13a) and indicates restratification accompanied by the conversion of potential energy in the lateral stratification to submesoscale KE. The resemblance between the horizontal structures of submesoscale KE and buoyancy production is apparent in Figs. 2.15(a,b), further reinforcing the importance of $\overline{B}$ for the submesoscale KE. The dissipation of the finescale (Fig. 2.15c) is concentrated in the vortex filaments, again pointing to the spatially localized, coherent organization of dissipative turbulence

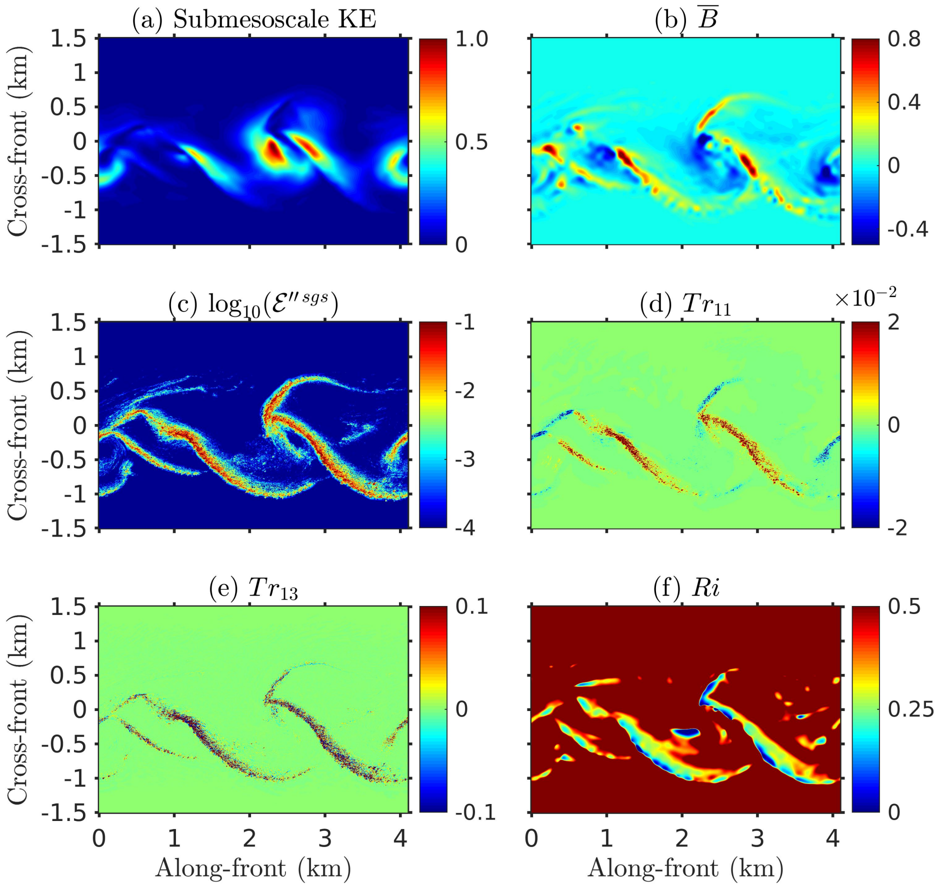

Figure 2.15: Variation at 10 m depth and $t = 79.7$h of submesoscale fluctuation (down-front mean removed) kinetic energy (a), selected energy budget terms at the submesoscale and the finescale (b-e), and submesoscale gradient Richardson number, Ri (f). Here, $Ri = (\partial\bar{b}/\partial z)[(\partial\bar{u}/\partial z)^2 + (\partial\bar{v}/\partial z)^2]^{-1}$. The submesoscale kinetic energy is normalized with $U_0^2/2$ and the energy budget terms are normalized with $U_0^2 f$.

in this problem. The dominant terms that transfer energy from the submesoscale to the finescale owing to horizontal strain (Fig. 2.15d) and vertical shear (Fig. 2.15e) are also localized in the vortex filaments. The gradient Richardson number (Ri_g) based on vertical shear and stratification of the submesoscale is plotted in Fig. 2.15f. The regions with subcritical $Ri_g < 0.25$ are within those where Tr_{13} is large. Thus, local shear instability is a driver of turbulence at these locations.

2.7 Frontogenesis

The formation of coherent structures, i.e., the vortex filaments and the coherent submesoscale eddies, show frontogenesis, notably large increase in M^2/f^2 from its initial value. The role of the coherent structures in vertical transport was addressed in section 2.5. In this section, the focus is on the processes that are responsible for frontogenesis and those which counteract to balance it. We investigate the time rate-of-change of horizontal buoyancy gradient at the submesoscale, $\nabla_h\overline{b}$, where $\nabla_h = \partial_x\hat{\mathbf{i}} + \partial_y\hat{\mathbf{j}}$ and $\hat{\mathbf{i}}$ and $\hat{\mathbf{j}}$ are unit vectors in x- and y-directions, respectively (e.g., Capet et al. (2008b)). It can be noted that buoyancy is directly related to the temperature deviation, $b = g\alpha T$. In particular, the following dynamical equation is quantified:

$$\begin{aligned}\frac{1}{2}\frac{D}{Dt}|\nabla_h\overline{b}|^2 &= \nabla_h\overline{b}.(\mathbf{Q_s} + \mathbf{Q_w} + \mathbf{Q_{dh}} + \mathbf{Q_{dv}}),\\ &= F_s + F_w + F_{dh} + F_{dv}.\end{aligned} \tag{2.20}$$

In the above equation, $\mathbf{Q_s}$ and $\mathbf{Q_w}$ denote contributions due to advection by the submesoscale and are given by

$$\begin{aligned}\mathbf{Q_s} &= -(\partial_x\overline{u}\partial_x\overline{b} + \partial_x\overline{v}\partial_y\overline{b},\ \partial_y\overline{u}\partial_x\overline{b} + \partial_y\overline{v}\partial_y\overline{b}),\\ \mathbf{Q_w} &= -(\partial_x\overline{w}\partial_z\overline{b},\ \partial_y\overline{w}\partial_z\overline{b}).\end{aligned} \tag{2.21}$$

Thus, $\mathbf{Q_s}$ corresponds to the straining of the buoyancy field by horizontal motion and $\mathbf{Q_w}$ is an analogous term related to vertical motion. The contributions from diabatic processes – molecular diffusion, and subgrid and residual fluxes – are included in $\mathbf{Q_{dh}}$ and $\mathbf{Q_{dv}}$. Between the two, $\mathbf{Q_{dh}}$ is associated with the horizontal diabatic processes, and $\mathbf{Q_{dv}}$ is associated with the vertical diabatic processes,

$$\mathbf{Q_{dh}} = \nabla_h(\nabla_h.(\kappa\nabla_h\overline{b}) - g\alpha\nabla_h.(\overline{\mathbf{q}}_{\mathbf{h}}^{\mathbf{sgs}} + \mathbf{q}_{\mathbf{h}}^{\mathbf{R}})),$$

$$\mathbf{Q_{dv}} = \nabla_h(\partial_z(\kappa\partial_z\overline{b}) - g\alpha\partial_z(\overline{q}_v^{sgs} + q_v^R)). \tag{2.22}$$

The forcing terms on the right hand side of Eq. 2.20, F_i, where $i = \{s, w, dh, dv\}$, are obtained by taking the dot-product of $\nabla_h\overline{b}$ with appropriate $\mathbf{Q}$-terms.

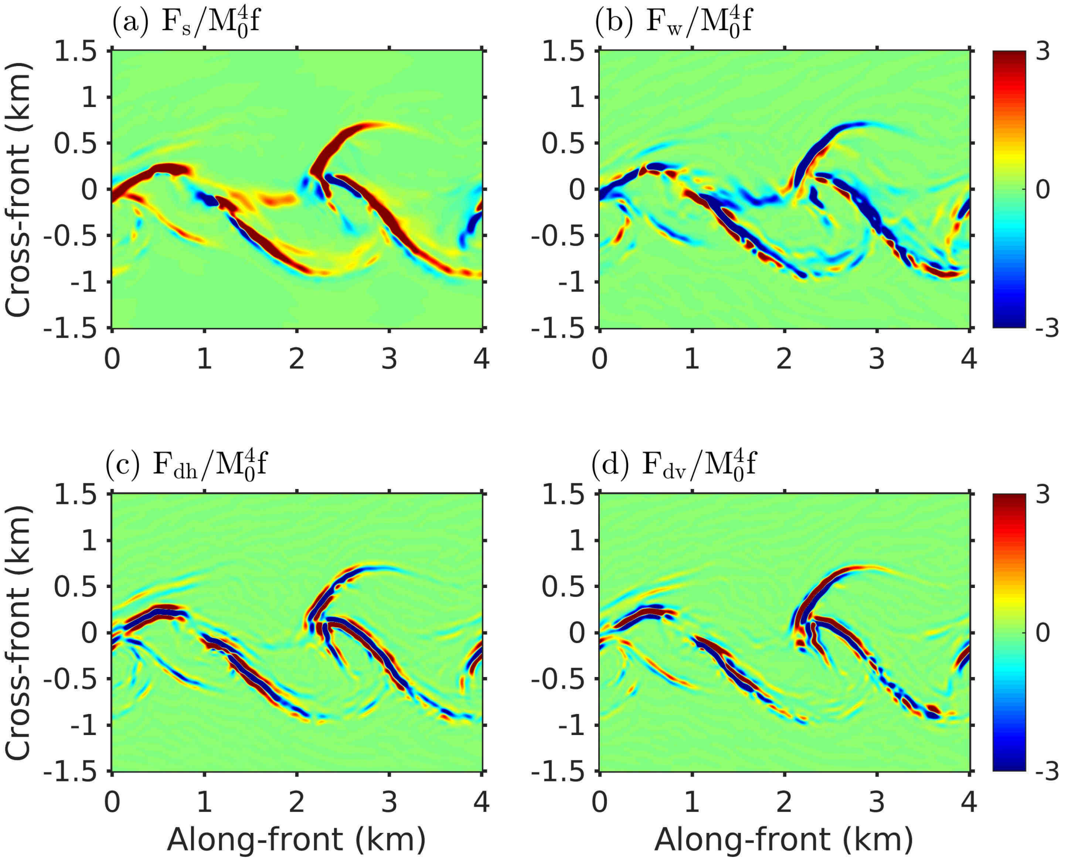

Figure 2.16: Different terms in the RHS of the transport equation for $|\nabla_h\overline{b}|^2$ (Eq. 2.20) are shown at 10 m depth and $t = 79.7$ h.

In Figs. 2.16 and 2.17, the forcing terms are plotted at depths 10 m and 30 m, respectively. Near the surface, F_s is predominantly positive in the vortex filaments and is frontogenetic,

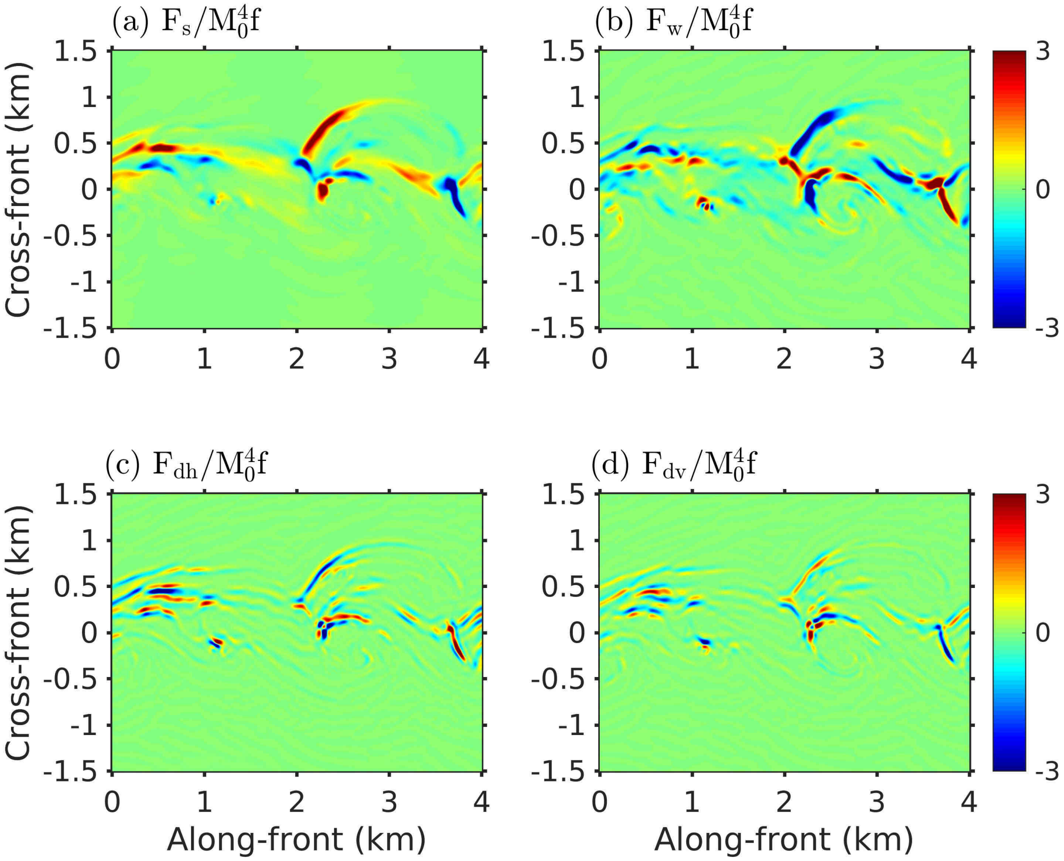

Figure 2.17: Different terms in the RHS of the transport equation for $|\nabla_h \bar{b}|^2$ (Eq. 2.20) are shown at 30 m depth and $t = 79.7$ h.

whereas F_w is predominantly negative and is frontolytic. On the other hand, F_{dh} and F_{dv} are both frontogenetic and frontolytic in these regions – F_{dh} being frontolytic in the center and frontogenetic at the edges, while F_{dv} being frontogenetic at the center and frontolytic at the edges. Near the mid-depth at 30 m, the forcing terms F_s and F_w have both positive and negative values, relatively more interspersed at the front. The magnitudes of the forcing terms F_s and F_w, as well as F_{dh} and F_{dv}, are much smaller compared to those near the surface. A qualitative balance between F_s and F_w and that between F_{dh} and F_{dv} can be observed at both depths. The vertical profiles of frontal-averaged ($0 < x < L_x$ and $-1.2 < y < 1.2$ km) forcing terms are shown in Fig. 2.18. Three distinct regions can be identified – upper, intermediate and bottom regions. In the upper, near-surface region (above 10 m depth), F_s is balanced by both F_w and F_{dh}. However, very close to the surface F_w goes to zero and the balance is provided only by F_{dh}. The balance between F_s and F_{dh} is partial at the surface, i.e. the frontal-averaged value of $|\nabla_h \overline{b}|^2$ continues to increase with time because the length of the thin O(100) m wide frontal regions continues to increase as BI proceeds.

In the intermediate region between $10-40$ m depth, there is a dominant balance between F_s and F_w; F_s is predominantly frontogenetic and F_w is predominantly frontolytic. This can also be observed in Figs. 2.16 and 2.17. Finally, near the bottom between $40-60$ m depth, there is relatively weak frontogenesis that arises from F_w. In all the three regions, the frontal averaged F_{dv} is small.

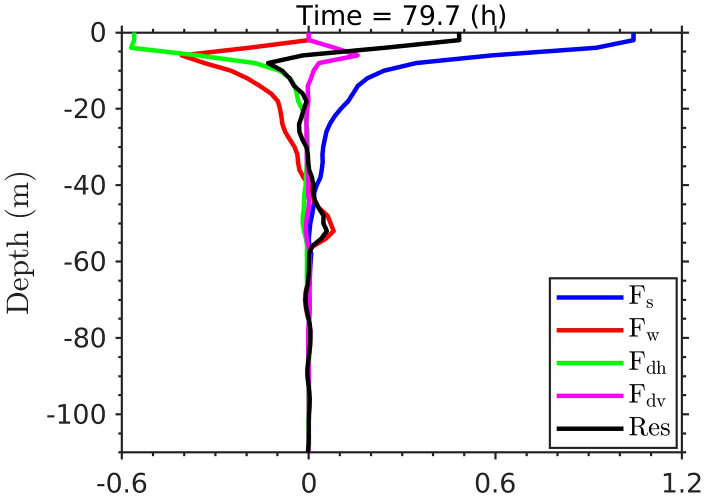

Figure 2.18: Forcing terms in Eq. 2.20 at t = 79.7 h. Each term is normalized with $M_0^4 f$. Here, the residual is defined by $\mathrm{Res} = \mathrm{F_s} + \mathrm{F_w} + \mathrm{F_{dh}} + \mathrm{F_{dv}}$.

The balance of the frontal-averaged buoyancy gradient described above corresponds to $t = 79.7$ h and reflects the behavior during the time the coherent eddies grow. Before the growth of BI, the forcing terms, $\langle F_i \rangle_{xy}$, remain small. As BI starts growing at $t \approx 40$ h, F_i begin to develop near the surface. When the eddies form and grow, $\langle F_i \rangle_{xy}$ become significantly large (Fig. 2.18). During this period the submesoscale KE also grows. Afterwards when the submesoscale KE saturates at $t \approx 100\,\mathrm{h}$, $\langle F_i \rangle_{xy}$ remain significant only in the upper region. In the intermediate and bottom regions, the magnitudes of frontal averaged forcing terms become small.

2.8 Discussion and conclusions

The spin-down of a mixed layer front is studied using a large eddy simulation (LES) model. The front of width 1.2 km is initially in geostrophic balance, has a moderate Rossby number of 0.32, and is confined to a weakly stratified ($Ri = 0.26$) mixed layer of thickness 50 m that lies above a strongly stratified thermocline. The non-hydrostatic, Boussinesq Navier-Stokes equations are numerically solved on a turbulence-resolving isotropic grid that discretizes a domain that is 4098 m in the along-front, 6146 m in the cross-front, and 130 m in the vertical with resolution of 2 m in all three coordinate directions. The high-resolution LES enables us to simulate submesoscale eddies, three-dimensional turbulence and their interaction.

The initial configuration with $Ri = 0.26$ is such that the potential vorticity is negative over the front, making it unstable to symmetric instability (SI) that then develops secondary KH instability (Taylor and Ferrari, 2009) and three-dimensional turbulence (Arobone and Sarkar, 2015). Although SI grows initially, the baroclinic instability (BI) soon becomes the dominant mode as Ri increases to beyond 0.95 during restratification of the front (Fox-Kemper et al., 2008, Haine and Marshall, 1998). The growth of BI is frontogenetic (Hoskins, 1982) and results in the formation of thin vortex filaments at the front. Furthermore, long vortex filaments, comparable in length to that of the wavelength of the dominant BI mode, roll up to produce coherent submesoscale eddies. These coherent structures are localized in space and characterized by large values of strain rate, vorticity, and density gradient. The local Rossby number in these structures is $O(10)$ indicating local loss of rotational control.

Previous studies of the mixed layer instability with turbulence-resolving simulations (e.g. Skyllingstad and Samelson (2012), Stamper and Taylor (2017)) have found vortex filaments, submesoscale eddies and turbulence during the flow evolution. In the present simulation of an isolated, unforced front, the turbulence that develops during BI occurs in localized regions at the sharpening filament structure similar to Skyllingstad and Samelson (2012) who simulated the evolution of a warm filament (double-front configuration with lateral periodicity). Given the sparseness and locality in physical space of the turbulence that develops in this problem, we are motivated to examine scale interactions in physical space rather than the classical wavenumber-based approach employed by Skyllingstad and Samelson (2012). Therefore, unlike previous studies of the mixed layer instability, we decompose the flow into a submesoscale field and a finescale field in physical space, describe the properties of these two fields, and quantify their interaction. The classical decomposition into an overall frontal average and a fluctuation would obscure the coherent submesoscale structures and prevent us from elucidating their important role in frontal dynamics. The present decomposition enables the direct quantification of how the coherent submesoscale contributes to processes such as transfer of mass, momentum and buoyancy to the bottom of the mixed layer and the interaction between the mixed layer and the pycnocline. A low-pass Lanczos spatial filter is used to decompose a given flow variable ϕ into the sum of a submesoscale component $\overline{\phi}$ and a finescale component ϕ''. Our finding of a change of kinetic energy spectrum slope and flow anisotropy at O (100) m length scale guides the choice of filter scale as O(100) m.

We find that the submesoscale component (e.g. left column of Fig. 2.8) represents the coherent structures that emerge during the evolution of the mixed layer instability and are distributed throughout the frontal region. The finescale component (e.g. right column of Fig. 2.8) represents small-scale turbulence that is spatially organized and concentrated in filamentary regions where the submesoscale field has large spatial gradients.

An important feature of submesoscale dynamics in frontal regions is the associated increase in vertical transport. The present simulation shows that w exceeds $0.005\,\mathrm{m\,s^{-1}}$ in several regions and becomes as large as $0.02\,\mathrm{m\,s^{-1}}$ within vortex filaments. Regions of positive and negative w are interspersed; it is the decomposition of w into the submesoscale ($\bar{w}$) and the finescale (w'') that allows us to separate upwelling from downwelling regions. Downwelling by $\bar{w}$ is concentrated at the filaments that curve into the submesoscale vortices while upwelling occurs over more spatially extensive regions in and around these vortices. The associated buoyancy flux is restratifying. Although the instantaneous magnitude of w'' has an order of magnitude large peak relative to $\bar{w}$, the additional net contribution by the finescale to the overall transport is small.

An examination of the submesoscale velocity over $y-z$ cross sections at different x (along-front) locations shows significant along-front variability. Thus, the secondary ageostrophic circulation, taken to be two-dimensional in simplified along-front averaged models, is three-dimensional owing to the action of the filaments and vortices in the flow. We define back-to-forward direction as aligned with the jet velocity (negative x-direction). Heavier fluid with downwelling velocity is found in the filament structure in the back regions of the eddies while the lighter fluid with upwelling velocity is found in the forward regions.

The coherent structures have enhanced relative vorticity. Cold filaments with denser fluid have concentrated positive submesoscale $\overline{\omega_z}$ that roll up into cyclonic submesoscale vortices with vorticity as large as $\omega_z/f \approx 5$ in the surface layer similar to the simulations of Gula et al. (2015) with 150 m horizontal resolution. The finescale vorticity, ω_z'', is an order of magnitude larger and is concentrated in the thin filaments.

The finescale kinetic energy (KE) is found to increase rapidly during the initial 20 h when SI is active and then its frontal average saturates although the local spatio-temporal variability is substantial. The submesoscale KE continues to increase after 20 h when SI becomes nonlinear; however, the bulk of the increase occurs during BI. The turbulent finescale is dissipative and an outstanding question is what maintains the energy of the finescale. To answer this question and have a better understanding of the energy pathways to and between the two components, we evaluate the KE transport equations separately for the submesoscale and finescale, and report vertical profiles of horizontally-averaged terms at a late time (t = 79.7 h) during the BI evolution.

With regards to the submesoscale KE, the buoyancy production term, which is significant between 10 m and the mixed layer base, acts as the main source. The pressure-transport term redistributes KE spatially from lower in the mixed layer to the 10 m near-surface region. Both the residual stress (explicitly computed from the flow field as $\tau^R_{ij} = \overline{u_i u_j} - \bar{u}_i \bar{u}_j$) and the subgrid stress (modeled) act to dissipate submesoscale KE. The dissipation by residual stress, $\overline{\mathcal{E}}^R$, is larger than the dissipation by subgrid stress, $\overline{\mathcal{E}}^{sgs}$, by a factor of about 2. Direct molecular dissipation is negligible at the O(100) m scale of the submesoscale.

The finescale KE is found to be primarily delivered by the transfer term, $Tr = -u_i'' u_j'' (\partial \bar{u}_i / \partial x_j)$, which represents the interaction of the finescale with the submesoscale velocity gradients. The transfer term, Tr, is further decomposed into Tr_h (which involves horizontal gradients) and Tr_v. As in several of the other diagnostics, the near-surface upper 10 m layer is qualitatively different in that Tr_h (Tr_{11}) is the primary source of finescale KE in contrast to the remainder of the mixed layer where it is Tr_v (Tr_{13}) that dominates. The buoyancy flux has a negligible contribution to the KE balance. This is in contrast to the submesoscale, where it is the buoyancy flux which energizes the submesoscale KE. The production of finescale KE by the residual stress τ^R_{ij} is an important contributor to the budget only in the top 10 m.

In the present study, horizontal strain ($\partial u / \partial x$) and vertical shear ($\partial u / \partial z$) of the submesoscale velocity field act as dominant production terms of finescale kinetic energy at different depths. In particular, in the 6 m near-surface region, it is the horizontal strain which dominates the transfer while, in the remainder of the mixed layer, the transfer is mediated by the vertical shear. Sullivan and McWilliams (2018) simulated the evolution of a cold (dense) filament in a background of strong ocean boundary layer (OBL) turbulence. BI did not emerge in the mixed layer, but there was frontogenesis by the ageostrophic circulation instigated by OBL turbulence leading to frontal turbulence. They found that in the down-front wind case and no wind (surface cooling) case, the horizontal shear was the dominant production term for the TKE while in the cross-front wind case it was the vertical shear. Thus, there are qualitative differences in frontal turbulence generation between a front undergoing BI with subsequent submesoscale meanders and vortices as in the present case, and a front that develops in a pre-existing field of strong OBL turbulence without exhibiting BI.

During the evolution of BI, horizontal currents (u, v) develop strong variability in the horizontal (x, y) that locally sharpen the front and intensify the buoyancy gradient ($\nabla_{\mathbf{h}} b$). The terms in the balance equation for the square of $\nabla_{\mathbf{h}} b$ are diagnosed to better understand the frontogenetic mechanisms. Instantaneous visualizations at 10 m depth shows active frontogenesis by F_s (which involves horizontal gradients of horizontal velocity), mainly at the filaments, while F_w (which involves horizontal gradients of vertical velocity) acts to counteract frontogenesis. Instantaneously, the diabatic (diffusive) terms act to both increase and decrease the local buoyancy gradient. An overall picture of the diabatic term emerges after performing horizontal averages in the frontal region. Horizontal diffusion, both resolved and subgrid, is the primary process in the upper 10 m that counteracts frontogenesis by F_s. In the remainder of the mixed layer it is primarily F_w (which involves horizontal gradients of vertical velocity) that counteracts frontogenesis by F_s. Capet et al. (2008b) in their analysis of frontogenesis during mesoscale-submesoscale transition in a simulation with 750 m horizontal resolution, found that F_{dv} (vertical diffusion) modeled by k-profile parametrization (KPP) was the primary term in the model counteracting F_s. Horizontal diffusion (F_{dh}) could not be calculated separately because it was implicit in the horizontal advection and the horizontal grid resolution was insufficient. In the present 2 m resolution LES, the front thins to O(100) m. We find that the contribution from horizontal diffusion (F_{dh}), calculated explicitly here, counteracts frontogenesis by F_s in the near-surface layer and, thus, plays an important role in limiting the width of the frontogenetic region.

In cold filaments that evolve in a turbulent boundary layer, surface frontogenesis results from the secondary circulation that occurs under the turbulent thermal wind (TTW) condition (McWilliams et al., 2015, Sullivan and McWilliams, 2018). Frontal sharpening proceeded to the grid scale of O (10) m in the 2-D numerical simulations (McWilliams et al., 2015) of this problem that were conducted with the k-profile parametrization (KPP) of vertical mixing, while Sullivan and McWilliams (2018) found that frontogenesis was arrested at O(100) m by shear-driven turbulence in a simulation that resolved the turbulent boundary layer. BI is excluded in the 2-D model of McWilliams et al. (2015) whereas, in the model of Sullivan and McWilliams (2018), the filament evolution process is fast and BI remains unimportant during this period. Although different from the BI-driven frontogenesis and localized turbulence of the present study, the arrest scale of frontogenesis observed by Sullivan and McWilliams (2018) is close to the value of O(100) m obtained in the present study. It is worth noting that features sharper than O(100) m can form in fronts. For example, Pham and Sarkar (2018) in their study of a strong front with large M^2/f^2 find sharpening down to O(10) m that precedes the release of a gravity current.

Although the submesoscale dynamics is studied here for a model front without any external influences, it exhibits processes which are also observed in the real ocean. The study of D'Asaro et al. (2018) using satellite-tracked surface drifters in the northern Gulf of Mexico revealed sharpened fronts which wrap into cyclonic eddies, a process that is resembled by the rolling-up of the filament structures into cyclonic eddies in the present study. The zipper structures, which form when two filaments combine into one as they wrap into the eddy, are similar to the joining of filaments structures from opposite sides of the front seen here. Moreover, the positive (cyclonic) vertical vorticity and downwelling at the front as well as their enhanced magnitudes in the convergent zipper region found by D'Asaro et al. (2018) are features that occur in the submesoscale dynamics of the present study. Similar to the asymmetry in the distribution of the positive and negative vertical vorticity observed in the study of Shcherbina et al. (2013), we find in the simulation that the anticyconic vertical vorticity is weaker ($\omega_z \approx -1.2f$) and spatially more extensive than the cyclonic vertical vorticity ($\omega_z \approx 5f$) that is concentrated in thin filaments. Furthermore, the large strain rate and positive vertical vorticity at the submesoscale are correlated in the simulation; both of these properties are characteristic of the filaments.

The present study underlines the importance of coherent structures, i.e. vortex filaments and coherent submesoscale eddies, in the dynamics of the spindown of an unforced front in a mixed layer by elucidating their role in vertical transport, frontogenesis and maintenance of fine-scale turbulence. The analysis was based on Eulerian statistics and, in future work, we hope to shed further light on subduction and mixing by Lagrangian tracer analysis. Surface forcing by wind, buoyancy and waves introduces additional complexities into the evolution of the baroclinic instability as has been shown by several recent numerical studies, e.g., Callies and Ferrari (2018), Hamlington et al. (2014), Mahadevan et al. (2010), Whitt and Taylor (2017): cooling at the surface can compete with the restratifying buoyancy flux generated by BI; a downfront wind can create negative buoyancy flux, counter restratification, and inhibit BI; and, Langmuir turbulence generated by the interaction between the Stokes drift by surface waves and the wind can inject kinetic energy directly at small scales and enhance mixing at the front. In several numerical models, BI is found to grow, albeit modified by the forcing and, somewhat surprisingly, even after the submesoscale is exposed to a storm in the study by Whitt and Taylor (2017). As discussed previously in this section, observational studies reveal submesoscale features and dynamics similar to the findings in the present unforced simulation. The net effect of the external forcing on submesoscale processes is dependent on the specifics of the problem and the strength of the forcing. It will be of interest to systematically study how the submesoscale/finescale properties and their mutual interaction change when other processes influence the mixed layer instability.

Acknowledgments

This chapter, in full, is a reprint of material published as follows: V. Verma, H. T. Pham and S. Sarkar, “The submesoscale, the finescale and their interaction at a mixed layer front,” *Ocean Model.*, 140, 101400 (2019). The dissertation author is the primary investigator and author of this work. I am pleased to acknowledge the support of ONR grants N00014-15-1-2578 and N00014-18-1-2137.

Chapter 3

Lagrangian three-dimensional transport and dispersion by submesoscale currents at an upper-ocean front

3.1 Introduction

Density fronts, ubiquitous in the upper ocean, are an important source of currents with submesoscale dynamics. The dynamics typically occur at length scales of 0.1 - 10 km and the time scale of $O(1\,\mathrm{day})$ and are characterized by $O(1)$ Rossby number, $Ro = U/fL$, and Richardson number, $Ri = N^2/(\partial_z U)^2$, where f is the Coriolis parameter, U is a characteristic velocity scale, L is a characteristic length scale, $N = \sqrt{-(g/\rho_0)(\partial\rho/\partial z)}$ is the buoyancy frequency corresponding to density ρ stratification, ρ_0 is a reference density, and g is the gravitational constant (McWilliams, 2016, Thomas et al., 2008). The submesoscale plays a significant role in the restratification of the upper ocean and the vertical transport of tracers such as buoyancy, salinity, and carbon from the surface ocean to the interior (Boccaletti et al., 2007, Omand et al., 2015, Thomas et al., 2008). These processes affect the upper-ocean structure and impact the interactions between the ocean and the atmosphere, thereby influencing the Earth's climate. Submesoscale currents also play a significant role in ocean's biochemical cycle by aiding phytoplankton growth through supply of nutrients from the upper thermocline into the surface layer (Mahadevan, 2016).

Many of the upper-ocean processes driven by the submesoscale dynamics are possible because of their ability to develop large vertical velocity (Mahadevan and Tandon, 2006), presumably with spatial and temporal coherence. This is in contrast to the small-scale turbulent motions, which are relevant for the local mixing, or the balanced mesoscale motions in which the vertical velocity is orders of magnitude smaller. The lateral transport is believed to be dominated by the mesoscale currents and eddies, but the role of submesoscales can be significant as they can provide interconnections between the mesoscale transport barriers and enhance the horizontal spread (Haza et al., 2016). The submesoscales are also important for predicting the dispersion of buoyant pollutants such as oil (D'Asaro et al., 2018). An understanding of the organization of vertical velocity and transport pathways is therefore crucial for understanding the submesoscale upper-ocean transport and dispersion processes.

Frontogenesis intensifies vertical motions. A zone with horizontal buoyancy contrast can undergo frontogenesis through straining by a large scale confluent flow as well as non-linear evolution of baroclinic instability (BI) (Hoskins, 1982, Hoskins and Bretherton, 1972). The initial stages of the frontogenetic development of BI at an atmospheric front have been studied in detail by Mudrick (1974). Recent studies have shown that the interaction of a cold filament in thermal wind balance with boundary layer turbulence can drive secondary circulations in the lateral-vertical plane that is frontogenetic and which survives in the presence of boundary-layer turbulenc (McWilliams et al., 2015, Sullivan and McWilliams, 2018). The ageostrophic circulation in the case of especially strong fronts can lead to nonlinear bores (Pham and Sarkar, 2018). Filament structures with cyclonic vorticity were observed in the northern Gulf of Mexico in an observational campaign utilizing a large number of satellite-tracked surface drifters (D'Asaro et al., 2018). The structures were smaller than 1 km in width, separated the dense and light water masses and were convergent, attracting surface drifters into a line that wrapped into a cyclonic eddy. The convergence of water mass implies downwelling and the measured vertical velocity was as large as $1-2\,\mathrm{cm\,s^{-1}}$. In comparison, the vertical velocity at a mesoscale front typically does not exceed $O(0.01)\,\mathrm{cm\,s^{-1}}$ (Rudnick, 1996).

The evolution of BI in upper-ocean density fronts is an important mechanism for generating submesoscale currents. The problem has been studied extensively using large-scale ocean models (Capet et al., 2008a) and turbulence resolving models (Hamlington et al., 2014, Skyllingstad and Samelson, 2012, Stamper and Taylor, 2017, Verma et al., 2019). Simulating a density front that is initially in thermal wind balance, Verma et al. (2019) (included as Chapter 2 of this thesis; hereafter VPS19) find that the evolution of BI generates long, thin vortex filaments with cyclonic vorticity and downwelling vertical velocity that roll into coherent submesoscale eddies. These submesoscale filaments and the large vertical velocity inside them are similar to the submesoscale filament-like features observed during the surface drifter measurements of D'Asaro et al. (2018). VPS19 showed that the coherent structures, i.e., vortex filaments and eddies, provide a 3D organization to the secondary circulation whose velocity field suggests that water is transported laterally and vertically across the front. Although there are organized 3D structures, the actual paths followed by the fluid parcels over time are not apparent from the instantaneous velocity field as the dynamics is transient; the spatial pattern of the velocity field changes when the coherent structures are transported by the sheared frontal jet. A Lagrangian framework is better suited for a study of material transport by the submesoscale, which is the subject of this paper. A related problem is about the time scale of subduction and restratification of the front. The vertical velocity observed in the filaments can be so large as to produce vertical displacement of $O(1\,\mathrm{km})$ in a day if sustained in magnitude and direction. However, the restratification is likely to progress on the time scale of baroclinic instability, which is $O(2\pi/f)$ (Stone, 1966). Here, we show evidence of a slow restratification at near-inertial time scale emerging from relatively fast motions in the filament structures.

Lagrangian drifters and floats have been widely used in the ocean for understanding flow properties and dynamics (e.g., see review article LaCasce (2008)). Single-particle metrics have been used for obtaining the mean flow, eddy kinetic energy, eddy diffusivity, and Lagrangian spectra characteristic of large spatial regions and sub-inertial to inertial frequencies. More recently, Lagrangian measurements have been extended to high-frequency motions of oceanic turbulence including turbulence at fronts (D'Asaro et al., 2011). Single-particle dispersion statistics are also a convenient tool for predicting the spread of a particle from the point of release by a velocity field that has coherent unsteady currents and turbulence. The particle-pair dispersion statistics, on the other hand, reveal the spread of particles about the center of mass (COM) of a particle cloud (Batchelor, 1952). Particle-pair statistics are often used to probe the scale dependence of dynamics. In a recent analysis of the trajectories of surface drifters deployed during the Grand Lagrangian Dynamics (GLAD) experiment in the Gulf of Mexico, Poje et al. (2014) found that the second-order velocity structure function showed power-law behavior from 200 m to 100 km, including the submesoscale range, suggesting the dominance of local advective dynamics. Balwada et al. (2016) applied a Helmholtz decomposition of the second-order structure function computed from the GLAD drifters into divergent and rotational components finding that the divergent component dominated at scales below 5 km, and also computed the third-order structure function. From their analysis, they inferred forward 3-D energy cascade below 5 km, 2-D enstrophy cascade between 5 to 40 km (the deformation radius), and an inverse energy cascade between 40 - 100 km. Beron-Vera and LaCasce (2016) examined pair-separation statistics in the submesoscale range, using synthetic drifter trajectories from data-assimilated NCOM simulations conducted with 1 km horizontal resolution. They found that the pair separation grew exponentially in accord with non-local dynamics. They further attributed the discrepancy of their result with the results from GLAD observational drifter trajectories to the strong inertial oscillations experienced by the GLAD drifters and their limited number of independent samples with possibly low statistical significance. In the ocean, internal gravity waves are likely to further complicate the statistical measure arising due to submesoscale dynamics.

Multiparticle studies have also been used, mainly to measure flow properties such as relative vorticity and horizontal divergence (Molinari and Kirwan Jr, 1975). Multiparticle statistics using groups of four particles (tetrads) can be used to investigate the changes in the shape of the particle clusters, which result from straining by the large-scale flows and dispersion by the finescale motions, as shown by Pumir et al. (2000).

In this study, we employ the model front of VPS19 to investigate the transport and dispersion characteristics of the submesoscale currents, including finescale turbulence, during the evolution of BI. VPS19 does not contain strong inertial motions, internal gravity waves or surface forcing, thus providing an ideal setup for studying the dispersion characteristics of submesoscale currents in isolation. Owing to the high resolution (2 m in all three directions) of the simulation, we are able to capture 3D turbulence generated during the evolution of BI. The domain size of 4 km captures a wide range of the submesoscale but not the mesoscale. The study is performed in the Lagrangian framework by releasing a large number of tracer particles that move with the local fluid velocity.

The paper is structured as follows. In section 2.2, the setup of the model front of VPS19 is summarized. In section 3.3, the 3D coherent structures observed in VPS19 are briefly described. The details about the tracer-particle simulation are given in section 3.4. In section 3.5, the 3D organization of the particles, the typical features of the transport pathways, and the restratification of the front are examined. In section 3.6, various time scales of the Lagrangian motion are investigated, and the vertical transport of tracer particles is studied by monitoring the centers of mass of particle clouds and the dispersion of particles within the clouds. Section 3.7 focuses on the dispersion characteristics of the submesoscale currents, including the localized three-dimensional finescale associated with the currents. In this section, single- and pair-particle dispersion statistics are investigated, and shape changes following groups of four particles (tetrads) are reported. Finally in section 3.8, conclusions are drawn based on the results, with a brief discussion about their implications.

3.2 Model setup

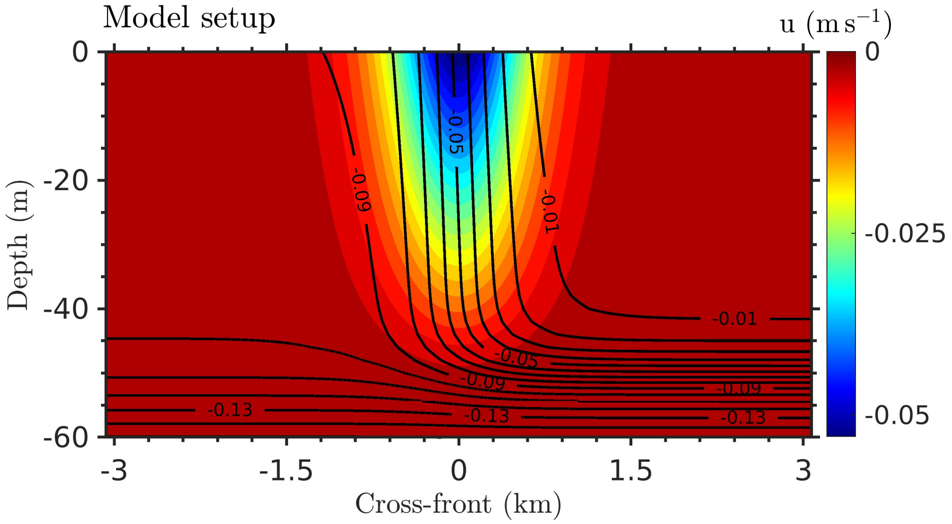

Figure 3.1: Initial profile of the along-front velocity with superposed temperature deviation (in Kelvin) contours.

The model, which is the same as the one employed by VPS19, is summarized. The problem is initialized as an upper-ocean front in thermal wind balance with a surface jet. The front of width $L = 1.2\,\mathrm{km}$ is confined to a surface layer of depth $H = 50\,\mathrm{m}$ situated above a strongly stratified thermocline. The front is aligned with the x-direction (along-front), and the temperature variation in y (cross-front) and z (vertical) coordinates sets the buoyancy contrast. The value of $M^2 = -(g/\rho_0)\partial\rho/\partial y$ at the center ($y = 0$) is $M_0^2 = 1.5 \times 10^{-7}\,\mathrm{s}^{-2}$. The square of buoyancy frequency ($N^2 = -(g/\rho_0)\partial\rho/\partial z$) takes the value of $N_M^2 = 3.0 \times 10^{-7}\,\mathrm{s}^{-2}$ in the 50 m depth surface layer and $N_T^2 = 10^{-5}\,\mathrm{s}^{-2}$ in the thermocline below the surface layer. The frontal jet, $U(y,z)$, is constructed from the density field by integrating the thermal wind relation, $\partial U/\partial z = -M^2/f$, where $f = 1.4 \times 10^{-4}\,\mathrm{s}^{-1}$ is the Coriolis parameter. The velocity $U(y,z)$ is negative as shown in Fig. 3.1. The potential vorticity at the front is initially negative and the setup is unstable to symmetric perturbations.

The evolution of the model front is studied numerically, utilizing the large eddy simulation (LES) approach and solving the non-hydrostatic Navier-Stokes equations under the Boussinesq approximation. VPS19 can be referred for the numerical algorithm. When the Navier-Stokes equations are scaled by the velocity scale $U_0 = M_0^2 H/f$ (the maximum geostrophic jet velocity at the surface) and the buoyancy scale $N_M^2 H$, the following set of non-dimensional parameters ensues: the Ekman number, $Ek = \nu/fH^2 = 2.86 \times 10^{-6}$; the non-dimensional lateral buoyancy gradient, $M_0^2/f^2 = 7.65$, and the Richardson number, $Ri = N_M^2 f^2/M_0^4 = 0.26$. The ratio $M_0^2/f^2 = 7.65$ is comparable to the values used in the studies of Skyllingstad and Samelson (2012) and Hamlington et al. (2014). The Rossby number, $Ro = U_0/fL$, based on the initial horizontal shear is 0.32 and the Reynolds number, $Re = U_0 H/\nu$, is 2.67×10^6.

The computational domain spans $0 \leq x \leq 4098\,\mathrm{m}$, $-3073\,\mathrm{m} \leq \mathrm{y} \leq 3073\,\mathrm{m}$ and $-130\,\mathrm{m} \leq \mathrm{z} \leq 0$. A uniform grid with $2050 \times 3074 \times 66$ points is employed initially, providing a grid resolution of 2 m in each direction. Later, during the evolution of baroclinic instability, the solution is obtained using a grid which is the same in the horizontal, but has 98 grid points in the vertical, with uniform stretching such that the grid spacing changes from 0.5 m near the surface to 1.5 m near the bottom. The finer grid resolution in the vertical is needed near the surface to resolve the surface intensified turbulence in the vortex filaments that develops during the nonlinear evolution of BI.

3.3 Submesoscale structures

The evolution of the front, which is discussed in detail in VPS19, is summarized here to motivate the Lagrangian studies of this paper. The initial setup is unstable to symmetric instability (SI). However, as the front restratifies, it becomes stable to SI (Arobone and Sarkar, 2015, Taylor and Ferrari, 2009). Most of the evolution of the front is therefore controlled by baroclinic instability (BI), which becomes dominant after SI subsides. The nonlinear growth of BI spawns submesoscale coherent structures such as vortex filaments and eddies. Additionally, the sharpest frontal features develop 3D shear instabilities that sustain turbulence, arresting frontogenesis.

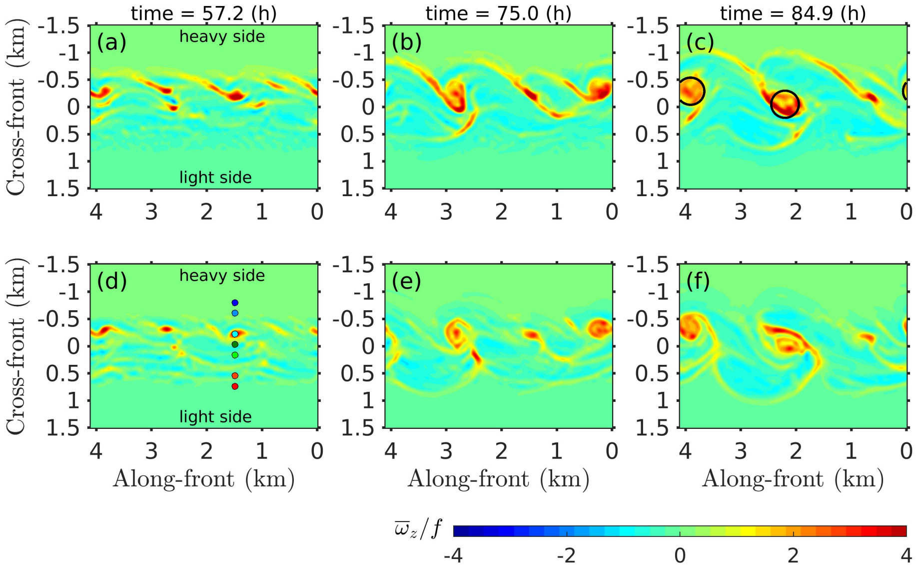

Figure 3.2: Evolution of coherent structures at the front, shown using submesoscale vertical vorticity at depths 10 m (a, b, c) and 30 m (d, e, f) at times $t = 57.2, 75$, and 84.9 h. The circles with diameter 500 m in panel (c) roughly identify the locations of the eddies at the front. In panel (d), solid circles depict the initial positions of the particles (P1-P7) whose trajectories are plotted in Fig. 3.4. Particles P1-P7 are arranged sequentially in the lateral with P1 at $y = -800$ m.

VPS19 separated the submesoscale ($\bar{\phi}$) from the turbulent finescale (ϕ'') by applying a 2D, low-pass Lanczos filter in x- and y-directions with a cutoff wavelength, $\lambda_c \equiv 2\pi/k_c = 157$ m. Figure 3.2 shows the submesoscale vertical vorticity at 10 m(Figs. 3.2a-c) and 30 m (Figs. 3.2d-f) depth at different times. Figure 3.2a, plotted at $t = 57.2$ h during the initial roll up of the front, reveals filaments of cyclonic vorticity which connect to the heavy edge of the front and wrap into the central coherent eddies. At this time, the eddies are small and only slightly larger than the filament width of $O(100)$ m. The eddies are vertically coherent and can be identified at 30 m depth in Fig. 3.2d. The structures are advected by the mean flow in the negative x-direction. As the instabilities evolve, the vorticity filaments grow in length and the eddies become larger in

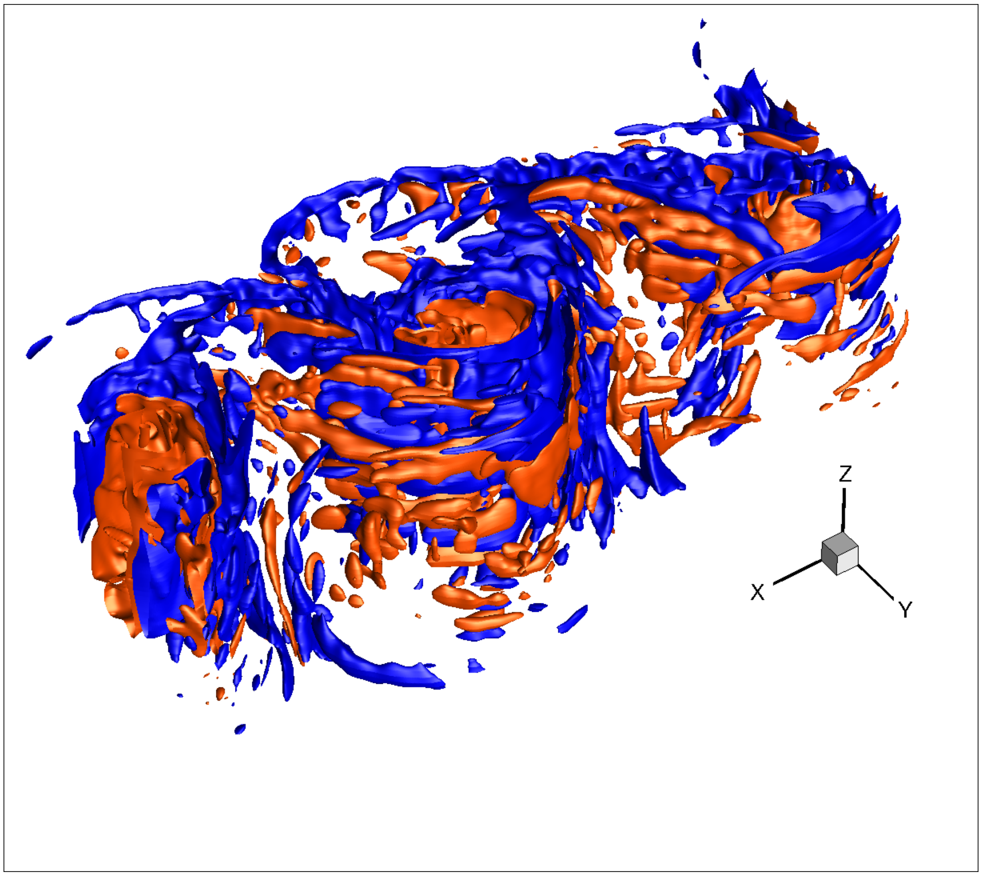

Figure 3.3: Visualization of coherent structures in 3D using the Q criterion on the submesoscale velocity field at $t = 84.9\,\mathrm{h}$. The iso-surfaces of submesoscale Q are plotted at $\overline{Q}/f^2 = 0.4$ (red) and $\overline{Q}/f^2 = -0.4$ (blue).

diameter (Figs. 3.2b,c). Isosurfaces of Q (Fig. 3.3) illustrate the three-dimensional organization of the coherent structures. Here, Q is calculated using the submesoscale velocity fields, i.e., $\bar{Q} = (\overline{\Omega}_{ij}^2 - \overline{S}_{ij}^2)/2$ where $\overline{\Omega}_{ij} = (\partial\bar{u}_i/\partial x_j - \partial\bar{u}_j/\partial x_i)/2$ and $\overline{S}_{ij} = (\partial\bar{u}_i/\partial x_j + \partial\bar{u}_j/\partial x_i)/2$. The regions with $\bar{Q} > 0$ represent rotation-dominated flow whereas those with $\bar{Q} < 0$ represent strain-dominated flow. The vertical coherence of the submesoscale coherent eddies is evident as are the interspersed regions of strain.

3.4 Setup of particle tracking

Tracer particles were introduced in the flow at $t_0 = 57.2\,\mathrm{h}$ to assess material transport under the influence of submesoscale currents. At this time, the vortex filaments have formed at the front and have begun to wrap into eddies (Figs. 3.2a,d). The particles are placed at the nodes of a regular lattice that occupies the entire domain $0 \leq x \leq 4.1\,\mathrm{km}$ in the along-front (x) direction, $-1.6 \leq y \leq 1.6\,\mathrm{km}$ in the lateral (y) direction, and $-70 \leq z \leq -2\,\mathrm{m}$ in the vertical (z) direction with resolution $16\,\mathrm{m} \times 16\,\mathrm{m} \times 2\,\mathrm{m}$. Before introducing the particles, the simulation run with a uniform $\Delta z = 2\,\mathrm{m}$ is interpolated to a grid with higher vertical resolution (0.5 m near the surface to 1.5 m near the bottom of the front) at $t \approx 56\,\mathrm{h}$.

The tracer particles are passive and, by definition, move with the local fluid velocity according to

$$\frac{d\mathbf{x_p}}{dt} = \mathbf{u}_f(\mathbf{x}_p, t), \tag{3.1}$$

where $\mathbf{u}_f(\mathbf{x}_p, t)$ is the fluid velocity at the particle position $\mathbf{x}_p$. Equation 3.1 is advanced in time with a third-order Runge-Kutta (RK3) scheme and $\mathbf{u}_f(\mathbf{x}_p, t)$ is obtained by the fourth-order Lagrange interpolation of a cell-centered velocity field. The Navier-Stokes solver stores the velocity components at the edge centers and cell-centering is achieved by linear interpolation. A CFL value smaller than one for particle advection ensures a stable numerical trajectory. More details about the particle advection code is included in Appendix A.

3.5 Advection of tracer particles

Individual particle trajectories differ considerably even for neighboring particles. Nevertheless, there is an overall organization in their motions influenced by the coherent structures as elaborated below. Anticipating differences in the particle behavior in the initial frontal zone from its edges, we distinguish among particle groups according to their cross-front (y) locations of release as follows: (i) central region, $-500\,\mathrm{m} \leq y \leq 500\,\mathrm{m}$, (ii) heavy edge, $y < -500\,\mathrm{m}$, and (iii) light edge, $y > 500\,\mathrm{m}$.

3.5.1 Particle trajectories

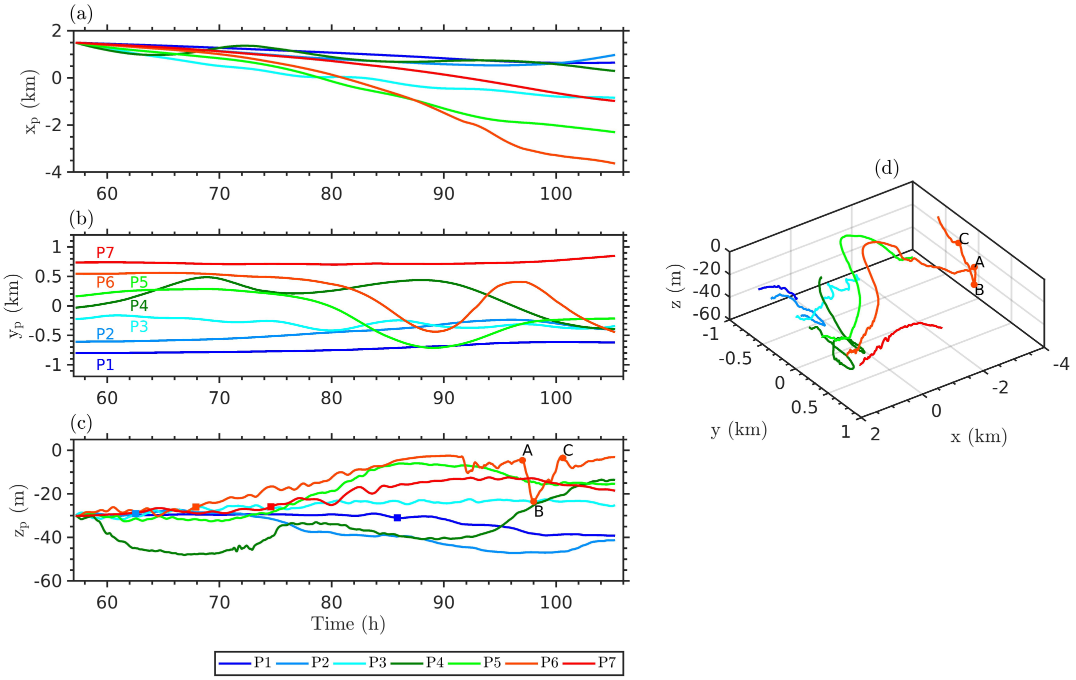

Figure 3.4: Particle trajectories: (a) $x_p(t)$, (b) $y_p(t)$, and (c) $z_p(t)$ plotted in time and (d) in 3D space. The particles are released at a cross-front transect (different y-locations) through $x = 1490\,\mathrm{m}$ and $z = -30\,\mathrm{m}$. The initial positions of the particles in the xy-plane at 30 m depth were shown in Fig. 3.2d. In panel (c), the solid squares in the trajectories of edge particles P1, P2, P6 and P7 denote the time when they start moving vertically. Points A, B, and C in the trajectory of P6 in panels (c) and (d) mark the different phases of a rapid downwelling-upwelling event: A-B corresponds to the downwelling phase and B-C to the upwelling phase.

The trajectories of particles (P1-P7) released at $z = -30\,\mathrm{m}$ and $x = 1490\,\mathrm{m}$ are shown in Fig. 3.4. The 3D trajectories in Fig. 3.4d reveal that the path followed by the particles are strikingly different from one another. However, transport characteristics common to particles within a group can be identified by examining the trajectories $x_p(t)$, $y_p(t)$ and $z_p(t)$ (Figs. 3.4a-c).

Depending on their initial y-coordinates (Fig. 3.4c), the particles can be distinguished as the heavy-edge particles (P1 and P2), the central-region particles (P3-P5), and the light-edge particles (P6 and P7). Particle P3 is selected such that it is located within a submesoscale eddy.

The vertical trajectories of the particles plotted in Fig. 3.4c reveal that the heavy-edge particles (P1 and P2) downwell, while the light-edge and central-region particles (P3-P7) upwell. A negative correlation between lateral (v_p) and vertical (w_p) velocity can be observed for central-region particles P4 and P5 and at late times for edge-particles P2 and P6. For example, P4 moves vertically downward when its lateral motion is in the positive y-direction, while it moves vertically upward when the lateral motion is in the negative y-direction. Moreover, the correlated y and z motions of P4 and P5 exhibit oscillations with a time period of about 25 h, which is twice the inertial time period ($T_i = 12.5\,\mathrm{h}$). The central-region particle P3 released within an eddy remains trapped inside the eddy and shows near-inertial oscillations in its y coordinates. The vertical trajectory of P6 shows a fast time-scale event with remarkably rapid transport in the vertical. This event starts at $t \approx 97\,\mathrm{h}$ when P6 downwells by approximately 20 m (from A to B) over a period of about an hour and then upwells back to the surface (from B to C) in the next 2.5 hours. The downwelling occurs when the particle gets attracted to a heavy-edge filament and is followed by upwelling when it finds itself in a denser background.

Edge particles begin to advect vertically at different times; the particles' motions farther away from the central region are delayed relative to the closer ones. In Fig. 3.4c, the approximate start of vertical transport is marked with solid squares in the trajectories. P1 starts moving vertically after P2 and P6 after P5, since P2 and P5 are closer to the central region than P1 and P6. We will show that the vertical transport of particles is initiated by coherent vortex filaments at the edges of the slumping front, and those outside are transported afterwards, as the front width increases slowly to reach them.

The along-front particle displacements are generally in the negative x-direction (Fig. 3.4a) following the mean u. However, a particle can acquire $u_p > 0$ especially when it reaches the bottom of the front (e.g., P2 during $t \approx 96-105$ h and P4 during $t \approx 64-72$ h). Notice that the x-trajectories of particles (e.g., P5 and P6) which cross the left domain boundary at $x = 0$ are continued into the negative x region considering the streamwise periodicity of the domain. Typically, the upwelling particles (P6 and P7) have larger negative x displacements compared to the downwelling particles (P1 and P2), as the upwelling particles tend to spend more time near the surface where the along-front speed is larger. Oscillations with small amplitudes can be observed in the vertical trajectories (e.g., P4, P5, and P6), indicating the influence of the finescales. However, the effect of the finescales on the along-front and cross-front displacements is weak.

3.5.2 Coherent transport pathways

Section 3.5.1 showed particle trajectories with multiple time scales and distinctive behavior depending on lateral particle location. Here, we demonstrate that the coherent structures seen in the Eulerian analysis of VPS19 organize the particle motion in a specific manner.

The positions of central-region particles are shown in Fig. 3.5 at $t = 84.9$ h, after a flight time of 27.7 h, along with their trajectories over the last 45 min. Particles, especially those near the surface, exhibit large lateral meanders. The coherent submesoscale eddies in the central region impart a cyclonic circulation to the particles. Moreover, the particles transported across the front to the light side ($y > 0.4$ km) exhibit a distinct organization into additional structures that are vertically inclined, reach down to the depth of up to 50 m (similar to the coherent eddies), and extend laterally towards the light edge of the front. Each lobe, although associated with an eddy, is a distinct structure having particles undergoing anticyclonic circulation, as opposed to the cyclonic circulation imparted the eddies. We refer to these inclined, anticyclonic structures as lobes. Two lobes – LB1 and LB2 – can be identified in Fig. 3.5 and are further discussed below.

We take a more comprehensive look at the 3D organization of particles by the submesoscale currents using particles released at 10 m and 40 m depth. Figures 3.6a-f shows temperature (T_p), lateral velocity (v_p), and vertical velocity (w_p) of the particles at the same time as Fig. 3.5.

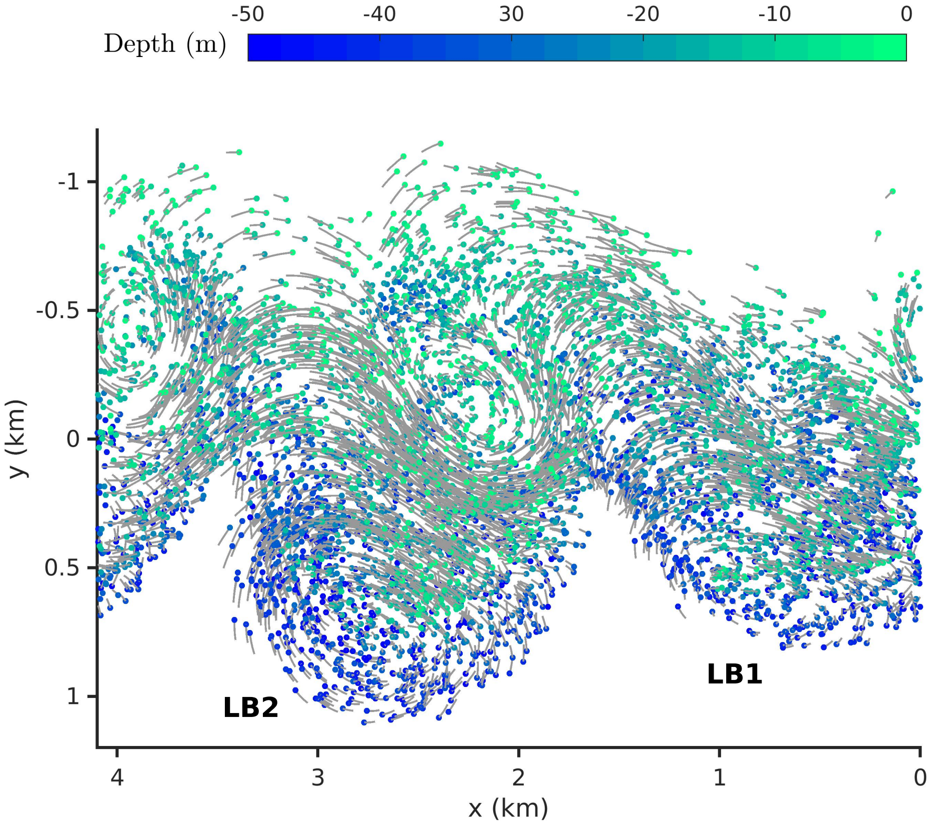

Figure 3.5: The organized motion of the central-region particles is depicted using particles released at 20 m depth. The $x-y$ positions of the particles at $t = 84.9$ h are shown as circles colored by the depth. To visualize the particle motion in time, trajectories from the last 45 min of advection are plotted in grey.

Lobes LB1 and LB2 can be observed within the front in all the figures. The lobes are stratified (Figs. 3.6a,b) having warm particles in the upper region and cold particles in the lower. The particle circulations are illustrated by v_p and w_p: Figs. 3.6c,e for the 10 m-depth particles and Figs. 3.6d,f for the 40 m-depth particles. The negative correlation between v_p and w_p seen for some of the particle trajectories of section 3.5.1 are revealed to be associated with motion in the lobes. For example, particles at the side LBF (marked by circles with dots in Fig. 3.6c) of lobe LB2 have positive v_p. At the same time, the mostly negative w_p in LBF (Figs. 3.6e,f) corresponds to downwelling. Eventually, v_p become negative when the particles reach side LBB (marked

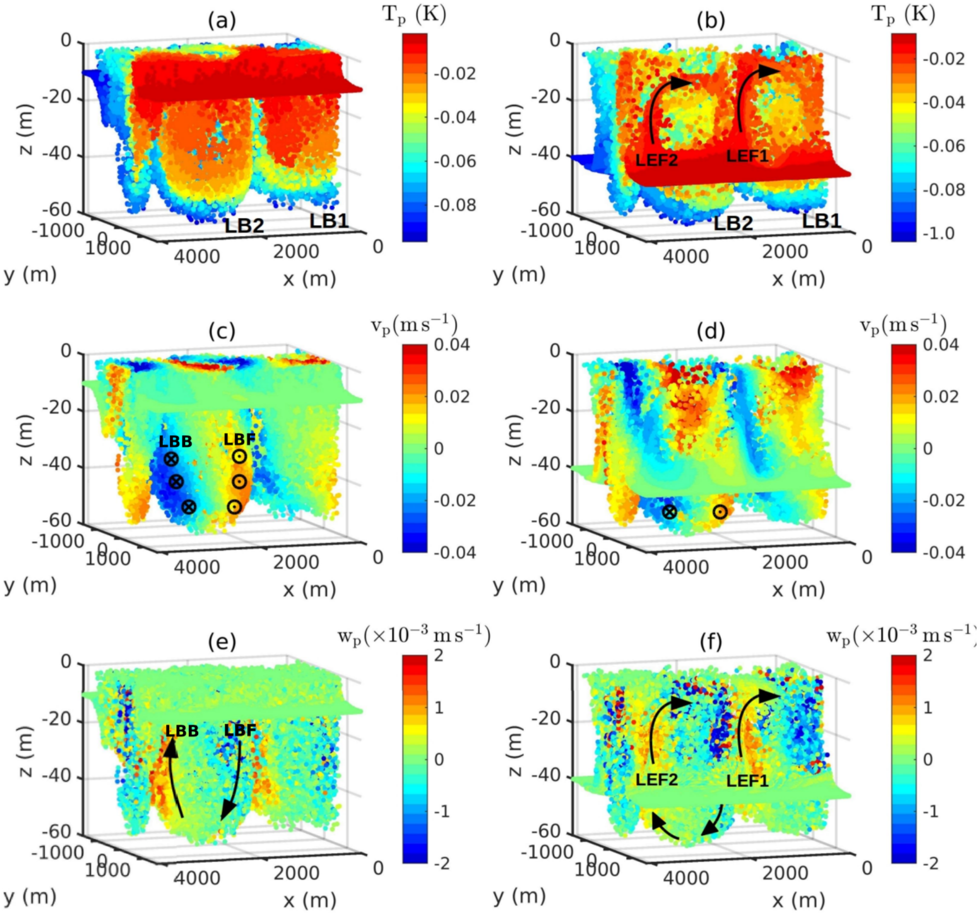

Figure 3.6: Plots of temperature (a, b), lateral velocity (c, d), and vertical velocity (e, f) at $t = 84.9$ h corresponding to the particles released at 10 m (left column) and 40 m (right column) depth. In panels (a) and (b), LB1 and LB2 are the two particle lobes corresponding to the two eddies at the front. In panels (c) and (d), the symbols with dots inscribed within circles mark the side in LB2 where the lateral velocity of the particles is generally positive, whereas the symbols with crosses inscribed within the circles mark the side where the overall lateral velocity is negative. The overall upwelling/downwelling vertical velocity of the particles at the two sides of LB2 are depicted by arrows in panels (e) and (f). The arrows in panels (b) and (f), denoted as LEF1 and LEF2, identify the upwelling particle filaments.

by circles with crosses in Fig. 3.6c) of lobe LB2. At LBB, w_p is mostly positive as seen in Fig. 3.6e, and the particles climb up the lobe. In general, the particles circulate within the same lobe, especially when the interaction between the neighboring eddies is weak.

It is worth noting that the correlation between v_p and w_p is such that the associated circulation in the lateral-vertical plane follows the isopycnal slope. In the present case, the lateral density gradient points in the negative x-direction and, therefore, v_p and w_p have negative correlation.

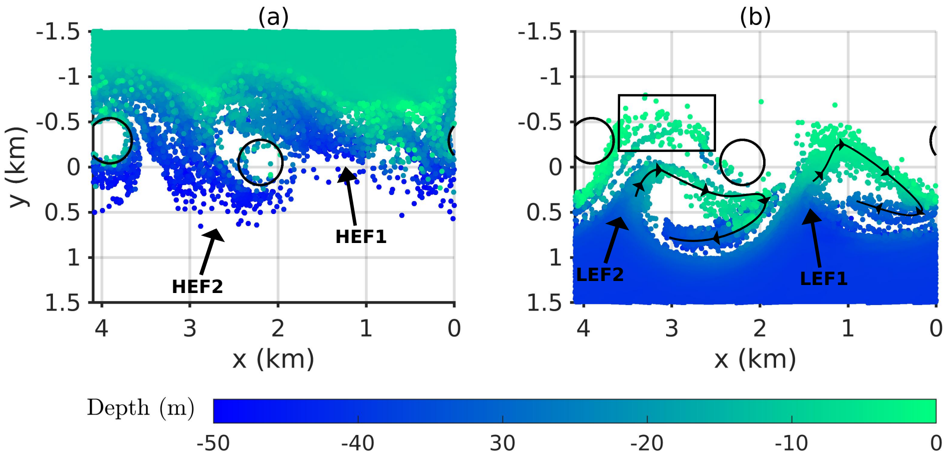

Figure 3.7: The horizontal organization of the particles with colormap depicting the z coordinates after a flight time of 27.7 h for particles released at $t = 57.2\,\text{h}$ and two different depths: (a) 10 m on the heavy edge, $y < -500$ m, and (b) 40 m on the light edge, $y > 500$ m. In panel (a), HEF1 and HEF2 denote the downwelling of the heavy-edge particles mediated by filaments, and in panel (b), LEF1 and LEF2 denote the upwelling of the light-edge particles through filaments, also identified in Figs. 3.6b, f. The solid black lines with arrows in panel (b) show the motion of the particles through filaments LEF1 and LEF2 with time, and the rectangular box encloses the particles that detach from the main branch LEF2 near the surface. The circles plotted in both figures roughly identify the submesoscale eddies, as shown in Fig. 3.2c.

The coherent vortex filaments are crucial to transporting edge particles into the central eddy-lobe circulation. Two light-edge filaments (LEF1 and LEF2) in Fig. 3.6b have mostly $w_p > 0$ (Fig. 3.6f) and lift the warm-edge particles towards the upper layers of the stratified lobes. Although not visible in Fig. 3.6, there are coherent filaments connected to the heavy edge of the front, as well. The role of the filament structures on the transport is made clearer by the positions at $t = 84.9\,\text{h}$ of heavy-edge particles released at $10\,\text{m}$ depth (Fig. 3.7a) and light-edge particles released at $40\,\text{m}$ depth (Fig. 3.7b). In Fig. 3.7a, particles at depth are seen at $y > 0$ as they are transported by heavy-edge vortex filaments (HEF1 and HEF2) across the front and downwell to the underside of the lobes. These downwelled particles collect within the lobes and undergo the previously described circulation of the lobe. The light-edge filaments (LEF1 and LEF2) in

Fig. 3.7b are located between the heavy-edge filaments. After being lifted upwards through the light-edge filament, particles branch back to the bottom of the front through the downwelling limb of the lobe. Interestingly, some particles detach from this main branch near the surface and spread laterally under the influence of the near-surface circulation. These particles are enclosed within the rectangular box shown in Fig. 3.7b.

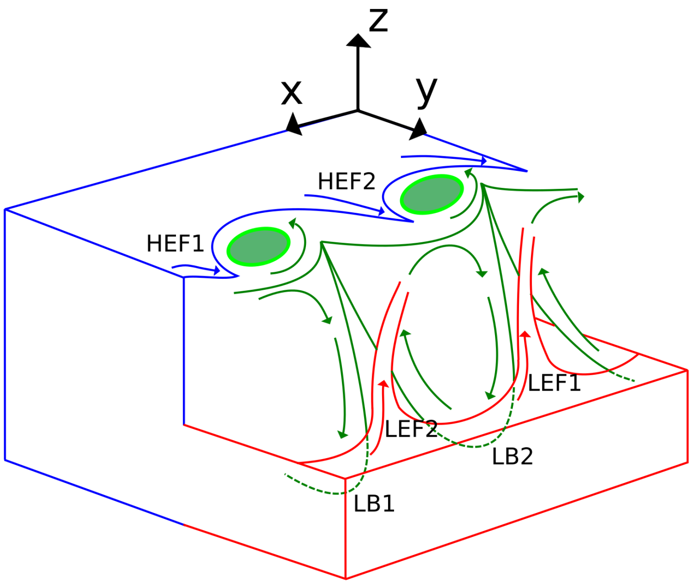

Figure 3.8: A schematic of transport mediated by the coherent vortex filaments and eddies, and the circulation of particles organized within the lobes. The downward sloping regions of HEF1 and HEF2 are behind the lobes and hidden in this view.

Figure 3.8 gives a consolidated picture of Lagrangian pathways at the front: transport to the central region by vortex filaments, stirring by the central submesoscale eddies, and circulations within vertically inclined lobes. The upwelling of light-edge fluid through vortex filaments to the upper layers of the lobes is shown, and the downwelling of heavy-edge fluid through vortex filaments to the undersides of the lobes is also partially shown.

3.5.3 Restratification process

Submesoscale currents lead to bulk restratification. The link between the stirring by the 3D filament-eddy-lobe motions to restratification of the *x*-averaged front is elaborated here.

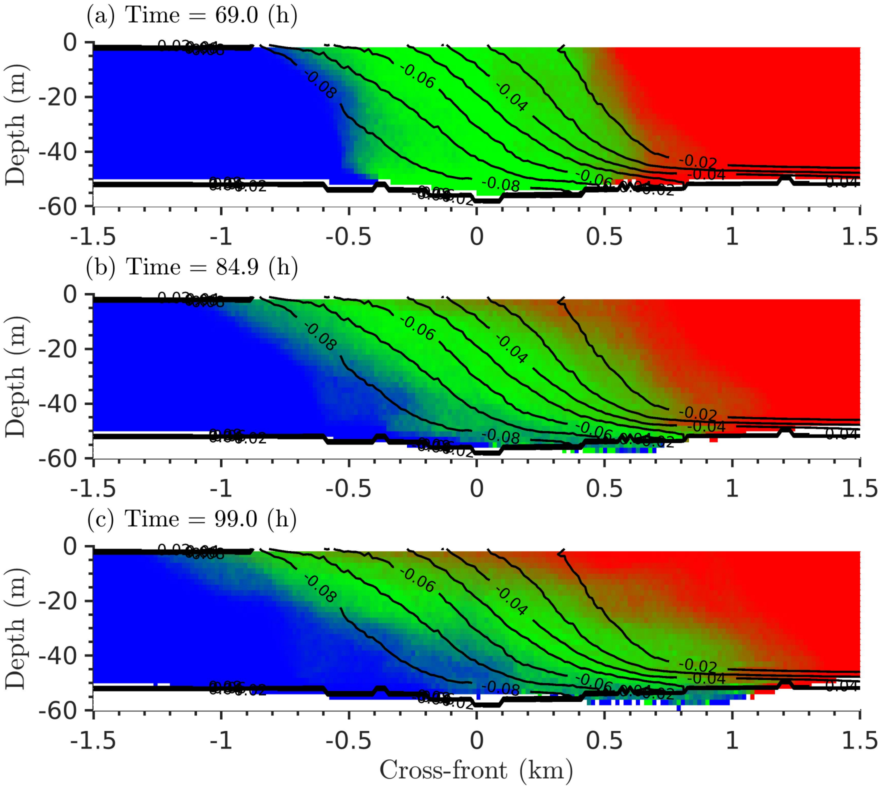

Figure 3.9: Adjustment of the front is shown by mean (*x*-averaged) particle positions and temperature at three different times: (a) 69 h, (b) 84.9 h and (c) 99 h. Particles are grouped by release location: central region with $-500\,\mathrm{m} \leq \mathrm{y_p} \leq 500\,\mathrm{m}$ in green, the heavy edge with $y_p < -500\,\mathrm{m}$ in blue, and the light edge with $y_p > 500\,\mathrm{m}$ in red. The particles are sampled into streamwise-elongated cells with $L_x = 4.1\,\mathrm{km}$ (entire along-front) and a rectangular cross-section with $\Delta_s y = 16\,\mathrm{m}$ and $\Delta_s z = 2\,\mathrm{m}$. Averaging over the *x*-variability of the three groups of particles at the boundaries leads to group intermingling in some of the cells. Such cells are colored by blending each group's color in proportion to that group's particle number. Isotherms of the mean temperature deviation (in Kelvin) are shown with solid lines.

Figure 3.9 characterizes how the particles released in the central, light and heavy regions redistribute spatially as time progresses. For identifying their *x*-averaged distribution, the particles are sampled in thin, long cells which extend over $L_x = 4.1\,\mathrm{km}$ (entire *x*-domain) and have dimensions of $\Delta_s y = 16\,\mathrm{m}$ and $\Delta_s z = 2\,\mathrm{m}$ in the cross-section. As the front evolves, the central-region cloud slumps. Its stable density contrast is maintained for the most part. Particles from the heavy edge primarily subduct below and those from the light edge spread above the slumping central region.

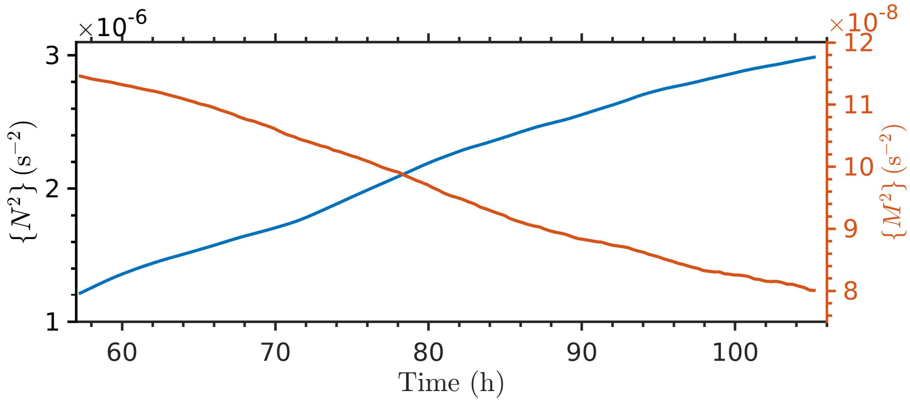

Figure 3.10: Evolution of the frontal stratification and lateral buoyancy gradient. $\{N^2\}(t)$ and $\{M^2\}(t)$ are volume averages in the region encompassing the entire x-domain, $-500 \leq y \leq 500$ m (central-front region) in the lateral, and $-45 < z < 0$ m in the vertical.

The time scale of the bulk restratification is of interest. The evolution of volume-averaged $\{N^2\}(t)$ and $\{M^2\}(t)$ is shown in Fig. 3.10. A significant portion of the restratification, which would lead to a final $N^2 \approx 3.6 \times 10^{-6}\mathrm{s}^{-2}$ upon completion of frontal slumping, takes place by $t = 100$ h. Taking $w_p = 10^{-3}\,\mathrm{ms}^{-1}$ to characterize speeds during significant downwelling events, leads to a time scale $t_{ML} = 13.9$ h for traversing the mixed layer of $H = 50$ m. Restratification is evidently slower than that suggested by the large values of w_p. VPS19 apply a Lanczos horizontal filter of $O(100)\,\mathrm{m}$ to w to obtain the coherent submesoscale velocity $\overline{w}$, identify the downwelling regions with $\overline{w} < 0$, and define the submesoscale vertical velocity in those regions as $\overline{w}^-$. Similarly, here we define $w^- = w$ in regions where $\overline{w} < 0$. The average of w^- over the front was found to be $\langle w^- \rangle \approx 10^{-4}\,\mathrm{ms}^{-1}$. A ML traverse time of $H/\langle w^- \rangle = 133$ h agrees better with the observed restratification time scale. The horizontal buoyancy gradient, $\{M^2\}(t)$, progressively decreases from its initial value of $M_0^2 = 1.5 \times 10^{-7}\,\mathrm{s}^{-2}$ as the front collapses but remains significant at $t = 100$ h because regions with vertical shear persist and frontogenesis continues to support regions with large local M^2. There is variability of N^2 too with larger values at the top and bottom of the considered volume.

3.6 Vertical transport

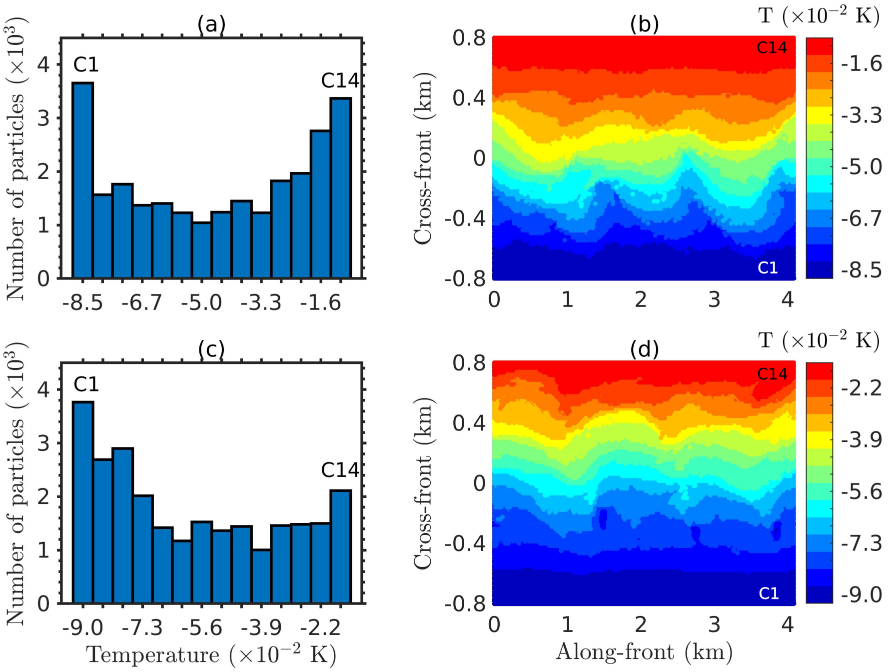

Figure 3.11: The initial configuration of the particle clouds released at 10 m (a, b) and 40 m (c, d) depth: the mean temperature and the number of tracer particles in each cloud (a, c) and the organization of the clouds in the horizontal (b, d). Each cloud has particles with a similar density ranging from high (C1) to low (C14). The particle clouds, especially in the central region, are in the form of long, thin meandering strips.

In this section, we investigate the collective motion of particles by tracking particle clouds. Lagrangian time scales are obtained and the statistics of vertical displacement are assessed. The finite-width clouds whose length extends across the streamwise domain are initialized with particles released at 10 m and 40 m depth (Figs. 3.11a-c). The cloud array covers

$-800 \leq y \leq 800\,\mathrm{m}$ across the front such that the particles constituting any given cloud have similar density and, therefore, have similar buoyancy control on the dynamics. At each depth, fourteen clouds (C1-C14) are constructed with average density (temperature) decreasing (increasing) progressively from cloud C1 to C14. Each cloud has more than 1000 particles, leading to reasonably converged statistics.

3.6.1 Separation of timescales

Different time scales involved in particle transport can be understood by examining the Lagrangian energy spectra and autocorrelation functions of the particle velocity. The Lagrangian spectra for cloud Ci are calculated as

$$S_{u_p}(\omega_f) = \langle |\hat{u}_p(\omega_f)|^2 \rangle_{Ci}, \quad S_{v_p}(\omega_f) = \langle |\hat{v}_p(\omega_f)|^2 \rangle_{Ci}, \tag{3.2}$$

$$S_{w_p}(\omega_f) = \langle |\hat{w}_p(\omega_f)|^2 \rangle_{Ci}, \tag{3.3}$$

where $\hat{u}_p(\omega_f)$, $\hat{v}_p(\omega_f)$, and $\hat{w}_p(\omega_f)$ are the Fourier transforms of the velocity time records, ω_f is the angular frequency, and $\langle \cdot \rangle_{Ci}$ represents averaging over all the particles in cloud Ci. The velocity data over $57.2 < t < 105.2$ h are considered. The non-uniform time data are interpolated to a uniform grid, and the Hanning window is applied.

The Lagrangian energy spectra for the central-region cloud C7 released at 10 m depth (Fig. 3.12a) reveal two dynamical regimes. At subinertial time scales with $\omega_f/f < 1$, the horizontal kinetic energy is much larger than the vertical component, reflecting strong submesoscale dynamics. On the other hand, at time scales with $10 < \omega_f/f < 100$, all three components have comparable energy, reflecting the influence of 3D finescale dynamics. Furthermore, unlike the horizontal components, the w_p spectrum shows little variability over $1 < \omega/f < 10$. This suggests that finescales are likely to have a significant influence on the vertical motion, whereas the horizontal motion of the particle is dominated principally by the slower subinertial submesoscale

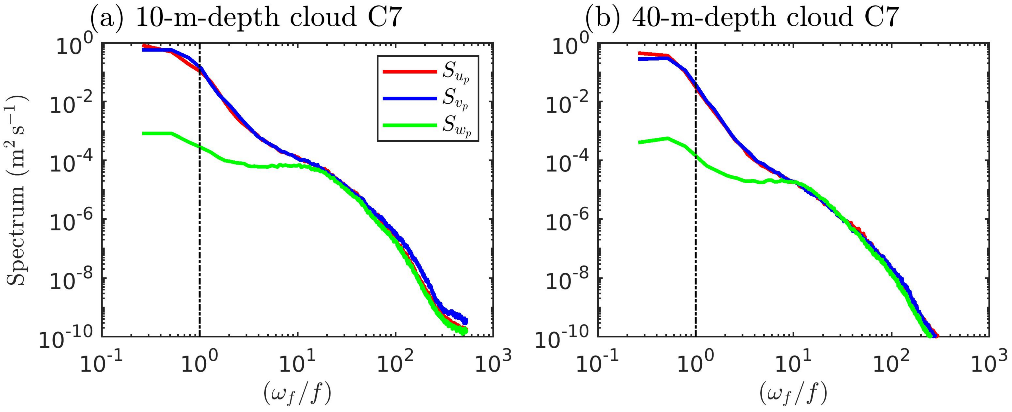

Figure 3.12: Lagrangian energy spectra $(S_{u_p}(\omega_f), S_{v_p}(\omega_f), S_{w_p}(\omega_f))$ for: (a) 10-m-depth of release in C7 and (b) 30-m-depth of release in C7.

dynamics. The energy spectra for the 40 m release depth in Fig. 3.12b are similar to those at 10 m release depth, suggesting similarity of particles motions in the central region over the depth of the front.

The fast time scale in the spectra can be related to the vertical shear of the horizontal velocity. In the model front with thermal wind balance, the vertical shear $|\partial U/\partial z| \equiv |M^2|/f = O(10)f$ corresponds to a time scale of about 1 h. At this time scale, as shown in Figs. 3.12a,b, the Lagrangian dynamics start to behave as three-dimensional.

The two-point autocorrelation is defined for the along-front velocity by

$$\rho_{u_p}(t,\tau) = \langle u_p(t)u_p(t+\tau)\rangle_{Ci} / \langle u_p^2(t)\rangle_{Ci}\,, \tag{3.4}$$

and similarly for the other two components. The autocorrelation functions for u_p and v_p (Figs. 3.13a,b) are dominated by subinertial time scales and do not vanish over the advection time considered here. The temporal oscillations in ρ_{u_p} and ρ_{v_p} arise from particle circulation within the coherent submesoscale eddies and lobes structures at the front. In contrast, ρ_{w_p} drops from its peak to a small value (~ 0.2) within an hour (shown in the insets) followed by a small-amplitude

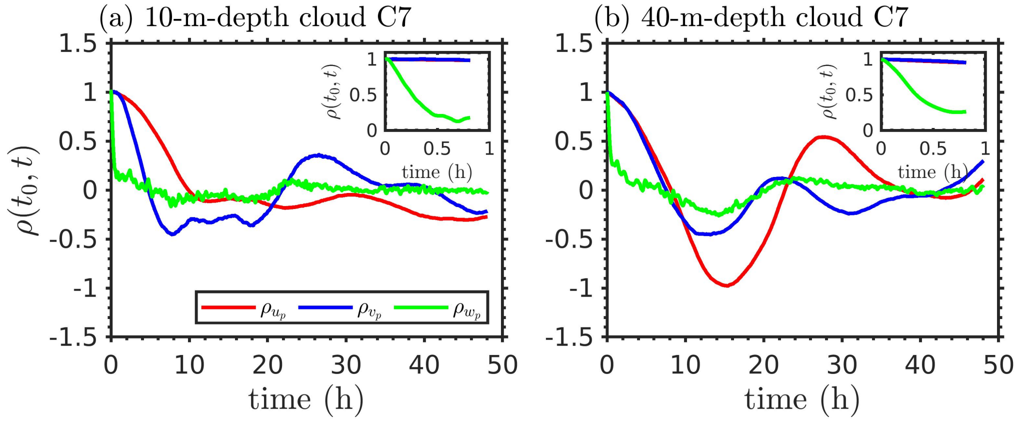

Figure 3.13: Velocity autocorrelation functions $(\rho_{u_p}(t_0,t), \rho_{v_p}(t_0,t), \rho_{w_p}(t_0,t))$ as defined in the text for two particle clusters. The insets in panels (a) and (b) show the variation over the initial one hour after particle release.

oscillation dominated by slow subinertial time scales, similar to that for the horizontal velocity components. The short time scale in ρ_{w_p} is due to two factors: motion in and near the filaments where w is large and rapidly varying, and near-N oscillations of w_p, noting that a Lagrangian mean $N^2 \approx 2.2 \times 10^{-6}$ s^{-2} leads to a time scale of 1.2 h.

3.6.2 Vertical transport of particle clouds

Here, the motion of the cloud's center of mass (COM) and the spread of the particles about the COM are examined. The COM of the cloud is defined by $\mathbf{x}^k_{com} = \sum_{i=1}^{N_k} \mathbf{x}^k_i / N_k$, where $\mathbf{x}^k_i$ is the position of the i^{th} particle in a cloud with index k and N_k is the total number of particles in the cloud. The spread of particles in a cloud is characterized by the root-mean-square (rms) displacement about the COM, $\mathbf{x}^k_{rms} = \sqrt{\sum_{i=1}^{N_k} (\mathbf{x}^k_i - \mathbf{x}^k_{com})^2 / N_k}$.

First, we examine the clouds released at 10 m depth (Figs. 3.14a,b). Typically, the clouds released over the heavy edge and the central region subduct, whereas those released at the light edge upwell. The trajectories of subducting clouds exhibit near-inertial oscillations superposed to a mean profile. Two different types of behavior can be noticed for these subducting clouds. Clouds

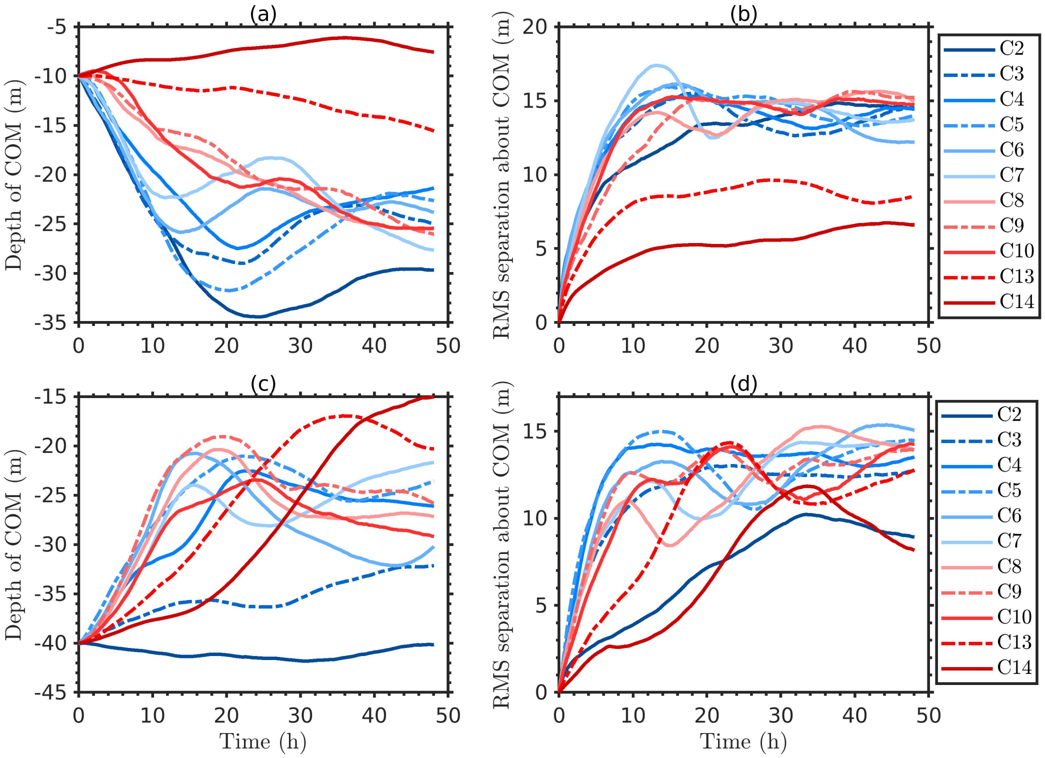

Figure 3.14: The vertical trajectories of the center of mass (COM) of the clouds released at 10 m depth (a), and 40 m depth (c). Also shown are the root-mean-square vertical displacements of constituent particles about the COM for the 10 m-depth release (b) and the 40 m-depth release (d).

C2-C7 exhibit significant vertical displacements over $1-2$ inertial time periods (inertial period is T = 12.5 h), which is followed by a slow adjustment. On the other hand, clouds C8-C10 show continuous subduction over the time considered here. Among the light-edge clouds (C13 and C14), C13 shows a weak subduction, while C14 shows upwelling. The plots of z_{rms} (Fig. 3.14b) reveal vertical spread of the particles as the clouds downwell/upwell at the front. The z_{rms} values grow over $1-2$ inertial time periods and saturate to constant values, oscillating with near-inertial frequencies. The clouds released over the heavy edge and the central region (C2-C10) saturate to $z_{rms} \approx 15\,\mathrm{m}$, and those released over the light edge (C13 and C14) saturate to $z_{rms} = 5-7\,\mathrm{m}$ indicating a more compact configuration.

In contrast, the z_{com} trajectories plotted in Fig. 3.14c for the 40 m-depth clouds show upwelling, except for C2 released at the heavy edge. An upwelling cloud typically moves upwards over $1-2$ inertial time periods to reach a peak and a slow adjustment follows subsequently. For the light-edge clouds C13 and C14, upwelling is delayed, and the peaks are reached later. The z_{com} trajectory of the heavy-edge cloud C3 reveals upwelling and that of C2 small downwelling. Similar to the 10-m-depth clouds, the particles in 40-m-depth clouds disperse vertically, as they upwell/downwell. The vertical spread of the constituent particles in the cloud z_{rms} with time is shown in Fig. 3.14d. The spread of the particles (Fig. 3.14d) in the central-region clouds (C3-C10) and the clouds immediately at the edges (C2 and C13) reaches peak values within $1-2$ inertial time periods and tends to asymptote to a constant value of about 14 m. The behavior of edge clouds (C2 and C14) is somewhat different. Since there is a time delay before the particles are put into motion by the coherent filaments, the peaks in z_{rms} develop late for C2 and C14; their long time-behavior is not clear in the present simulation.

The upwelling/downwelling of clouds, especially from the edges, over near-inertial time scales and subsequent adjustment of the constituent particles can be explained in terms of transport and organization of the particles by the coherent structures. The coherent vortex filaments associated with the heavy- and light-edges of the front draw the neighboring particles into the central region over $1-2$ inertial periods, reaching a maximum/minimum in the z_{com} trajectory, and transfer the particles to the lobes, where they adjust to the local circulation and stratification. The near-inertial time scale suggests the control of submesoscale dynamics driven by BI on the vertical transport.

3.7 Dispersion

3.7.1 Single-particle dispersion

Single-particle or absolute dispersion is the mean square displacement,

$$A^2(t) = \langle (\mathbf{x}(t) - \mathbf{x}(0))^2 \rangle, \tag{3.5}$$

where $\mathbf{x}(t) - \mathbf{x}(0)$ is the displacement of a tracer particle, and $\langle \cdot \rangle$ represents the mean taken over an ensemble of particles. Equation 3.5 can be expressed as $A^2(t) = A_x^2(t) + A_y^2(t) + A_z^2(t)$, where $A_x^2(t)$, $A_y^2(t)$ and $A_z^2(t)$ arise from the x, y and z displacements, respectively.

Unlike homogeneous isotropic turbulence, particle dispersion is anisotropic in this problem since the particles move in a stratified environment under the action of coherent structures and a mean downfront jet with vertical and lateral shear. Initially, the dispersion is ballistic so that $A_x^2(t)$, $A_y^2(t)$ and $A_z^2(t)$ in Fig. 3.15 grow as t^2. The vertical dispersion $A_z^2(t)$ starts to deviate from t^2 behavior at $t \approx 0.5\,\mathrm{h}$, when the rms vertical displacement is about $2\,\mathrm{m}$, and saturates to $O(10\,\mathrm{m})$ at late times. $A_x^2(t)$ and $A_y^2(t)$ grow as t^2 over longer time durations.

The autocorrelation functions associated with the particle's x and y velocity components (Figs. 3.13a,b) show a time scale of $\sim 10\,\mathrm{h}$ over which the functions drop below zero and become negative. In accordance with this time scale, we find that the behavior of $A_x^2(t)$ and $A_y^2(t)$ changes from t^2 when $t \approx 10\,\mathrm{h}$. Subsequently, a long-time behavior emerges after $t \approx 35\,\mathrm{h}$, which is super-diffusive in the x direction with $A_x^2(t) \sim t^\alpha$, where $\alpha > 1$, and diffusive in the y direction with $A_y^2(t) \sim t$. We calculate the exponent α using linear regression and find that its value depends on the depth at which the central-zone particles are released. The exponent varies as $\alpha = 1.3 - 1.7$ for the particles released between $10\,\mathrm{m}$ to $40\,\mathrm{m}$ depth; for the particles released at $30\,\mathrm{m}$, $\alpha \approx 1.6$. The exponent α is typically larger for the particles released at depth compared to those released near the surface. The reason is that the depth particles upwell (e.g. Fig. 3.14b) and tend to advect near the surface, where the along-front velocity is relatively larger. Therefore, the particles spread faster with respect to their initial locations and have a higher value for the exponent α. In comparison, the surface particles downwell and their along-front advection is slower, resulting in a smaller exponent α. In Fig. 3.15, the long-time dispersion behavior in x direction is compared with the nominal exponent of $\alpha = 1.5$ for the particles released at 10 m and 30 m depth.

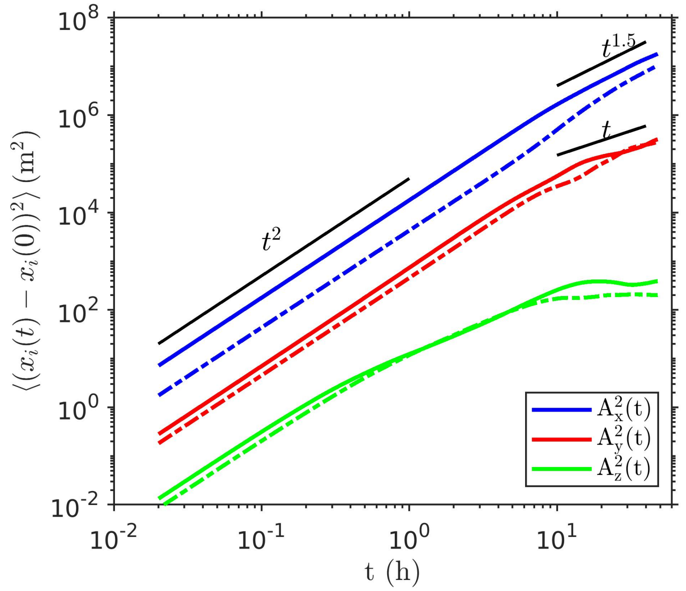

Figure 3.15: Absolute-dispersion components in x (blue), y (red) and z directions (green) plotted as a function of time for the particles released in the central region, $-500\,\mathrm{m} \leq \mathrm{y} \leq 500\,\mathrm{m}$, at 10 m (solid lines) and 30 m (dashed-dotted lines) depth.

At late times, diffusive behavior is commonly anticipated in a turbulent flow as the particle performs random walk while moving under the influence of different eddies. The observed super-diffusive behavior in $A_x^2(t)$ can be attributed to the horizontal and vertical shear of mean u. Simple stochastic models demonstrate that, in a sheared velocity field, absolute dispersion can grow as t^{α} where $1 \leq \alpha \leq 3$, and the value of the exponent α depends on the shear profile (LaCasce, 2008). For example, if mean u has a constant shear along y then the random walk by advecting particles in y exhibits dispersion with $A_x^2(t) \sim t^3$. Super-diffusive behavior has been observed in other flow configurations as well. In stratified turbulence, this behavior arises due to

$\partial u/\partial z$ in the layers between coherent pancake eddies (van Aartrijk et al., 2008).

The behavior of $A_x^2(t)$, $A_y^2(t)$, and $A_z^2(t)$ is qualitatively similar between particles released at 10 m and 30 m depth. One difference is that the initial increase of $A_x^2(t)$ is considerably faster for the particles released at 10 m depth compared to those released at 30 m depth. This behavior arises since u is strongest near the surface and decreases to zero at the bottom of the front. At late times, the dispersion curves tend to converge as the particles released at both depths become vertically dispersed, and those advecting near the surface dominate the statistics, leading to a super-diffusive growth for $A_x^2(t)$. The depth particles have a higher tendency to remain near the surface, which gives rise to a relatively faster growth at late times.

3.7.2 Particle-pair dispersion

Particle-pair or relative dispersion is the mean-square pair separation given by

$$R^2(t) = \langle (\mathbf{x}^{(1)}(t) - \mathbf{x}^{(2)}(t))^2 \rangle, \tag{3.6}$$

where $\mathbf{x}^{(1)}(t)$ and $\mathbf{x}^{(2)}(t)$ are the positions of the paired particles and $\langle \cdot \rangle$ represents the mean taken over all the selected pairs. From Eq. 3.6, $R^2(t) = R_x^2(t) + R_y^2(t) + R_z^2(t)$ with $R_x^2(t)$, $R_y^2(t)$ and $R_z^2(t)$ arising from x, y, and z separations, respectively.

The short- and long-time behaviors of $R^2(t)$ are easily understood. For short times, the difference between $\mathbf{u}^{(1)}(t)$ and $\mathbf{u}^{(2)}(t)$ is nearly constant since the particles are nearby, and $R^2(t)$ grows ballistically as t^2. On the other hand, the particles in a pair become widely separated at long times, and their uncorrelated motions lead to a long-time pair-dispersion behavior which is similar to the single-particle dispersion.

The time evolution of relative dispersion for the particle pairs released in the central region of the front ($-500\,\text{m} < \text{y} < 500\,\text{m}$) are shown in Fig. 3.16. Different pairs are considered for calculating various components – the nearest neighbors separated in y for $R_x^2(t)$, in x for $R_y^2(t)$, and both in x and y for $R_z^2(t)$.

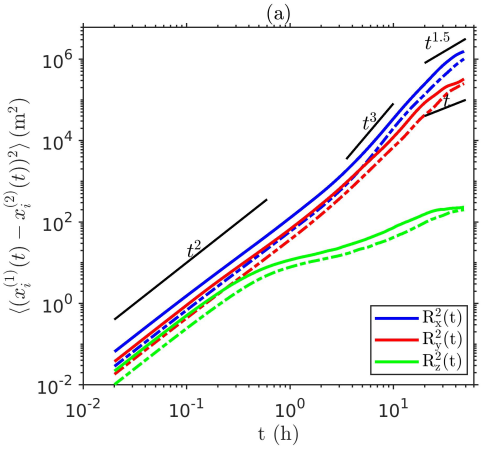

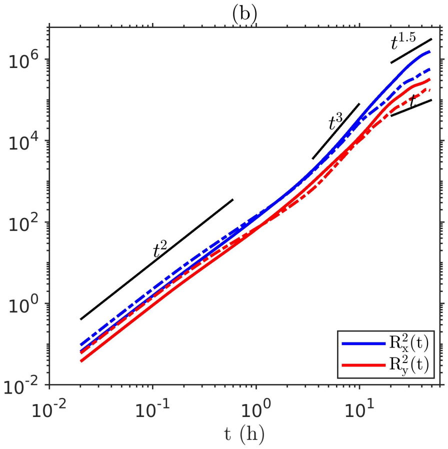

Figure 3.16: Relative-dispersion components in x (blue lines), y (red line) and z directions (green lines) plotted as a function of time: (a) pairs released at 10 m (solid lines) and 30 m (dashed-dotted lines) depth, and (b) pairs released at the surface (dashed-dotted lines) and 10 m (solid lines) depth. The z component is not plotted in panel (b) since for the surface particles $w = 0$. In both (a) and (b), only those pairs released in the central region, $-500\,\text{m} \leq \text{y} \leq 500\,\text{m}$, are considered.

Consider the particles released at 10 m depth (solid lines in Fig. 3.16a). Initially, all three components of relative dispersion grow as t^2 and, unlike absolute dispersion, have similar magnitudes. The vertical component starts to deviate from t^2 at $t \approx 0.4$ h, grows slowly, and subsequently $\sqrt{R_z^2}$ saturates at $O(10)$ m, similar to $\sqrt{A_z^2}$. The late time behavior of $R_x^2(t)$ and $R_y^2(t)$ is not apparent in Fig. 3.16a and the statistics over a longer time duration is needed. However, their behavior is expected to converge to the single-particles statistics of $A_x^2(t)$ and $A_y^2(t)$. The relative dispersion of the particle pairs released at 30 m depth behaves qualitatively similar to the pairs released at 10 m depth, and the dispersion curves follow closely for the two particle groups.

During the intermediate times, $R_x^2(t)$ and $R_y^2(t)$ exhibit t^3 growth and the rms relative displacement is $O(100)$ m, which is comparable to the width of the vortex filaments. Inertial-range turbulence with forward energy cascade displays t^3 behavior for the relative dispersion. However, there are fundamentally different flow configurations, not necessarily turbulent, that can also lead to similar dispersive behavior, e.g., shear dispersion. To further investigate the intermediate-scale dynamics, we examine the relative dispersion of the particle pairs released at the surface, where they are constrained to have $w_p = 0$. In Fig. 3.16b, interestingly, the surface pairs also exhibit t^3 growth of $R_x^2(t)$ and $R_y^2(t)$ during the intermediate times. However, the visualization of surface particles in time reveals dispersion primarily by the horizontal shear and straining in the vortex filaments, where the particles get attracted after their release. It is the energetic submesoscale rather than the turbulent finescale that controls particle dispersion. The surface pairs transition to the long-time behavior with $(R_x^2(t), R_y^2(t)) \sim t^{1.8}$ earlier than the particles released at 10 m depth. Since the front is of finite width, $R_y^2(t)$ is likely to ultimately saturate to a growth reflective of the widening of the front.

Lastly, we note that the submesoscale turbulence simulated here does not show any evidence of exponential growth for the relative dispersion components in x and y below the deformation radius, which is comparable to the diameter of the submesoscale eddies. This is consistent with the fact that the energy spectra $E(k) \sim k^{-\beta}$ in VPS19 have β in the range 2-3. For nonlocal dispersion with exponential growth of pair separation, 2D turbulent flows are required to have $\beta \geq 3$ (Bennett, 1984).

3.7.3 Multiparticle dispersion

Isotropic finescale turbulence increases the average volume of a multiparticle cluster while large-scale coherent structures can lead to the cluster's deformation into flow-specific geometries. Pumir et al. (2000) introduced a statistical measure using three or more material points to probe the geometry of Lagrangian dispersion. Here, we investigate the shape changes by tracking groups of four particles. Following Pumir et al. (2000), the geometry of a tetrad is defined by the following three vectors:

$$\mathbf{r}_1 = \frac{1}{\sqrt{2}}(\mathbf{x}_p^{(1)} - \mathbf{x}_p^{(2)}), \tag{3.7}$$

$$\mathbf{r}_2 = \frac{1}{\sqrt{6}}(2\mathbf{x}_p^{(3)} - \mathbf{x}_p^{(1)} - \mathbf{x}_p^{(2)}), \tag{3.8}$$

$$\mathbf{r}_3 = \frac{1}{\sqrt{12}}(3\mathbf{x}_p^{(4)} - \mathbf{x}_p^{(1)} - \mathbf{x}_p^{(2)} - \mathbf{x}_p^{(3)}), \tag{3.9}$$

where $\mathbf{x}_p^{(i)}$ with $i = 1, 2, 3, 4$, are the position vectors of the four particles at the vertices of a tetrahedron. The radius of gyration of the cluster is $R^2 = \sum_{i=1}^{3} \mathbf{r}_i^2$ and measures the spatial extent of the tetrad. The vectors involving position differences are combined into a second order tensor

$$\mathbf{g} = \mathbf{r}\mathbf{r}^t, \tag{3.10}$$

where $\mathbf{r} = [\mathbf{r}_1, \mathbf{r}_2, \mathbf{r}_3]$ is a second order tensor with $\mathbf{r}_1$, $\mathbf{r}_2$, and $\mathbf{r}_3$ as its column vectors. The eigenvalues of $\mathbf{g}$ ($g_1 > g_2 > g_3$) characterize the cluster shape. For example, $g_1 = g_2 = g_3$ corresponds to an isotropic object, $g_1 \approx g_2 \gg g_3$ to a pancake-like object with vertical scale much smaller than horizontal, and $g_1 \gg g_2, g_3$ to a needle-like object. To compare the shapes at different times, the eigenvalues are normalized by the radius of gyration $R^2 = \mathrm{Trace}(\mathbf{g})$ and denoted by $I_i = g_i/R^2$. The multiparticle statistical measure described above has been used to study cluster shape behavior in homogeneous isotropic turbulence and stably stratified homogeneous turbulence. The present study is an application to a flow with submesoscale currents.

For the multiparticle study, two additional particles were added for each node of the particle lattice at 10 m and 30 m depth. A tetrad was formed with the nodal particle, the two added particles, and the particle above in the original lattice. The construction of tetrads is illustrated in the inset of Fig. 3.17a and further described in the figure caption. The multiparticle statistics are calculated using tetrads released in the central region $-500\,\mathrm{m} < \mathrm{y} < 500\,\mathrm{m}$.

The normalized eigenvalues I_1, I_2 and I_3, averaged over the tetrads, are plotted as a

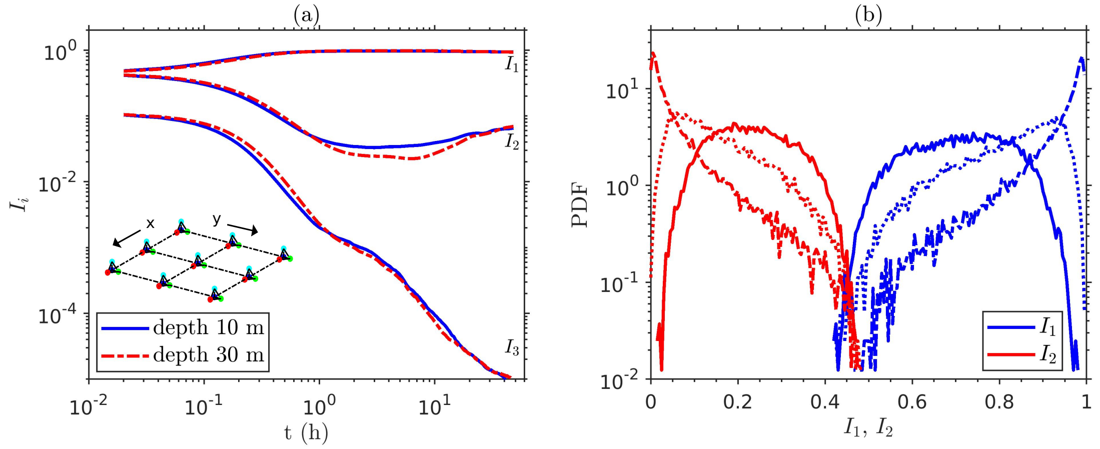

Figure 3.17: The distortion in the shape of tetrad particle clusters. (a) Normalized eigenvalues I_1, I_2, and I_3 as a function of time. (b) PDFs of I_1 and I_2 at different times after the release of the clusters: $t = 20\,\text{min}$, solid lines; $t = 40\,\text{min}$, dotted lines; $t = 1.2\,\text{h}$, dotted-dashed lines. In the inset of panel (a), the construction of tetrads is illustrated over a small patch of the horizontal domain. Each tetrad is composed of four particles: a node particle at the base-level (10 m or 30 m depth), a particle displaced by 2 m in the x-direction, a particle displaced by 2 m in the y-direction, and a fourth particle from the lattice one level above, i.e., 2 m above the base level.

function of time in Fig. 3.17a. The tetrads rapidly deform into flattened, needle-like objects within an hour after release as $\langle I_2 \rangle$, $\langle I_3 \rangle \approx 0$ and $\langle I_1 \rangle \approx 1$. Subsequently, $\langle I_2 \rangle$ plateaus during $t = 1 - 10\,\text{h}$ and increases slightly at late times but always remains $\ll \langle I_1 \rangle$. On the other hand, $\langle I_3 \rangle$ continues to drop. The fast $O(1\,\text{h})$ time scale of the initial distortion is consistent with the relative dispersion R_z^2 in Fig. 3.16, which commences to flatten at about 1 h and saturates by about 20 h.

Although the average I_1, I_2 and I_3 show the predominance of needle-like objects by $t \approx 1\,\text{h}$, other shapes may also be present after the release of the tetrads. The PDFs of I_1 and I_2 in Fig. 3.17b show the shape distribution at different times. Within $t = 20\,\text{min}$, the peak in the PDF of I_1 shifts to a value greater than 0.5 and that of I_2 to a value smaller than 0.5. However, there are tetrads that can be considered pancake-like. After $t = 40\,\text{min}$, distinct peaks appear for I_1 and I_2 close to 0.9 and 0.1, respectively. As time progresses, the peak at 0.9 moves towards 1 and that at 0.1 moves towards 0. Most of the clusters deform into primarily flat, needle-like objects by $t = 1.2\,\mathrm{h}$ and remain so at late times. Visualization reveals that particles are attracted to the coherent filaments after they are released. The high strain rates found in the filaments and at the outer edges of the submesoscale eddies act on the clusters to deform them into needle-like objects.

The overall long-time shape distribution observed in the present problem with submesoscale currents and the finescale organized in vortex filaments can be compared with that in other turbulent flows. In homogeneous and isotropic turbulence, the uncorrelated long-time motions of the particles leads to $\langle I_1 \rangle_G \approx 0.748$, $\langle I_2 \rangle_G \approx 0.222$ and $\langle I_3 \rangle_G \approx 0.03$. The small value of $\langle I_3 \rangle_G$ compared to $\langle I_1 \rangle_G$ and $\langle I_2 \rangle_G$ suggests that the shapes are dominated by flat objects (Biferale et al., 2005, Pumir et al., 2000). In stratified turbulence, van Aartrijk et al. (2008) found that $\langle I_1 \rangle$ becomes larger and $\langle I_2 \rangle$ smaller as stratification grows stronger. In their study with strong stratification (N100 with $N = 0.98\,\mathrm{s}^{-1}$) the shapes overall were needle-like, but the shape distribution examined by plotting the PDFs of I_1 and I_2 revealed the presence of a significant number of flat objects. In the present work, the PDFs of I_1 and I_2 shows that most of the tetrads are deformed into needle-shaped objects.

3.8 Discussion and conclusions

We investigate material transport and dispersion by submesoscale turbulent currents generated during the evolution of baroclinic instability at an upper-ocean front. The study employs a LES model and is performed in the Lagrangian framework by releasing a large number of tracer particles that move with the local fluid velocity. The presence of coherent structures is a typical feature of submesoscale dynamics. From the Lagrangian analysis, we elucidate how these structures provide the primary pathways for the three-dimensional transport by submesoscale currents and provide a quantitative assessment of time/space scales of Lagrangian motion.

The coherent particle motion is mediated by a filament/eddy/lobe framework. Particles experience rapid vertical motions with displacements of $O(10\,\mathrm{m})$ over an hour in the filaments, as well as slower motions at near-inertial time scales while moving under the influence of coherent eddies and lobes. It is possible to identify some common features that dictate the overall transport. The central-region particles cluster into inclined lobes, each associated with a coherent eddy. The lateral and vertical velocity of these particles reveals a clockwise circulation when viewed from above, which is opposite to the cyclonic circulation induced by the coherent central-zone eddies. Moreover, the vortex filaments connect the heavy and light edges of the front with the central region and play a critical role in vertical and lateral transport and the restratification of the front. The process can be described as follows. The coherent filaments draw the edge particles into the central region and transfer them to the lobes – heavy-edge particles to the undersides and the light-edge particles to the top layers – conforming to the local stratification. The flux of new edge-particles into the central region causes the central-region particles to adjust, which leads the front to restratify. A significant portion of the restratification is accomplished by 100 h, which is slower than the $O(10\,\mathrm{h})$ suggested by the events of significant downwelling with $w_p = 10^{-3}\,\mathrm{ms}^{-1}$ but consistent with the average downwelling speed of $w_p = 10^{-4}\,\mathrm{ms}^{-1}$.

We find that the lateral (v_p) and vertical (w_p) velocity of the particles moving through filaments and circulating in lobes have a near-inertial time scale of $O(2\pi/f)$ and have a correlation which is consistent with the lateral buoyancy gradient. For the present case where the cross-front density gradient is negative, the correlation is also negative. The centers of mass z_{com} of particle clouds subduct/upwell through the vortex filaments over $1-2$ inertial time periods and a slow adjustment follows after the particles are accommodated in the lobes. The root-mean-square vertical displacement (z_{rms}) of the constituent particles with respect to the COM saturates to $\sim 14-15\,\mathrm{m}$.

Lagrangian energy spectra show considerably more subinertial and inertial energy in the horizontal relative to the vertical, but for super-inertial $\omega_f \geq 10f$ the components are comparable. Further, the Lagrangian autocorrelation functions of u_p and v_p exhibits oscillatory decay with a subinertial time scale with the oscillations reflecting circulation within submesoscale eddies and lobes. The vertical velocity component shows a fast timescale ($\sim 1\,\mathrm{h}$) decorrelation corresponding to the turbulent finescale as well as a subinertial oscillatory modulation. The observed subinertial timescales are consistent with the timescale of the growth of baroclinic instability.

The process of restratification in the present model front under BI is considerably different than the restratification process depicted in Spall (1995), which assumes sliding of a fluid parcel from the heavy side of the front across to the light side. In contrast, the process described here is three-dimensional and involves continuous stirring of the central-region fluid by submesoscale coherent eddies and the injection of edge particles into the central region by the coherent vortex filaments. Thus, after being subducted, a heavy-edge fluid parcel continues to move under the influence of the eddies at the front.

We also find that the vertical distribution of the particles released at a depth remains confined within $\sim 50\,\mathrm{m}$ depth from the surface over time, which is also the initial depth of the front. As shown in VPS19, the vertical velocity in the thermocline is non-zero, but the particles do not subduct below the surface layer. This behavior correlates with the fact that coherent structures control the vertical transport of the particles at the front. Since these structures are contained within the front, so are the particles. Vertical transport below the mixed layer is possible with deeper fronts, e.g., in observations of subduction of particulate organic matter by Omand et al. (2015), the simulations of Gula et al. (2014) which show deep penetrating cold filaments and the simulations of Balwada et al. (2018) which show that permitting the submesoscale enhances the transport of tracers below the mixing layer. Taylor et al. (2020) find a modest increase of particle concentration below the mixed layer but their model has important differences with the present model, e.g., the use of an advective-diffusion equation for concentration instead of Lagrangian tracers and convective forcing at the surface.

The near-inertial oscillations observed here can be contrasted with the inertial oscillations associated with the geostrophic adjustment of an initially unbalanced (fully or partial) front analyzed by Tandon and Garrett (1994). In this system, inertial oscillations are generated when the unbalanced front tries to slump by releasing potential energy, but the Coriolis force acts on the developed velocity field and provides a restoring tendency towards the original configuration. Tandon and Garrett (1994) find that the oscillatory adjustment continues at inertial time scale and, due to the lack of dissipation in their simplified model, the system does not return to a stable stationary state. In LES of an initially balanced upper-ocean front, unstable to symmetric instabilities, Skyllingstad and Samelson (2020) observe inertial oscillations when the geostrophic shear is disrupted due to surface wind or buoyancy forcing. However, the inertial currents are short lived and subside owing to vertical mixing and the onset of baroclinic instability. In contrast, the near-inertial oscillations in the present simulation result primarily from the circulation of the particles within the lobes and eddies. Furthermore, the dynamics here are driven by BI.

The dispersion characteristics of the turbulent submesoscale currents have been studied. In both single- and pair-particle dispersion, the vertical component is restricted by the front depth and the rms of vertical displacement saturates to $O(10\,\mathrm{m})$ at long times. The along-front component of single-particle dispersion shows super-diffusive behavior at late times, and the mean-square displacement increases as t^{α} with $\alpha = 1.5 \pm 0.2$; the exponent α is typically larger for the particle released at depth compared to those released near the surface. The observed super-diffusive behavior for the along-front component can be related to the mean frontal jet with horizontal and vertical shear. The particle-pair dispersion in x and y directions show t^3 behavior at intermediate times when the rms displacement is $O(100\,\mathrm{m})$, which is comparable to the lateral width of the vortex filaments. Although t^3 behavior is consistent with a Kolmogorovian inertial range, the role of horizontal shear on relative dispersion cannot be ruled out. The long-time behavior of particle pairs is consistent with single-particle dispersion. The multiparticle analysis reveals strong filamentogenesis, as the tetrads deform into a thin, needle-like mean shape within a short time scale of $O(1\,\mathrm{h})$. Probability density functions of shape metrics indicate that there is a strong propensity to form needle-shaped structures, more so than in homogeneous stratified turbulence. The filamentogenesis is associated with the strong strain field within the coherent vortex filaments in the evolving submesoscale front.

Acknowledgments

This chapter, in full, is a reprint of material under review for publication as follows: V. Verma and S. Sarkar, “Lagrangian three-dimensional transport and dispersion by submesoscale currents at an upper-ocean front,” *Ocean Model.*, 2021. The dissertation author is the primary investigator and author of this work. I am pleased to acknowledge the support of ONR grant N00014-18-1-2137.

Chapter 4

Interaction between upper-ocean submesoscale currents and convective turbulence

4.1 Introduction

The upper-ocean with widespread fronts and filaments provide a conducive environment for the generation of quasi-2D submesoscale dynamics, which tend to restratify the mixed layer by laterally sliding the light water over the dense water. The restratification releases the potential energy stored in the front and energizes the submesoscale motions. The upper ocean is also a host of finescale 3D turbulence, driven by surface forcing such as wind, waves, and cooling, responsible for mixing and homogenizing the surface layer. The two dynamical regimes thus have opposing tendencies but, acting together, dictate the upper ocean properties through which the interior ocean and the atmosphere interact. This, in turn, has profound implications for the ocean's biochemistry and Earth's climate system. The large-scale ocean models can not resolve these processes, and their effects need to be parameterized appropriately (Fox-Kemper et al., 2008, Large et al., 1994). It is unclear as to what extent the interaction would change their intrinsic dynamics or if the existing parameterizations would successfully capture those changes. A detailed understanding of this interaction is therefore required.

Baroclinic instability growing at upper-ocean fronts, also known as mixed layer instability (MLI), is one of the dominant mechanisms for generating submesoscale dynamics, occurring in the horizontal length scale range of 0.1 - 10 km and the time scale of the order of one day (Boccaletti et al., 2007, Capet et al., 2008a, McWilliams, 2016, Thomas et al., 2008). Observations and models have revealed some interesting features of the dynamics (D'Asaro et al., 2018, Ozgokmen et al., 2011, Shcherbina et al., 2013, Stamper and Taylor, 2017, Verma et al., 2019). The dynamics remain largely balanced, but include thin ($O(100\,\mathrm{m})$) convergent filaments with significant local imbalance and large vertical vorticity ($\omega_z/f > 1$) and vertical velocity. Moreover, the filament roll-ups lead to the generation of coherent submesoscale eddies at the front. Frontogenesis, the process which rapidly sharpens the lateral density gradients and the associated horizontal velocity gradients, is an important feature of the submesoscale dynamics (Barkan et al., 2019, McWilliams, 2021) responsible for generating the coherent filaments (Verma et al., 2019). The frontogenesis mechanism, however, is not unique. The straining of a front by large-scale currents is a classic problem that leads to frontogenesis (Hoskins and Bretherton, 1972); secondary ageostrophic circulations resulting from the interaction between a cold filament and boundary layer turbulence, as well as strong down-front winds also lead to frontogenesis (McWilliams et al., 2015, Sullivan and McWilliams, 2018, Thomas and Lee, 2005). Numerical models identify frontogenesis to play a crucial role in the vertical transport of surface water to the interior (Freilich and Mahadevan, 2021, Spall, 1995). Typically, the coherent structures generated by upper-ocean fronts remain confined within its depth, but deep-reaching fronts and structures observed in recent models and field experiments suggest that these structures can also be important for the material transport in the ocean interior (e.g. Balwada et al., 2018, Siegelman et al., 2020). Despite their significant role in transport, the way these structures respond to the boundary layer turbulence is not fully understood.

The turbulence resolving models exhibit strong interaction and multiscale energy exchanges between the submesoscale and the finescale regimes (Callies and Ferrari, 2018, Hamlington et al., 2014, Skyllingstad and Samelson, 2020, Whitt and Taylor, 2017). The present study aims to investigate how surface cooling can influence the energy interaction between these two regimes, especially the extraction of submesoscale kinetic energy by the turbulent convection. The surface forcing such as wind and cooling extracts potential vorticity from the front that may assist the growth of secondary instabilities (Thomas et al., 2013). Can these instabilities also suppress baroclinic instability and to what extent is unclear? There are observations which find the evidence of forced symmetric instability (SI) in the front, likely due to the downfront wind in the region (D'Asaro et al., 2011, Ramachandran et al., 2018). However, numerical models with strong winds and surface cooling indicate persistence of MLI, which maintains a stable stratification even in the presence of strong boundary layer turbulence (Callies and Ferrari, 2018, Haine and Marshall, 1998, Hamlington et al., 2014, Skyllingstad and Samelson, 2020, Whitt and Taylor, 2017). These findings are in contrast to the large eddy simulations of Sullivan and McWilliams (2018), where they observe a cold filament to restratify within hours due to the interaction with the boundary layer turbulence, even before baroclinic mixed layer instability could develop to become finite amplitude. Typically, an SI unstable system develops marginal stability once the forcing is stopped (Arobone and Sarkar, 2015, Taylor and Ferrari, 2009).

In the present study, we impose surface cooling fluxes of different magnitudes to generate convective turbulence of varying strengths. Turbulence develops through gravitational instability, which in a 1D stratified fluid column gives rise to plume structures that drive a vertical buoyancy flux in response and create a mixing layer. Convective plumes also entrain cold fluid from below the mixing layer, thereby deepening the layer (Deardorff, 1980, Fedorovich et al., 2004). The plumes typically have horizontal scales comparable to the vertical and have a characteristic velocity scale of $(B_sH)^{1/3}$, where B_s is the surface buoyancy flux and H is the depth of the mixing layer (Deardorff, 1980). Thus, turbulent kinetic energy depends on both B_s and H in convection and becomes more energetic as the mixing layer grows. However, at upper-ocean fronts with evolving submesoscale dynamics, a coupling with convection is possible through one or a combination of interactions that can influence the dynamics at both regimes. First, the submesoscale currents can restratify the fluid column and suppress the growth of convective plumes, thereby restricting the mixing layer from deepening. The submesoscale coherent structures are likely to influence this interaction, as they create inhomogeneity within the front with flow properties varying considerably between the coherent structures and the rest of the front. Second, convective turbulence can mix away the vertical gradient of thermal wind, disrupt the balance, and modify the submesoscale dynamics. It is possible that strong convection mixes all the vertically sheared thermal wind velocity, completely suppressing the submesoscale dynamics. Third, convective turbulence can also fundamentally alter submesoscale dynamics by enhancing horizontal mixing and weakening the submesoscale frontogenesis. Fourth, surface cooling can enable conditions for the growth forced instabilities, such as SI, by extracting potential vorticity from the front. An outstanding question has been whether these instabilities suppress MLI, or they coexist together.

A suitable framework that decomposes the flow into submesoscale and finescale components is needed to address the coupling between the two components. We adopt here the approach of Verma et al. (2019) for the flow decomposition using a 2D $(x-y)$ low-pass filter and explicitly investigate the interaction between submesoscale dynamics and the finescale convection. In Verma et al. (2019), the finescales were generated by the growing MLI and were confined in vortex filaments and the peripheries of eddies. However, the simulations discussed here have expansive finescales originating from the uniformly applied surface cooling. Further, the strength of the finescale convection can be modulated, independent of MLI, through the applied surface cooling magnitude.

The problem of baroclinic mixed layer instability growing with convection has been previously dealt by Whitt and Taylor (2017) and Callies and Ferrari (2018), using an idealized Eady model. We summarize their results to help interpret ours wherever possible. Whitt and Taylor (2017) investigated the effect of a storm on submesoscale dynamics. They showed that during the passing of the storm, the domain remains stratified in patches, suggesting the persistence of submesoscale dynamics. Both submesoscales as well as finescales became energized; however, it is unclear if the submesoscale energization is due to the wind or the modified submesoscale dynamics. Contrary to this finding, they observed a decrease in the submesoscale kinetic energy when a time dependent surface buoyancy flux was applied, replicating the Ekman buoyancy flux generated by the storm. Callies and Ferrari (2018) studied the growth of baroclinic instability with convection by changing the imposed cooling/heating fluxes at the surface/bottom over two order of magnitudes. They observed that MLI grows in all cases and eventually a domain filling eddy persists with convective plumes. In cases with weak surface cooling, submesoscale dynamics appear to shut off convection, and the front remains stratified with positive potential vorticity over much of the vertical domain. With moderate cooling, slantwise convection is expected since the horizontally-averaged stratification remains non-zero, but potential vorticity becomes zero. When the strength of surface cooling is further increased, the plumes become more upright, and stratification becomes vanishingly small. In this paper, we expand on the studies of Whitt and Taylor (2017) and Callies and Ferrari (2018) and investigate the interaction between submesoscale dynamics and finescale convection explicitly, utilizing their energy budgets.

This paper is organized as follows. In section 4.2, the setup of model warm filament with edge fronts is described, and the methodologies used to study the interaction between the submesoscale and the finescale are elaborated. The flow evolution prior to applying the surface cooling fluxes is also discussed, and a length scale is identify for decomposing the flow into the submesoscale and finescale components after convection sets in the domain. The effect of submesoscale dynamics on convection is analyzed in section 4.4. In section 4.5, the changes in the submesoscale dynamics is discussed and the imbalance at the front is quantified. The coupling between the two dynamical regimes is further investigated by examining the kinetic energy and potential energy balance equations at both scales in section 4.6. The effect of finescales on submesoscale frontogenesis is also examined. In section 4.7, the development of secondary instabilities is elaborated by analyzing PV, Richardson number, and Rossby number within the front, and their role in the extraction of energy from submesoscale velocity is examined. Finally, we conclude based on our results and discuss their implications in section 4.8.

4.2 Problem formulation and methods

4.2.1 Model setup

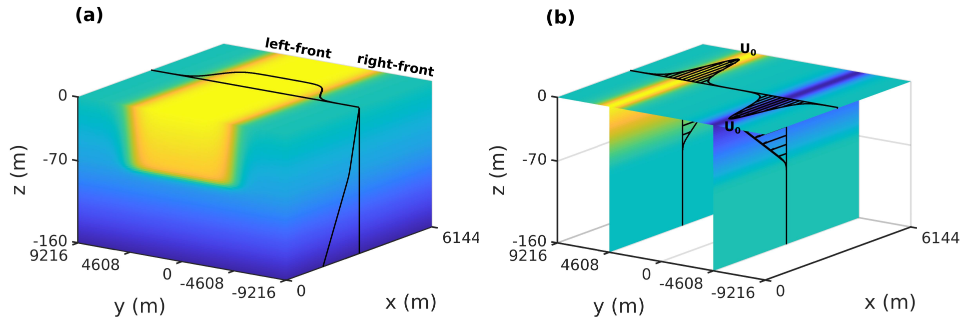

Figure 4.1: Model front: (a) initial temperature and (b) initial thermal-wind velocity.

We use the model setup (Fig. 4.1) of a warm filament in a weakly stratified upper layer overlaying a strongly stratified thermocline. The warm filament is aligned in the x direction with temperature varying in the lateral (y) and vertical (z) directions. The density (ρ) and temperature (T) deviations from reference values are related by $\rho/\rho_0 = \alpha T$. The initial temperature profile is constructed by joining two profiles given by

$$\text{for } y<0, \quad T^{<}(y,z) = -\frac{M_0^2 L}{\alpha g}\left[1-0.25\left(1+\tanh\left(\frac{y-Y_0}{0.5L}\right)\right)\left(1+\tanh\left(\frac{z+H}{\delta_h}\right)\right)\right] + \frac{0.5}{\alpha g}\left[(N_M^2+N_T^2)z+\delta_H(N_M^2-N_T^2)\log\left(\frac{\cosh((z+H)/\delta_H)}{\cosh(H/\delta_H)}\right)\right], \quad (4.1)$$

$$\text{for } y>0, \quad T^{>}(y,z) = -\frac{M_0^2 L}{\alpha g}\left[1-0.25\left(1-\tanh\left(\frac{y-Y_0}{0.5L}\right)\right)\left(1+\tanh\left(\frac{z+H}{\delta_h}\right)\right)\right] + \frac{0.5}{\alpha g}\left[(N_M^2+N_T^2)z+\delta_H(N_M^2-N_T^2)\log\left(\frac{\cosh((z+H)/\delta_H)}{\cosh(H/\delta_H)}\right)\right]. \tag{4.2}$$

The temperature profile $T(y,z)$ is symmetric in y coordinate as $T^{>}(y,z) = T^{<}(-y,z)$, and there are two fronts: a right front centered at $y = -Y_0$ and a left front centered at $y = Y_0 = 4608\,\mathrm{m}$. The width of each front is $L = 2\,\mathrm{km}$, the thickness of the upper layer containing the front is $H = 70\,\mathrm{m}$, and $\delta_H = 5\,\mathrm{m}$ controls the thickness of the transition layer between the upper layer and the thermocline. The weakly stratified upper layer and the pycnocline have square of buoyancy frequency $N_M^2 = 5.0\times10^{-7}\,\mathrm{s^{-2}}$ and $N_T^2 = 1.0\times10^{-4}\,\mathrm{s^{-2}}$, respectively. The lateral density gradient described by $M^2 = -(g/\rho_0)(\partial\rho/\partial y)$ varies laterally and has a peak magnitude of $M_0^2 = 6.0\times10^{-8}\,\mathrm{s^{-2}}$ at the centerlines $y = \pm Y_0$ of the two fronts

The fronts are initialized to be in thermal wind balance and the along-front (x) velocity is calculated using the relation $\partial U/\partial z = -M^2/f$, where $f = 8.62\times10^{-5}\,\mathrm{s^{-1}}$ is the Coriolis parameter. The frontal jet has the peak speed of $U_0 = M_0^2 H/f = 0.05\,\mathrm{m\,s^{-1}}$ at the the surface and the center of each front. Moreover, 3D broadband noise with amplitude $5\times10^{-4}\,\mathrm{m\,s^{-1}}$ is added to trigger instabilities of the system. Key nondimensional parameters at the center of each front are as follows: Richardson number $Ri_0 \equiv N_M^2 f^2/M_0^4 = 1$, frontal strength $M_0^2/f^2 = 8$ and Rossby number $Ro \equiv U_0/fL = 0.3$.

Table 4.1: The list of parameters for different cases.

	$Q_s\,(\mathrm{W\,m^{-2}})$	$B_s\,(\mathrm{m^2\,s^{-3}})$	$r = B_s/B_f$	$\tilde{r} = B_s/(0.06B_f)$
Qs5	5	2.4×10^{-9}	0.012	0.2
Qs15	15	7.2×10^{-9}	0.035	0.6
Qs25	25	1.2×10^{-8}	0.059	1.0
Qs40	40	1.9×10^{-8}	0.094	1.5

The magnitude of the surface cooling flux (Q_s) is varied in a parametric study with four cases: $Q_s = 5$, 15, 25, and $40\,\mathrm{W\,m^{-2}}$. Before application of the cooling, the front is allowed to evolve until the surface layer develops multiscale variability at the submesoscale. Cooling is initiated at $t = 231\,\mathrm{h}$ when multiple coherent structures representative of MLI have formed. The surface buoyancy flux (B_s) introduced by cooling competes with the restratifying vertical buoyancy flux of the submesoscale currents which has been parameterized by Fox-Kemper et al. (2008) as $C_e B_f$, where the dimensional group is $B_f = M_0^4 H^2/f$ and the efficiency factor is $C_e = 0.06$. The relative strength of cooling can be measured by the ratio $r = B_s/B_f$ (Callies and Ferrari, 2018) or, equivalently, $\tilde{r}$ with $C_\varepsilon B_f$ (Mahadevan et al., 2010, Whitt and Taylor, 2017) in the denominator. As shown in Table 4.1, the value of r varies from 0.01 to 0.1 and the ratio $\tilde{r}$ from 0.2 to 1.5. Thus, based on $\tilde{r}$, the simulations span the regimes of weak to moderate ($\tilde{r} = O(1)$) convection but not those with very strong convection ($\tilde{r} \gg O(1)$). The transient evolution is studied for about 25 h after cooling, which is sufficient to encompass a night of cooling as well as an inertial period.

We employ a large-eddy simulation (LES) model (Pham and Sarkar, 2018, Verma et al., 2019) to numerically solve the following incompressible, nonhydrostatic, Boussinesq Navier-Stokes equations for the velocity u_i, the temperature T, and the dynamic pressure p:

$$\frac{\partial u_j}{\partial x_j} = 0, \tag{4.3}$$

$$\frac{\partial u_i}{\partial t} + \frac{\partial u_i u_j}{\partial x_j} + \varepsilon_{ijk} f_j u_k = -\frac{1}{\rho_0}\frac{\partial p}{\partial x_i} + \alpha T g \delta_{i3} - \frac{\partial \tau_{ij}}{\partial x_j}, \tag{4.4}$$

$$\frac{\partial T}{\partial t} + \frac{\partial u_j T}{\partial x_j} = -\frac{\partial q_j}{\partial x_j}. \tag{4.5}$$

The stress tensor (τ_{ij}) and the heat flux (q_j) include subgrid and molecular components. The subgrid viscosity (ν^{sgs}) is parameterized following Ducros et al. (1996) and the turbulent Prandtl number $Pr^{sgs} \equiv \nu^{sgs}/\kappa^{sgs} = 1$ sets the subgrid diffusivity (κ^{sgs}). The molecular viscosity is $\nu = 10^{-6}\,\mathrm{m^2 s^{-1}}$, and the molecular Prandtl number $Pr \equiv \nu/\kappa = 7$. The governing equations are advanced in time using a mixed third-order Runge-Kutta (for advective fluxes) and Crank-Nicolson (for diffusive fluxes) scheme. Second-order finite difference discretization is used to compute spatial derivatives. The dynamic pressure is obtained by solving the Poisson equation with a multi-grid iterative method.

The computational domain of $6147\,\mathrm{m} \times 18435\,\mathrm{m} \times 161\,\mathrm{m}$ is discretized in the horizontal using 2050×6146 grid points with $\Delta x = \Delta y = 3\,\mathrm{m}$, and in the vertical using 98 grid points where Δz varies from $1\,\mathrm{m}$ at the surface to $1.69\,\mathrm{m}$ at the bottom of the warm filament. The horizontal directions are periodic. The bottom boundary is a free-slip wall and has a constant heat flux which maintains the thermocline temperature gradient. The free-slip surface has a specified heat flux.

4.2.2 Submesoscale (SMS) - finescale (FS) decomposition

For investigating the interaction between small-scale convective turbulence and larger-scale submesoscale currents, we separate the two contributions by the decomposition, $\phi = \bar{\phi} + \phi''$, where $\bar{\phi}$ is the submesoscale (SMS) component and ϕ'' is the finescale (FS) component of a field variable ϕ. Following Verma et al. (2019), which can be consulted for the details, $\bar{\phi}$ is obtained by applying a two-dimensional (x-y) Lanczos filter to ϕ and the finescale is the remainder $\phi'' = \phi - \bar{\phi}$. The Lanczos filter, although implemented in physical space, provides a relatively sharp cutoff in spectral space. The cutoff wavenumber (k_c) chosen for the filter corresponds to a change in the slope of energy spectra (discussed later in section 4.3) from quasi-2D to 3D behavior. Note that, if desired, the SMS field $\bar{\phi}$ can be further averaged along the front (x) and the deviation of $\bar{\phi}$ from $\langle\bar{\phi}\rangle_x$ can be obtained as an 'eddy' component.

In later sections, we will quantitatively examine energy transfers to and between convective turbulence and the submesoscale flow. To do so, equations governing the submesoscale and finescale derived in the appendix of this paper are utilized. The SMS equations are obtained by applying the homogeneous filter function to the Navier-Stokes equations. Filtering gives rise to new terms in the SMS equations: the residual stress $\tau_{ij}^R = \overline{u_i u_j} - \overline{u}_i \overline{u}_j$ in the momentum equation and the residual flux $q_j^R = \overline{u_j T} - \overline{u}_j \overline{T}$ in the temperature equation. In the FS equations, the residual stress and residual heat flux appear with signs opposite to those in the SMS equations. The residual stress and residual heat flux are responsible for energy transfers between SMS and

FS fields.

The kinetic energy (KE) and potential energy (PE) reservoirs at the front and the applied surface buoyancy flux (B_s) feed energy into the flow instabilities and there are energy transfers between the SMS and FS. We will discuss the energy pathways in section 4.6 by the quantification of the KE and PE evolution equations for the two scales. The evolution equation for the submesoscale KE ($\bar{E}_k = \bar{u}_i\bar{u}_i/2$) is obtained from the submesoscale momentum equation (Eq. 2.11) by multiplying it with $\overline{u}_i$ and is given by

$$\frac{\partial}{\partial t}\bar{E}_k = -\frac{\partial \overline{T}_j}{\partial x_j} + \overline{B} - \mathcal{P}^R - \overline{\mathcal{E}}. \tag{4.6}$$

The slumping of the front feeds submesoscale KE through the buoyancy production ($\overline{B} = \bar{b}\bar{w}$). Submesoscale velocity gradients act on the finescale through $\mathcal{P}^R = -\tau^R_{ij}(\partial\bar{u}_i/\partial x_j)$ to act as a production term for the finescale KE (in Chapter 2, $\mathcal{P}^R$ was denoted by $\mathcal{E}^R$). Energy is dissipated by $\overline{\mathcal{E}} = -\bar{\tau}_{ij}(\partial\bar{u}_i/\partial x_j)$, which includes both molecular and subgrid contributions. The transport term ($\overline{T}_j$), which redistributes energy in physical space, has contributions from advection, pressure, diffusion and the residual stress.

Similarly, the following balance equation for the finescale KE ($E''_k = u''_i u''_i/2$) is obtained,

$$\frac{\partial}{\partial t}\frac{u''_i u''_i}{2} = -\frac{\partial T''_j}{\partial x_j} + Tr + B'' + \mathcal{P}''^R - \mathcal{E}''. \tag{4.7}$$

We will show that, overall, the finescale velocity is energized by the submesoscale motions through the transfer ($Tr = -u''_i u''_j(\partial\bar{u}_i/\partial x_j)$) which represents the action of submesoscale velocity gradients on finescales. There is also self-generation of the finescale by the residual-stress production ($\mathcal{P}''^R = -\tau^R_{ij}(\partial u''_i/\partial x_j)$) which represents the action of the finescale velocity gradients on the resolved stress. Note that in Chapter 2, $\mathcal{P}''^R$ was denoted by $-\mathcal{E}''^R$. The finescale buoyancy production ($B'' = b''w''$) will be shown to be an additional third source which becomes increasingly important as surface cooling increases. The dissipation ($\mathcal{E}'' = -\tau''_{ij}(\partial u''_i/\partial x_j)$) is a sink and the transport term (T_j'') spatially redistributes the finescale KE.

MLI leading to submesoscale currents is energized through the stored available potential energy (PE) in the front, and there is PE input by the applied surface cooling flux which will be shown to energize the finescale within the front. Therefore, it is useful to consider the balance of PE defined by $E_p = -zb$, where $b = \alpha g T$ is the buoyancy. Employing the equation for submesoscale temperature, the balance of submesoscale PE ($\overline{E}_p = -z\bar{b}$) is derived to be

$$\frac{\partial \overline{E}_p}{\partial t} + \frac{\partial \bar{u}_j \overline{E}_p}{\partial x_j} = -\bar{B} + \alpha g z \left(\frac{\partial \bar{q}_j}{\partial x_j} - \frac{\partial q_j^R}{\partial x_j} \right) . \tag{4.8}$$

The SMS vertical buoyancy flux ($\bar{B} = \bar{b}\bar{w}$) is a sink for the submesoscale PE and a source for the submesoscale KE where it appears with the opposite sign. The divergence of diffusive and residual heat flux (last two terms on the right) changes buoyancy and thereby PE. The balance is completed by tendency (first term on left) and advection (second term on left).

The finescale contribution to the PE is $-zb''$. The horizontal average of $-zb''$ is close to zero and, besides, it will be seen that diagnostics of the submesoscale PE is sufficient to understand the energization of the SMS and FS velocity. Therefore, we do not further consider $-zb''$.

4.2.3 Evolution prior to cooling

The simulation is run without surface cooling flux in the beginning, allowing baroclinic MLI at the fronts to evolve into its nonlinear stage. The evolution is similar at the two fronts, one at each edge of the warm filament. Therefore, we discuss only the right front in the result to follow. Prior to surface cooling, the front evolves as in other previous idealized studies of upper-ocean fronts. As MLI grows, the front meanders and develops vortex filaments with concentrated vertical vorticity. Further, the vortex filaments merge and grow in length as the instability progresses. Subsequently, the long filaments, comparable in length to the wavelength

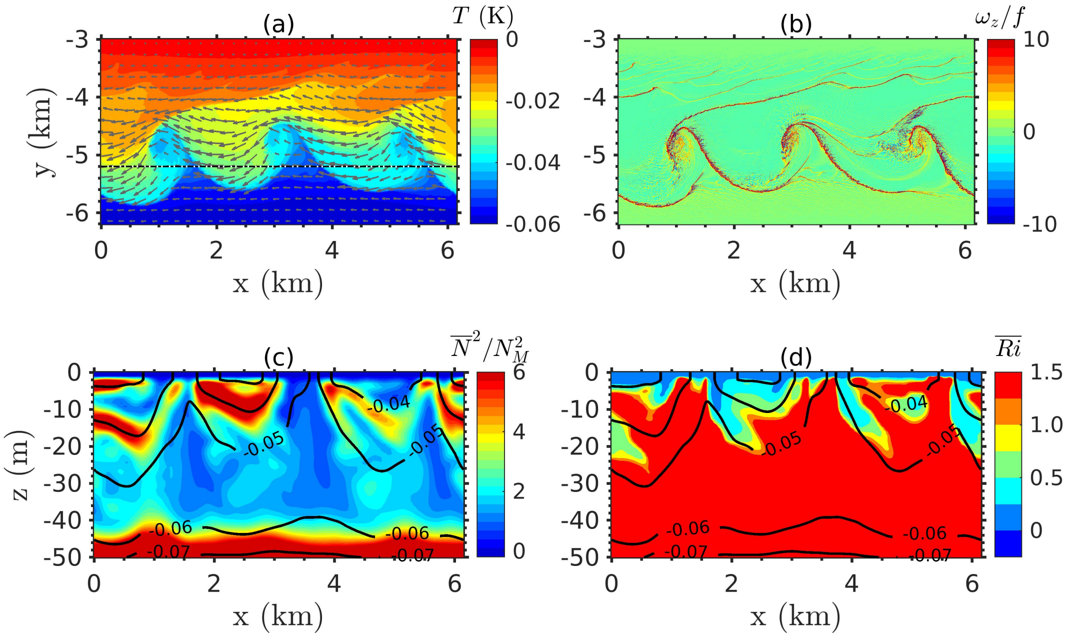

Figure 4.2: The right front flow field at t = 231 h just before initiation of surface. Horizontal sections at depth of 1 m: (a) temperature, (b) vertical vorticity. Vertical-alongfront sections at y = -5.2 km: (c) buoyancy frequency, (d) Richardson number. Velocity vectors in (a) and isocontours of temperature deviation in (c) and (d) are superposed.

of the most dominant baroclinic mode, begin to wrap into coherent submesoscale eddies.

Surface cooling is initiated at $t = 231\,\mathrm{h}$ when three submesoscale eddies have formed as shown in Figs. 4.2a,b. Significant restratification in the interior of the front has occurred as can be seen by the increase of $\overline{N^2}$ and $\overline{Ri}$ (computed using the submesoscale fields) in panels (c)-(d) relative to their initial stratification (N_M^2) and the initial $Ri = 1$, respectively.

4.3 Spectra and separation of scales

Surface cooling generates convective plumes with horizontal scales comparable to the time-evolving depth of the mixing zone (Fig. 4.4). The convective plumes belong to the finescale range when the mixed layer is not deep. Here, we investigate the energy spectra to examine energy content at different scales and also to demonstrate the existence of scale separation, which enables the SMS-FS decomposition. The spectra of the velocity components (u, v, w) are computed as follows

$$\begin{aligned} S^u(k) &= \frac{1}{2}\left\langle |\hat{u}(k)|^2 \right\rangle_y, \quad S^v(k) = \frac{1}{2}\left\langle |\hat{v}(k)|^2 \right\rangle_y, \\ S^w(k) &= \frac{1}{2}\left\langle |\hat{w}(k)|^2 \right\rangle_y, \end{aligned} \tag{4.9}$$

where $\hat{u}(k)$, $\hat{v}(k)$, $\hat{w}(k)$ are the Fourier coefficients of the velocity components as a function of the x direction wavenumber (k) and $\langle\cdot\rangle_y$ is the average over the initial width of the right front, $-5.8 < y < -3.8\,\text{km}$.

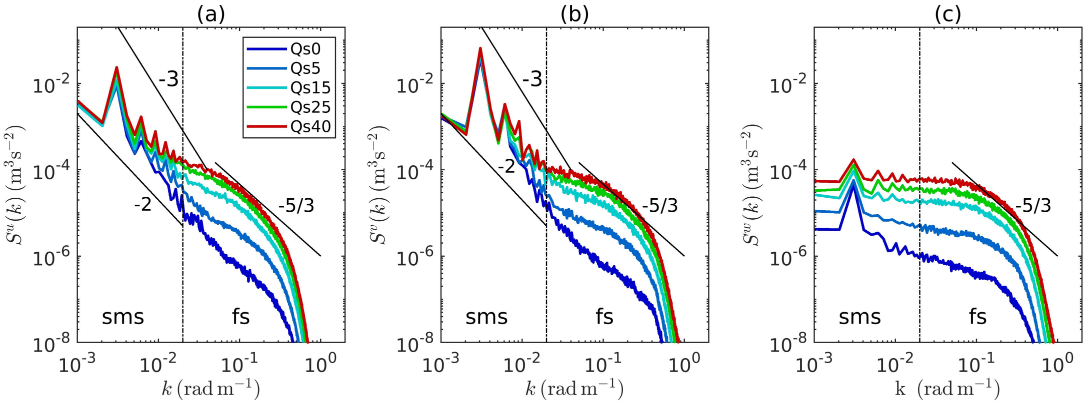

Figure 4.3: Velocity spectra at 20 m depth and $t \approx 250\,\text{h}$: (a) $S^u(k)$, (b) $S^v(k)$ and (c) $S^w(k)$.

In every case, the energy spectra (shown at 20 m in Fig. 4.3) exhibits a peak at $k \approx 3.0 \times 10^{-3}\,\text{m}^{-1}$ or $\lambda \approx 2\,\text{km}$. The peak scale corresponds to the fastest-growing baroclinic mode and is consistent with the capture of three filament-eddy structures by the chosen domain. Two different dynamical regimes are clearly distinguishable: a quasi-2D submesoscale regime with the horizontal components energetically dominating the vertical, and a 3D finescale regime at $< O(100)\,\text{m}$ where u, v and w have comparable energy. The spectral slope of u and v in the submesoscale regime is between -2 to -3, which is consistent with previous studies, (e.g. Skyllingstad and Samelson, 2012, Verma et al., 2019). At the finescale, the spectral slope is approximately -5/3 (the inertial-range power law of 3D turbulence) over a small range of wavenumbers before falling off steeply.

The spectra for Qs5 are similar to the unforced simulation and the contribution of convective turbulence to kinetic energy is relatively weak across the scales, including the finescale. The effect of convective turbulence on energy spectra is significant in cases Qs25 and Qs40 where the spectra reveal more energetic 3D turbulence compared to Qs5. The large scales are also modified. The change in $S^w(k)$ is particularly striking, as the largest scales of w are significantly more energetic than in Qs5. The large-scale horizontal components also have somewhat higher energy in Qs25 and Qs40 compared to Qs5. Nevertheless, u and v remain much more energetic than w in all cases, and the flow behavior changes from quasi-2D, a characteristic of the submesoscale, to 3D turbulent finescales when the length scale drops below $O(100)\,\mathrm{m}$. This is also reflected in the spectral slope, which changes across $O(100)\,\mathrm{m}$ scale.

Exploiting the change in flow behavior, we separate the two ranges with very different behavior, namely, the submesoscale and the finescale, to study how the two ranges evolve and affect each other. We choose the cutoff length scale at $\lambda_c = 314\,\mathrm{m}$, corresponding to a cutoff wavenumber $k_c = 0.02\,\mathrm{rad\,m^{-1}}$, from case Qs40 and apply a low-pass Lanczos filter (a = 2) in the horizontal to separate the submesoscale from the finescale. Integrating the spectra for $k > k_c$ in case Qs40, we find that the finescale has comparable energy in the three components: $E''_w/E''_u = 0.99$ and $E''_w/E''_v = 0.88$. For consistency, the same cutoff length scale is employed in all the cases.

4.4 Convection inside and outside the front

The frontal region evolves differently relative to that outside since submesoscale currents set up by the initial horizontal buoyancy gradient restrict convection. At a given time, the difference between inside and outside of the front (only the right front is discussed) depends on

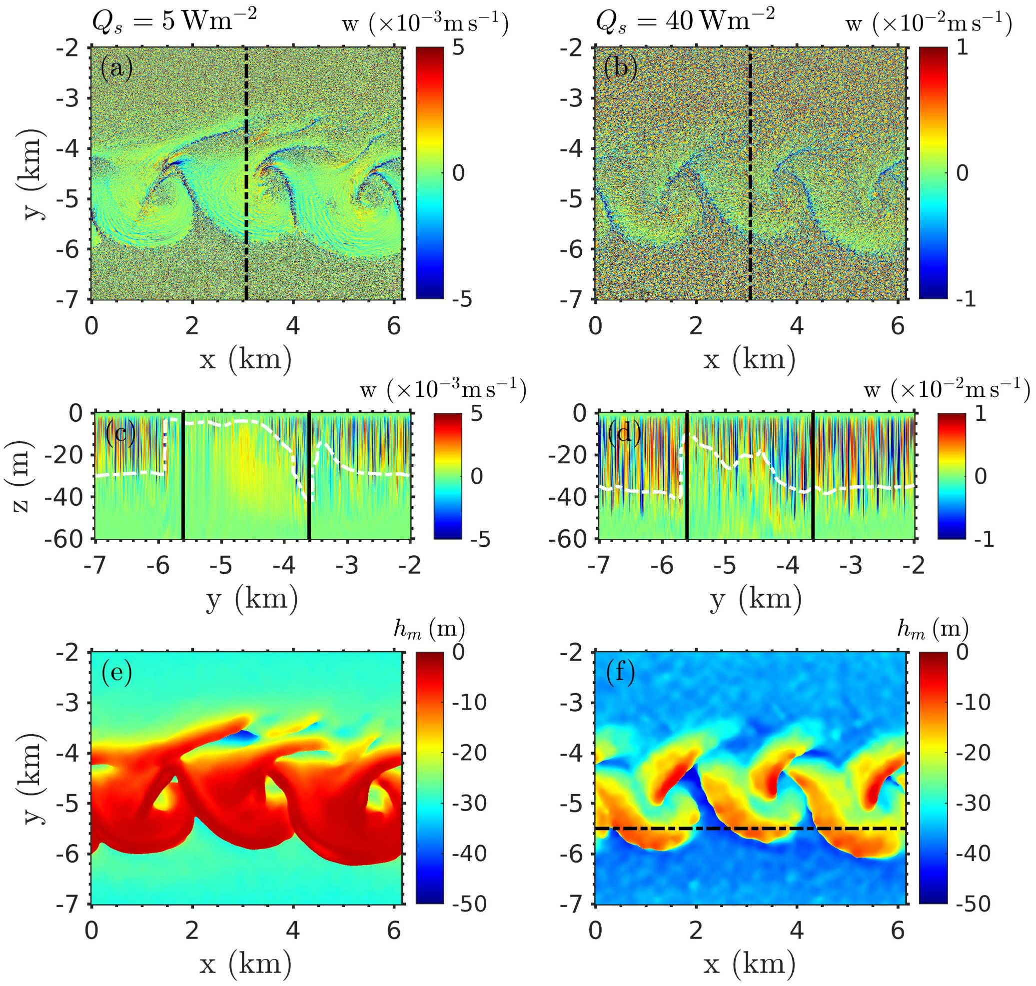

Figure 4.4: Effect of front on convection for cases Qs5 (a,c,e) and Qs40 (b,d,f) is shown at 250 h. Vertical velocity is plotted on a horizontal plane at 10 m depth in (a, b) and on a on a lateral-vertical plane ($x = 3$ km) in (c, d). The dash-dotted line in (a) and (b) shows the lateral transect shown in (c, d). Panels (e, f) show the mixing zone depth (h_m), also shown by dash-dotted white lines in (c,d). The solid vertical lines in (c) depict the edges of the initial front on the right side of the warm filament. The dash-dotted horizontal line in panel (f) corresponds to the vertical plane ($y = -5.5$ km) utilized later in Fig. 4.9.

the strength of the surface cooling flux. This dependence has been illustrated in Figs. 4.4a-f for cases Qs5 and Qs40 at $t \approx 250$ h, about 19 h after the initiation of cooling. In both cases, there are finescale structures (convective plumes) with significant w (both positive and negative) at 10 m depth outside the front. Inside the front, the plumes are limited to the vortex filaments and eddies in Qs5. Note that it is difficult to separate out regions with coherent downwelling inside the front and we will see in the next section that the SMS-FS decomposition is able to do so. The vertical cross-section at the $x = 3\,\mathrm{km}$ cross-front transect (Fig. 4.4c) shows that plumes with significant w remain mostly confined near the surface inside the front. An exception is the vortex filament near the light edge ($y = -3.6\,\mathrm{km}$) where the plumes penetrate down to $z \approx -40\,\mathrm{m}$, even deeper than the $\approx -30\,\mathrm{m}$ value outside the front. Case Qs40 with a strong surface cooling flux is very different. Plumes with significant w (Figure 4.4b) are present everywhere at 10 m depth within the front. At the same time, the imprint of coherent submesoscale structures on the organization of the plumes is also visible. In contrast, the plumes outside the front are horizontally homogeneous. In case Qs40, the plumes reach a depth of $\sim 25\,\mathrm{m}$ (Fig. 4.4d) in the front, excluding regions where coherent structures are present. In the vortex filaments and outside the front, plumes penetrate up to $\sim 40\,\mathrm{m}$ depth.

Submesoscale currents at the front influence the deepening of the turbulent mixing zone. The mixing zone with depth h_m is identified as a region with a weak stratification of $\overline{N}^2 < 2 \times 10^{-7}\,\mathrm{s}^{-2}$, and it is closely related to the region with Richardson number $\bar{Ri} < 0.25$ where shear instability as well as gravitational instability are supported. There is considerable variability of h_m (Figs. 4.4 e,f). Within the front, the mixing zone is shallower outside vortex filaments and eddies. There is a distinct change of h_m at the boundaries of these coherent structures and the change is especially large when the surface cooling is strong as in Qs40.

Convective mixing continually competes with restratification and lateral advection by MLI. Figures 4.5a-c shows $h_m(x,y)$ at 3 different times for case Qs40. By $t = 238\,\mathrm{h}$, there is significant deepening within the front, especially in the vortex filamentary roll-ups from the dense side ($y < 5.5\,\mathrm{km}$) which deepen further at $t = 245\,\mathrm{h}$. However, there are also regions that remain shallow at both times. Interestingly, at the later time of $t = 255\,\mathrm{h}$ in panel (c), there is a qualitative change in that h_m decreases relative to panels (a) and (b) within several regions of the front. The horizontally averaged value of h_m (blue curve in panel d) confirms the late-time decrease of

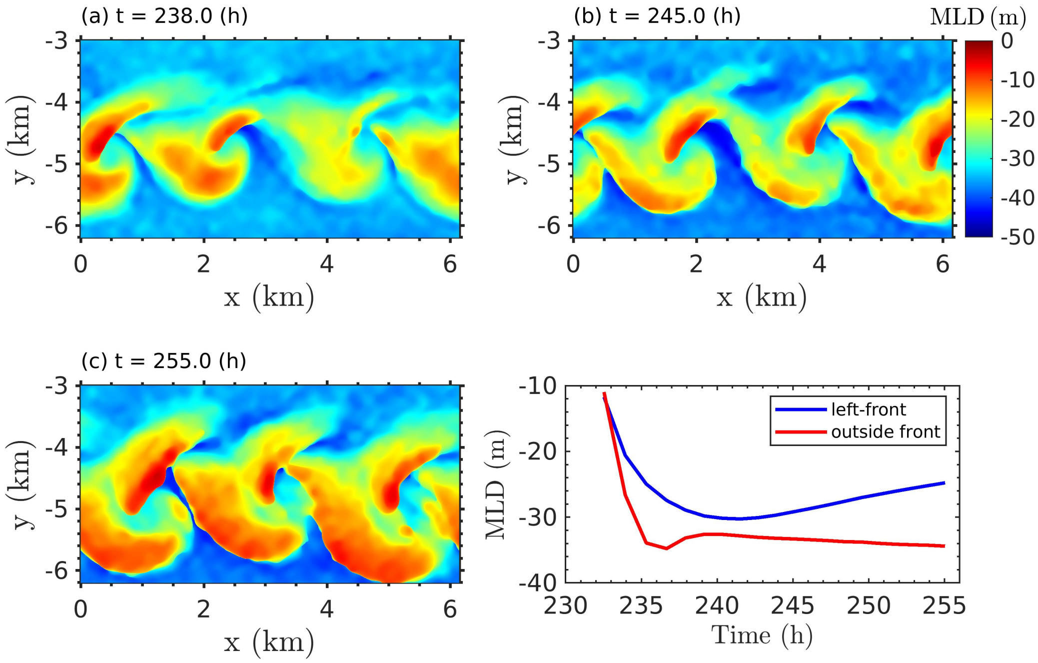

Figure 4.5: Evolution of the mixing zone depth during the period of cooling in case Qs40. Contours of $h_m(x,y))$ at the right front: (a) t = 238 h, (b) t = 245 h and (c) t = 255 h. Panel (d) compares the evolution inside the front with that outside the front.

mixing zone depth when the average is confined to the front. Furthermore, the frontal average of h_m is significantly smaller than the average value outside the front.

Convective turbulence at fronts is modified by the submesoscale currents. It was shown that the plumes penetrate deeper in vortex filaments but remain shallow in the remainder of the front. Additionally, the finescales inside and outside vortex filaments exhibit different behaviour as illustrated by vertical profiles of the velocity variances (Fig. 4.6) in the strong cooling case Qs40. The velocity variances are based on the region $-6.2\,\mathrm{km} < \mathrm{y} < -3.0\,\mathrm{km}$ in the right front and are normalized by w^{*2}, where $w^* = (B_s H)^{1/3}$ is a velocity scale for the convective turbulence in a mixed layer with depth H. The vortex filaments are identified as regions with significant downwelling, $\overline{w} < -2.0 \times 10^{-4}$ ms^{-1}. For comparison, the velocity variances in the central part without lateral buoyancy gradient, $-2.5\,\mathrm{km} < \mathrm{y} < 2.5\,\mathrm{km}$, are also shown. The statistics are calculated below 2 m depth.

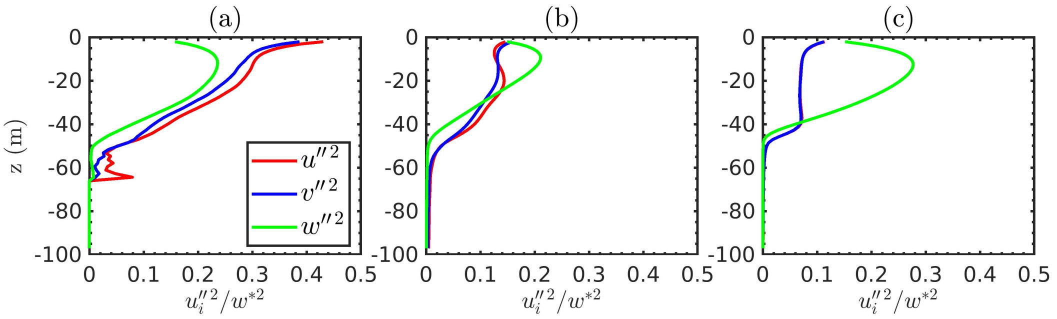

Figure 4.6: Vertical profiles of the finescale velocity variances $\langle u''^2 \rangle$, $\langle v''^2 \rangle$, and $\langle w''^2 \rangle$ normalized with w^{*2}, where w^* is the velocity scale of convective turbulence. Panel (a) is based on velocity inside the vortex filaments of the right front and panel (b) on the velocity outside the filaments but inside the right front where the right front spans $-6.2\,\mathrm{km} < \mathrm{y} < -3.0\,\mathrm{km}$. Panel (c) is calculated in the central region, $-2.5\,\mathrm{km} < \mathrm{y} < 2.5\,\mathrm{m}$, where the lateral buoyancy gradient is negligible and the finescale is purely due to convection.

Within the vortex filaments (Fig. 4.6a), the horizontal components have comparable energy which exceeds that of the vertical component over the entire depth of the front. This behavior stands in contrast to that in the central region (Fig. 4.6c) without frontal gradients. In the convective turbulence of the central region, the vertical finescale component is much more energetic than the horizontal components over the entire mixed layer depth, except near the surface where w goes to zero because of the free-slip wall boundary condition. The finescale velocity variances within the front, but excluding the vortex filaments, is plotted in Fig. 4.6b. The vertical component is more energetic than the horizontal, akin to convective turbulence, in the upper layer before becoming less energetic below 25 m. Comparing Figs. 4.6a,b with Fig. 4.6c clearly shows that the the finescale inside the front is modified, more so in the vortex filaments.

The available potential energy stored in the front because of the lateral density gradient is the principal source of energy for the baroclinic MLI. If the upper-layer temperature outside the front would decrease uniformly in response to convection driven by surface cooling, convection would not change the overall buoyancy contrast across the front as it evolves. Profiles of the along-front averaged temperature, $\langle T \rangle_x (y)$, at 10 m depth and different times (not shown) show that the change of buoyancy contrast over the 25 hr cooling period is small. This small change is associated with less cooling on the left side of the front centerline since warmer (lighter) water migrates towards the heavy edge as part of the frontal restratification.

4.5 Adjustment in submesoscale dynamics

In section 4.4, it was shown that the presence of a lateral buoyancy gradient induces strong changes in upper-layer convection. We find that, in turn, convection also modifies the submesoscale currents set up by the lateral buoyancy gradient and elaborate on these modifications in this section. Note that, for the range of nondimensional buoyancy fluxes considered here, submesoscale currents and associated restratification persist although they are substantially modified at the higher values of r or $\tilde{r}$.

4.5.1 Effect on coherent structures

To assess the effect of convection on the filament/eddy structures at the front, we contrast the submesoscale (SMS) vertical velocity, vertical vorticity, and horizontal buoyancy gradient at 10 m depth between cases Qs5 and Qs40 in Figs. 4.7a-f. Recall that the SMS was separated from the finescale (FS) in the velocity and buoyancy by applying a Lanczos filter with cutoff wavenumber at the transition from quasi-2D motions to 3D fluctuations. The adopted filter meets our objective of separating the coherent field from the incoherent finescale. For example, the small-scale patchiness in the full w field (Fig. 4.4b) is much reduced in its SMS counterpart $\overline{w}$ (Fig. 4.7b). A distinct submesoscale flow organization can be identified for both Qs5 and Qs40, with some changes between the two. Increasing the cutoff length scale from its chosen value of 314 m does not modify the submesoscale flow structures, except making them smoother.

The organization of downwelling ($\overline{w} < 0$) and upwelling ($\overline{w} > 0$) regions changes from Qs5 to Qs40 (compare Fig. 4.7a to b). In Qs40, vortex filaments with downwelling have sharp edges, and the velocity magnitude is large compared to Qs5. Enhancement of w in the large

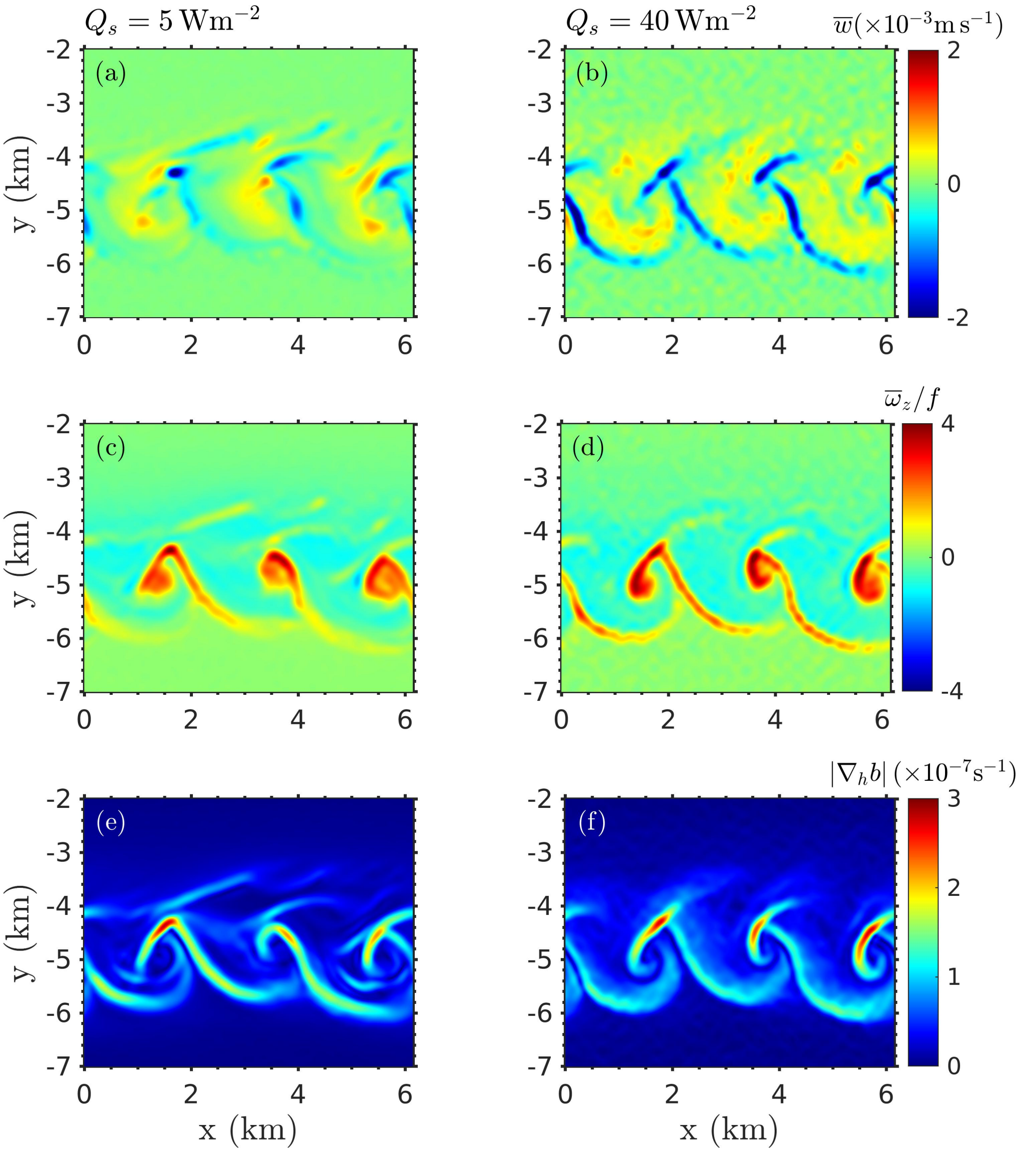

Figure 4.7: Submesoscale flow quantities on a horizontal plane at 10 m depth and $t \approx 250$ h for Qs5 (left column) and Qs40 (right column): (a,b) vertical velocity, (c,d) vertical vorticity normalized by f, and (e,f) horizontal buoyancy gradient magnitude.

(submesoscale) scales was also reflected in its spectrum, S^w (Fig. 4.3c). The organization of upwelling has also changed qualitatively; it has now become concentrated adjacent to the vortex filaments (Figs. 4.7b). These adjustments in $\overline{w}$ indicate a modification of the secondary circulation in the lateral-vertical plane, which is induced by the coherent vortex filaments and the eddies.

The cyclonic relative vorticity (ω_z) in the vortex filaments is also stronger in Qs40 than Qs5 (Figs. 4.7c,d). The horizontal shear of the x and y velocity components are directly related to the vertical vorticity and these shears also become elevated in the vortex filaments. The enhanced downwelling and cyclonic vorticity of the vortex filaments in Qs40 are a product of submesoscale frontogenesis and imply strengthening of the process, contrary to strong diffusion and mixing by the finescale convective turbulence which would be a reasonable a priori expectation. We quantify the changes in submesoscale frontogenetic tendency induced by the interaction with the finescale convective turbulence in section 4.6.3.

In contrast, the horizontal buoyancy gradient magnitude in the vortex filaments is relatively weaker and more diffuse in Qs40 than Qs5, which is a result of relatively strong convective turbulence in the former.

We further quantify the effect of convection on submesoscale vertical velocity in Fig. 4.8a. For convenience, we split the velocity component as $\overline{w} = \overline{w}^- + \overline{w}^+$, where $\overline{w}^- = \overline{w}$ when $\overline{w} \leq 0$, otherwise $\overline{w}^- = 0$ and, conversely, $\overline{w}^+ = \overline{w}$ when $\overline{w} > 0$, otherwise $\overline{w}^+ = 0$. The frontal-averaged $\langle \overline{w}^- \rangle_{xy}$ and $\langle \overline{w}^+ \rangle_{xy}$ with depth are shown in the figure, which reveals a systematic increase in downwelling/upwelling over the entire depth of the front as the surface cooling becomes stronger among the cases studied here, including the unforced case. As noted earlier, this suggests enhanced frontogenesis due to the interaction with energetic convective turbulence. In Fig. 4.8b, the frontal mean of the finescale vertical velocity w'' in the downwelling ($\overline{w} \leq 0$) and upwelling ($\overline{w} > 0$) regions – $\langle w'' | (\overline{w} \leq 0) \rangle_{xy}$ and $\langle w'' | (\overline{w} > 0) \rangle_{xy}$ – are plotted with depth. Although w'' has larger magnitudes, the frontal averages are an order smaller compared to the submesoscale counter parts, revealing a dominance of the submesoscale motions on vertical transport.

4.5.2 Restratification at the front

Convective turbulence is effective at eroding any vertical gradient of density or velocity, creating a mixed zone that thickens vertically. Yet, we find that submesoscale dynamics inhibits

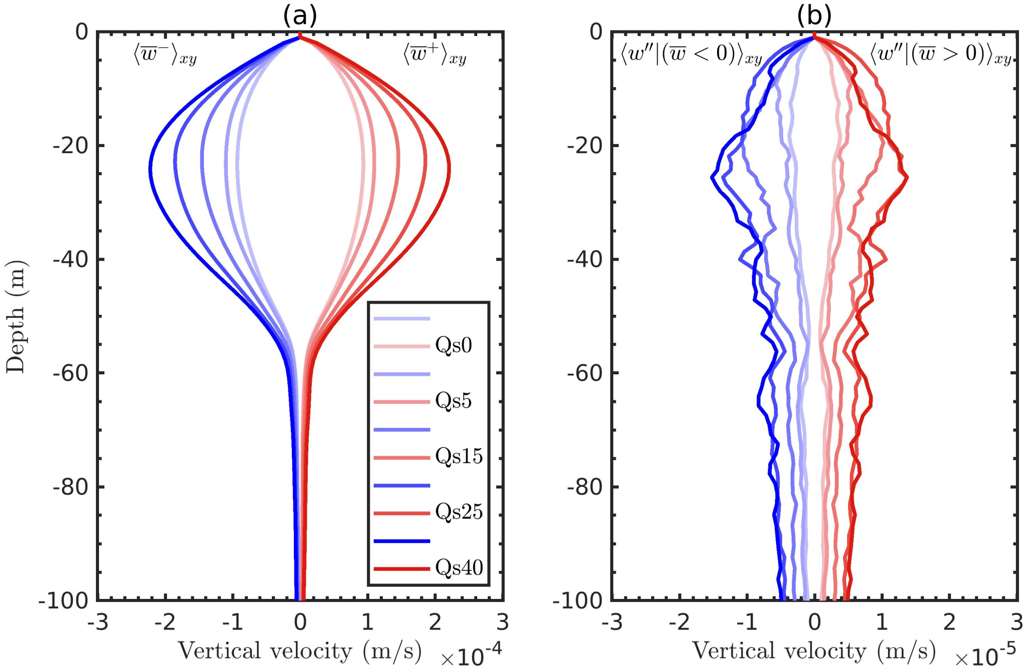

Figure 4.8: Effect of convection on vertical transport at the right front among different cases: (a) The frontal mean of $\overline{w}^-$ (blue curves) and $\overline{w}^+$ (red curves) are plotted with depth, and (b) the frontal mean of w'' in the downwelling ($\overline{w} \leq 0$) and upwelling ($\overline{w} > 0$) regions are plotted with depth and depicted in blue and red curves, respectively. In both panels, the mean at each depth is calculated by taking the area average over the right front, employing a rectangular region encompassing the entire x domain and $-6.2\,\text{km} < \text{y} < -3.0\,\text{km}$ in the lateral.

the growth of convective plumes in certain regions of the front (see Figs. 4.4e,f) even in the nominally strong-convection case Qs40 with $\tilde{r} = 1.5$. The restratification by submesoscale currents plays a central role in this effect on convective deepening as illustrated by a vertical-along front section in Fig. 4.9. Figures 4.9a,b show $\overline{b}_z$ and $\sqrt{\overline{u}_z^2 + \overline{v}_z^2}$, respectively, where the subscript z represents the partial derivative with respect to z. In Fig. 4.9a, the mixing zone depth (h_m) shows significant along-front variability. We observe that, below the regions with shallow h_m, there are patches at mid-depth where stratification is non-zero. At the center of these patches, the stratification is particularly strong and can be as large as five times the initial value of the model setup. At depth, the stratification is again weak, which suggests that the mid-depth strong $\overline{b}_z$ patches form at the interface between approximately homogeneous water masses of different

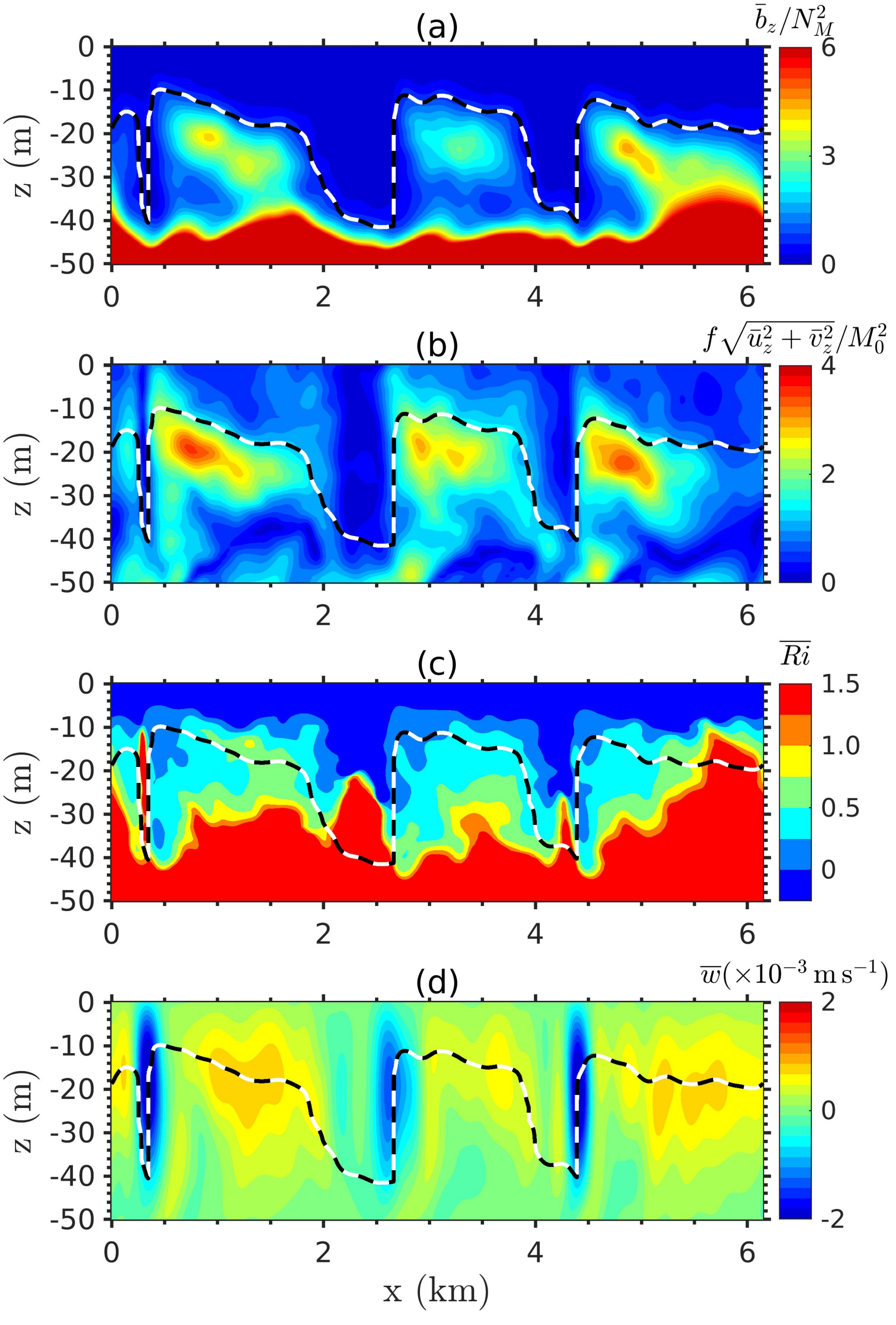

Figure 4.9: Vertical-alongfront section at $y = -5.5\,\mathrm{km}$ and $t = 250\,\mathrm{h}$ of submesoscale fields: (a) stratification $\overline{b}_z$, (b) vertical shear of the horizontal velocity $\sqrt{\overline{u}_z^2 + \overline{v}_z^2}$, (c) Richardson number, and (d) vertical velocity. Black-white line shows the mixing zone boundary ($z = h_m$).

density. The variability of h_m correlates well with the submesoscale vertical velocity, and it is generally shallow in the region of upwelling, but deep where $\overline{w}$ is downwelling (Figs. 4.9a,d).

The vertical shear of horizontal velocity (Fig. 4.9b) is enhanced at the mid-depth stratified patches. In the neighborhood of the mixing zone interface, there is thin layer with $\overline{Ri} < 0.25$ which is unstable to Kelvin-Helmholtz (KH) instability (Fig. 4.9c). Additionally, below the KH-unstable layer, $\overline{Ri}$ remains smaller than one because of the strong vertical shear, which may lead to negative PV in the layer, making the region potentially unstable to secondary SI. The role of PV will be discussed later in section 4.7.

The modified organization of vertical shear, stratification, and vertical velocity (compare with Fig. 4.2) is related to the changes in secondary circulation, which occur in response to the developing convection. The fact that secondary circulation changes is evident from vertical velocity plotted in Figs. 4.7a,b. The organization of vertical shear is particularly interesting, as it can break down the growing convective plumes and suppress its further growth. From the observed changes in the flow quantities, it can be inferred that submesoscale dynamics adapts to surface cooling, but the circulations change in such a way that modify the convective plumes and allow both competing dynamics to coexist at the front.

The response of submesoscale dynamics to convection depends on the loss of balance at the front. With higher imbalance, the submesoscale dynamics can easily extract the available potential energy from the front. The loss of balance can be assessed by probing the departure from gradient-wind balance (Capet et al., 2008b). In contrast to geostrophic balance between Coriolis and pressure gradient forces, gradient-wind balance also accounts for the curvature of the velocity, which can be significant in submesoscale currents with coherent eddies. Following Capet et al. (2008b), a parameter ε_{gw} is defined using submesoscale fields as

$$\varepsilon_{gw} = \frac{|\nabla_h \cdot (\overline{\mathbf{u}}_h \cdot \nabla_h \overline{\mathbf{u}}_h) - f\overline{\omega}_z + (1/\rho_0)\nabla_h^2 \overline{p}\,|}{|\nabla_h \cdot (\overline{\mathbf{u}}_h \cdot \nabla_h \overline{\mathbf{u}}_h| + f|\overline{\omega}_z| + (1/\rho_0)|\nabla_h^2 \overline{p}\,| + \mu}, \tag{4.10}$$

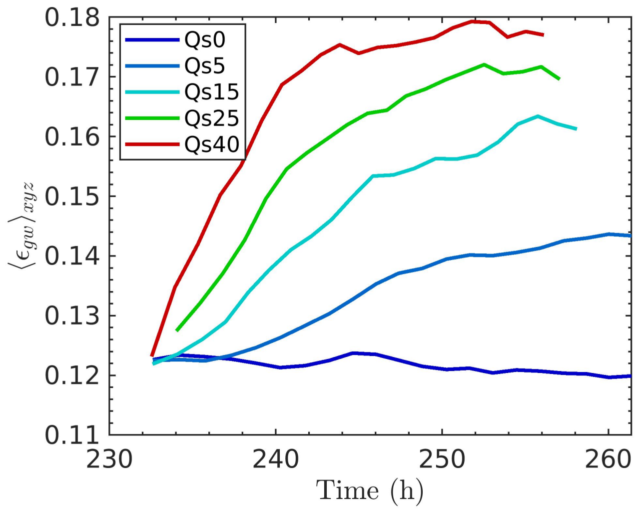

Figure 4.10: Plot of volume-averaged ε_{gw} with time for different cases. The volume average is calculated in a region encompassing the right front.

where subscript h denotes the horizontal components. In the definition of ε_{gw}, $\mu = f\langle|\overline{\omega}_z|\rangle_{xyz} + (1/\rho_0)\langle|\nabla_h^2\overline{p}|\rangle_{xyz}$ is added in the denominator to exclude regions with weak force divergences from appearing as unbalanced. The imbalance is intensified in the vortex filaments with particularly large magnitudes in all cases, including the unforced simulation. The volume averaged ε_{gw} (Fig. 4.10) reveals that the imbalance at the front grows as the as surface cooling increases in magnitude. Moreover, for a given case, the imbalance increases with time as convective plumes deepen and finescales become more energetic. Later, we show that correlated with the imbalance, the extraction of available potential energy by the submesoscale buoyancy production increases, which energizes the submesoscale motions.

4.6 Submesoscale-finescale interaction

In previous sections, we showed that uniform cooling leads to mixing depths and turbulence profiles inside the front which are different from those outside and also characterized the submesoscale adjustment to convective forcing. In this section, we investigate the submesoscale, finescale and their interaction by quantifying the SMS and FS energy equations.

4.6.1 Submesoscale energy conversions

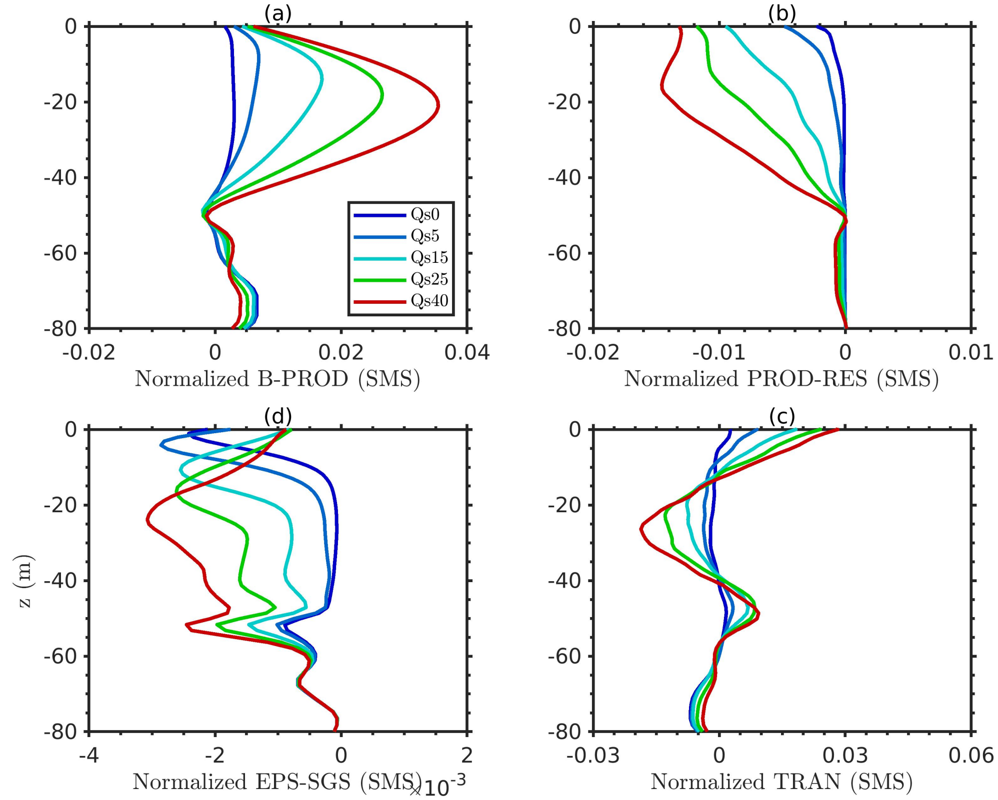

Figure 4.11: The submesoscale KE balance equation terms compared across different cases at $t \approx 250\,\mathrm{h}$. The terms plotted are (a) buoyancy production (B-PROD), (b) residual production of the finescale (PROD-RES), (c) subgrid dissipation (EPS-SGS), (d) transport term (TRAN). All plotted terms are normalized by $U_0^2 f$.

Consider the submesoscale KE balance, Eq. 4.6. The submesoscale KE is energized by the submesoscale buoyancy production ($\overline{B}$) and dissipated ($\overline{\mathcal{E}}$) by the action of subgrid and molecular diffusion. The residual production term ($\mathcal{P}^R$) converts the submesoscale KE into the finescale KE. There are no surface stresses injecting KE into the system and the transport term ($-\partial\overline{T}_j/\partial x_j$) redistributes the submesoscale KE through out the volume.

The profiles of horizontal averages (denoted by $\langle\cdot\rangle_{xy}$) of the budget terms are shown in Fig. 4.11. As cooling strengthens, the peak of buoyancy production (Fig. 4.11a) increases and it moves away from the surface. For case Qs40, the peak has shifted to mid-depth ($\approx 25\,\mathrm{m}$), and the profile has become nearly symmetric about this depth. The depth of peak $\overline{B}$ for the different cases is approximately the case-dependent average mixing depth h_m over the front. The increase in $\overline{B}$ correlates with the increased submesoscale KE observed from the energy spectra in Fig. 4.3. Based on the proposed parameterization of submesoscale vertical buoyancy flux (Fox-Kemper et al., 2008) and the maximum value of $\langle\overline{B}\rangle_{xy}(z)$, we can define an efficiency factor as $C_e = \left[\langle\overline{B}\rangle_{xy}\right]_{max}/B_f$ where $B_f = M_0^4 H^2/f$. Clearly, the efficiency factor varies among the cases studied here and is found to lie in the range $C_e = 0.005 - 0.035$.

The increase of the the source ($\overline{B}$) of submesoscale KE is accompanied by an increase of the sink, namely, the residual production $\langle -\mathcal{P}^R\rangle_{xy}$, which moves energy from the SMS to the FS (Figure 4.11b). The direct dissipation ($\overline{\mathcal{E}}$) of submesoscale KE is small. In Qs40, $\langle -\mathcal{P}^R\rangle_{xy}$ is nearly uniform down to the depth of $\sim 20\,\mathrm{m}$, below which it decreases monotonically and nearly vanishes in the pycnocline. In all the forced cases, the residual production peaks near the surface, which is where this term generates the most finescales. Nevertheless, the submesoscale buoyancy production is relatively large in all the cases and replenishes the loss of submesoscale KE due to the residual production. As a result, the submesoscale KE typically increases in the convectively forced cases. The transport of submesoscale KE also changes with increased cooling. Figure 4.11d shows that transport act to remove submesoscale KE from mid-depth and transport it to the surface and the bottom layers.

The time-dependent effect of convection is assessed by the temporal evolution of the volume-averaged submesoscale KE and its budget terms in Fig. 4.12 (a). Surface cooling energizes the overall submesoscale KE in the domain. After an initial transient ($\sim$ 10 h), the along-front energy (Fig. 4.12 a) increases. Lateral and vertical KE components (Fig. 4.12 b-c) also increase in time. The amount of increase in all three KE components is enhanced by strengthening Q_s.

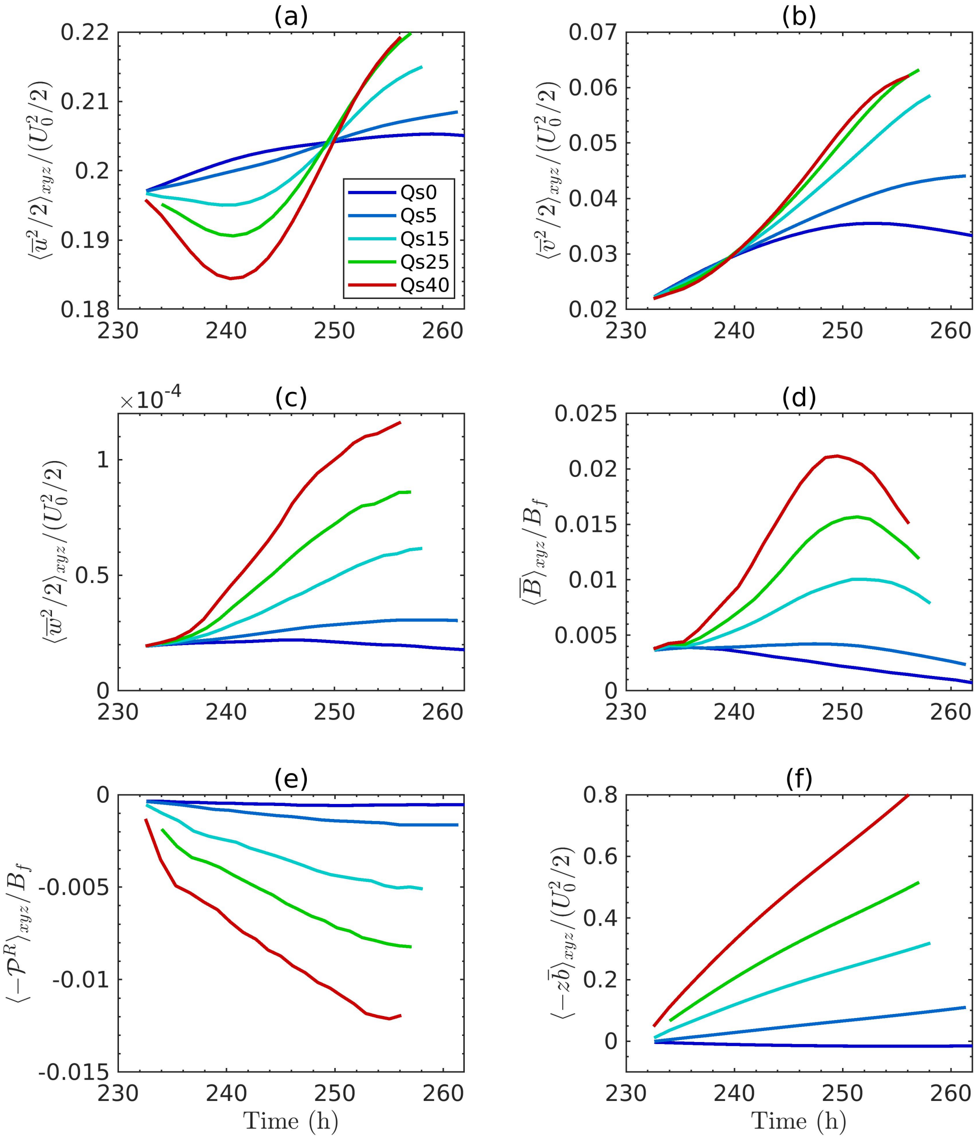

Figure 4.12: Time evolution of volume-averaged submesoscale quantities. Kinetic energy contributions: (a) along-front, $\overline{u}^2/2$, (b) cross-front $\overline{v}^2/2$, and (d) vertical, $\overline{w}^2/2$. Dominant SMS kinetic energy budget terms: (d) source, buoyancy production $\overline{B}$, (e) sink, residual production term (-P^R). SMS potential energy in (f).

Notice that the energy content of z-velocity component is at least an order of magnitude smaller than that of the y-velocity component. This is consistent with the energy spectra, which reveal the submesoscale flow to be quasi-2D.

The two dominant terms in the KE budget, namely, the source provided by buoyancy ($\langle \overline{B} \rangle_{xyz}$ in Fig. 4.12d) and the sink associated with producing the finescale ($\langle -\mathcal{P}^R \rangle_{xyz}$ in Fig. 4.12e) are also shown. Figure 4.12d shows that $\langle \overline{B} \rangle_{xyz}$ increases to reach a maximum and then decreases in all cases, except the weakly forced Qs5. The maximum of $\langle \overline{B} \rangle_{xyz}$ is relatively large and also develops earlier when the surface cooling is stronger. The increase of submesoscale KE agrees well with the temporal evolution of its source $\langle \overline{B} \rangle_{xyz}$, except during the initial phase when the submesoscale KE decreases but $\langle \overline{B} \rangle_{xyz}$ increases. During this initial phase, $\langle -\mathcal{P}^R \rangle_{xyz}$, which is a sink for the submesoscale KE, dominates as convective turbulence begins to develop at the front. Eventually, the submesoscale buoyancy production dominates and energizes the submesoscale.

It is apparent from above discussion that the submesoscale buoyancy production is critical for generating the submesoscale KE by an energy transfer from the PE of the front. The PE balance equation sheds more light on energy transfers from the PE. Consider the balance equation for volume-averaged submesoscale PE ($\langle \overline{E}_p \rangle_{xyz}$, which is obtained from Eq. (4.8),

$$\frac{\partial}{\partial t} \langle \overline{E}_p \rangle_{xyz} = -\langle \overline{w}\overline{b} \rangle_{xyz} - \alpha g \langle \overline{q}_z \rangle_{xyz} - \alpha g \langle q_z^R \rangle_{xyz} + \frac{\alpha g}{H} \left[z \langle (\overline{q}_z + q_z^R) \rangle_{xy} \right]_{z=0}^{z=H}, \tag{4.11}$$

$$\approx -\langle \overline{w}\overline{b} \rangle_{xyz} - \alpha g \langle q_z^R \rangle_{xyz} + \alpha g [\langle \overline{q}_z \rangle_{xy} + \langle q_z^R \rangle_{xy}](z=0), \tag{4.12}$$

where the reference level is selected at the bottom of the upper layer at $z = -50\,\mathrm{m}$. The diffusive flux $-\alpha g \langle \overline{q}_z \rangle_{xyz}$, second term on the right, is small and can be ignored. The boundary term corresponds to the imposed surface heat flux , i.e., $\alpha g [\langle \overline{q}_z \rangle_{xy} + \langle q_z^R \rangle_{xy}]_{(z=0)} = B_s$, and is an input to the PE of the submesoscale field. The submesoscale vertical buoyancy flux $\langle \overline{w}\overline{b} \rangle_{xyz}$ appears here with a negative sign and extracts PE from the front. The residual flux term $\alpha g q_z^R \equiv -(\overline{bw} - \bar{b}\bar{w})$ also plays a significant role. We find that the volume-averaged $\alpha g \langle q_z^R \rangle_{xyz} \approx -\langle b''w'' \rangle_{xyz}$, and a similar relationship exists between the horizontal averages. Since $b''w''$ appears with the opposite sign in the finescale KE budget, we can interpret $b''w''$ as a term through which PE energizes the finescale motions. Figure 4.12f shows the change in $\langle \overline{E}_p \rangle_{xyz}$ with respect to its value at the start of cooling for all the simulated cases. In the unforced case, PE decreases corresponding to the energy extraction by the submesoscale buoyancy production. However, the potential energy increases for cases with surface cooling, and the growth is larger for stronger surface cooling.

4.6.2 Finescale energy conversions

The finescale KE differs in energy content as well as its distribution among u, v and w inside the front relative to the outside with purely convective turbulence, as was illustrated for QS40 in Fig. 4.6 of section 4.4. The finescale KE balance Eq. 4.7 is examined here to better understand how surface cooling affects the sources and sinks of finescale energy inside the front.

The applied surface cooling in forced cases drives a finescale vertical buoyancy flux B'' which we find to be the primary source of finescale KE inside the front. The submesoscale is an additional source of finescale KE. In particular, the transfer term (Tr) extracts finescale kinetic energy from the submesoscale velocity. To distinguish the contributions from horizontal and vertical gradients of the submesoscale velocity, Tr is separated into Tr_h and Tr_v as follows,

$$Tr_h = -\left(u''u''\frac{\partial \overline{u}}{\partial x} + u''v''\frac{\partial \overline{u}}{\partial y} + v''u''\frac{\partial \overline{v}}{\partial x} + v''v''\frac{\partial \overline{v}}{\partial y} + w''u''\frac{\partial \overline{w}}{\partial x} + w''v''\frac{\partial \overline{w}}{\partial y} \right), \qquad (4.13)$$

$$Tr_v = -\left(u''w''\frac{\partial \overline{u}}{\partial z} + v''w''\frac{\partial \overline{v}}{\partial z} + w''w''\frac{\partial \overline{w}}{\partial z} \right), \qquad (4.14)$$

where Tr_h consists of all the terms with the horizontal (x, y) gradients of the submesoscale velocity, and Tr_v consists of those with the vertical gradient.

Figure 4.13 compares the vertical profiles of the dominant budget terms for the cases with surface cooling. The terms are normalized by the imposed surface buoyancy flux B_s. The magnitude of B_s varies substantially among different cases taking values in Qs15, Qs25, and Qs40 which are 3, 5, and 8 times stronger compared to that of Qs5. The FS buoyancy flux (B'' shown in Fig. 4.13a) is the dominant source and scaling with B_s provides a reasonable collapse of its profiles, especially for cases Qs15, Qs25, Qs40. The maximum value of B'' is about $0.8B_s$ in

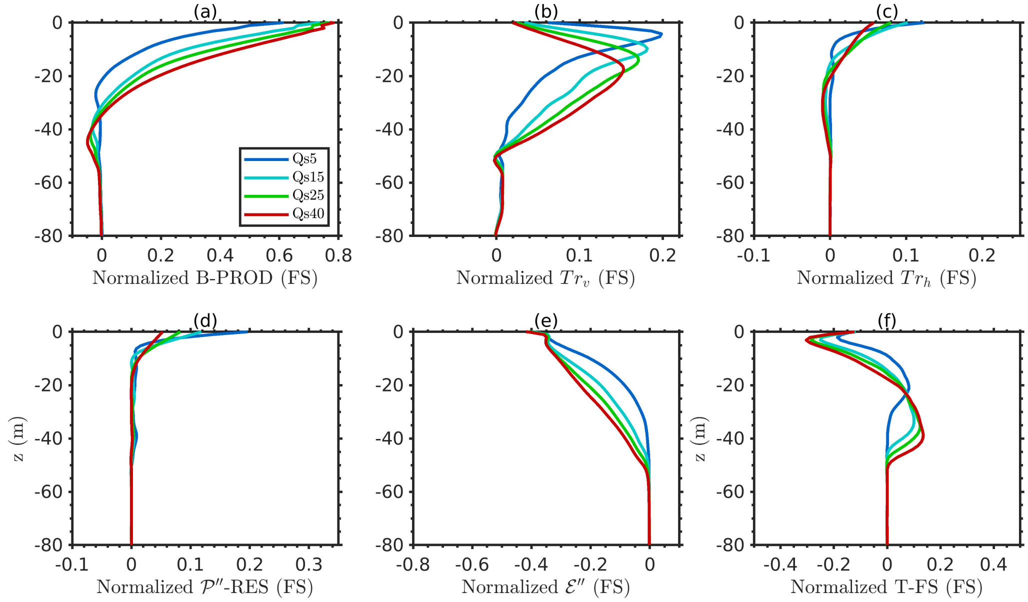

Figure 4.13: Dominant terms in the finescale KE balance equation at $t \approx 250\,\text{h}$: (a) finescale buoyancy production (B-PROD), (b) Tr_v, (c) Tr_h, (d) finescale residual production ($\mathcal{E}''$-RES), (e) subgrid dissipation ($\mathcal{E}''$-SGS), and (f) transport by the finescale velocity (T-FS). All budget terms are normalized by the surface buoyancy flux B_s. We note that B_s in Qs15, Qs25, and Qs40 are, respectively, 3, 5, and 8 times stronger than in Qs5.

Qs40 showing that most of the surface buoyancy flux supplied by surface cooling appears in the finescale buoyancy flux.

The transfer Tr_v by vertical shear is found to be a significant additional source of finescale KE in all the forced cases (Fig. 4.13b). Scaling by B_s provides an approximate collapse of the maxima of the Tr_v profiles among the cases, showing the importance of surface cooling to the transfer term. The location of the peak Tr_v follows the peak of the SMS buoyancy flux ($\overline{b}\overline{w}$) associated with restratification. Horizontal shear through Tr_h (Figs. 4.13c) also contributes as a source in the near-surface region. Inside the front, the volume average of $Tr_v + Tr_h$ is as large as 50% of the volume-averaged B'' for case Qs40 at late times. The role played by SMS shear as a source of finescale KE explains the change of turbulence anisotropy inside the front from purely convective turbulence towards shear-driven turbulence.

The subgrid dissipation (Fig. 4.13e) is the primary sink of finescale KE and increases with increased cooling. It tracks the finescale buoyancy flux and transfer from the SMS kinetic energy to counteract these sources. The self-generation by finescale shear through $\mathcal{P}''^R$ (Fig. 4.13d) also acts as a source, but its contribution to the finescale KE is relatively small. The transport (Fig. 4.13f) acts to transfer finescale KE from the surface layer to below mid-depth.

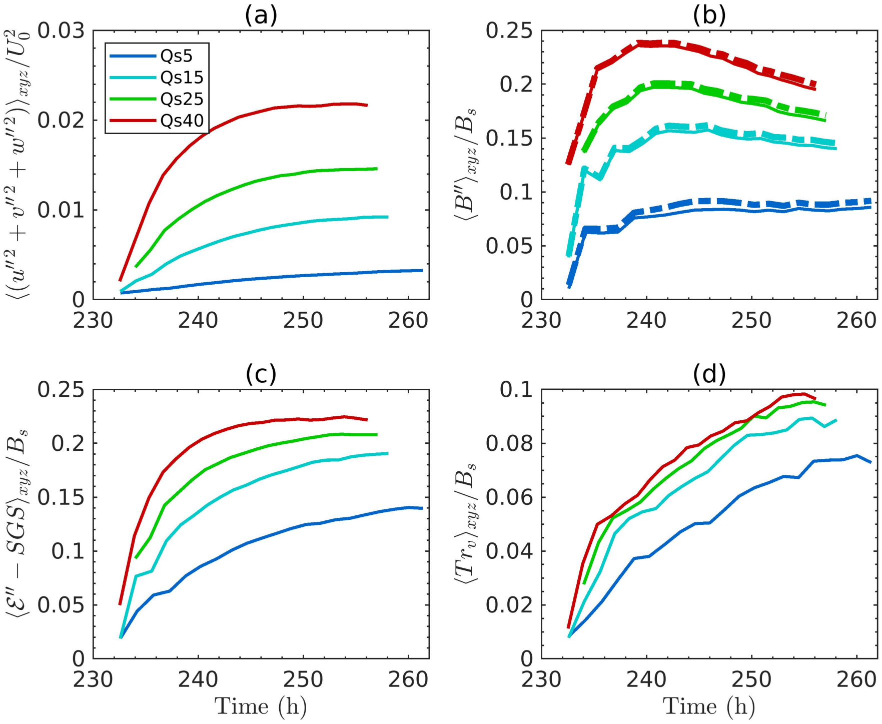

Figure 4.14: The time evolution of volume-averaged quantities: (a) finescale KE, (b) finescale buoyancy production, (c) subgrid dissipation, and (d) Tr_v. The finescale KE budget terms from each case are normalized by the surface buoyancy flux B_s, whereas the finescale KE curves are normalized by $U_0/2$, same as the submesoscale KE. The thick dash-dotted lines in panel (b) depict $\langle q_z^R \rangle_{xyz}$ in time.

To gain further insights into the transient growth of the finescale, we also investigate the time evolution of volume-averaged finescale KE and the dominant terms in the finescale KE budget (Fig. 4.14). In each case, the finescale KE increases as convection develops and eventually becomes approximately constant. The finescale KE is the largest for Qs40 with the most surface cooling. A similar time evolution can also be noted for the volume-averaged subgrid dissipation of the finescale KE (Fig. 4.14c), suggesting a strong correlation between the two quantities, consistent with the picture of 3D turbulence with downward cascade of KE. The time evolution of the volume-averaged buoyancy production, on the other hand, behaves differently (Figs. 4.14b). The buoyancy production starts to decrease after reaching a peak value in simulations Qs15, Qs25, and Qs40; in Qs5, the buoyancy production remains uniform after the initial growth. It is also apparent that the rate with which B'' decreases depends on B_s, being steepest for Qs40 with strongest B_s. The decrease in volume-averaged B'' is related to the generation of negative B'' at the bottom, corresponding to the entrainment of bottom fluid by convection, which is strongest for Qs40. Interestingly, during the time when B'' decreases, the production by Tr_v rises (Fig. 4.14d), compensating for the decreased transfer from the submesoscale and allowing the finescale KE to remain approximately constant.

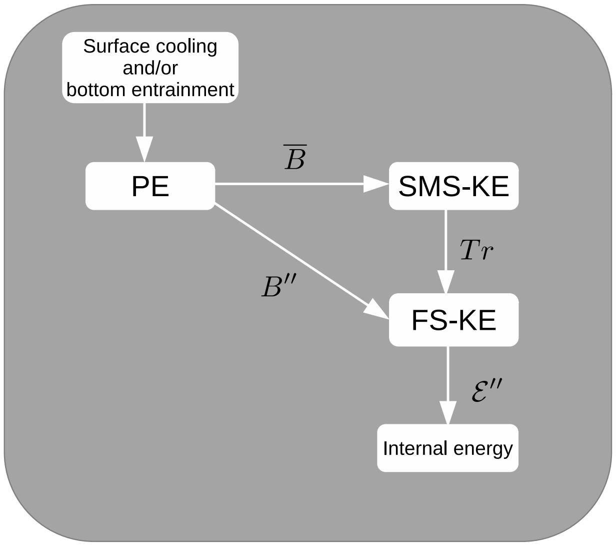

Figure 4.15: A schematic of energy pathways among the PE, submesoscale (SMS) KE and the finescale (FS) KE reservoirs.

The above results lead to the following overall picture (Fig. 4.15) of the energy pathways involved in the problem. The PE reservoir, through the mixed-layer BI and the attendant submesoscale flux $\overline{B} = \overline{b}\overline{w}$, energizes the SMS kinetic energy reservoir. Surface cooling adds to the PE reservoir. The application of the cooling flux creates a surface layer which is gravitationally unstable and breaks down into turbulent motions. Energetically, there is an associated finescale vertical buoyancy flux ($B'' = b''w''$) which transfers energy from the PE reservoir to the finescale KE reservoir. There is also substantial production of the finescale by shear (primarily vertical) of the submesoscale motions through the transfer term (Tr). We find, as will be demonstrated in section 4.7, that forced secondary instabilities such as SI and KH instability play a role in mediating this transfer from the SMS to the FS. The dissipation of KE is primarily at the finescale by the modeled subgrid processes. Note that the submesoscale currents persist through extraction of the PE stored in the front because the lateral buoyancy gradient persists in the face of convective turbulence.

4.6.3 Frontogenesis and horizontal convergence

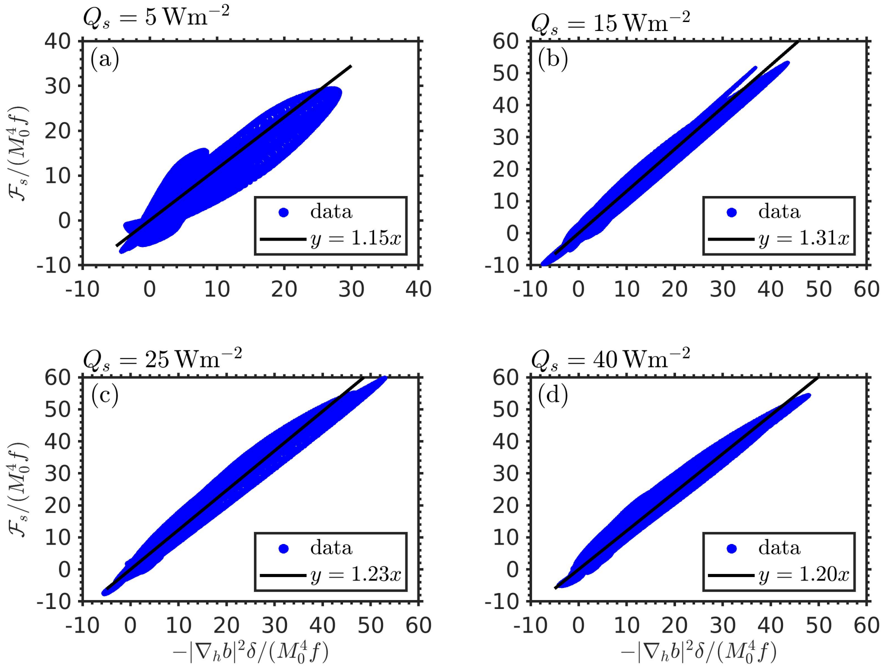

Figure 4.16: Scatter plots of normalized F_s and $-|\nabla_h b|^2\delta$ at the right front over the lateral expanse between $-6.2\,\mathrm{km}$ to $-3.0\,\mathrm{km}$ at 10 m depth for forced simulations. The solid-black lines depict the linear curve fits.

Employing an asymptotic model, Barkan et al. (2019) show that frontogenetic tendency in submesoscale dynamics is inherently linked to the horizontal convergence of velocity. An important result is that the frontogenetic forcing given by $\mathcal{F}_s$, which is defined in Eq. (2.20), can be expressed as $\mathcal{F}_s = -\delta|\nabla_h b|^2$ where $\delta = \nabla_h \cdot u_h$ is the horizontal divergence of velocity. Thus, increased horizontal convergence (negative $\nabla_h \cdot u_h$) strengthens frontogenesis. The scatter plot of $\mathcal{F}_s$ and $-|\nabla_h b|^2\delta$ at 10 m depth is plotted for the forced cases in Fig. 4.16. The points cluster along a line $\mathcal{F}_s = -c_1|\nabla_h b|^2\delta$, with $c_1 \approx 1$ validating the applicability of the result of Barkan et al. (2019) to the present case of a convectively forced front. The maximum value of $\mathcal{F}_s$ increases, relative to Qs5, in the cases with moderate to strong cooling. Thus, frontogenetic tendency strengthens as submesoscale currents adjust to convection. The increased $\mathcal{F}_s$ assists in sustaining the vortex filaments by opposing mixing by the horizontal finescale fluxes associated with convection. This also correlates with the enhanced submesoscale vertical velocity observed at the front with convective turbulence.

4.7 Secondary instabilities

We have seen that, as the submesoscale currents adjust to the imposed cooling, regions of enhanced vertical shear develop adjacent to the deepening convective plumes and also that there is an overall energy transfer from the SMS to the FS mediated by said shear. Thus, apart from the primary cooling-induced gravitational instability, there are regions of the front which could be unstable to secondary instabilities such as symmetric and inertial instabilities. These secondary instabilities can be diagnosed by analyzing potential vorticity (PV), along with Richardson and Rossby numbers, e.g. Thomas et al. (2013). PV is defined using the submesoscale fields as follows:

$$\overline{\Pi} = (f\hat{k} + \overline{\omega}) \cdot \nabla \overline{b}, \tag{4.15}$$

where $\hat{k}$ is a unit vector in the vertical, and $\overline{\boldsymbol{\omega}} = \nabla \times \overline{\mathbf{u}}$ is the submesoscale relative vorticity computed from the submesoscale velocity field.

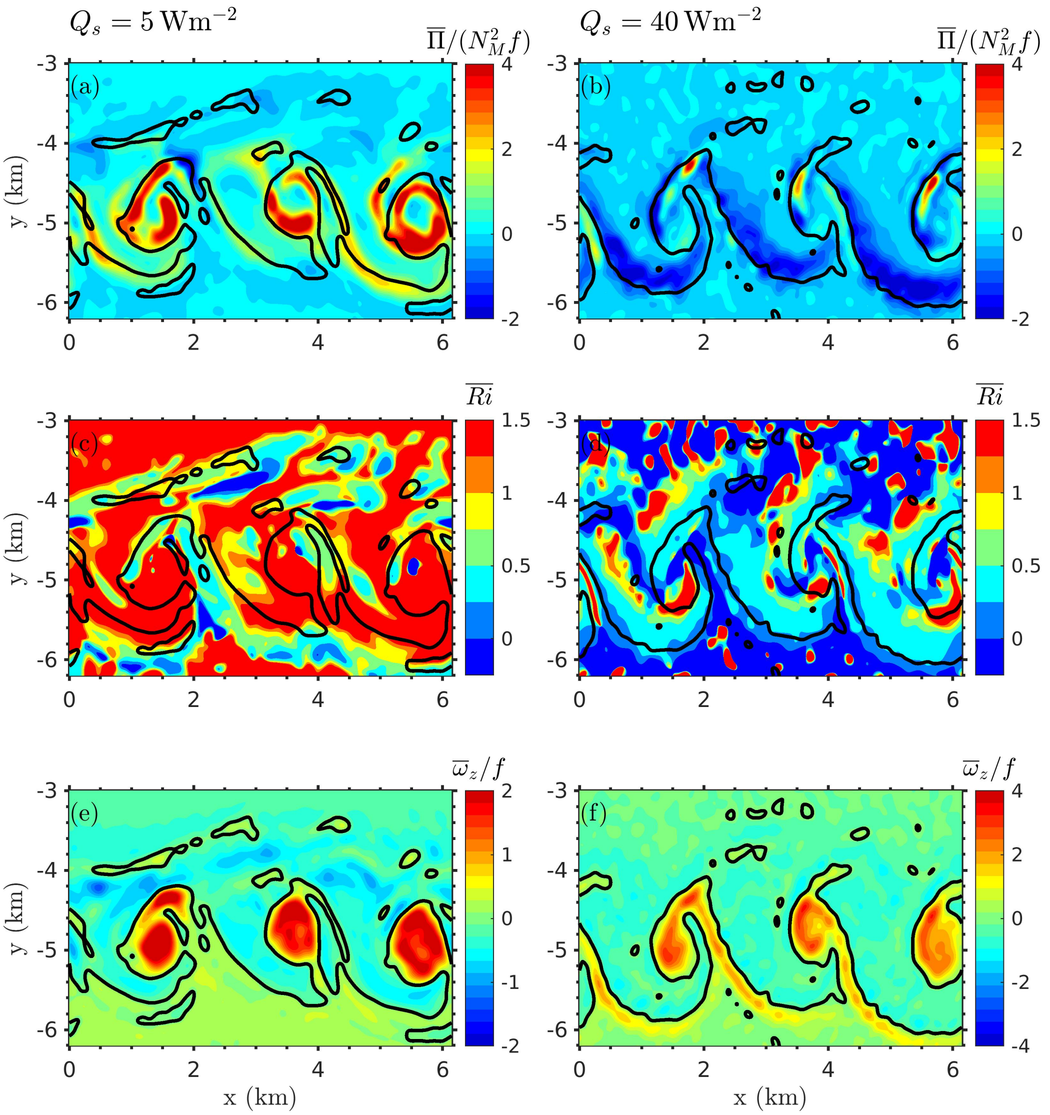

Figure 4.17: Submesoscale (a, d) potential vorticity, (b, e) Richardson number, and (c, f) vertical vorticity are shown at 20 m depth and $t \approx 250\,\mathrm{h}$ for cases Qs5 (left column) and Qs40 (right column). The black solid lines in (a) and (d) depict $\overline{\omega}_z/f = 1$ contours to delineate the coherent structures.

The PV distribution at 20 m for Qs5 (Fig. 4.17a) reveals that it is positive in the vortex filaments and the eddies, especially at the periphery, and nearly zero in other regions of the front.

The coherent structures are identified in Fig. 4.17a by overlaying contours of $\overline{\omega}_z/f = 1$ in black. The plot of Richardson number (Fig. 4.17b) calculated using SMS flow quantities show small patches in the vortex filaments with values smaller than 1. Although weak, PV is negative in these regions indicating susceptibility to SI. For Qs40 with stronger cooling, the PV distribution is considerably different compared to Qs5 (compare Figs. 4.17a - b). It is nearly zero in most parts of the vortex filaments and the eddies because the fluid is mostly well mixed in the top 20 m. Adjacent to vortex filaments, there are regions with strongly negative PV in Qs40 and $\overline{Ri}$ (Fig. 4.17d) takes values between 0 and 1. These conditions are favorable for forced SI. We recall that before applying surface cooling, the front evolves with unforced BI and is stable to SI. Outside the core of the front, patches with the imprint of convective plumes with large positive and negative $\overline{Ri}$ are encountered. In these regions, the fluid has weak vertical shear and stratification such that $\overline{Ri}$ is large in magnitude and changes sign from one convection patch to another.

The secondary instabilities can be further characterized based on the generation of the finescale. In SI, the finescale velocity is generated principally by the vertical shear of the horizontal velocity. In inertial instability, it is the horizontal shear that leads to production of finescale KE. In Fig. 4.18, the finescale generation by Tr_h and Tr_v as well as the subgrid dissipation are assessed at 20 m depth for cases Qs5 and Qs40. In both cases, the finescale generation is dominated by Tr_v rather than Tr_h (Fig. 4.18c-f), suggesting the presence of forced SI. In Qs5, the finescale generation is concentrated primarily at the peripheries of the eddies where vortex filaments wrap around the eddies. In Qs40, regions with negative PV of magnitude greater than $2N_M^2 f$ in Fig. 4.17 have significant values of Tr_v. The regions with $0 < \overline{Ri} < 1$ (Fig. 4.17d) also correlate well with Tr_v.

In both Qs5 and Qs40, the generation of finescales by the forced SI enhance subgrid dissipation, compared to the outside region dominated by convection alone (Figs. 4.18a,b). The finescale generation by SI and enhanced dissipation (ε'') are significantly more pronounced in

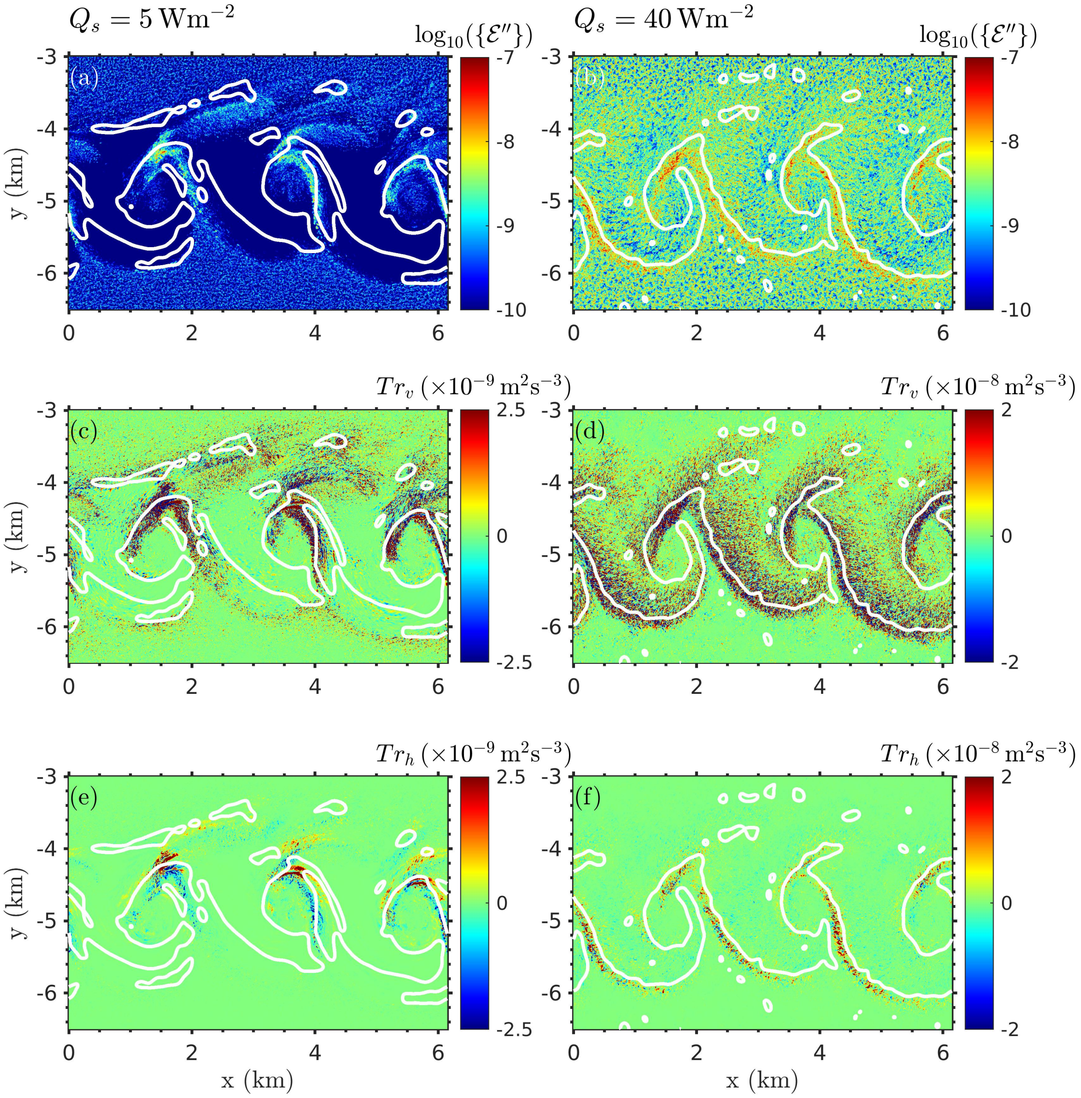

Figure 4.18: The finescale subgrid dissipation (a, b), the transfer term components Tr_v (c, d) and Tr_h (e,f) are plotted at 20 m depth and $t \approx 250\,\mathrm{h}$ for cases Qs5 (left column) and Qs40 (right column). The white solid lines in panels depict $\overline{\omega}_z/f = 1$ contours to delineate the coherent structures.

Qs40 than Qs5, where the former has more cooling, stronger convective turbulence, and a deeper mixing depth than the latter. The transfer term Tr_h, which collects contributions from horizontal gradients of velocity, contribute to the finescale generation primarily in the vortex filaments and outer edges of the eddies (Figs. 4.18e,f). However, excluding the near surface region, the overall contribution of Tr_h to the finescale generation is relatively weak compared to Tr_v

4.8 Conclusions and discussion

In this paper, we examine the evolution of baroclinic mixed layer instability (MLI) at upper-ocean fronts in a background of convective boundary layer turbulence to understand their interaction. We utilize the model setup of a wide warm filament with edge fronts of width 2 km confined in the weakly stratified surface layer of depth 70 m. The fronts, initially in thermal wind balance, are unstable to MLI and evolve nearly independent of each other, developing submesoscale coherent vortex filaments and eddies during the nonlinear growth. After the mixed layer structures have been established, we apply surface cooling to study the time-evolving interaction of the submesoscale structures with boundary-layer convective turbulence. The cooling flux takes various values between $Q_s = 5$ and $40\,\mathrm{W\,m^{-2}}$ and is applied for a period of 25 hrs, larger than a night of cooling and about an inertial period.

Surface cooling affects the coherent eddy/filament structures of the submesoscale (SMS), which, in turn, affects the three-dimensional, turbulent fluctuations of the finescale (FS) in different ways. A decomposition using a sharp filter in physical space successfully separates the SMS and the FS (including convective turbulence), allowing characterization of how surface cooling separately affects the SMS and FS ranges. By constructing energy balance equations for fluctuations in both ranges, we are able to quantitatively examine their individual energetics as well as their interaction.

The turbulent finescale shows strong horizontal variability across the front. Vortex filaments inside the surface layer of the unforced front have coherent downwelling velocity (Verma et al., 2019) leading to sustained downward vertical transport of tracer particles. The convective plumes deepen through the downwelling vortex filaments and reach deeper depths than the plumes outside the front. In contrast, the depth of the mixing zone is suppressed in other parts of the front where continued restratification is maintained by MLI. In the shallow region, the vertical velocity is typically upwelling and strong shear and stratification are encountered at the base of the local mixing zone. The energy in the finescale also shows strong horizontal variability. Relative to the convective turbulence outside the front, the cases with stronger cooling have more energetic horizontal components within the front and especially so within the vortex filaments.

The submesoscales are also strongly affected and shows strengthening of several aspects rather than weakening by convection. The coherent downwelling through the vortex filaments increases as does the upwelling. The upwelling regions are spatially more concentrated near the vortex filaments relative to the unforced case. As a consequence of the increased downwelling and upwelling motions, potential energy extraction by the submesoscale buoyancy flux ($\overline{B} = \bar{b}\bar{w}$) increases, which energizes the submesoscale motions. The peak value of the horizontally-averaged value of $\overline{B}$ in Qs40 increases by a factor of 4 with respect to the weak cooling case Qs5. The imbalance at the front increases as the magnitude of Q_s increases. The imbalance also increases with time as the plumes grow and the finescale become more energetic. The frontogenetic forcing term ($\mathcal{F}_s$) increases relative to the unforced case, thereby enabling the preservation of vortex filaments (with enhanced horizontal buoyancy gradient and enhanced cyclonic vorticity) in the face of increased horizontal mixing by convective turbulence.

Callies and Ferrari (2018), in their study of a doubly-periodic re-entrant channel with constant $M^2/f^2 = 1$ and upward buoyancy flux at the top and bottom walls found that mixed-layer baroclinic instabilities are remarkably resilient to convection in the final equilibrated state. In the present problem of a finite-width front with larger initial $M^2/f^2 = 8$, we similarly find that MLI persists in the face of convection during the time-evolving deepening of the mixed layer. Whitt and Taylor (2017) simulated the response of submesoscale motions to the passage of a storm with downfront (destabilizing Ekman buoyancy flux) wind. They find that the submesoscales are resilient and grow stronger in response to the wind. Significant energization of the submesoscale component was observed during the passing of a storm in the simulations of Whitt and Taylor (2017).

The important energy pathways among the submesoscale and the finescale KE reservoirs and the PE reservoir in this problem are summarized by the simplified diagram of Fig. 4.15. Surface cooling leads to finescale plume structures which drive a positive buoyancy flux $b''w''$ that energizes the finescale KE. Most of the imposed surface buoyancy flux appears as the finescale buoyancy flux with its horizontal average as large as 80% of B_s. As the magnitude surface cooling grows, the transfer term Tr by SMS velocity gradients becomes an increasingly important source of finescale kinetic energy and its volume-integrated values reaches about 50% of the volume-integrated $b''w''$. Overall, the transfer Tr_v by vertical gradients of submesoscale velocity dominates Tr_h by horizontal gradients of submesoscale velocity. Ultimately, the subgrid processes dissipate the finescale KE, which dominates the dissipation of the total KE at the front.

The finescale generation by the transfer term in the unforced MLI study of Verma et al. (2019) was found to be weak relative to the submesoscale buoyancy production. This suggested that submesoscale dynamics were not effective in transferring the KE from the quasi-2D submesoscale to three-dimensional finescale turbulence. In contrast, we find in this study that a background of convective turbulence promotes energy extraction from the submesoscale velocity. In the upper layer of the front, PV becomes negative with a magnitude that increases with surface cooling. A map of instability criteria (e.g. Thomas et al. (2013)) shows that the frontal regions conducive to SI become more prevalent when surface cooling is strong (e.g., Qs40 compared to Qs5). Since SI draws energy from the KE reservoir, the transfer term from submesoscale to finescale kinetic energy is enhanced by the presence of convection. We note that negative PV regions have been observed at surface ocean fronts under wind conditions (e.g., D'Asaro et al., 2011, Ramachandran et al., 2018). In the present study, the negative PV regions develop due to destabilizing surface buoyancy forcing.

In the presence of wind-driven boundary turbulence and including the effect Langmuir turbulence Hamlington et al. (2014) showed that both submesoscale and finescale buoyancy fluxes are enhanced, similar to what is found in the present study. Interestingly, finescale interaction enhances the submesoscale vertical buoyancy flux in both cases, even though turbulence is generated differently.

Acknowledgments

This chapter, in full, is a reprint of material in preparation for publication as follows: V. Verma, H. T. Pham, and S. Sarkar, “Interaction between submesoscale currents and convection at upper-ocean fronts,” 2021. The dissertation author is the primary investigator and author of this work. I am pleased to acknowledge the support of ONR grant N00014-18-1-2137.

Chapter 5

Conclusions

The upper-ocean submesoscale (0.1 - 10 km) dynamics have been studied using large eddy simulation (LES) models of isolated density fronts and warm filaments. A novel aspect of the simulations is the resolution of O(1 m) turbulent scales in conjunction with the submesoscale. Submesoscale dynamics emerges as instabilities such as symmetric and baroclinic instabilities grow at the front. Our focus is to examine the role of submesoscale dynamics in vertical transport and the transfer of kinetic energy to small scales where molecular processes can ultimately dissipate the energy. We first investigate an idealized scenario of an unforced front to understand the behavior of the submesoscale dynamics in isolation of the boundary layer turbulence of the upper ocean. Subsequently, we also investigate baroclinic mixed layer instability (MLI) with convective turbulence. With LES approach, we are able to examine the two-way coupling between the instability-generated submesoscale and convective turbulence.

Chapter 2 discusses the evolution of an unforced upper-ocean front. The model setup of an isolated density front is employed for the simulation. Although the initial configuration is unstable to symmetric instability (SI), its nonlinear evolution restratifies the front, making it stable to symmetric perturbations. Modulating the remnant of SI, baroclinic mixed layer instability (MLI) emerges and dominates the subsequent evolution of the front. The growth of MLI leads to the meandering of the front, which generates coherent vortex filaments with concentrated vertical vorticity. Furthermore, the vortex filaments grow in length and roll up to form coherent eddies in the frontal zone. These vortex filaments and eddies are similar to the coherent structures observed during the Lagrangian Submesoscale Experiment (LASER) in the Gulf of Mexico (D'Asaro et al., 2018). The simulation revealed strong influence of the submesoscale coherent structures on the dynamics of the front.

The local Rossby number, defined as the ratio of vertical relative vorticity ω_z and Coriolis parameter f, was large ($O(10)$) in the vortex filaments and the periphery of the coherent eddies, indicating significant loss of balance within these structures. The simulation showed the generation of finescales locally within the coherent structures where they remained confined. The vertical velocity on a horizontal plane near the surface has large magnitudes (up to $0.02\,\mathrm{m\,s^{-1}}$), but distinct upwelling and downwelling regions were not apparent. The localized turbulence generation motivated us to separate the flow into submesoscale and finescale components utilizing a 2D low-pass Lanczos filter in the horizontal, enabling a direct investigation of the interaction between the flow components. For this decomposition, we identified a cutoff length scale of $O(100\,\mathrm{m})$ by examining velocity spectra and noticing a change in flow behavior from quasi-2D to 3D below this scale and also a change in the spectral slope.

The separation of finescales brought to light an underlying structure to the submesoscale vertical velocity influenced by coherent structures, elucidating vertical transport at the front. At the submesoscale, vertical velocity exhibits well-separated upwelling and downwelling regions. Near the surface, the submesoscale vertical velocity is negative mainly in the vortex filaments, whereas it is positive in the rest of the front, over a more expansive region. Although large in magnitude, the mean contribution from the finescale in the submesoscale upwelling/downwelling regions were 7-8 time smaller, suggesting dominance of submesoscale on vertical transport. This analysis underlines a very interesting quality of the submesoscale vortex filaments. They are thin, which allow them to develop large vertical velocity, but they are also long and can efficiently transport water masses across the front to facilitate its restratification. The filament like structures are ubiquitous and have been observed in various parts of the upper ocean. This study shows that the filament structures associated with a mixed-layer front play a central role in vertical transport in the surface ocean.

The scale decomposition permitted an explicit investigation of the energy interaction between the quasi-2D submesoscale and the 3D turbulent finescale. The conversion of submesoscale kinetic energy (KE) to finescale KE occurs through the transfer term in the finescale KE balance equation, and it is related to the finescale residual production term in the submesoscale KE balance. It was found that the finescale residual production was around two times larger than the submesoscale subgrid dissipation, but was significantly smaller than the submesoscale buoyancy production that energizes submesoscale motions. Overall, the submesoscale internal dynamics at an unforced front was found to be weak at transferring large-scale energy to the turbulent scales. Nevertheless, it is worth mentioning that the reservoirs of submesoscale potential and kinetic energy are large.

In this study, the role of frontogenesis in the submesoscale dynamics was also investigated by examining the transport equation for the square of horizontal buoyancy gradient. We showed that over much of the depth, including the near-surface region, the horizontal strain and shear of the horizontal velocity lead to frontogenesis that forms the vortex filaments. We were also able to examine frontolysis – the process that arrests the ever-sharpening front. Near the surface (above 10 m depth), frontal sharpening was countered by the horizontal diffusion (resolved and subgrid) and at depth by the horizontal gradients of the vertical velocity. It is worth noting that frontogenesis studied here is a result of inherent submesoscale dynamics. In the real ocean, other processes such as straining by the large-scale currents (e.g. the strain field between two mesoscale eddies) can also be important.

The way surface water subducts to the ocean's interior is an important problem in oceanography, often difficult to measure in the ocean because vertical velocity component is orders of magnitude weaker than the horizontal components. A simple setup such as the one analyzed in Chapter 2 can help elucidate this process. The simulation showed that the submesoscale coherent structures formed during the nonlinear evolution of baroclinic MLI play an important role in vertical transport and subduction. The dynamics is transient as the flow velocity changes due to advection of the coherent structures by the mean flow. The path fluid parcels follow are complex and can not be understood by examining the snapshots of the Eulerian velocity field. A Lagrangian study is better suited for the analysis.

In Chapter 3, we investigated the Lagrangian transport and dispersion characteristics of submesoscale dynamics by releasing a large number of tracer particles that move with the local fluid velocity, i.e., they behave like material points. By analyzing particle trajectories, we discovered a filament/eddy/lobe framework that clarifies upwelling/dowelling at the front. In the central region, particles circulate in inclined lobes with anticyclonic circulation when viewed from the top. Each lobe is associated with a coherent cyclonic eddy, and both structures move together at the front. In addition, there are coherent filaments that connect the light/heavy edge of the front with the lobes in the central region. These filaments transfer edge particles to the lobe – light-edge particles to the top surface while heavy-edge particles to the underside. The influx of edge particles into the central region causes particles circulating in the lobes to adjust, which leads to slumping and restratification of the front.

The time scale of vertical transport was also examined by monitoring the vertical motion of the center of mass of particle clouds. The analysis revealed a subinertial time scale for vertical transport, which is comparable to the time scale of MLI growing at the front. The time evolution of the volume-averaged stratification also suggested the slow time scale. However, the particles moving through the vortex filaments or circulating in lobes can have large vertical velocities (up to $0.02\,\mathrm{m\,s^{-1}}$), and their role in vertical transport is not readily evident. The filament/eddy/lobe framework suggests that vertical velocity alone does not control vertical transport. It also depends on the rate at which the edge particles are drawn into the front. This whole process is controlled by submesoscale dynamics evolving at subinertial time scales.

Lagrangian spectra of the particle velocity show a separation in the time scale: the motions are 3D at fast time scales with angular frequencies $\omega_f < 10f$ (smaller than $\sim 1\,\mathrm{h}$) but are quasi-2D at subinertial time scales. The autocorrelation functions of the horizontal velocity components exhibit a substantial control of the subinertial component, as their amplitudes decrease oscillating with the near-inertial frequency. In contrast, the autocorrelation function of the vertical velocity shows a sharp decrease in its amplitude over an hour followed by a slower, near-inertial time response, similar to what was observed for the horizontal components. The investigation of single-particle dispersion shows super-diffusive behavior (exponent $\alpha = 1.5 \pm 0.2$) at late times (after about three inertial time periods), corresponding to the vertically and horizontally sheared mean current in the along-front direction. This super-diffusive regime was also observed for the pair-dispersion. Additionally, the pair-dispersion reveals a t^3 regime. However, the existence of an inertial subrange associated with the forward energy cascade is not guaranteed. The reason is that the same regime was also discovered with the surface particle pairs, strongly influenced by strain and shear of the horizontal velocity. The study of multiparticle statistics using groups of four particles (tetrads) reveals filamentogenetic tendencies in the vortex filaments. Tetrads passing through the filaments are deformed into needle-like objects, which occurs as a fast time scale process within an hour.

We have considered a more realistic scenario of the upper-ocean front evolving in a turbulent environment in Chapter 4. The model setup uses a warm-filament with 2 km wide fronts, in thermal wind balance at the left and right edges. The warm-filament is contained in a weakly stratified upper-layer of depth 70 m, overlying a strongly stratified thermocline. In this setup, turbulence is generated by applying surface cooling fluxes, after the vortex filaments and eddies develop in an unforced evolution. The interaction between the submesoscale dynamics and the finescale convection is investigated in a parametric study by varying the magnitude of surface cooling. Depending on the strength of imposed surface buoyancy flux relative to the buoyancy flux generated by the submesoscale dynamics, the cases range from weak to strong; the strong case has surface cooling which is comparable to the unforced submesoscale vertical buoyancy flux.

The simulations showed a two-way coupling between submesoscale dynamics and the finescale convective turbulence. It was found that the growth of convective plumes is inhomogeneous within the front affected by the coherent structures. The plumes grow through vortex filaments but are suppressed in other parts of the front, i.e., the shallow regions. However, the plumes are deeper in shallow regions when the cooling is larger. This reveals the influence of submesoscale dynamics on convection but the effect on submesoscale motions is not apparent.

We find that the flow can still be effectively decomposed into submesoscale and finescale (now comprising both convective turbulence and that resulting from the secondary symmetric instability) components, and follow the approach utilized in Chapter 2 for the decomposition. The effect on the submesoscale dynamics is readily noticeable from the submesoscale fields. The submesoscale vertical velocity shows enhanced downwelling in the vortex filaments in the case with strong cooling compared to the case with weak cooling. Interestingly, this result implies strengthening of submesoscale frontogenesis, as opposed to weakening due to increased horizontal mixing by convective turbulence.

The interaction between submesoscale dynamics and convection was further quantified by examining the kinetic and potential energy balance equations for the two regimes. It was observed that with imposed surface cooling, the imbalance within the front grows, which depends on both the magnitude of the surface cooling flux and time, since convection becomes more energetic as plumes develop. In accordance with the increased imbalance, it was observed that buoyancy production increases, leading to enhanced available potential energy extraction from the front. With the strongest cooling, the peak extraction was found to be four times stronger compared to the weak cooling. The potential energy extracted by the submesoscale buoyancy production energizes the the submesoscale velocity. There is also a conversion of submesoscale

KE into finescales through residual production term, which is closely related to the transfer term in finescale KE balance equation. Although the unforced MLI is not effective at extracting energy from the submesoscale velocity, the interaction with strong boundary layer turbulence can be significant. It was found that in strong cooling case, the production of finescales from submesoscale velocity can be as large as about half of that by the finescale buoyancy production.

We also showed that regions with negative potential vorticity develop at the front as surface cooling takes out potential vorticity from the system. These regions are unstable to symmetric instability, which draws energy from the vertical shear of the submesoscale velocity. We found symmetric instability to be an important source of finescales at depth. Furthermore, these instabilities grow stronger as the surface cooling flux is increased.

This thesis presents a detailed analysis of submesoscale dynamics with and without surface forcing, focusing on vertical transport and interaction with turbulent finescale. However, there are other related problems that remain unexplored, and the present work can be extended. Below, a few problems are described. The impact of surface wind on submesoscale coherent structures is unclear. In addition to generating turbulence, winds also cause Ekman transport that can interact with these structures. Surface cooling has been shown to affect the organization of the submesoscale velocity; however, the change in the behavior of lobe/eddy/filament structures identified in the unforced simulation is not apparent. The presence of finescales in the interior of the front is likely to complicate the coherent transport pathways of the fluid parcels. Finally, the Lagrangian study presented here can be extended to include inertial particles. These studies can shed light on the transport of small but buoyant pollutants such as oil droplets and microplastics to the interior by the submesoscale currents.

Appendix A

Description of particle advection code

For the Lagrangian transport and dispersion studies performed in Chapter 3, a particle advection code was developed. Here, we describe the numerical schemes utilized for the code and discuss the test cases used for its validation. The particle code was finally run coupled with our in-house Navier-Stokes solver (Chapter 2, Brucker, 2009). We also briefly discuss the integration of the particle code with the fluid solver. The particle solver uses some of the data structures of the cfd2lcs library. This inclusion has considerably simplified the structure of the particle code, while making its integration with the fluid solver much simpler. The cfd2lcs library performs particle tracking to compute the forward and backward finite-time Lyapunov exponents; some of the examples are discussed in the paper by Finn and Apte (2013).

A.1 Particle advection

We are interested in the Lagrangian description of the flow and want to know how the material points, i.e., tracer particles, move. Specifically, we are interested in the motion of these particles at a mixed-layer front, evolving with nonlinear barolinic instability in a transient dynamics dominated by submesoscale coherent structures. The position $\mathbf{x}_p(t) = (x_p(t), y_p(t), z_p(t))$ of a tracer particle is given by

$$\frac{d\mathbf{x}_p}{dt} = \mathbf{u}(\mathbf{x}_p, t), \tag{A.1}$$

where $\mathbf{u} = (u, v, w)$ is the time dependent fluid velocity at the particle's position at time t. We obtain the particle's trajectory by numerically integrating Eq. A.1 in time, when the fluid velocity $\mathbf{u}(\mathbf{x}_p, t)$ is know. However, the fluid velocity obtained from the CFD solver is known only at discrete grid points in space and time. This restricted availability of fluid velocity necessitates its interpolation to an arbitrary location within the domain at an arbitrary time. We elaborate on the process of trajectory computation below.

A.2 Computation of particles' trajectories

We run the particle solver synchronized with the CFD solver. First, the CFD solver marches the flow in time, using a time step decided by specifying the Courant-Friedrichs-Lewy (CFL) number. Subsequently, the particle solver updates the particle trajectories over the same time interval. The particle solver may employ a different CFL number, generating a different time step for the particle advection. Nevertheless, the time step is adjusted so that it is an integer multiple of the flow time step.

Consider the time step $\Delta T_N = T_{N+1} - T_N$ during which the CFD solver advances the fluid velocity from $\mathbf{u}(\mathbf{x}, T_N)$ to $\mathbf{u}(\mathbf{x}, T_{N+1})$. Further, assume that the particle solver during the same time interval updates particle trajectories n times using a step size of $h^N = \Delta T_N / n$. Thus, $t_i^N = T_N + ih^N$, where $i = 1, 2, \ldots, n$, and $t_n^N = T_{N+1}$.

A.2.1 Time marching

An explicit third-order Runge-Kutta (RK3) scheme has been used for time-marching the trajectories. The particle trajectory $\mathbf{x}_p(t)$ during the time interval $[t_m^N, t_{m+1}^N]$ is advanced as follows:

$$\mathbf{x}_p(t_{m+1}^N) = \mathbf{x}_p(t_m^N) + \frac{1}{6}(\mathbf{k}_1 + 4\mathbf{k}_2 + \mathbf{k}_3), \tag{A.2}$$

where

$$\mathbf{k}_1 = h^N \mathbf{u}(\mathbf{x}_p(t_m^N), t_m^N), \tag{A.3}$$

$$\mathbf{k}_2 = h^N \mathbf{u}(\mathbf{x}_p(t_m^N) + \frac{1}{2}\mathbf{k}_1, t_m^N + \frac{h^N}{2}), \tag{A.4}$$

$$\mathbf{k}_3 = h^N \mathbf{u}(\mathbf{x}_p(t_m^N) - \mathbf{k}_1 + 2\mathbf{k}_2, t_m^N + h^N). \tag{A.5}$$

Notice that in the Runge-Kutta time-marching scheme discussed above, we need to use an interpolation method in space for calculating $\mathbf{u}(\mathbf{x}_p(t_m^N), t_m^N)$, while both spatial and time interpolations for calculating $\mathbf{u}(\mathbf{x}_p(t_m^N) + \frac{1}{2}\mathbf{k}_1, t_m^N + \frac{h^N}{2})$ and $\mathbf{u}(\mathbf{x}_p(t_m^N) - \mathbf{k}_1 + 2\mathbf{k}_2, t_m^N + h^N)$. The particle solver uses a CFL number smaller than one to ensure a stable trajectory calculation.

A.2.2 Interpolation of fluid velocity in time

Linear interpolation is used in time for computing the fluid velocity at an intermediate time $t \in [t_N, t_{N+1}]$. Thus,

$$u(\mathbf{x}, t) = (1 - r)u(\mathbf{x}, t_N) + ru(\mathbf{x}, t_{N+1}), \tag{A.6}$$

where $r = (t - t_N)/(t_{N+1} - t_N)$.

A.2.3 Interpolation of fluid velocity in space

Fourth order Lagrange interpolation is used for the spatial interpolation in 3D. CFD solver stores the velocity components (u, v, w) at the face-centers of the grid cells: u-velocity

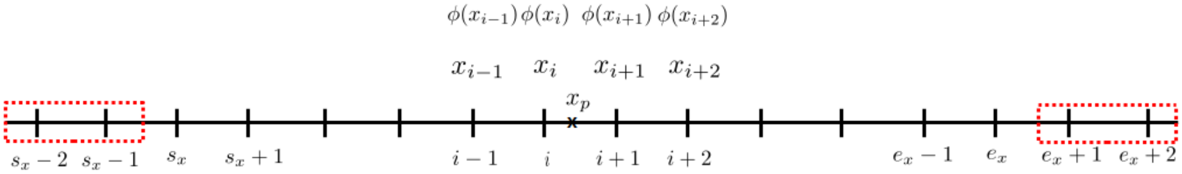

Figure A.1: An example of 1D grid in the x direction. The internal points as well as boundary points (enclosed by dotted rectangles) have been identified in this figure. A group of four points $(x_{i-1}, x_i, x_{i+1}, x_{i+2})$ are shown for interpolating $\phi(x)$ at x_p.

component at faces perpendicular to x axis, v-velocity component at faces perpendicular to y axis, and w-velocity component at faces perpendicular to z axis. For the spatial interpolation, all the velocity components are interpolated to the cell centers. Thus, all the flow variables (e.g., pressure p and temperature T), including the velocity components, are now stored at the cell centers and can be interpolated following the same procedure. For the consideration of spatial interpolation, the time dependence of the discrete flow variable is not important. We only focus on the spatial variability of the flow variable.

For simplicity, we first describe the method in 1D; its generalization to 3D is straight forward. Consider the interpolation of a scalar $\phi(x_i)$ at a point x_p within the domain (i.e. $0 \le x_p \le L_x$); the scalar $\phi(x_i)$ is defined over a grid x_i spanning the whole domain, with $i \in [s_x - 2, e_x + 2]$. In the grid, $i \in [s_x, e_x]$ are interior points, and rest are the boundary points, two at each end. The fourth-order Lagrange interpolation involves cubic basis functions generated using a set of four consecutive grid points. Typically $N_x = e_x - s_x + 1$ is much larger than four, and the points must be selected appropriately. We identify the grid interval $[x_i, x_{i+1}]$ containing x_p and the four points selected for the interpolation are x_{i-1}, x_i, x_{i+1}, and x_{i+2} (Fig. A.1). The Lagrangian basis functions associated with the chosen grid points are the following:

$$L_{i-1}(x) = \frac{(x-x_i)(x-x_{i+1})(x-x_{i+2})}{(x_{i-1}-x_i)(x_{i-1}-x_{i+1})(x_{i-1}-x_{i+2})}, \tag{A.7}$$

$$L_i(x) = \frac{(x-x_{i-1})(x-x_{i+1})(x-x_{i+2})}{(x_i-x_{i-1})(x_i-x_{i+1})(x_i-x_{i+2})}, \tag{A.8}$$

$$L_{i+1}(x) = \frac{(x-x_{i-1})(x-x_i)(x-x_{i+2})}{(x_{i+1}-x_{i-1})(x_{i+1}-x_i)(x_{i+1}-x_{i+2})}, \tag{A.9}$$

$$L_{i+2}(x) = \frac{(x-x_{i-1})(x-x_i)(x-x_{i+1})}{(x_{i+2}-x_{i-1})(x_{i+2}-x_i)(x_{i+2}-x_{i+1})}, \tag{A.10}$$

and the interpolation of $\phi(x_i)$ at x_p is given by $\phi(x_p) \approx \sum_{l=i-1}^{i+2} \phi(x_l) L_l(x_p)$.

In 3D, we have $\phi(x,y,z)$ defined over a regular grid with ordered points (x_i, y_j, z_k), where $i = s_x-2, s_x-1, s_x, \ldots, e_x, e_x+1, e_x+2$, $j = s_y-2, s_y-1, s_y, \ldots, e_y, e_y+1, e_y+2$, and $k = s_z-2, s_z-1, s_z, \ldots, e_z, e_z+1, e_z+2$. In order to extend the fourth-order Lagrange interpolation to 3D, we analogously identify a cell with diagonally opposite vertices as (x_i, y_j, z_k) and $(x_{i+1}, y_{j+1}, z_{k+1})$ containing the point (x_p, y_p, z_p). Furthermore, sets of Lagrangian basis functions, such as Eqs. A.7-A.10 in 1D, are calculated in each coordinate direction: $(L_{i-1}(x), L_i(x), L_{i+1}(x), L_{i+2}(x))$ associated with points $(x_{i-1}, x_i, x_{i+1}, x_{i+1})$ on a grid line along x, $\left(M_{j-1}(y), M_j(y), M_{j+1}(y), M_{j+2}(y)\right)$ associated with points $(y_{j-1}, y_j, y_{j+1}, y_{j+1})$ on a grid line along y, and $(N_{k-1}(z), N_k(z), N_{k+1}(z), N_{k+2}(z))$ associated with points $(z_{k-1}, z_k, z_{k+1}, z_{k+1})$ on a grid line along z. A continuous function $\tilde{\phi}(x,y,z)$ approximating $\phi(x_i, y_j, z_k)$ over the identified cube can be obtained by successively introducing Lagrange basis functions along x, y, and z directions. Thus,

$$\tilde{\phi}(x,y,z) = \sum_{l=i-1}^{i+2} \phi(x_l, y, z) L_l(x_p), \tag{A.11}$$

$$= \sum_{l=i-1}^{i+2} \sum_{m=j-1}^{j+2} \phi(x_l, y_m, z) L_l(x_p) L_m(y_p), \tag{A.12}$$

$$= \sum_{l=i-1}^{i+2} \sum_{m=j-1}^{j+2} \sum_{n=k-1}^{k+2} \phi(x_l, y_m, z_n) L_l(x_p) M_m(y_p) N_n(z_p), \tag{A.13}$$

and we get $\phi(x_p, y_p, z_p) \approx \tilde{\phi}(x_p, y_p, z_p)$.

A.3 Parallelization of the particle code

To be able to simulate a large number of tracer particles and to run the particle solver on-the-fly with our fluid solver, the particle code is parallelized following domain decomposition. In the parallel setting, the treatment of particles crossing the subdomain boundaries and their exchange with the neighboring subdomain requires careful handling. More details on these two aspects are discussed below.

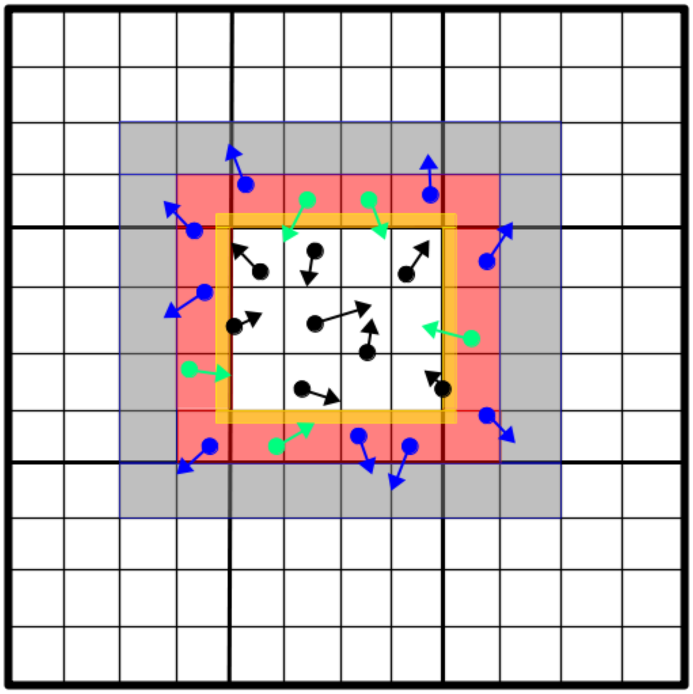

Figure A.2: The figure shows a subdomain in 2D, with two layers of ghost cells employed for the particle advection; the first layer is shown in red and the second layer in gray. The particles in the first ghost cells in the thin yellow region adjacent to the subdomain boundary are excluded from exchange with the neighboring subdomains. Furthermore, in the remaining parts of the first ghost cells only blue particles that have a tendency to move out of the subdomain are exchanged, while green particles that tend to re-enter the subdomain are retained. In this figure, the interior particles are shown in black.

A.3.1 Extended subdomain and ghost cells

A subdomain can have its boundaries in the interior of the domain or coinciding with the physical boundaries of the domain. During an RK3 substep, some of the particles in the cells adjacent to the subdomain boundaries may exit the subdomain. To handle velocity interpolation for these particles, the subdomain is extended by adding two layers of ‘ghost’ cells. The ghost cells across an interior boundary is an extension of the subdomain in the fluid domain, while those adjacent to a physical boundary represent a fictitious extension outside the domain and are included for numerical convenience. The condition of CFL < 1 in the particle solver ensures that the particles exiting the domain remain in the first layer of the ghost cells and can be treated appropriately in the extended subdomain.

After completing a full RK3 step, the particles in the first ghost layer are exchanged with the neighboring subdomains. However, not all of the first ghost layer particles are exchanged. The flow studied here involves strong circulations created by coherent eddies, and some of the particles that exit the subdomain tend to re-enter. These re-entering particles are often very close to the subdomain boundaries and have small velocity magnitudes. Therefore, we create a thin region within the first layer of ghost cells attached to the subdomain boundaries, and the particles residing there are excluded from the exchange. Only those particles outside this thin region layer with velocity directed outward of the subdomain are exchanged; the particles that have the tendency to move into the subdomain are also retained. The way boundary particles are identified for exchange with the neighbors is illustrated in Fig. A.2 using a domain decomposition in 2D. Note that the particle solver developed here computes trajectories in 3D.

The physical boundaries of the domain are modeled as either periodic or slip walls. The ghost cells associated with periodic boundaries are treated in the same manner as the interior ghost cells. However, the ghost cells associated with the walls use the velocity of the first interior cells. Since the wall normal velocity is zero, the tracer particles do not cross this boundary. Thus the exchange of particles across the wall boundaries is not required.

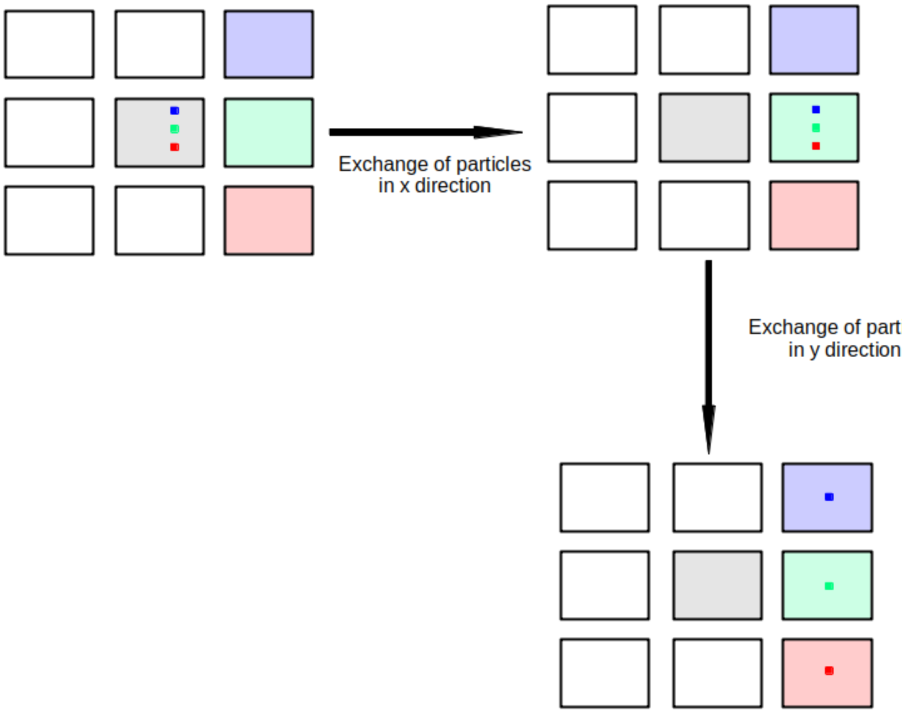

Figure A.3: Figure illustrating the exchange of boundary particles with the neighboring subdomains, in the domain decomposition of a 2D problem. During the exchange in the x direction, the center subdomain sends the boundary particles (blue, green, and red packets) to the right neighbor, which is shown in green. Subsequently, during the exchange of the particles in the y direction, the green subdomain retains the particles in the green packet, but transfer the particles in blue and red packets to its top and bottom neighbors, where they are supposed to go from the center subdomain.

A.3.2 Exchanging particles with the neighboring subdomains

In a domain decomposition with 3D topology, a rectangular subdomain can exchange particles with 26 neighbors – 6 with shared faces, 12 with shared edges, and 8 with shared vertices. Identifying particles and exchanging them with the neighbors can be cumbersome.

We avoid this problem by exchanging particles only across the faces of the subdomain and performing the exchange in sequence along each coordinate direction. First, the eligible particles found outside the subdomain boundaries in the x direction are exchanged with the neighboring subdomains. The exchanged particles are then included in the pool of subdomain particles. Next, the eligible particles outside the subdomain boundaries in the y direction are identified and exchanged with the face sharing neighbors. Finally, this process is repeated in the z direction. Once the particles are exchanged in all three coordinate directions, they become distributed among the neighboring subdomains as required. This processes has been illustrated in Fig. A.3 for a simple 2D setup.

A.4 Validations for the particle code

We investigate the performance of the fourth-order Lagrange interpolation implemented in the code and examine advection of tracer particles by known velocity fields.

A.4.1 Accuracy of the interpolation scheme

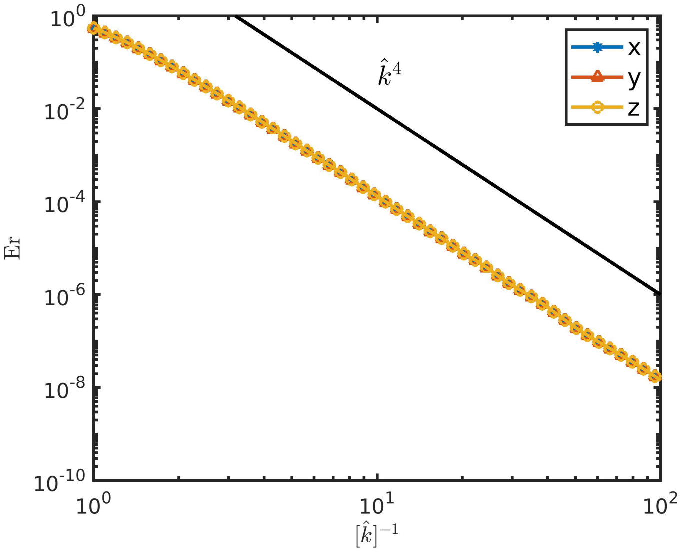

Figure A.4: Error in the interpolation of single Fourier modes along x, y, and z direction. The nondimensional $\hat{k} = kL/(2\pi N)$ changes over two orders of magnitude between 0.01 and 1. The smallest wavelength 2Δ resolved by the grid corresponds to $\hat{k} = 0.5$.

We adopt the single mode analysis of Balachandar and Maxey (1989) to validate the interpolation method used in the particle code. A domain of size L^3 is discretized with N grid points in each coordinate direction. The velocity components (u, v, w) are initialized with single Fourier modes $(\sin(kx), \sin(ky), \sin(kz))$ and the wavenumber is varied such that the nondimensionalized wavenumber $\hat{k} = kL/(2\pi N)$ changes from 0.01 to 1; $\Delta = L/N$ is the grid spacing in each coordinate direction, and the smallest wavelength (2Δ) resolved by the grid corresponds to $\hat{k} = 0.5$. In a numerical simulation, the velocity components can be considered as a linear superposition of a large number of such modes, with wavenumbers having components in all three directions. We introduce uniformly spaced particles along arbitrary lines along x, y and z axes and compute the interpolated velocity components $(\tilde{u}_p, \tilde{v}_p, \tilde{w}_p)$ for the particles. The spacing between two adjacent particle is 5 times smaller than Δ. The root-mean-square of the difference between the interpolated velocity and the Fourier mode provides an estimate for the error in the interpolation. The error estimates for the Fourier modes in x, y and z directions are shown is Fig. A.4. It can be observed from the figure that the interpolation error can be significant at the grid scale. However, the error decreases as $\hat{k}^4$ at larger scales and the accuracy improves. The drop in the interpolation error as $\hat{k}^4$ is consistent with the fourth order accuracy of the interpolation method employed here.

A.4.2 Particle advection in the ABC flow

As the first test case, we advect tracer particles in the Arnold, Beltrami, Childress (ABC) flow. In the rectangular Cartesian coordinates, the flow has 2π-periodicity in x, y, and z-directions and the velocity (u, v, w) is given by

$$u = A\sin(z) + C\cos(y), \tag{A.14}$$

$$v = B\sin(x) + A\cos(z), \tag{A.15}$$

$$w = C\sin(y) + B\cos(x), \tag{A.16}$$

Where A, B, and C are three real parameters; the values chosen for the simulation are $A = \sqrt{3}$, $B = \sqrt{2}$, and $C = 1$. The ABC flow is a steady state solution of the Euler's equation. Although

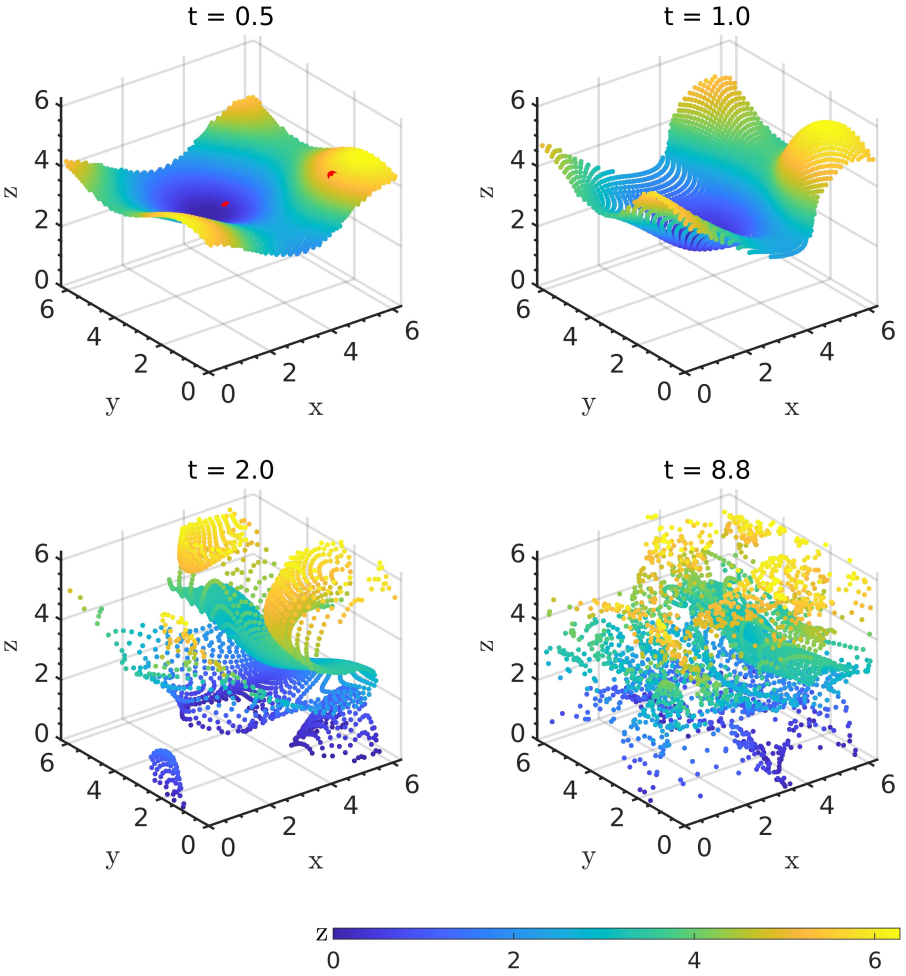

Figure A.5: Particles released at $z = 3.2$ are plotted at different times as they advect with the ABC flow.

steady, the flow exhibits Lagrangian chaos by which the trajectories of two particles close to each other diverge exponentially with time, while remaining in a bounded domain (Dombre et al., 1986). In such systems, a particle trajectory can fill the entire domain and the position of the particle after a long time becomes unpredictable.

The tracer particles were seeded over the whole domain and advected for 10 time units. The time evolution of the particles initially at $z = 3.2$ has been shown in Figs. A.5a-d. The horizontal surface over which the particles were distributed initially deforms with time and,

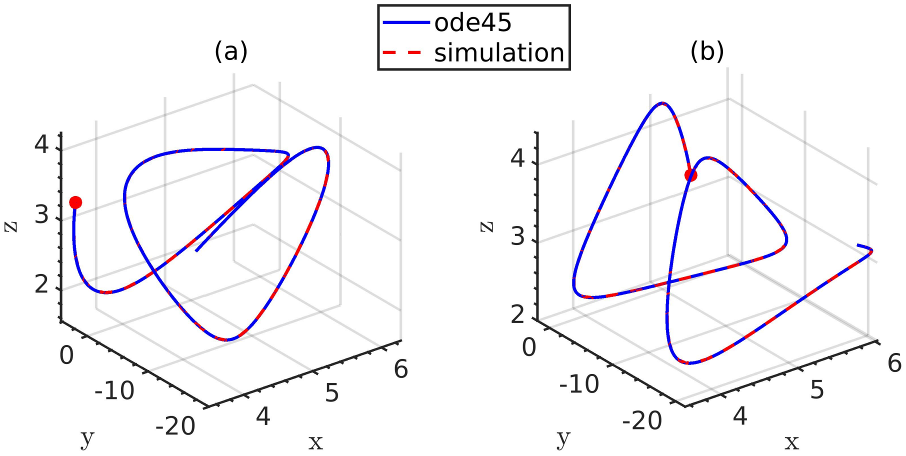

Figure A.6: Comparing the trajectories of two randomly selected particles computed from the particle simulation and MATLAB ode45 subroutine. The particles are shown in Fig. A.5a by solid-red circles.

by $t = 10$, a significant potion of the particle become randomly dispersed in the domain. We arbitrarily select any two particles, shown by solid-red circles in Fig. A.5a., and compare their trajectories from the simulation with the trajectories calculated using MATLAB ode45 subroutine. As shown in Figs. A.6a,b, the trajectories calculated using the two methods are practically identical.

A.4.3 Particle advection in the double-gyre flow

We also test the advection of the particle in the time varying double-gyre flow. The flow is a simplified representation of the double-gyre configuration often encountered in the geophysical flows and has been utilized extensively for investigating the embedded Lagrangian coherent structures (Allshouse and Peacock, 2015, Shadden et al., 2005). The stream function for this flow is given by

$$\psi(x,y,t) = A\sin(\pi f(x,t))\sin(\pi y), \tag{A.17}$$

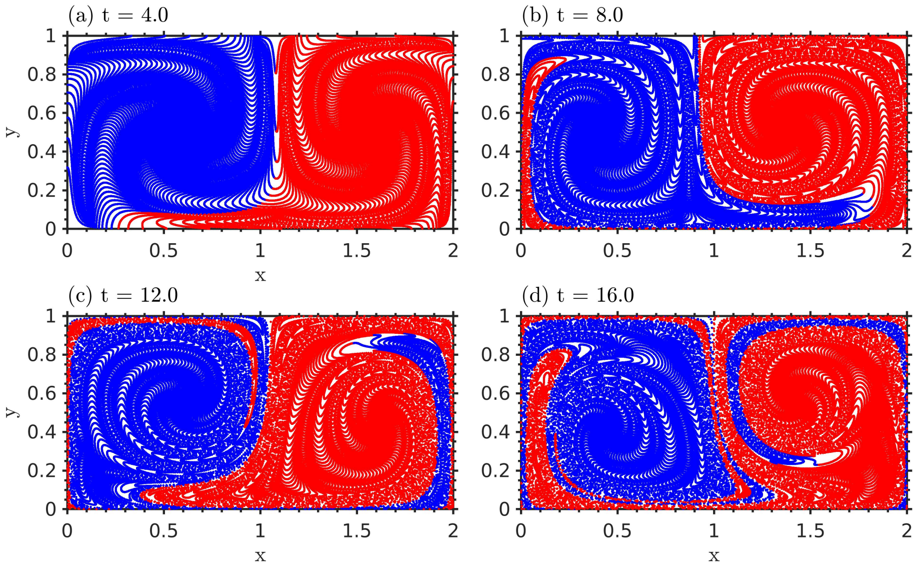

Figure A.7: Particles released in the double-gyre flow plotted at different times as they advect.

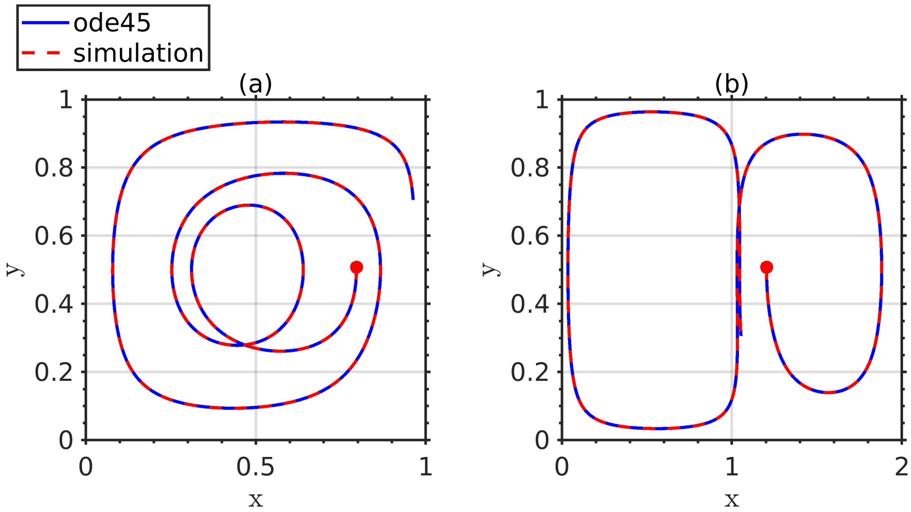

Figure A.8: Comparing the trajectories of two chosen particles computed from the particle simulation and MATLAB ode45 subroutine. The particles were initially at (0.8, 0.5) and (1.2, 0.5)

where

$$f(x,t) = a(t)x^2 + b(t)x, \tag{A.18}$$

$$a(t) = \varepsilon \sin(\omega t), \tag{A.19}$$

$$b(t) = 1 - 2\varepsilon \sin(\omega t); \tag{A.20}$$

The flow is confined within a rectangular domain with $L_x = 2$ in the x direction and $L_y = 1$ in the y direction. Using the stream function, the velocity (u,v) in the double-gyre can be calculated as

$$u \equiv -\frac{\partial\psi}{\partial y} = -\pi A \sin(\pi f(x,t)) \cos(\pi y), \tag{A.21}$$

$$v \equiv \frac{\partial\psi}{\partial x} = \pi A \cos(\pi f(x,t)) \sin(\pi y) \frac{\partial f}{\partial x}. \tag{A.22}$$

If $\varepsilon \neq 0$, then the flow is time dependent and the left and right gyres expand and contract in the x direction periodically with angular frequency ω. The parameter ε controls the amount by which the line separating the two gyres move from its neutral position $x = 1$. The parameter values used for the double-gyre flow advecting the particles are the following: $A = 0.1$, $\varepsilon = 0.1$, and $\omega = 2\pi/10$. Thus the time period for the expansion and contraction of the gyres is 10 units.

The time evolution of the tracer particles in the double gyre is depicted in Figs. A.7a-c. The particles in the left gyre is shown in blue color and those in the right gyre are shown in red. The figures reveal intrusion of fluid from the right gyre into the left with time and vice-versa. At late times (e.g, t = 16), the advection of particles by the flow leads to the generation of small-scale local features, and the particles in these regions become disordered. We also compare the trajectories of two selected particles, initially located at (0.8, 0.5) and (1.2, 0.5), with their trajectories calculated using the MATLAB ode45 subroutine (Figs. A.8a,b). Again, the trajectories match perfectly.

A.5 Integration with the CFD solver

The integration of the particle solver with the fluid solver is straightforward. The particle code replicates exactly the same subdomain topology as the CFD solver for the domain decomposition. This allows an efficient communication of the fluid velocity fields from the fluid solver to the particle solver. After the CFD solver advances the flow from T_N to T_{N+1}, the velocity fields stored at the face centers are interpolated to the cell centers and sent to the particle code. The velocity components, however, have only one layer of ghost cells. The particle solver add one additional layer after receiving the velocity fields. It also has the extended fluid velocity at T_N stored in the memory. Subsequently, particles' positions are updated performing n RK3 steps (see Section A.2) until $t_m^N = T_{N+1}$, i.e., when the advection time become synchronized with the simulation time of the CFD solver. Thereafter, the control is returned to the CFD code and the process is repeated.

Bibliography

Allshouse, M. R. and Peacock, T. (2015). Lagrangian based methods for coherent structure detection. Chaos, 25(9):097617.

Arobone, E. and Sarkar, S. (2015). Effects of three-dimensionality on instability and turbulence in a frontal zone. J. Fluid Mech., 784:252–273.

Balachandar, S. and Maxey, M. R. (1989). Methods for evaluating fluid velocities in spectral simulations of turbulence. J. Comput. Phys., 83(1):96–125.

Balwada, D., LaCasce, J. H., and Speer, K. G. (2016). Scale-dependent distribution of kinetic energy from surface drifters in the Gulf of Mexico. Geophys. Res. Lett., 43(20):10856–10863.

Balwada, D., Smith, K. S., and Abernathey, R. (2018). Submesoscale vertical velocities enhance tracer subduction in an idealized Antarctic Circumpolar Current. Geophys. Res. Lett., 45(18):9790–9802.

Barkan, R., Molemaker, M. J., Srinivasan, K., McWilliams, J. C., and D'Asaro, E. A. (2019). The role of horizontal divergence in submesoscale frontogenesis. J. Phys. Oceanogr., 49(6):1593–1618.

Batchelor, G. K. (1952). Diffusion in a field of homogeneous turbulence: II. the relative motion of particles. Math. Proc. Camb. Philos. Soc, 48(2):345–362.

Bennett, A. F. (1984). Relative dispersion: Local and nonlocal dynamics. J. Atmos. Sci., 41(11):1881–1886.

Beron-Vera, F. J. and LaCasce, J. H. (2016). Statistics of simulated and observed pair separations in the Gulf of Mexico. J. Phys. Oceanogr., 46(7):2183–2199.

Biferale, L., Boffetta, G., Celani, A., Devenish, B. J., Lanotte, A., and Toschi, F. (2005). Multiparticle dispersion in fully developed turbulence. Phys. Fluids, 17(11):111701.

Boccaletti, G., Ferrari, R., and Fox-Kemper, B. (2007). Mixed layer instabilities and restratification. J. Phys. Oceanogr., 37:2228–2250.

Brucker, K. A. (2009). Numerical investigation of momentumless wakes in stratified fluids. PhD thesis, UC San Diego.

Callies, J. and Ferrari, R. (2018). Baroclinic instability in the presence of convection. J. Phys. Oceanogr., 48:45–60.

Callies, J., Ferrari, R., Klymak, J. M., and Gula, J. (2015). Seasonality in submesocale turbulence. Nat. Commun., 6(6862).

Capet, X., McWilliams, J. C., Molemaker, M. J., and Shchepetkin, A. F. (2008a). Mesocale to submesoscale transition in the California Current system. Part I: Flow structure, eddy flux, and observational tests. J. Phys. Oceanogr., 38:29–43.

Capet, X., McWilliams, J. C., Molemaker, M. J., and Shchepetkin, A. F. (2008b). Mesoscale to submesoscale transition in the California Current system. Part II: Frontal processes. J. Phys. Oceanogr., 38:44–64, doi:10.1175/ 2007JPO3672.1.

Capet, X., McWilliams, J. C., Molemaker, M. J., and Shchepetkin, A. F. (2008c). Mesoscale to submesoscale transition in the California Current System. Part iii: Energy balance and flux. J. Phys. Oceanogr., 38(10):2256 – 2269.

Charney, J. G. (1971). Geostrophic turbulence. J. Atmos. Sci., 28(6):1087–1095.

D'Asaro, E. A., Lee, C. M., Rainville, L., Harcourt, R. R., and Thomas, L. N. (2011). Enhanced turbulence and energy dissipation at ocean fronts. Science, 322(318–322, doi:10.1126/science.1201515).

D'Asaro, E. A., Shcherbina, A. Y., Klymak, J. M., Molemaker, J., Novelli, G., Guigand, C. M., Haza, A. C., Haus, B. K., Ryan, E. H., Jacobs, G. A., Huntley, H. S., Laxague, N. J. M., Chen, S., Judt, F., McWilliams, J. C., Barkan, R., Kirwan, A. D., Poje, A. C., and Özgökmen, T. M. (2018). Ocean convergence and the dispersion of flotsam. Proc. Natl. Acad. Sci., 115(6):1162–1167.

Deardorff, J. W. (1980). Stratocumulus-capped mixed layers derived from a three-dimensional model. Bound.-Layer Meteorol., 18(4):495–527.

Dombre, T., Frisch, U., Greene, J. M., Hénon, M., Mehr, A., and Soward, A. M. (1986). Chaotic streamlines in the ABC flows. J. Fluid Mech., 167:353–391.

Ducros, F., Comte, P., and Lesieur, M. (1996). Large-eddy simulation of transition to turbulence in a boundary layer developing spatially over a flat plate. J. Fluid Mech., 326:1–36.

Eady, E. T. (1949). Long waves and cyclone waves. Tellus, 1:33–52.

Fedorovich, E., Conzemius, R., and Mironov, D. (2004). Convective entrainment into a shear-free, linearly stratified atmosphere: Bulk models reevaluated through large eddy simulations. J. Atmos. Sci., 61(3):281–295.

Finn, J. and Apte, S. V. (2013). Integrated computation of finite-time Lyapunov exponent fields during direct numerical simulation of unsteady flows. Chaos, 23(1):013145.

Fox-Kemper, B., Ferrari, R., and Hallberg, R. (2008). Parameterization of mixed layer eddies. Part I: Theory and diagnosis. J. Phys. Oceanogr., 38:1145–1165.

Freilich, M. and Mahadevan, A. (2021). Coherent pathways for subduction from the surface mixed layer at ocean fronts. J. Geophys. Res. Oceans, n/a(n/a):e2020JC017042.

Germano, M. (1986). A proposal for a redefinition of the turbulent stresses in the filtered Navier–Stokes equations. Phys. Fluids, 29(7):2323–2324.

Gula, J., Molemaker, M. J., and McWilliams, J. C. (2014). Submesoscale cold filaments in the Gulf Stream. J. Phys. Oceanogr., 44:2617–2643.

Gula, J., Molemaker, M. J., and McWilliams, J. C. (2015). Gulf Stream dynamics along the southeastern U.S. seaboard. J. Phys. Oceanogr., 45(3):690–715.

Haine, T. W. N. and Marshall, J. (1998). Gravitational, symmetric and baroclinic instability of the ocean mixed layer. J. Phys. Oceanogr., 28:634–658.

Hamlington, P. E., Van Roekel, L. P., Fox-Kemper, B., Julien, K., and Chini, G. P. (2014). Langmuir-submesoscale interactions: Descriptive analysis of multiscale frontal spindown simulations. J. Phys. Oceanogr., 44:2249–2272.

Haza, A. C., Özgökmen, T. M., and Hogan, P. (2016). Impact of submesoscales on surface material distribution in a gulf of Mexico mesoscale eddy. Ocean Modelling, 107:28–47.

Hosegood, P., Gregg, M. C., and Alford, M. H. (2006). Sub-mesoscale lateral density structure in the oceanic surface mixed layer. Geophys. Res. Lett., 33(22).

Hoskins, B. J. (1974). The role of potential vorticity in symmetric stability and instability. Q. J. Royal Meteorol. Soc., 100:480–482.

Hoskins, B. J. (1982). The mathematical theory of frontogenesis. Ann. Rev. Fluid Mech., 14:131–151.

Hoskins, B. J. and Bretherton, F. P. (1972). Atmospheric frontogenesis models: Mathematical formulation and solution. J. Atmos. Sci., 29:11–37.

Kraichnan, R. H. (1967). Inertial ranges in two-dimensional turbulence. 10(7):1417–1423.

LaCasce, J. H. (2008). Statistics from Lagrangian observations. Prog. Oceanogr., 77(1):1–29.

Lapeyre, G., Klein, P., and Hua, B. L. (2006). Oceanic restratification forced by surface frontogenesis. J. Phys. Oceanogr., 36(8):1577–1590.

Large, W. G., McWilliams, J. C., and Doney, S. C. (1994). Oceanic vertical mixing: A review and a model with a nonlocal boundary layer parameterization. Rev. Geophys., 32(4):363–403.

Lévy, M., Klein, P., and Treguier, A.-M. (2001). Impact of sub-mesoscale physics on production and subduction of phytoplankton in an oligotrophic regime. J. Mar. Res., 59(4):535–565.

Mahadevan, A. (2016). The impact of submesoscale physics on primary productivity of plankton. Ann. Rev. Mar. Sci., 8(1):161–184.

Mahadevan, A. and Archer, D. (2000). Modeling the impact of fronts and mesoscale circulation on the nutrient supply and biogeochemistry of the upper ocean. J. Geophys. Res. Oceans, 105(C1):1209–1225.

Mahadevan, A., Dasaro, E., Lee, C., and Perry, M. J. (2012). Eddy-driven stratification initiates North Atlantic spring phytoplankton blooms. Science, 337(6090):54–58.

Mahadevan, A. and Tandon, A. (2006). An analysis of mechanisms for submesocale vertical motion at ocean fronts. Ocean Modelling, 14:241–256.

Mahadevan, A., Tandon, A., and Ferrari, R. (2010). Rapid changes in mixed layer stratification driven by submesoscale instabilities and winds. J. Geophys. Res., 115:C03017.

McWilliams, J. C. (2016). Submesoscale currents in the ocean. Proc. R. Soc. A, 472:20160117.

McWilliams, J. C. (2017). Submesoscale surface fronts and filaments: secondary circulation, buoyancy flux, and frontogenesis. J. Fluid Mech., 823:391–432.

McWilliams, J. C. (2021). Oceanic frontogenesis. Ann. Rev. Mar. Sci., 13(1):227–253.

McWilliams, J. C., Gula, J., Molemaker, J. M., Renault, L., and Shchepetkin, A. F. (2015). Filament frontogenesis by boundary layer turbulence. J. Phys. Oceanogr., 45:1988–2005.

Mensa, J. A., Garraffo, Z., Griffa, A., Özgökmen, T. M., Haza, A., and Veneziani, M. (2013). Seasonality of the submesoscale dynamics in the Gulf stream region. Ocean Dyn., 63:923–941.

Molinari, R. and Kirwan Jr, A. D. (1975). Calculations of differential kinematic properties from Lagrangian observations in the western Caribbean sea. J. Phys. Oceanogr., 5(3):483–491.

Mudrick, S. E. (1974). A numerical study of frontogenesis. J. Atmos. Sci., 31(4):869–892.

Munk, W., Armi, L., Fischer, K., and Zachariasen, F. (2000). Spirals on the sea. In Proc. R. Soc. Lond. A, volume 456, pages 1217–1280.

Omand, M. M., D'Asaro, E. A., Lee, C. M., Perry, M. J., Briggs, N., Cetinić, I., and Mahadevan, A. (2015). Eddy-driven subduction exports particulate organic carbon from the spring bloom. Science, 348(6231):222–225.

Ou, H. W. (1984). Geostrophic adjustment: A mechanism for frontogenesis. J. Phys. Oceanogr., 14:994–1000.

Ozgokmen, T. M., Poje, A. C., Fischer, P. F., and Haza, A. C. (2011). Large eddy simulations of mixed layer instabilities and sampling strategies. Ocean Modelling, 39:311–331.

Pham, H. T. and Sarkar, S. (2018). Ageostrophic secondary circulation at a submesoscale front and the formation of gravity currents. J. Phys. Oceanogr., 48(10):2507–2529.

Poje, A. C., Özgökmen, T. M., Lipphardt, B. L., Haus, B. K., Ryan, E. H., Haza, A. C., , et al. (2014). Submesoscale dispersion in the vicinity of the Deepwater Horizon spill. Proc. Natl. Acad. Sci., 111(35):12693–12698.

Pumir, A., Shraiman, B. I., and Chertkov, M. (2000). Geometry of Lagrangian dispersion in turbulence. Phys. Rev. Lett., 85(25):5324–5327.

Ramachandran, S., Tandon, A., Mackinnon, J., Lucas, A. J., Pinkel, R., Waterhouse, A. F., Nash, J., Shroyer, E., Mahadevan, A., Weller, R. A., and Farrar, J. T. (2018). Submesoscale processes at shallow salinity fronts in the Bay of Bengal: Observations during the winter monsoon. J. Phys. Oceanogr., 48(3):479–509.

Rudnick, D. L. (1996). Intensive surveys of the Azores front: 2. inferring the geostrophic and vertical velocity fields. J. Geophys. Res., 101:16,291–16,303.

Samelson, R. M. and Skyllingstad, E. D. (2016). Frontogenesis and turbulence: A numerical simulation. J. Atmos. Sci., 73(12):5025–5040.

Sengupta, D., Bharath Raj, G. N., Ravichandran, M., Sree Lekha, J., and Papa, F. (2016). Near-surface salinity and stratification in the north Bay of Bengal from moored observations. Geophys. Res. Lett., 43(9):4448–4456, doi: 10.1002/2016GL068339.

Shadden, S. C., Lekien, F., and Marsden, J. E. (2005). Definition and properties of Lagrangian coherent structures from finite-time Lyapunov exponents in two-dimensional aperiodic flows. Physica D, 212:271–304.

Shcherbina, A. Y., D'Asaro, E. A., Lee, C. M., Klymak, J. M., Molemaker, M. J., and McWilliams, J. C. (2013). Statistics of vertical vorticity, divergence, and strain in a developed submesoscale turbulence field. Geophys. Res. Lett., 40(17):4706–4711.

Siegelman, L., Klein, P., Rivière, P., Thompson, A. F., Torres, H. S., Flexas, M., and Menemenlis, D. (2020). Enhanced upward heat transport at deep submesoscale ocean fronts. Nat. Geosci., 13(1):50–55.

Skyllingstad, E. D. and Samelson, R. M. (2012). Baroclinic frontal instabilities and turbulent mixing in the surface boudary layer. Part I: Unforced simulations. J. Phys. Oceanogr., 42:1701–1716.

Skyllingstad, E. D. and Samelson, R. M. (2020). Instability processes in simulated finite-width ocean fronts. J. Phys. Oceanogr., 50(9):2781–2796.

Spall, M. A. (1995). Frontogenesis, subduction, and cross-front exchange at upper ocean fronts. J. Geophys. Res., 100:2543–2557.

Stamper, M. A. and Taylor, J. R. (2017). The transition from symmetric to baroclinic instability in the Eady model. Ocean Dynamics, 67:65–80.

Stone, P. H. (1966). On non-geostrophic baroclinic stability. J. Atmos. Sci., 23:390–400.

Stone, P. H. (1970). On non-geostrophic baroclinic stability: Part II. J. Atmos. Sci., 27:721–726.

Su, Z., Wang, J., Klein, P., Thompson, A. F., and Menemenlis, D. (2018). Ocean submesoscales as a key component of the global heat budget. Nat. Commun., 9(1):1–8.

Sullivan, P. P. and McWilliams, J. C. (2018). Frontogenesis and frontal arrest of a dense filament in the oceanic surface boundary layer. J. Fluid Mech., 837:341–380.

Tandon, A. and Garrett, C. (1994). Mixed layer restratification due to a horizontal density gradient. J. Phys. Oceanogr., 24(1419-1424).

Taylor, J. R. and Ferrari, R. (2009). On the equilibration of a symmetrically unstable front via a secondary shear instability. J. Fluid Mech., 622:103–113.

Taylor, J. R., Smith, K. M., and Vreugdenhil, C. A. (2020). The influence of submesoscales and vertical mixing on the export of sinking tracers in large-eddy simulations. J. Phys. Oceanogr., 50(5):1319–1339.

Thomas, L. N. and Lee, C. M. (2005). Intensification of ocean fronts by down-front winds. J. Phys. Oceanogr., 35:1086–1102.

Thomas, L. N., Tandon, A., and Mahadevan, A. (2008). Submesoscale processes and dynamics. in Eddy Resolving Ocean Modeling, Geophys. Monogr. Ser., 177:17–38.

Thomas, L. N., Taylor, J. R., Ferrari, R., and Joyce, T. M. (2013). Symmetric instability in the Gulf Stream. Deep-Sea Research II, 91:96–110.

Timmermans, M. L., Cole, S., and Toole, J. (2012). Horizontal density structure and restratification of the Arctic Ocean surface layer. J. Phys. Oceanogr., 42:659–668.

van Aartrijk, M., Clercx, H. J. H., and Winters, K. B. (2008). Single-particle, particle-pair, and multiparticle dispersion of fluid particles in forced stably stratified turbulence. Phys. Fluids, 20(2):025104.

Verma, V., Pham, H. T., and Sarkar, S. (2019). The submesoscale, the finescale and their interaction at a mixed layer front. Ocean Modelling, 140:101400.

Wenegrat, J. O. and McPhaden, M. J. (2016). Wind, waves and fronts: Frictional effects in a generalized Ekman model. J. Phys. Oceanogr., 46:371–394.

Whitt, D. B. and Taylor, J. R. (2017). Energetic submesoscales maintain strong mixed layer stratification during an autumn storm. J. Phys. Oceanogr., 47:2419–2427.